

NIST Technical Note 2180

**Structural Performance of Nuclear Power
Plant Concrete Structures Affected by
Alkali-Silica Reaction (ASR)**

**Task 3: Assessing Cyclic Performance
of ASR-Affected Concrete Shear
Walls**

Jonathan M. Weigand

Fahim Sadek

Travis Thonstad

Sorin Marcu

Rudy Villegas

Long T. Phan

Engineering Laboratory

National Institute of Standards and Technology

Adam L. Pinar

Information Technology Laboratory

National Institute of Standards and Technology

Travis Thonstad

Civil and Environmental Engineering

University of Washington

NIST Technical Note 2180

**Structural Performance of Nuclear Power
Plant Concrete Structures Affected by
Alkali-Silica Reaction (ASR)**

**Task 3: Assessing Cyclic Performance
of ASR-Affected Concrete Shear
Walls**

Jonathan M. Weigand
Fahim Sadek
Sorin Marcu
Rudy Villegas
Long T. Phan

*Engineering Laboratory
National Institute of Standards and Technology*

Adam L. Pintar
*Information Technology Laboratory
National Institute of Standards and Technology*

Travis Thonstad
*Civil and Environmental Engineering
University of Washington*



<https://doi.org/10.6028/NIST.TN.2180>
January 2022

U.S. Department of Commerce
Gina Raimondo, Secretary

National Institute of Standards and Technology
James K. Olthoff, Acting Under Secretary of Commerce for Standards and Technology and Director

Disclaimer No. 1

Certain commercial entities, equipment, or materials may be identified in this document in order to describe an experimental procedure or concept adequately. Such identification is not intended to imply recommendation or endorsement by the National Institute of Standards and Technology, nor is it intended to imply that the entities, materials, or equipment are necessarily the best available for the purpose.

Disclaimer No. 2

The policy of NIST is to use the International System of Units in all publications. In this document, however, units are presented in the system prevalent in the relevant discipline, although in some cases more than one system of units may be presented.

Copyright

This NIST publication is a work of the United States Government not subject to copyright protection within the United States under Title 17 United States Code § 105. This publication may include copyrighted content (such as photographs) used with permission of the credited copyright holder. Reproduction, redistribution or reuse of such copyrighted content apart from this publication may require permission, which should be sought from the credited copyright holder. Where no copyright holder or source is credited for a figure or table in this publication, the source is NIST, which would appreciate attribution.

National Institute of Standards and Technology Technical Note 2180
Natl. Inst. Stand. Technol. Tech. Note 2180, 211 pages (January 2022)
<https://doi.org/10.6028/NIST.TN.2180>
CODEN: NTNOEF

ACKNOWLEDGEMENTS

The authors wish to express gratitude and appreciation to the following current and former NIST colleagues who have provided advice and guidance, ideas and expertise, collaborations, technical contributions, and assistance throughout the duration of this research effort:

- Mses. LeeAnn Ginsburg, Ami Reisinger, Gwynaeth Broome, and Melissa Logan for budgetary advice and administrative and logistical supports, including procurements, acquisitions, meetings, and shipping and receiving;
- Messrs. Patrick Murphy, John Murray, John Hagan and Richard Eason for lending equipment and providing critical assistance with the preparation, instrumentation, and construction of the test specimens;
- Dr. Christopher Segura for offering his expertise and assistance with the design of the test specimens;
- Messrs. Brian Story and Anthony R. Chakalis, and Drs. Christopher Segura and Matthew Speicher for their efforts in the installation of Concrete Structural Reaction Block;
- Dr. James J. Filliben for lending his insights and expertise on the statistical design of experiments; and
- Mr. Louis Potts for his contributions in all the experimental phases of this research, including samples preparation and testing, through a related NIST laboratory project.

Last but not least, the authors would like to sincerely thank United States Nuclear Regulatory Commission staff, for their support and technical guidance throughout the duration of this NRC-sponsored research to study the structural performance of Nuclear Power Plant structures affected by Alkali-Silica Reaction.

ABSTRACT

This report describes the results of Task 3 of a five-task comprehensive research program conducted at the National Institute of Standards and Technology (NIST) under the sponsorship of the U.S. Nuclear Regulatory Commission (NRC). The overall study aims to develop a technical basis for evaluating effects of Alkali-Silica Reaction (ASR), which occurs when the high pH concrete pore solution reacts with certain aggregate mineral phases to form expansive ASR gel and create internal expansive forces that cause cracking in concrete, and may result in degradation of engineering properties and structural capacities of reinforced concrete structures. The report provides detailed information on experimental planning, observations, testing, measurements, and statistical analysis performed to achieve the objective of Task 3, Evaluation of seismic response characteristics of ASR-affected concrete shear walls. It presents experimental results of three ASR-affected shear walls and one nonreactive shear wall subjected to a constant axial compression and reversed cyclic lateral load, along with rigorous statistical analyses that quantify the effects of ASR-induced expansion/degradation and confinement provided by transverse reinforcement in the walls' boundary elements on walls' (1) deformation capacity including cumulative drift capacity, drift at yield moment, drift at peak flexural capacity, drift at 20 % reduction in peak flexural capacity, and peak drift capacity (or ductility); (2) flexural capacity including normalized peak flexural capacity and normalized yield moment; and (3) energy dissipation capacity including cumulative hysteretic energy and hysteretic energy by stage (at a given drift level corresponding to a certain performance objective).

Keywords:

Alkali-silica Reaction; ASR; Compressive Strength; Concrete; Confinement; Cyclic Loading; Ductility; Energy Dissipation; Expansion; Experimental; Flexural Strength; Seismic Testing; Hysteresis; Shear Walls

PREFACE

The technical work reported herein is part of a comprehensive research program carried out by the Engineering Laboratory of the National Institute of Standards and Technology (NIST) on the structural performance of nuclear power plant concrete structures affected by alkali-silica reaction (ASR). The work is funded by the U.S. Nuclear Regulatory Commission (NRC) under Inter-agency agreement NRC-HQ-60-14-I-0004.

TABLE OF CONTENTS

Acknowledgements.....	iii
Abstract.....	iv
Preface	v
Table of Contents.....	vi
List of Figures.....	x
List of Tables.....	xviii
List of Acronyms, Abbreviations, and Notations.....	xix
Metric Conversion Table	xxii
Executive Summary.....	xxv
E.1 Introduction	xxv
E.2 NIST Task 3 Experimental Program.....	xxv
E.3 Findings	xxvii
E.3.1 Concrete Expansion and Reinforcing bars Strain Development	xxvii
E.3.2 Concrete Mechanical Properties	xxviii
E.3.3 Concrete Cracking.....	xxviii
E.3.4 Structural Capacity	xxix
E.4 Conclusions	xxx
Chapter 1 INTRODUCTION.....	1
1.1 Background	1
1.2 Relevant Literature on Seismic Performance of RC Shear Walls	2

1.3	Scope of the NIST Task 3 Study.....	5
1.4	Report Outline	7
Chapter 2	EXPERIMENTAL PROGRAM	9
2.1	Experimental Design and Test Variables.....	9
2.2	Concrete Mixture for Wall Panels.....	11
2.3	Design and Fabrication of RC Wall Specimens.....	12
2.4	Curing of RC Wall Specimens	25
2.5	Test Setup and Loading Protocol	30
2.6	Instrumentation	34
2.7	Project Timeline	42
Chapter 3	OBSERVED RESPONSE.....	44
3.1	ASR-Induced Expansion	44
3.2	Wall Cyclic Testing	48
3.2.1	Non-reactive Wall 4.....	48
3.2.2	Reactive Walls 1 and 3.....	56
3.2.3	Reactive Wall 2	61
Chapter 4	MEASURED RESPONSE during ASR Expansion.....	65
4.1	Concrete Mechanical properties	65
4.1.1	Uniaxial Compressive Strength.....	66
4.1.2	Modulus of Elasticity	69
4.1.3	Splitting Tensile Strength	73
4.2	Reinforcement Mechanical Properties	76
4.3	Expansion Prisms	79
4.4	Environmental Conditions	82
4.5	Strains in the Reinforcement during ASR-Induced Expansion	84
Chapter 5	MEASURED RESPONSE DURING CYCLIC TESTING	96
5.1	Evaluation of Experimental Control System	96

5.2	Response of Wall 1.....	99
5.3	Response of Wall 2.....	108
5.4	Response of Wall 3.....	112
5.5	Response of Wall 4.....	116
5.6	Backbone Responses.....	121
5.7	Summary Quantities and Direct Comparisons between Wall Responses	123
5.7.1	Wall 2 and Wall 4 – Isolated Influence of ASR.....	128
5.7.2	Wall 1 and Wall 2 – Isolated Influence of Transverse Reinforcement Ratio	130
5.7.3	Wall 1 and Wall 3 – Replicate Specimens.....	131
5.7.4	Walls 1, 2, 3, and 4	133
5.8	Summary and Key Observations	136
Chapter 6 STATISTICAL ANALYSIS OF MEASURED DATA		138
6.1	Methodology.....	139
6.1.1	Choosing the LASSO Penalty.....	139
6.1.2	Statistical Significance	140
6.1.3	Baseline Parametrization	140
6.1.4	Uncertainty in Effects Estimates	140
6.2	Results of Statistical Analysis	141
6.2.1	Cumulative Drift Capacity.....	141
6.2.2	Drift Ratio at Yield Moment d_y	146
6.2.3	Drift Ratio at Peak Flexural Capacity, $d_{M_{max}}^+$	148
6.2.4	Drift Ratio at 20 % Reduction in Peak Flexural Capacity, d_u^+	150
6.2.5	Peak Drift Capacity, d_{fail}	151
6.2.6	Normalized Peak Flexural Capacity, M_{max}^+/M_n	152
6.2.7	Normalized Yield Moment, M_y/M_n	154
6.2.8	Cumulative Hysteretic Energy	155
6.2.9	Cumulative Hysteretic Energy by Stage.....	157
6.3	Augmented Normalized Peak Flexural Capacity	159

6.4 Summary	163
Chapter 7 SUMMARY, FINDINGS, AND CONCLUSIONS.....	166
7.1 Summary	166
7.2 Findings	167
7.2.1 Effects of ASR on concrete expansion and reinforcing bar strain development, concrete mechanical properties, and concrete cracking	168
7.2.2 Effects of ϵ_{ASR} and ρ_t on walls' structural capacities.....	169
7.3 Conclusions	171
REFERENCES	173
APPENDIX A MEASUREMENT UNCERTAINTIES	175

LIST OF FIGURES

Figure 1.1: Geometry and dimensions of Oh et al (2002) test specimen (all dimensions in mm). Figure copied from open literature. 1.00 in = 25.4 mm	4
Figure 1.2: Geometry and dimensions of Habibi et al. (2018) test specimen (all dimensions in mm). Figure copied from open literature. 1.00 in = 25.4 mm.	5
Figure 2.1: All 20 designs over the grid $\{-1, 0, 1\} \times \{-1, 0, 1\}$ meeting the experimental constraints. The designs are ordered from top left to bottom right according to their value of the D -criterion. The design in the top left panel is the D-optimal design selected for the experiment.....	11
Figure 2.2: Schematic showing the effect of wall aspect ratio on predominant behavior and failure mode under lateral loading.....	13
Figure 2.3: Geometry and overall dimensions of the shear wall specimens	14
Figure 2.4: Typical reinforcement of wall panels. 1.00 in = 25.4 mm.....	16
Figure 2.5: Reinforcement cage for footing and top cap. 1.00 in = 25.4 mm.....	17
Figure 2.6: Tie-downs for footing and top cap. 1.00 in = 25.4 mm.....	18
Figure 2.7: Formwork and reinforcement of (a) footing, (b) wall, and (c) top cap of the shear wall specimens.	21
Figure 2.8: Concrete placement into the footings formwork and consolidation using vibrators.....	21
Figure 2.9: Loading of aggregates into volumetric truck mixer	22
Figure 2.10: Loading the volumetric truck contents to a concrete mixer truck via a conveyer belt (telebelt).....	22
Figure 2.11: Concrete placement into wall’s formwork and consolidation using vibrators.....	23
Figure 2.12: Loading of aggregates into concrete mixer truck	24
Figure 2.13: Concrete placement into the top cap formwork and consolidation using vibrators.....	25
Figure 2.14. Custom wood frame environmental chamber (a) top view, (b) sectional elevation. 1.00 in = 25.4 mm.	27
Figure 2.15. Bottom of the wood environmental chamber and the footings of wall specimens set in the final position	28
Figure 2.16. Construction of the environmental chamber: (a) exterior wall panels installed immediately after construction of wall specimens; (b) Closed loop spraying system attached to the chamber’s roof; (c) Assembly of the custom environmental chamber completed; and (d) Moisture Room Control Panel (MRCP) + chamber access door (SW corner)	29

Figure 2.17. Experimental setup for testing ASR-affected concrete shear wall specimens (1.000 kip = 4.448 kN).....	30
Figure 2.18. Partially transparent view of test setup for testing concrete shear walls, with applied actuator forces shown as arrows. The vertically spanning actuators apply tension in force control and the horizontally spanning actuator applies tension and compression in displacement control. 32	
Figure 2.19. Five phases of loading for ASR-affected concrete shear wall specimens: elastic loading, three phases corresponding to Immediate Occupancy, Life Safety, and Collapse Prevention performance objectives, and loading to failure. 1.0 in = 25.4 mm.....	33
Figure 2.20. Loading protocol for testing ASR-affected concrete shear wall specimens. Colors denote the five phases of loading for ASR-affected concrete shear wall specimens: elastic loading, three phases corresponding to Immediate Occupancy, Life Safety, and Collapse Prevention performance objectives, and loading to failure.....	34
Figure 2.21. Wall displacement transducer locations (elevation view - West side). 1.0 in = 25.4 mm.....	35
Figure 2.22. Wall deformation measurement locations (elevation view - East side). 1.00 in = 25.4 mm. 36	
Figure 2.23. Nominal location of inclinometers used to measure wall rotations during testing (elevation view – East side). 1.00 in = 25.4 mm.....	37
Figure 2.24. Location and nomenclature of strain gages (west and east curtains) for Walls 1 and 3. 1.00 in = 25.4 mm.	38
Figure 2.25. Location and nomenclature of strain gages (stirrups and ties) for Walls 1 and 3. 1.00 in = 25.4 mm.	39
Figure 2.26. Location and nomenclature of strain gages (west and east curtains) for Walls 2 and 4. 1.00 in = 25.4 mm.	40
Figure 2.27. Location and nomenclature of strain gages (stirrups and ties) for Walls 2 and 4. 1.00 in = 25.4 mm.	41
Figure 2.28. Location of strain gages on west reinforcement curtain of the three reactive walls that were monitored during curing. 1.00 in = 25.4 mm.....	42
Figure 3.1. Wall 2 ASR-induced cracking: (a) north end, (b) south end, and (c) west face. Shown also in (c) is the 20.0 in × 20.0 in (508 mm × 508 mm) square drawn on the west face for cracking index calculation. Cracks highlighted using permanent marker.	46
Figure 3.2. Exudation of a white substance on the face of reactive walls. Cracks highlighted using permanent marker.....	47
Figure 3.3. Cracks on the west face of Wall 4 at a drift ratio of 0.500 % (Cycle 11). Cracks highlighted using permanent marker.	49
Figure 3.4. Cracks on the west face of Wall 4 at a drift ratio of 1.000 % (Cycle 17). Cracks highlighted using permanent marker.	50

Figure 3.5. Maximum crack width versus drift ratio for the four walls during cyclic testing (1.00 in = 25.4 mm).....	51
Figure 3.6. Damage to Wall 4 at a drift ratio of 2.000 % (Cycle 27): (a) spalling of concrete on compression zone and (b) cracks on the west face. Cracks highlighted using permanent marker....	53
Figure 3.7. Spalling of concrete in compression zone of Wall 4 at a drift ratio of 3.000 % (Cycle 29) exposing buckled reinforcement in the boundary element	54
Figure 3.8. Wall 4 at failure at a drift ratio of 4.000 % (Cycle 31): (a) west face and (b) rupture of longitudinal reinforcing bar in the boundary element	55
Figure 3.9. Cracks on the west face at a drift ratio of 1.000 %: (a) Wall 1 (Cycle 22) and (b) Wall 3 (Cycle 20). Cracks highlighted using permanent marker.	58
Figure 3.10. Buckling of longitudinal bars and concrete spalling in the compressive zone (a) Wall 1 at drift ratio of 2.000 % (Cycle 26) and (b) Wall 3 at drift ratio of 1.250 % (Cycle 22)	59
Figure 3.11. Failure of Walls 1 and 3: (a) Wall 1 west face and north end at drift ratio of 3.000 % (Cycle 29) and (b) Wall 3 west face and north end at drift ratio of 2.000 % (Cycle 27).....	60
Figure 3.12. Cracks on the west face of Wall 2 at a drift ratio of 1.500 % (Cycle 23). Cracks highlighted using permanent marker.	62
Figure 3.13. Damage to Wall 2 at a drift ratio of 2.000 % (Cycle 27): (a) cracks on the west face and (b) spalling of concrete on compression zone. Cracks highlighted using permanent marker.	63
Figure 3.14. Wall 2 at failure at a drift ratio of 4.000 % (Cycle 31): (a) west face and (b) rupture of longitudinal reinforcing bar in the boundary element	64
Figure 4.1. Compressive strength of concrete used in the footings (1.00000 psi = 0.00689 MPa).....	66
Figure 4.2. Compressive strength of concrete used in the top caps (1.00000 psi = 0.00689 MPa)	67
Figure 4.3. Compressive strength of reactive and non-reactive concrete used in the wall panels (1.00000 psi = 0.00689 MPa)	68
Figure 4.4. Compressive modulus of elasticity of concrete used in the footings (1.00000 ksi = 0.00689 GPa).....	69
Figure 4.5. Compressive modulus of elasticity of concrete used in the top caps (1.00000 ksi = 0.00689 GPa).....	70
Figure 4.6. Compressive modulus of elasticity of reactive and non-reactive concrete used in the wall panels (1.00000 ksi = 0.00689 GPa)	71
Figure 4.7. Compressive modulus of elasticity versus the square root of compressive strength for cylinders from all wall panels (1.00000 psi = 0.00689 MPa, 1.00000 ksi = 0.00689 GPa)	72
Figure 4.8. Splitting tensile strength of concrete used in the footings (1.00000 psi = 0.00689 MPa).....	73
Figure 4.9. Splitting tensile strength of concrete used in the top caps (1.00000 psi = 0.00689 MPa)	74

Figure 4.10. Splitting tensile strength of reactive and non-reactive concrete used in the wall panels (1.00000 psi = 0.00689 MPa)	75
Figure 4.11. Splitting tensile strength versus the square root of compressive strength for cylinders from all wall panels (1.00000 psi = 0.00689 MPa, 1.00000 ksi = 0.00689 GPa)	76
Figure 4.12. Engineering stress-strain curves for the reinforcing bars used in the wall panels: (a) No. 3 bars, (b) No. 4 bars (1.000 ksi = 6.894 MPa)	78
Figure 4.13. Measured length change for prisms for (a) reactive Walls 1 and 2, (b) reactive Wall 3, and (c) non-reactive Wall 4	81
Figure 4.14. Temperature histories inside the environmental chamber ($^{\circ}\text{F} = 32 + 9^{\circ}\text{C}/5$)	82
Figure 4.15. Measured temperatures inside the reactive walls ($^{\circ}\text{F} = 32 + 9^{\circ}\text{C}/5$)	83
Figure 4.16. Measured strains on reinforcing bars of Wall 1: (a) longitudinal bars in the boundary elements at low heights, (b) longitudinal bars in the boundary elements at intermediate heights, (c) transverse bars at low height, (d) transverse bars at intermediate height, (e) transverse bars at large height, and (f) through-depth ties. 1.00 in/in = 1.00 mm/mm	87
Figure 4.17. Measured strains on reinforcing bars of Wall 2: (a) longitudinal bars in the boundary elements at low heights, (b) longitudinal bars in the boundary elements at intermediate heights, (c) transverse bars at low height, (d) transverse bars at intermediate height, (e) transverse bars at large height, and (f) through-depth ties. 1.00 in/in = 1.00 mm/mm	90
Figure 4.18. Measured strains on reinforcing bars of Wall 3: (a) longitudinal bars in the boundary elements at low heights, (b) longitudinal bars in the boundary elements at intermediate heights, (c) transverse bars at low height, (d) transverse bars at intermediate height, (e) transverse bars at large height, and (f) through-depth ties. 1.00 in/in = 1.00 mm/mm	93
Figure 5.1: Ratio of applied (measured) to target (specified) drift ratio for (a) Wall 1, (b) Wall 2, (c) Wall 3, and (d) Wall 4	97
Figure 5.2: Measured axial load by the 110 kip (498 kN) capacity vertical actuators throughout duration of seismic loading protocol for (a) Wall 1, (b) Wall 2, (c) Wall 3, and (d) Wall 4 (1.000 kip = 4.448 kN)	98
Figure 5.3: Total applied axial load throughout duration of seismic loading protocol for (a) Wall 1, (b) Wall 2, (c) Wall 3, and (d) Wall 4 (1.000 kip = 4.448 kN)	99
Figure 5.4: Response of Wall 1: (a) lateral displacement history, (b) lateral force history, and (c) force-drift hysteresis (1.00 in = 25.4 mm; 1.000 kip = 4.448 kN)	101
Figure 5.5: Point sensor measurements up the height of the Wall 1: (a) horizontal deformation history, (b) rotation history, and (c) in-plane lateral deformation profiles at peak/valley (1.00 in = 25.4 mm)	103
Figure 5.6: Measured strains in longitudinal bars of Wall 1 at height of 0.0 in (0.0 mm): (a) NBW1 (outer bar) and (b) NBW2 (inner bar)	104

Figure 5.7: Hysteretic energy, shown as blue shaded area, of (a) Cycle 05 (Immediate Occupancy), (b) Cycle 14 (Life Safety), (c) Cycle 20 (Collapse Prevention), and (d) Cycle 26 (To Failure). 1.00 in = 25.4 mm; 1.000 kip = 4.448 kN.	105
Figure 5.8: Cyclic hysteretic energy of Wall 1, calculated as area bounded by force-displacement curve for each cycle (a) incremental, and (b) cumulative (1.000 kip in = 0.113 kN m)	106
Figure 5.9: Magnified view of three cycles near peak displacement of 1.80 in (45.7 mm) showing points and regression lines used to extract approach and unload stiffness from cyclic force-displacement hysteresis. (1.000 kip = 4.448 kN, 1.00 in = 25.4 mm)	106
Figure 5.10: Approach and unload stiffness of Wall 1: (a) in units of kip/in (1.000 kip/in = 0.175 kN/mm), and (b) normalized by wall initial stiffness	107
Figure 5.11: Response of Wall 2: (a) lateral displacement history, (b) lateral force history, and (c) force-drift hysteresis (1.00 in =25.4 mm; 1.000 kip = 4.448 kN)	109
Figure 5.12: Point sensor measurements up the height of the Wall 2: (a) horizontal deformation history, (b) rotation history, and (c) in-plane lateral deformation profiles at peak/valley (1.00 in = 25.4 mm)	110
Figure 5.13: Measured strains in longitudinal bars of Wall 2 at height of 0.0 in (0.0 mm): (a) NBW1 (outer bar) and (b) NBW2 (inner bar)	111
Figure 5.14: Cyclic hysteretic energy of Wall 2, calculated as area bounded by force-displacement curve for each cycle (a) incremental, and (b) cumulative (1.000 kip in = 0.113 kN m)	111
Figure 5.15: Cyclic stiffness response of Wall 2: (a) in units of kip/in (1.000 kip/in = 0.175 kN/mm), and (b) normalized by wall initial stiffness	112
Figure 5.16: Response of Wall 3: (a) lateral displacement history, (b) lateral force history, and (c) force-drift hysteresis (1.00 in = 25.4 mm; 1.000 kip = 4.448 kN)	113
Figure 5.17: Point sensor measurements up the height of the Wall 3: (a) horizontal deformation history, (b) rotation history, and (c) in-plane lateral deformation profiles at peak/valley (1.00 in = 25.4 mm)	114
Figure 5.18: Measured strains in longitudinal bars of Wall 3 at height of 0.0 in (0.0 mm): (a) NBW1 (outer bar) and (b) NBW2 (inner bar)	115
Figure 5.19: Cyclic hysteretic energy of Wall 3, calculated as area bounded by force-displacement curve for each cycle (a) incremental, and (b) cumulative (1.000 kip in = 0.113 kN m)	115
Figure 5.20: Cyclic stiffness response of Wall 3: (a) in units of kip/in (1.000 kip/in = 0.175 kN/mm), and (b) normalized by wall initial stiffness.	116
Figure 5.21: Response of Wall 4: (a) lateral displacement history, (b) lateral force history, and (c) force-drift hysteresis (1.00 in = 25.4 mm; 1.000 kip = 4.448 kN)	117

Figure 5.22: Point sensor measurements up the height of the Wall 4: (a) horizontal deformation history, (b) rotation history, and (c) in-plane lateral deformation profiles at peak/valley (1.00 in = 25.4 mm)	118
Figure 5.23: Distribution of total strains along length of north and south longitudinal rebar in boundary elements of Wall 4 at peaks/valleys during phases of loading protocol: (a) elastic, (b) immediate occupancy, (c) life safety, (d) collapse prevention (1.00 in = 25.4 mm)	119
Figure 5.24: Measured strains in longitudinal bars of Wall 4 at height of 0.0 in (0.0 mm): (a) NBW1 (outer bar) and (b) NBW2 (inner bar)	120
Figure 5.25: Cyclic hysteretic energy of Wall 4, calculated as area bounded by force-displacement curve for each cycle (a) incremental, and (b) cumulative (1.000 kip in = 0.113 kN m)	120
Figure 5.26: Cyclic stiffness response of Wall 4: (a) in units of kip/in (1.000 kip/in = 0.175 kN/mm), and (b) normalized by wall initial stiffness	121
Figure 5.27: Backbone response curves (M/M _n versus drift ratio) for: (a) Wall 1, (b) Wall 2, (c) Wall 3, and (d) Wall 4.....	122
Figure 5.28: Adopted notation for coordinates of key points on wall backbone response curve.....	123
Figure 5.29: Example of backbone curve with and elastic and inelastic areas calculated in both negative (-) and positive (+) flexure. 1.000 kip·ft = 1.356 kN·m.	127
Figure 5.30: Comparison of backbone curve with and elastic and inelastic areas calculated in both negative (-) and positive (+) flexure for (a) Wall 1, (b) Wall 2, (c) Wall 3, and (d) Wall 4. 1.000 kip·ft = 1.356 kN·m.	128
Figure 5.31: Comparison between normalized responses of Walls 2 and 4 (a) cyclic hysteresis, and (b) backbone curves	129
Figure 5.32: Comparison of hysteretic energy between Walls 2 and 4 (a) incremental, and (b) cumulative (1.000 kip in = 0.113 kN m)	130
Figure 5.33: Comparison between normalized responses of Walls 1 and 2 (a) cyclic hysteresis, and (b) backbone curves	130
Figure 5.34: Comparison of hysteretic energy between Walls 1 and 2 (a) incremental, and (b) cumulative (1.000 kip in = 0.113 kN m)	131
Figure 5.35: Comparison between normalized responses of Walls 1 and 3 (a) cyclic hysteresis, and (b) backbone curves	132
Figure 5.36: Comparison of hysteretic energy between Walls 1 and 3 (a) incremental, and (b) cumulative (1.000 kip in = 0.113 kN m)	132
Figure 5.37: Comparison between normalized responses of Walls 1, 2, 3, and 4 (a) cyclic hysteresis, and (b) backbone curves.....	133

Figure 5.38: Comparison of hysteretic energy between Walls 1, 2, 3, and 4 (a) incremental, and (b) cumulative (1.000 kip in = 0.113 kN m)	134
Figure 5.39: Percent relative rotation by height for (a) Wall 1, (b) Wall 2, (c) Wall 3, and (d) Wall 4.....	135
Figure 6.1: Estimated regression coefficients as a function of the LASSO penalty. The color indicates the coefficient.	143
Figure 6.2: BIC plotted versus the LASSO penalty.....	144
Figure 6.3: Estimated regression coefficients for two LASSO penalties (large dark-colored points) and bootstrap replicates of them (small light-colored points) for cumulative drift capacity	145
Figure 6.4: Estimated mean cumulative drift capacity for four combinations of ϵ_{ASR} and ρ_t (large dark-colored points), and 100 bootstrap replicates of the estimated mean cumulative drift capacity (small light-colored points).	146
Figure 6.5: Estimated regression coefficients for two LASSO penalties (large dark-colored points) and bootstrap replicates of them (small light-colored points) for drift at yield moment.	147
Figure 6.6: Estimated mean drift at yield moment at the ASR present and absent conditions and $\rho_t = 0.5\%$ (large red circles), and 100 bootstrap replicates of the estimated mean drift at yield moment (small grey circles).	148
Figure 6.7: Estimated regression coefficients for two LASSO penalties (large dark-colored points) and bootstrap replicates of them (small light-colored points) for drift at peak flexural capacity.	149
Figure 6.8: Estimated mean drift at peak flexural capacity at the ASR present and absent conditions and $\rho_t = 0.5\%$ (large red points), and 100 bootstrap replicates of the estimated mean drift at peak flexural capacity (small grey points).	149
Figure 6.9: Estimated regression coefficients for two LASSO penalties (large dark-colored points) and bootstrap replicates of them (small light-colored points) for drift at 20% reduction in flexural capacity.	150
Figure 6.10: Estimated mean drift at ultimate flexural capacity at $\rho_t = 2.0\%$ and 0.5% and ASR absent (large red points), and 100 bootstrap replicates of the estimated mean drift at 20% reduction in flexural capacity (small grey points).	151
Figure 6.11: Peak drift capacity for the four walls, circles slightly moved horizontally and vertically so that the four circles are visible.	152
Figure 6.12: Estimated regression coefficients for two LASSO penalties (large dark-colored points) and bootstrap replicates of them (small light-colored points) for M_{max}^+/M_n	153
Figure 6.13: Estimated mean normalized peak flexural capacity at the ASR present and absent conditions and $\rho_t = 0.5\%$ (large red circles), and 100 bootstrap replicates of the estimated mean M_{max}^+/M_n (small grey circles).	153
Figure 6.14: Estimated regression coefficients for two LASSO penalties (large dark-colored points) and bootstrap replicates of them (small light-colored points) for M_y/M_n	154

Figure 6.15: Estimated mean normalized yield moment at the ASR present and absent conditions and $\rho_t = 0.5\%$ (large red circles), and 100 bootstrap replicates of the estimated M_y/M_n (small grey circles).	155
Figure 6.16: Estimated regression coefficients for two LASSO penalties (large dark-colored points) and bootstrap replicates of them (small light-colored points) for cumulative hysteretic energy	156
Figure 6.17: Estimated mean cumulative hysteretic energy for four combinations of ϵ_{ASR} and ρ_t (large dark-colored points), and 100 bootstrap replicates of the estimated mean cumulative hysteretic energy (small light-colored points). 1.000 kip in = 0.113 kN m	157
Figure 6.18: Estimated regression coefficients (large dark point) and bootstrap replicates of them (small light-colored points) for the longitudinal hysteretic energy response	159
Figure 6.19: Normalized peak flexural capacity response for both the NIST experiments and the experiments from Oh et al. (2002), but with peak flexural capacity from the NIST experiment normalized similarly to the data from the experiments in Oh et al. (2002). Colors delineate ASR condition, and shape delineates experiment.	162
Figure 6.20: Estimated regression coefficients for two LASSO penalties (large dark-colored points) and bootstrap replicates of them (small light-colored points) for the M^+_{max}/M_n	162
Figure 6.21: Estimated mean normalized peak flexural capacity for four combinations of ϵ_{ASR} and ρ_t (large dark-colored points), and 100 bootstrap replicates of the estimated mean M^+_{max}/M_n (small light-colored-points).	163

LIST OF TABLES

Table E.1. Key parameters of the NIST Task 3 wall specimens	xxvi
Table 1.1. Key parameters of the NIST Task 3 wall specimens	6
Table 2.1. ASR Mix 3 Concrete Proportions	12
Table 2.2. Project timeline	43
Table 3.1. Average cracking index for the reactive wall specimens prior to testing	48
Table 3.2. Maximum crack width measurement uncertainty.....	51
Table 4.1. Compressive strength of reactive and non-reactive concrete used in the wall panels	68
Table 4.2. Compressive modulus of elasticity of reactive and non-reactive concrete used in the wall panels.....	71
Table 4.3. Splitting tensile strength of reactive and non-reactive concrete used in the wall panels.....	75
Table 4.4. Measured properties of reinforcement	78
Table 5.1. Summary of wall response quantities in negative (-) and positive (+) flexure.....	124
Table 5.2. Summary of wall response quantities in negative (-) and positive (+) flexure, normalized by the responses of the Wall 4, which did not have ASR	125
Table 5.3. Concrete shear wall specimen initial stiffness (in units of lateral force divided by lateral displacement) and elastic and inelastic areas in negative (-) and positive (+) flexure	126
Table 6.1. Measured performance data for NIST wall specimens	142
Table 6.2. Normalized peak flexural capacity for the NIST wall specimens and the specimens from Oh et al. (2002). In contrast to Table 6.1, the peak flexural capacity is normalized to the measured yield strength of the reinforcing bars instead of the nominal yield strength.	161

LIST OF ACRONYMS, ABBREVIATIONS, AND NOTATIONS

Acronyms

ACI	American Concrete Institute
AISC	American Institute of Steel Construction
ASCE	American Society of Civil Engineers
ASR	Alkali-silica reaction
ASTM	American Society for Testing and Materials
BIC	Bayesian Information Criterion
CI	Cracking index
CP	Collapse Prevention
CSRB	Concrete Structural Reaction Block
EL	Engineering Laboratory
IO	Immediate Occupancy
LASSO	Least absolute shrinkage and selection operator
LBF	lateral bracing frame
LS	Life Safety
MRCP	Moisture Room Control Panel
NIST	National Institute of Standards and Technology
NPP	Nuclear power plant
NRC	Nuclear Regulatory Commission
OLS	ordinary least squares
RC	Reinforced concrete
RH	Relative humidity

Abbreviations

d	day
ft	foot

gal	gallon
GPa	gigapascal
h	hour
in	inch
kg	kilogram
kip	a force equal to 1,000 pound force
kN	kilonewton
ksi	kip per square inch
lbf	pound force
L	liter
m	meter
min	minute
mm	millimeter
MPa	Megapascal
psi	pounds per square inch
s	second
yd	yard

Notation

A_g	Gross concrete sectional area
d_{fail}	Peak drift capacity (drift ratio at failure)
d_{Mmax}	Drift ratio at peak flexural capacity
d_u	Drift ratio at 20 % reduction in flexural capacity
d_y	Drift ratio at yield moment
E_c	Modulus of elasticity of concrete, psi
f'_c	Specified compressive strength of concrete
f_{cm}	Measured average compressive strength of concrete
f_{ct}	Measured average splitting tensile strength of concrete
f_u	Ultimate tensile strength of reinforcement
f_y	Yield strength of reinforcement

h_w	Overall wall height between the point of lateral load application and the top of the specimen footing
k	Coverage factor
K	Wall's initial stiffness
l_w	Wall length
M_{max}	Maximum measured moment strength during testing
M_n	Nominal moment capacity of the wall section based on ACI318-19
M_y	Moment at yield of longitudinal reinforcement
n	Number of measurements
N	Number of degrees of freedom
P	Applied force
RH	Relative humidity
u_c	Combined standard uncertainty
U	Uncertainty measure
y_i	Measured response of wall i
α	Intercept of regression equation
β_ε	Regression coefficient corresponding to ASR expansion
$\beta_{\varepsilon\rho}$	Regression coefficient corresponding to the interaction of ASR expansion and confinement effects
β_ρ	Regression coefficient corresponding to Volumetric ratio of transverse reinforcement in the boundary element
δ_i	Random error
ε_{ASR}	ASR-induced linear expansion
$\varepsilon_{ASR-ult}$	Design ultimate expansion level of a concrete mixture
μ_c	Mean value of a variable
ρ_t	Volumetric ratio of transverse reinforcement in the boundary element
ρ_l	longitudinal reinforcement ratio = Ratio of area of longitudinal reinforcement to cross sectional area of concrete
θ	Drift ratio

METRIC CONVERSION TABLE

To convert from	to	Multiply by
AREA AND SECOND MOMENT OF AREA		
square foot (ft ²)	square meter (m ²)	9.290 304 E-02
square inch (in. ²)	square meter (m ²)	6.4516 E-04
FORCE		
kilogram-force (kgf)	newton (N)	9.806 65 E+00
kilopond (kilogram-force) (kp)	newton (N)	9.806 65 E+00
kip (1 kip=1,000 lbf)	newton (N)	4.448 222 E+03
kip (1 kip=1,000 lbf)	kilonewton (kN)	4.448 222 E+00
pound-force (lbf)	newton (N)	4.448 222 E+00
FORCE DIVIDED BY LENGTH		
pound-force per foot (lbf/ft)	newton per meter (N/m)	1.459 390 E+01
pound-force per inch (lbf/in.)	newton per meter (N/m)	1.751 268 E+02
LENGTH		
foot (ft)	meter (m)	3.048 E-01
inch (in)	meter (m)	2.54 E-02
MASS and MOMENT OF INERTIA		
kilogram-force second squared per meter (kgf · s ² /m)	kilogram (kg)	9.806 65 E+00
pound foot squared (lb · ft ²)	kilogram meter squared (kg · m ²)	4.214 011 E-02
pound inch squared (lb · in. ²)	kilogram meter squared (kg · m ²)	2.926 397 E-04

To convert from	to	Multiply by
PRESSURE or STRESS (FORCE DIVIDED BY AREA)		
kilogram–force per square centimeter (kgf/cm ²)	pascal (Pa)	9.806 65 E+04
kilogram–force per square meter (kgf/m ²)	pascal (Pa)	9.806 65 E+00
kilogram–force per square millimeter (kgf/mm ²)	pascal (Pa)	9.806 65 E+06
kip per square inch (ksi) (kip/in. ²)	pascal (Pa)	6.894 757 E+06
kip per square inch (ksi) (kip/in. ²)	kilopascal (kPa)	6.894 757 E+03
pound–force per square foot (lbf/ft ²)	pascal (Pa)	4.788 026 E+01
pound–force per square inch (psi) (lbf/in. ²)	pascal (Pa)	6.894 757 E+03
pound–force per square inch (psi) (lbf/in. ²)	kilopascal (kPa)	6.894 757 E+00
psi (pound–force per square inch) (lbf/in. ²)	pascal (Pa)	6.894 757 E+03
psi (pound–force per square inch) (lbf/in. ²)	kilopascal (kPa)	6.894 757 E+00



EXECUTIVE SUMMARY

E.1 INTRODUCTION

This report describes work that is part of a comprehensive research program conducted by the Engineering Laboratory (EL) of the National Institute of Standards and Technology (NIST) to study the effects of alkali-silica reaction (ASR) on the structural performance of nuclear power plant concrete structures. The work is funded by the U.S. Nuclear Regulatory Commission (NRC) under Inter-Agency Agreement NRC-HQ-60-14-I-0004. The objective of this research is to develop a technical basis for generic regulatory guidance for evaluation of ASR-affected nuclear power plant (NPP) concrete structures through its service life. The research program is specifically designed to develop measurements for evaluation of (1) the effects of ASR on structural performance and capability to perform intended functions under design basis static and dynamic loads, and (2) characteristics of an aging management program to adequately monitor and manage aging effects of ASR degradation such that intended functions are maintained through the period of extended operation of renewed licenses. The intended outcome is a methodology for determining, for an existing ASR-affected structure, its (1) in-situ structural capacity to resist design-basis static and dynamic loads and (2) future structural capacity.

The overall research program is made up of five tasks, each with an associated major objective:

Task 1: Assess effects of ASR on in-situ mechanical properties of concrete;

Task 2: Assess development and lap-splice lengths of reinforcing bars in ASR-affected concrete;

Task 3: Evaluate seismic response characteristics of ASR-affected concrete structural members;

Task 4: Estimate the degree of reaction in ASR-affected concrete and the corresponding expansion; and

Task 5: Predict future and ultimate ASR expansion in ASR-affected concrete.

This report focuses on Task 3, evaluation of the seismic performance of ASR-affected reinforced concrete (RC) shear walls. Specifically, this report describes the experimental planning (material selection to achieve target ASR expansion; specimens design, instrumentation, fabrication, curing, and reversed cyclic lateral load test protocol); pre-test measurements; data collection and analysis of test results; and findings and conclusions that pertain to Task 3 of this NRC-sponsored research program.

E.2 NIST TASK 3 EXPERIMENTAL PROGRAM

The NIST Task 3 experimental program conducted pseudo-static, reversed cyclic lateral loading under constant axial compression test to evaluate the seismic performance of four reinforced concrete shear wall specimens, with three having their wall panels made of reactive concrete (using reactive coarse and

fine aggregates), and one having its wall panel made of the same reactive concrete, but treated with a lithium nitrate solution to mitigate ASR as control specimen. The three reactive specimens were made of the same reactive concrete mixture ASR 3 used in the NIST Task 1 and Task 2 experimental programs (with ultimate ASR-induced expansion $\epsilon_{ASR-ult} = 0.3\%$, see Sections 2.2, and Sadek et al. (2021) and Thonstad et al. (2021) for ASR 3 mixture proportions and other properties). The three reactive specimens were cured in the NIST environmental chamber at high temperature and relative humidity to accelerate ASR expansion in the test wall panels to a specified target level prior to structural testing.

The experimental program was designed to facilitate examination of the influence of two primary variables: (1) the level of ASR-induced expansion, $0\% \leq \epsilon_{ASR} \leq 0.25\%$, measured as averaged maximum recorded strains in the reinforcements in the test wall panels; and (2) the level of confinement in the boundary elements of the wall panels, $0.5\% \leq \rho_t \leq 2.0\%$, as measured by the volumetric ratio of transverse reinforcement in the boundary element, on the walls' structural performance in terms of their flexural capacity (yield and peak moment capacities), deformation capacity (drift ratios corresponding to various load levels), and energy dissipation capacity (hysteretic energy at a given drift level corresponding to a certain performance objective and cumulative hysteretic energy).

All four NIST shear wall specimens had a rectangular cross section of 8.0 in (203 mm) thick \times 60.0 in (1520 mm) long (l_w); and a height between the footing and the top cap of 80.0 in (2030 mm), resulting in an overall height, h_w , between the point of lateral load application and the top of the specimen footing of 120.0 in (3048 mm) and a height-to-length aspect ratio h_w/l_w of 2.0. All had a longitudinal reinforcement ratio ρ_l of 0.61%, with the transverse reinforcement ratios in the walls' boundary elements ρ_t varied from 0.5% to 2.0%. The geometry and the reinforcement ratios of the NIST wall specimens were selected to match non-reactive walls previously tested by Oh et al. (2002) to facilitate independent comparisons of the test results. Key parameters of the NIST Task 3 shear wall specimens are shown on Table E.1.

Table E.1. Key parameters of the NIST Task 3 wall specimens

Specimen	Wall Aspect Ratio ⁽¹⁾		Transverse Reinforcement Ratio in Boundary Elements ρ_t (%)	Longitudinal Reinforcement Ratio ρ_l (%)	Target Expansion ϵ_{ASR} at Test Time ⁽²⁾ (% of $\epsilon_{ASR-ult}$)
	h_w/l_w	l_w/h			
Wall 1	2.0	7.5	0.5	0.61	50
Wall 2	2.0	7.5	2.0	0.61	100
Wall 3	2.0	7.5	0.5	0.61	100
Wall 4	2.0	7.5	2.0	0.61	0 (non-reactive, control specimen)

⁽¹⁾ h_w : wall height; l_w : wall length; h : wall thickness. h_w/l_w : wall height-to-length aspect ratio; l_w/h : length-to-thickness (shear) aspect ratio.

⁽²⁾ These represent "experimentally planned" expansion levels at test time. See actual measured ϵ_{ASR} at test time for each wall specimen in Section 4.5.

During cyclic load testing, all specimens were subjected to a constant 200 kip (890 kN) axial compression, which is equivalent to $0.093 A_g f'_c$ (where A_g is the gross sectional area of the wall and f'_c is the specified compressive strength of concrete) on the test wall panels, while undergoing increasing levels of cyclic lateral deformations at drift ratios corresponding to ASCE 41-17 Seismic Evaluation and Retrofit of Existing Buildings (ASCE, 2017)'s performance objectives, namely Elastic; Immediate Occupancy (IO); Life Safety (LS); Collapse Prevention (CP); and To Failure. The purpose of the selected levels of cyclic loading was to cover a range of structural performance from elastic to failure, with measurements regularly interspersed throughout the intermediate stages.

In addition to the four wall specimens, a sufficient number of companion concrete cylinders and prisms were also made, cured, and tested at certain time intervals for use in characterizing variations in the concrete mechanical properties (compressive strength, modulus of elasticity, and splitting tensile strength) and ASR-induced linear expansion as functions of age.

Finally, statistical analyses of the test results using the least absolute selection and shrinkage operator (LASSO) regression models were performed to quantify the effects of the test variables ϵ_{ASR} and ρ_t on the structural performance of ASR-affected shear walls.

E.3 FINDINGS

Specific findings of the NIST experimental program are statistically valid over the ranges of experimental parameters examined (ϵ_{ASR} of about 0.25 %; $0.5 \% \leq \rho_t \leq 2.0 \%$; and $h_w/l_w = 2.0$), and for the selected mixture proportioning, types of aggregate used, and curing regime. The findings are summarized below, grouped below in terms of effects of ϵ_{ASR} and ρ_t on the following performance characteristics:

E.3.1 Concrete Expansion and Reinforcing bars Strain Development

- No significant differences were observed between the ASR-induced expansions, ϵ_{ASR} , of the three reactive concrete shear walls, measured as averaged maximum recorded strain on the reinforcements. Taken together, strain data from the three reactive walls showed that the largest recorded strain measurement was about 0.25 % for Walls 1 and 3 and 0.23 % for Wall 2 at the end of the curing period and prior to structural testing. These strain values might have been exceeded in the reinforcing bars that experienced yielding since no meaningful data was available after yielding.
- ASR-induced expansion was less for regions with more restraint. In general, for the longitudinal reinforcing bars in the boundary elements, strain gages near the footings, which were cast from conventional, nonreactive concrete, recorded less strains than those placed at mid-height of the wall panel. Similarly, transverse bars at mid-height of the wall also recorded the largest tensile strains, being farther from the constraint of the wall's footing and top cap. This trend was expected due to the restraint to the wall expansion provided by the non-expansive wall's footing and top cap.

-
- Unrestrained ASR-induced concrete linear expansion, measured using unreinforced standard prisms made with the same concrete and cured under the same regime as the reactive wall specimens, was up to 0.25 %. This level of unrestrained concrete linear expansion was consistent with the averaged maximum recorded strain measured by strain gages on the reinforcing bars of the reactive wall specimens ($\epsilon_{ASR} = 0.25\%$ for Walls 1 and 3, and $= 0.23\%$ for Wall 2, see above and Section 4.5). However, this is likely just a coincidence as the strain recorded at various discreet locations on the reinforcements might actually underrepresent the overall walls' expansion (strain gages not located at places where maximum expansion occurred, and gages malfunctioned shortly after yielding of the reinforcements).
 - Toward the end of the curing period and prior to structural testing, several reinforcing bars might have yielded or were approaching yielding. These included the longitudinal bars in the boundary elements at approximately mid-height (between 10.0 in [254 mm] and 40.0 in [1016 mm] above the footings) and the transverse reinforcing bars at different heights.
 - The average ASR-induced strains in the longitudinal bars in the boundary elements at their interface with the footings was found to be $0.113\% \pm 0.013\%$. This value was taken as the pre-existing, ASR-induced, pre-strain at the base of the wall where failure is expected to start and propagate during cyclic testing.

E.3.2 Concrete Mechanical Properties

- Concrete mechanical properties, measured by standard testing at different ages of 4.0 in (102 mm) \times 8.0 in (203 mm) cylinders that were cast at the same time with the wall specimens and cured under the same environmental conditions, decreased with increasing ASR-induced expansion. The maximum reductions, relative to their measured 28-day values, were about 30 %, 70 %, and 40 % for the compressive strength, compressive modulus of elasticity, and splitting tensile strength, respectively. These decreases in the mechanical properties are consistent with the findings of the Task 1 report (Sadek et al., 2021) and Task 2 report (Thonstad et al., 2021), albeit with different reduction magnitudes. For the non-reactive cylinders from Wall 4, no such reduction in compressive strength, compressive modulus of elasticity, or tensile strength was observed. On the contrary, strengths of the non-reactive concrete were consistently larger than their measured 28-day values.
- The relationship between the concrete modulus of elasticity and the compressive strength for normalweight, nonreactive concrete prescribed by ACI 318-19 (Section 19.2.2.1(b)) overpredicted the compressive modulus of the reactive concrete by up to 50 %. This was particularly evident at higher expansion values and indicates that the modulus of elasticity degraded faster with increased ASR expansion than did the compressive strength. This was consistent with the findings of the Task 1 report (Sadek et al., 2021) and Task 2 report (Thonstad et al., 2021).

E.3.3 Concrete Cracking

- Significant ASR-induced surface cracking was observed on all three reactive wall panels prior to structural testing, along with exudation of a substance, presumed to be ASR gel, from the cracks onto the panel surfaces. The pattern of ASR-induced cracking was randomly oriented and did not appear to be preferentially aligned with the embedded reinforcement. No discoloration was observed that would suggest corrosion of the reinforcement bars prior to structural testing. No discernable differences were found between the cracking pattern on the surfaces of the three reactive wall panels despite their differences in age at the time of observation and the amount of transverse confinement in the boundary elements.

E.3.4 Structural Capacity

Deformation Capacity

- Both the presence of ASR and decreasing the transverse reinforcement ratio in the boundary elements, ρ_t , were found to have a negative effect on the walls' cumulative drift capacity, causing a reduction of 10 % and almost 20 %, respectively. Relative to the ASR absent and $\rho_t = 2.0$ % combination, these are decreases of 8 % and 16 %, respectively. The regression model (see Equation 6.1) showed that from a wall without ASR and high ρ_t (ASR absent [$\epsilon_{ASR} = 0$ %] and $\rho_t = 2.0$ %) to a wall with ASR and low ρ_t (ASR present [$\epsilon_{ASR} = 0.25$ %] and $\rho_t = 0.5$ %), the estimated mean cumulative drift capacity decreases by about 10 % + 20 % = 30 % (or 24 % relative). There is no evidence that the effect of one variable on the walls' cumulative drift capacity depends on the other variable (i.e., no evidence of an interaction).
- The presence of ASR negatively affected the drift at yield moment d_y (i.e., the presence of ASR decreases d_y). For the level of ϵ_{ASR} examined in this study (≤ 0.25 %), the mean d_y of reactive Walls 1, 2, and 3 decreased by 54 % when compared with that of non-reactive Wall 4. This decrease is attributed to the ASR-induced pre-strain in the longitudinal reinforcing bars of the three reactive specimens prior to structural testing, which led to the onset of inelasticity at lower drift ratios during testing. There was no evidence that decreasing transverse reinforcement ratio in the boundary element, ρ_t , affects drift at yield moment d_y .
- The presence of ASR also negatively affected drift at peak flexural capacity d_{Mmax}^+ . By direct comparison, the average d_{Mmax}^+ in negative and positive flexure of reactive Walls 1 through 3 were 50.7 % and 56.8 %, respectively, relative to those of non-reactive, control Wall 4. The statistical analysis estimated that, for the level of ϵ_{ASR} considered in this study, there was a reduction of 23 % in the mean d_{Mmax}^+ when ASR is present. There was no evidence that decreasing transverse confinement ratio ρ_t affects drift at peak flexural capacity d_{Mmax}^+ .
- There was no evidence that the presence of ASR affected drift at 20 % reduction in flexural capacity, d_u , while decreasing transverse reinforcement ratio, ρ_t , was found to negatively affect d_u (as ρ_t decreases, d_u decreases). It is estimated that decreasing ρ_t from 2.0 % to 0.5 % caused a 21 % reduction in d_u .
- The walls' ductility, measured by the peak drift capacity d_{fail} , was not adversely affected by the presence of ASR for any of the walls tested; however, ductility was influenced by the transverse reinforcement ratio, ρ_t , in the boundary elements; i.e., decreasing ρ_t resulted in decreasing d_{fail} . Both

specimens with $\rho_t = 0.5\%$ achieved $d_{fail} = 3.0\%$ drift ratio, while both specimens with $\rho_t = 2.0\%$ achieved $d_{fail} = 4.0\%$ drift ratio. These observations were made only from inspection of the test data. The statistical methods of Chapter 6 were not applied for the reasons discussed within it.

- Reduction of the initial stiffness of the ASR-affected walls' force-drift flexural response, K , (see Chapter 5) was not observed despite the observed ASR-induced cracking and reduction of concrete mechanical properties.

Flexural Capacity

- The presence of ASR had a statistically significant negative effect on the yield moment of the walls and caused a reduction of about 26 % in the walls' mean normalized yield moment capacity, M_y/M_n . None of the ASR-affected walls met the ACI 318-19 design criteria, which is based on yielding of the longitudinal bars in the boundary elements ($M_y/M_n < 1.0$), the estimated mean value of M_y/M_n was less than 1.0, and approximately 90 % of the bootstrap replicates of the estimated mean of M_y/M_n were less than 1.0.
- The presence of ASR also had a statistically significant negative effect on the peak flexural capacity of the walls. The measured average peak flexural resistance in negative and positive flexure of reactive Walls 1 through 3 were 85.6 % and 88.1 %, respectively, relative to those of the non-reactive control wall specimen (Wall 4). Averaging the measured flexural capacities in both negative and positive flexure, the presence of ASR was estimated to cause a reduction of about 11 % in the walls' mean normalized peak flexural capacity M^*_{max}/M_n .
- There was no evidence that variation of the transverse reinforcement ratio, ρ_t , in the walls' boundary elements ($0.5\% \leq \rho_t \leq 2.0\%$) had an effect on either walls' normalized yield moment (M_y/M_n) or normalized peak flexural capacity (M^*_{max}/M_n).

Energy Dissipation Capacity

- The presence of ASR and decreasing ρ_t negatively affected cumulative hysteretic energy. Relative to the ASR absent and $\rho_t = 2.0\%$ combination, for the level of ϵ_{ASR} in this study, it is estimated that the mean cumulative hysteretic energy decreases by 14 % with the presence of ASR, and changing ρ_t from 2.0 % to 0.5 % is estimated to cause a decrease in mean cumulative hysteretic energy by about 17 %.
- The presence of ASR generally increased the amount of hysteretic energy dissipated in a given cycle, because reactive walls yielded at lower drift ratios, due to the ASR-induced pre-strain in the longitudinal bars of their boundary elements, leading to increased inelasticity and energy dissipation at lower drifts.
- The non-reactive, control Wall 4 specimen dissipated the largest total hysteretic energy, not because it dissipated more energy per cycle, but because it achieved the largest cumulative drift capacity compared with the three reactive Walls 1 through 3.

Behavior and Failure Modes

- Non-reactive Wall 4 and reactive Wall 2, both with $\rho_t = 2.0\%$, exhibited flexural-shear behavior characterized by a combination of horizontal and diagonal cracks. Reactive Wall 1 and 3, both with ρ_t

= 0.5 %, exhibited predominantly flexural behavior that was characterized primarily by horizontal cracks. In all reactive walls, cracks already present at the beginning of testing due to ASR-induced expansion then grew and propagated with increased drift ratio.

- Under the cyclic load testing of the four walls, the walls failed primarily in a flexural mode, with (1) buckling of longitudinal reinforcement in the boundary element resulting in spalling/crushing of concrete and exposing of the buckled reinforcement at the compression zone, and (2) excessive yielding and in some cases fracture of the longitudinal reinforcing bars of the boundary element on the tensile zone. Reactive Walls 1 and 3 with $\rho_t = 0.5\%$ lost their axial capacity and collapsed in a “squash mode” under the effect of the 200 kip (890 kN) vertical load that was still in effect.

E.4 CONCLUSIONS

The conclusions presented below, and the specific findings presented above, should be interpreted within the scope of the experimental program conducted and the ranges of experimental variables examined:

- Consistent with observations made in the NIST Task 1 report (Sadek et al., 2021) and Task 2 report (Thonstad et al., 2021), the presence of ASR caused significant cracking and degradation in concrete mechanical properties of the NIST shear wall specimens (30 %, 70 %, and 40 % reduction in compressive strength, modulus of elasticity, and splitting tensile strength, respectively).
- The presence of ASR and its associated effects on concrete material properties and cracking were found to cause statistically significant degradation in the structural capacities of shear walls. Specifically, within the bounds of the experimental parameters examined, the presence of ASR caused a reduction of 11 % in the mean normalized peak moment capacity (M_{max}^*/M_n) and of 26 % in the mean normalized yield moment capacity (M_y/M_n) of the shear walls tested in this program.
- More importantly, the structural capacity degradation that resulted from the presence of ASR brought the normalized yield moment capacity ratios M_y/M_n for all ASR-affected walls in this test program to less than 1.0 (0.79, 0.67, and 0.68 for Walls 1, 2, and 3, respectively). As the nominal wall’s moment capacity M_n is computed using ACI 318 calculation procedure based on yielding of the longitudinal bars in the wall, the measured yield moment capacity M_y being less than M_n means that ACI 318 capacity calculation procedure is unconservative and not applicable for walls affected by ASR.
- Since the NIST test program effectively examined only two ASR expansion levels ($\epsilon_{ASR} = 0\%$ and $0.23\% \leq \epsilon_{ASR} \leq 0.25\%$), it’s not possible to interpolate to determine the effect of intermediate expansion levels within those two limits on the walls’ structural capacity with statistical confidence.
- ASR also caused statistically significant degradation in the walls’ deformation and energy dissipation capacities, including drift at yield moment d_y , drift at peak flexural capacity d_{Mmax}^* , and cumulative hysteretic energy.

-
- While increasing the transverse reinforcement ratio in the boundary element ρ_t was not found to influence the wall's peak flexural capacity, the reduction in the deformation and energy dissipation capacity with the presence of ASR was less severe for shear walls with higher ρ_t .
 - Finally, the completion of this NIST Task 3 test program has provided the second set of known experimental data examining the effect of ASR on shear wall's structural performance beside that of Habibi et al. (2018) to date. While important knowledge and understanding have been developed as a result, it's important to recognize that there are still limitations, mostly due to the experimental parameters studied, that make comparison and generalization of the findings from both test programs beyond the range of experimental parameters not advisable. Additional test data of shear walls with different cross-sectional geometry (I-shaped and rectangular cross section); wall height-to-length aspect ratios h_w/l_w (between and beyond 1.1 tested by Habibi et al., 2018 and 2.0 tested by NIST and Oh et al., 2002), with and without wall boundary elements; and intermediate and additional levels of ASR expansion ($0.0\% \leq \epsilon_{ASR} \leq 0.3\%$) would be needed before interpolation or extrapolation of the experimental results for predicting the performance of walls with different design parameters can be considered appropriate.

Chapter 1

INTRODUCTION

1.1 BACKGROUND

Alkali-silica reaction (ASR) has long been recognized as a major cause of concrete internal cracking and deterioration (Stanton, 1940). This concrete deterioration mechanism begins with reaction between the alkali hydroxides in the cement paste and certain amorphous or micro-crystalline siliceous phases in the aggregates, which produces an alkali-silica gel that forms initially in the partially saturated pore space of the hardened cement paste. The alkali-silica gel is hygroscopic, absorbing moisture in the concrete matrix and expanding. This expansion will persist if moisture and other necessary conditions are present. Expansion of alkali-silica gel creates increasing internal pressure that leads to internal cracking and corresponding degradation of the mechanical properties of concrete (Hansen, 1944; Taylor, 1990; Phan et al., 2019; Sadek et al., 2021; Thonstad et al., 2021).

The rate of ASR expansion is relatively slow and is a function of the reactivity of the mineral phases, the alkalinity of the pore solution, and the availability of moisture. The onset of ASR-induced cracking can take years or decades after construction. However, once initiated, this deterioration at the material level has generally been shown to induce (1) expansion in the concrete and tensile stress in the reinforcement, (2) possible degradation of bond between the reinforcement and concrete, and (3) possible degradation of the overall structural capacity and service life of reinforced concrete members or systems.

At present, the industry solution is to identify the reactive aggregates and avoid using them through sourcing of materials for construction, and/or use fly ash pozzolan to control reactivity. Although this approach helps to avoid or mitigate ASR in new construction, it does not address the problem in existing structures. Given knowledge gaps on the effects of ASR on structural capacities and lack of consensus standards and code provisions to account for these effects, questions remain on how to (1) predict the progression of ASR-induced deterioration once initiated, and (2) evaluate the residual material properties and in-situ structural capacity of the ASR-affected structures. These considerations are particularly relevant for safety critical components of the nation's infrastructure such as dams, bridges, and nuclear power plants. Reasonable predictions of the progression of ASR and future, residual structural capacities can provide critical support for decisions on whether the ASR-affected structures can continue to perform their functions without significantly increased risk to public safety.

This report describes work that is part of a comprehensive research program conducted by the Engineering Laboratory of the National Institute of Standards and Technology (NIST) to study the effects of ASR on the structural performance of nuclear power plant concrete structures. The work is funded by the U.S. Nuclear Regulatory Commission (NRC) under Inter-Agency Agreement NRC-HQ-60-14-I-0004. The objective of this research is to develop a technical basis for generic regulatory guidance for evaluation of ASR-affected nuclear power plant (NPP) concrete structures through its service life. The research program was specifically designed to develop measurements for evaluation of (1) the effects of ASR on structural performance and capability to perform intended functions under design basis static and dynamic loads,

and (2) characteristics of an aging management program to adequately monitor and manage aging effects of ASR degradation such that intended functions are maintained through the period of extended operation of renewed licenses. The intended outcome is a methodology for determining, for an existing ASR-affected structure, its (1) in-situ structural capacity to resist design-basis static and dynamic loads and (2) future structural capacity.

The overall research program is made up of five tasks, each with an associated major objective:

Task 1: Assess effects of ASR on in-situ mechanical properties of concrete;

Task 2: Assess development and lap-splice lengths of reinforcing bars in ASR-affected concrete;

Task 3: Evaluate cyclic response characteristics of ASR-affected concrete structural members;

Task 4: Estimate the degree of reaction in ASR-affected concrete and the corresponding expansion; and

Task 5: Predict future and ultimate ASR expansion in ASR-affected concrete.

The focus of Task 3 is evaluation of the seismic performance of ASR-affected reinforced concrete (RC) shear walls. Specifically, this report describes the experimental planning (material selection to achieve target ASR expansion; specimens design, instrumentation, fabrication, curing, and reversed cyclic lateral load test protocol); pre-test measurements; data collection and analysis of test results; and findings and conclusions that pertain to Task 3 of this NRC-sponsored research program described above.

1.2 RELEVANT LITERATURE ON SEISMIC PERFORMANCE OF RC SHEAR WALLS

There exists test data on the seismic performance of RC structural walls. Most of these data are compiled and stored in the Joint American Concrete Institute (ACI)-American Society of Civil Engineers (ASCE) Subcommittee 445-B Structural Wall Performance Database (https://purr.purdue.edu/dataviewer/view/publication:dsl/prj_db_1217_73f6b9aac89601c528539ffc83c2b7afae6aca35/?v=1, ACI 445B, 2017). As of its most recent update in April 2017, the ACI 445B database contained 521 wall tests providing information on the effects of (1) concrete strength (normal and high-strength concrete); (2) welded wire mesh reinforcement; (3) high-strength reinforcement (80 ksi [550 MPa]); (4) wall cross-section (rectangular and I-shaped); (5) axial load level; (6) degree of transverse reinforcement confinement in the wall boundaries; (7) anchorage detailing; (8) wall web reinforcement discontinuity; (9) slenderness; and (10) static vs. dynamic loading on the seismic performance of structural walls with aspect ratios ranging from 0.2 (low-rise “squat” wall that fails predominantly due to shear) to 4.2 (tall wall that fails predominantly due to flexure). The aspect ratio of a wall is typically defined as the height of the wall, h_w , between the point of lateral load application and the top of the specimen’s footing, divided by the length of the wall, l_w . In these tests, the walls were typically subjected to combined reversed cyclic lateral displacements simulating earthquake motions and constant axial compressive stress simulating the service load supported by the walls. However, none of the tests in this existing database have considered the effects of ASR.

Of relevance to the NIST Task 3 study are two sets of experimental data: one by Oh et al. (2002), which studied the influence of transverse reinforcement ratio in the wall boundary elements on the seismic performance of normal, non-reactive RC structural walls, and the other by Habibi et al. (2018); the only study examining the effects of ASR on shear wall's seismic performance. The data by Oh et al. (2002) is included in the ACI 445-B database but the data by Habibi et al. (2018) is not included in the database.

In the study by Oh et al. (2002), four non-reactive RC wall specimens (three with rectangular plan cross-section and one with an I-shaped plan cross-section), all with a height-to-length aspect ratio of 2.0 (walls with this intermediate height-to-length aspect ratio typically fail under combined flexural and shear mode), were tested under combined constant axial compression and reversed cyclic lateral displacements to simulate earthquake loading conditions. Figure 1.1 shows the typical geometry and dimensions of the wall specimens tested by Oh et al. (2002). The concrete had a design compressive strength of 4,000 psi (27.6 MPa). The reinforcement details for confinement of the boundary elements consisted of both open hoops and cross ties with spacings varied to produce four levels of volumetric transverse reinforcement ratios ρ_t in the boundary elements of 0 %, 0.99 %, and 1.97 % for the rectangular walls and 0.94 % for the I-shaped wall. Test results indicated that (1) the specimens failed primarily in flexure, with yielding followed by buckling of longitudinal reinforcement and crushing failure of concrete in the compression zone, and (2) increasing the amount of transverse reinforcement ρ_t in the boundary elements of the wall resulted in increased capacity to resist the effects of combined compressive force from gravity loading and overturning moment due to reversed cyclic loading. Increased transverse reinforcement in the boundary elements also enhanced the walls' seismic performance in terms of deformation capacities (increased drift capacity, ductility, and energy dissipation capacity).

The study by Habibi et al. (2018) was performed at the University of Toronto under the sponsorship of the Canadian Nuclear Safety Commission and is, to the authors' knowledge, the only test data available in the literature on seismic performance of structural walls affected by ASR. In their study, five squat shear walls with boundary columns (I-shaped plan cross section, two with normal non-reactive concrete and three with varying degrees of ASR expansion), all representing low-rise structures with a height-to-length aspect ratio of 1.1 (typically referred to as low-rise or "squat" and predominantly fail in the shear) were tested under reversed cyclic lateral displacements while simultaneously applying constant axial compression, similar to the tests conducted by Oh et al. (2002). All five wall specimens had identical geometry and reinforcement details. Each wall had a volumetric transverse reinforcement ratio $\rho_t = 2.1$ % in the boundary elements provided by stirrups with 45°-degree hooks. Figure 1.2 shows the geometry and dimensions of the typical specimens tested by Habibi et al. (2018). The primary test variable was the degree of ASR free expansion (linear ASR-induced expansion was measured in companion plain concrete prisms in accordance with ASTM C1293 at the time of wall testing), which varied within a narrow range of 0.19 %, 0.21 %, and 0.22 % for the three reactive specimens. Test results indicated that (1) all specimens failed primarily in a shear-dominated failure mode and (2) the presence of ASR, while not affecting the maximum peak load capacity of RC walls, did adversely affect their seismic performance in terms of deformation and energy dissipation capacities (i.e., a reduction of approximately 30 % in both ductility and energy dissipation capacity).

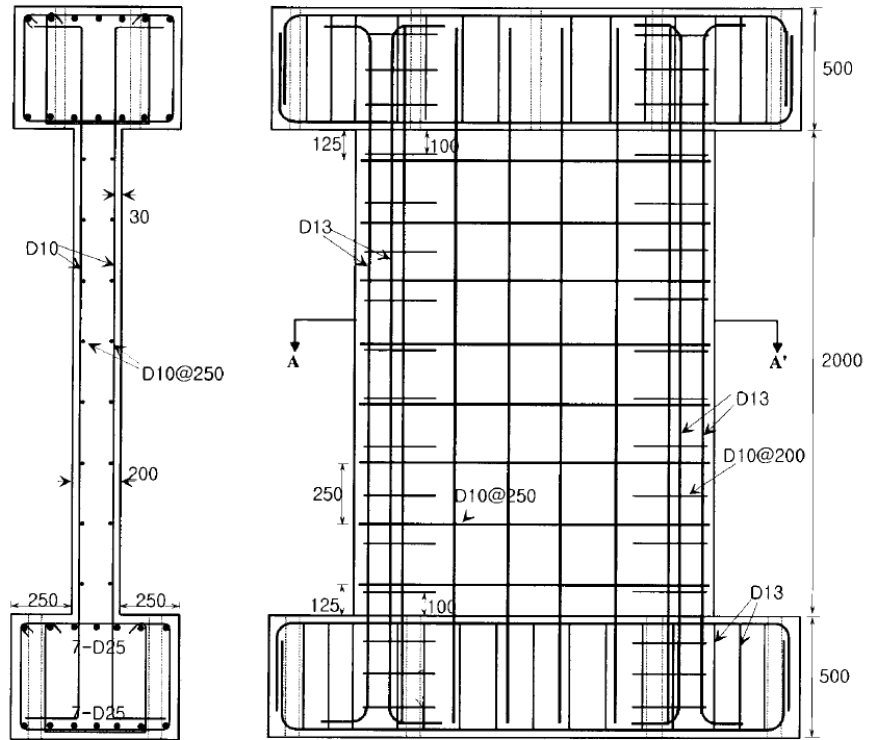


Figure 1.1: Geometry and dimensions of Oh et al (2002) test specimen (all dimensions in mm). Figure copied from open literature. 1.00 in = 25.4 mm

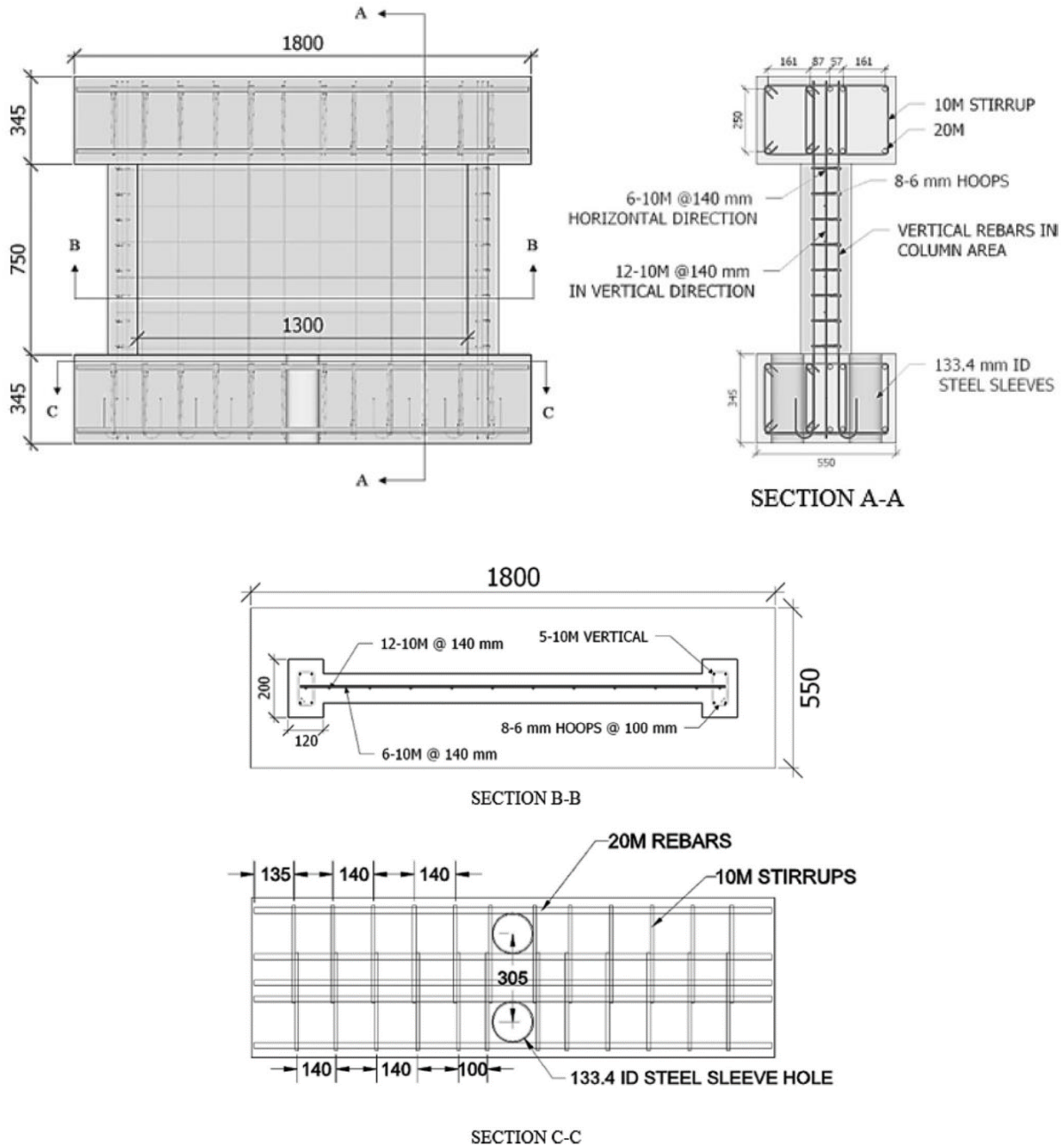


Figure 1.2: Geometry and dimensions of Habibi et al. (2018) test specimen (all dimensions in mm). Figure copied from open literature. 1.00 in = 25.4 mm.

1.3 SCOPE OF THE NIST TASK 3 STUDY

Given the need for more comprehensive understanding of how ASR and other factors might affect the structural performance of RC systems in general and RC structural walls in particular, the NIST experimental plan for Task 3, evaluation of seismic response characteristics of ASR-affected concrete structural members, was developed with incorporation of many of the test parameters used in the Oh et

al. (2002) study, but with both degree of ASR expansion (ϵ_{ASR}) and degree of transverse reinforcement confinement of the boundary elements (ρ_t) considered as test variables. Specifically, the NIST wall specimens were designed to have the same geometry and aspect ratios as specimens tested by Oh et al. (2002). The aim was to (1) facilitate independent comparisons between the NIST and Oh et al. (2002) test results regarding the effect of transverse reinforcement confinement ρ_t and (2) obtain a larger pool of baseline, non-reactive, test data for further statistical quantification of the effect of ϵ_{ASR} . Additionally, by studying the effects of ASR on RC walls with a height-to-length aspect ratio of 2.0, that would tend to fail predominantly in a flexural-shear mode, these NIST data will permit investigation of the effects of ASR on the seismic performance of RC walls within the intermediate range of aspect ratio (see Section 2.3). When combined with results from Habibi et al. (2018) for squat walls with lower aspect ratio of 1.1, with shear dominant failure mode, these data from NIST will further elucidate the effects of ASR and allow an assessment on the applicability of the findings on a larger range of wall constructions.

Based on the above considerations and experimental design to facilitate rigorous statistical evaluation of the effects of the two primary test variables, the target degree of ASR expansion ϵ_{ASR} and transverse reinforcement ratio in the boundary element ρ_t , and their potential interaction on seismic performance of RC walls (whether the effect of ρ_t is further influenced by the presence or absence of ϵ_{ASR}), see Section 2.1, the test plan shown in Table 1.1 was developed. The test plan consists of four wall specimens with different levels of ρ_t and ϵ_{ASR} at test time.

Table 1.1. Key parameters of the NIST Task 3 wall specimens

Specimen	Wall Aspect Ratios ⁽¹⁾		Transverse Reinforcement Ratio in Boundary Elements ρ_t (%)	Longitudinal Reinforcement Ratio ρ_l (%)	Target Expansion ϵ_{ASR} at Test Time ⁽²⁾ (% of $\epsilon_{ASR-ult}$)
	h_w/l_w	l_w/h			
Wall 1	2.0	7.5	0.5	0.61	50
Wall 2	2.0	7.5	2.0	0.61	100
Wall 3	2.0	7.5	0.5	0.61	100
Wall 4	2.0	7.5	2.0	0.61	0 (non-reactive, control specimen)

⁽¹⁾ h_w : wall height; l_w : wall length; h : wall thickness. h_w/l_w : wall height-to-length aspect ratio; l_w/h : length-to-thickness (shear) aspect ratio.

⁽²⁾ These represent “experimentally planned” expansion levels at test time. See actual measured ϵ_{ASR} at test time for each wall specimen in Section 4.5.

In Table 1.1, $\epsilon_{ASR-ult}$ is defined as the design ultimate expansion of the concrete material used. For this Task 3 experimental program, reactive concrete mixture ASR 3, with $\epsilon_{ASR-ult} = 0.3\%$ (see Section 2.2, in addition to Sadek et al. 2021 and Thonstad et al. 2021 for ASR 3 mixture proportions and other properties), is used for all wall panels of the test specimens to induce ASR expansion and degradation in these panels,

with Wall 4 wall panel treated with a lithium nitrate solution to mitigate the reaction of the aggregates and inhibit ASR expansion to make it the non-reactive, control specimen.

In addition to the four wall specimens, a sufficient number of companion concrete cylinders and prisms were also made, cured, and tested at certain time intervals for use in characterizing variations in the concrete mechanical properties (compressive strength, modulus of elasticity, and splitting tensile strength) and ASR-induced linear expansion as functions of age.

Finally, similar to the loading protocols used by Oh et al. (2002) and Habibi et al. (2018), the four NIST wall specimens were also subjected to a constant axial compression equivalent to approximately 10 % of their axial load capacity while simultaneously undergoing reversed cyclic lateral displacements corresponding to drift ratios prescribed for different performance objectives by ASCE/SEI 41-17 (ASCE, 2017), namely: Elastic, Immediate Occupancy, Life Safety, Collapse Prevention, and To Failure. The purpose of the selected levels of cyclic loading was to cover a range of structural performance from elastic to failure, with measurements regularly interspersed throughout the intermediate stages.

1.4 REPORT OUTLINE

The focus of this report is to present the results of the experimental program and to describe subsequent statistical analysis, which aimed to capture the major features of the observed experimental response. A brief description of each chapter is as follows:

- Chapter 2 provides detailed descriptions of the NIST Task 3 experimental program, including the factorial experimental design used to select the optimized number of test specimens that are sufficient for statistical evaluation of the test results; the concrete mixture used; specimens dimensions and reinforcement details; specimen construction and curing; instrumentation; and test setup and loading protocol.
- Chapter 3 describes cracking that was observed in the three reactive shear walls due to the effects of ASR-induced expansion prior to structural loading, and the progression of damage including crack development and concrete spalling and crushing failure with different drift levels that was observed in all four walls during cyclic testing.
- Chapter 4 provides measurements taken of concrete mechanical properties (compressive strength, elastic modulus, and splitting tensile strength), concrete linear free expansion (of standard prisms), specific curing conditions (temperature and relative humidity), and ASR-induced strain developments in the steel reinforcement as function of time during the curing phase of the specimens.
- Chapter 5 presents (1) structural response data obtained for each specimen, including force-drift hysteresis and measured peak moment capacity, ductility, and cumulative hysteretic energy capacity, and (2) comparisons between specimens for examination of the effects of test variables on their seismic performance.

- Chapter 6 describes the statistical analysis of the NIST test results, separately and also augmented with test results from Oh et al. (2002), for quantification of the effects of test variables, ϵ_{ASR} and ρ_t , on the seismic performance of RC walls, measured in terms of drift capacity and ductility, flexural capacity, and hysteretic energy.
- Chapter 7 presents a detailed summary, findings, and practical conclusions of the NIST Task 3 experimental program

Chapter 2

EXPERIMENTAL PROGRAM

This chapter describes the experimental program used in assessment of the cyclic performance of ASR-affected concrete shear walls. The chapter includes the following sections:

- Section 2.1 provides the statistical basis for the design of experiment of the shear walls and introduces the input parameters considered in the design;
- Section 2.2 presents the reactive and non-reactive concrete mixtures used in the wall panels of the specimens;
- Section 2.3 describes the design, details, and construction of the four reinforced concrete shear wall specimens;
- Section 2.4 describes the environmental chamber and controls installed for curing the reactive shear wall specimens under controlled temperature and humidity;
- Section 2.5 presents the experimental setup and loading protocol used to subject the shear wall specimens to combined vertical and lateral cyclic loading;
- Section 2.6 describes the instrumentation plan, including embedded strain gages and externally-applied displacement transducers and inclinometers; and
- Section 2.7 provides a timeline of key events for the experimental study including concrete placements, operation of environmental chamber, and cyclic testing.

2.1 EXPERIMENTAL DESIGN AND TEST VARIABLES

The experimental study considered two input parameters:

- the level of confinement in the boundary elements of the shear walls (see Section 2.3), as measured by the volumetric ratio of transverse reinforcement in the boundary elements, ρ_t , and
- The level of ASR-induced expansion, ϵ_{ASR} , in the wall panels, as measured by the average maximum recorded strains in the reinforcing bars in the wall panels prior to cyclic testing.

The sample size for the design of experiments was four shear wall specimens. The canonical design in this situation is a two-level factorial design, i.e., the corners of the square $\{-1,1\} \times \{-1,1\}$. However, there were further physical and engineering constraints, namely that the (ϵ_{ASR}, ρ_t) point $(-1, 1)$ was required to be in the study, but no other points of the form $(-1, x)$ with $-1 \leq x \leq 1$ could be. Note that the factor combination $(-1, 1)$ represents ϵ_{ASR} at its lowest level (non-reactive concrete) and ρ_t at its highest level. This implies that to fit a regression model with both main effects and the one two factor interaction, at least three levels of ϵ_{ASR} would be needed. Symmetrically, we also consider three potential levels of ρ_t . Thus, we search for the best four points of the set of seven possible points $\{-1, 0, 1\} \times \{-1, 0, 1\} \setminus \{(-1, 0), (-1, 1)\}$. The three levels of ϵ_{ASR} are 0 %, 50 %, and 100 % of the design ultimate expansion level, $\epsilon_{ASR-ult}$, of 0.3 % for the concrete mixture (see Thonstad et al., 2021), which correspond to -1, 0, and 1, respectively

in what follows. The three levels of ρ_t are 0.5 %, 1.25 %, and 2 %, corresponding to -1, 0, and 1, respectively, in what follows.

A common approach for choosing a design with constraints is to search over the set of possible designs and select the one that optimizes a scalar numerical summary. A common numerical summary is the determinant of the variance-covariance matrix for the parameters of a statistical model. Under Gaussian distributional assumptions, the volume of a confidence ellipsoid for the model parameters is proportional to the determinant. Since confidence ellipsoids with smaller volume are desirable (less volume corresponds to less uncertainty), a reasonable approach is to choose the design that minimizes the determinant of the variance-covariance matrix. This is broadly known as D-optimal design.

With four runs (wall specimens) in two factors (ϵ_{ASR} and ρ_t), a natural statistical model is a linear model with an intercept, both main effects (linear terms in ϵ_{ASR} and ρ_t), and the two-factor interaction (product of ϵ_{ASR} and ρ_t). The design matrix for the disallowed two-level factorial design is

$$\begin{pmatrix} 1 & 1 & 1 & 1 \\ 1 & 1 & -1 & -1 \\ 1 & -1 & 1 & -1 \\ 1 & -1 & 1 & 1 \end{pmatrix}$$

For design matrix X , the variance-covariance matrix for the model parameters is proportional to $(X^T X)^{-1}$. Thus, we choose the design that minimizes $|(X^T X)^{-1}|$, or equivalently, that maximizes $|X^T X|$. For the design matrix above

$$X^T X = \begin{pmatrix} 4 & 0 & 0 & 0 \\ 0 & 4 & 0 & 0 \\ 0 & 0 & 4 & 0 \\ 0 & 0 & 0 & 4 \end{pmatrix}$$

and $|X^T X| = 256$. Designs for which $X^T X$ is a diagonal matrix are called orthogonal designs since the dot product between any two columns of the design matrix is zero.

Figure 2.1 shows the 20 designs over the grid $\{-1, 0, 1\} \times \{-1, 0, 1\}$ that meet the three design constraints:

1. Four runs
2. The point (-1, 1) is in the design
3. The points (-1, 0) and (-1, 1) are not in the design

Figure 2.1 also lists the value of the D-criterion of each design. The panels are ordered according to the value of the D-criterion, from largest in the top left to smallest in the bottom right. The design depicted in the top left panel of Figure 2.1 was the D-optimal design for this study and was selected for the experiment. In summary, the selected D-optimal experimental design specified the following four runs:

- Wall 1: $\rho_t = 0.5 \%$, tested at 50 % of $\epsilon_{ASR-ult}$
- Wall 2: $\rho_t = 2.0 \%$, tested at 100 % of $\epsilon_{ASR-ult}$
- Wall 3: $\rho_t = 0.5 \%$, tested at 100 % of $\epsilon_{ASR-ult}$
- Wall 4: $\rho_t = 2.0 \%$, tested at 0 % of $\epsilon_{ASR-ult}$ (non-reactive)

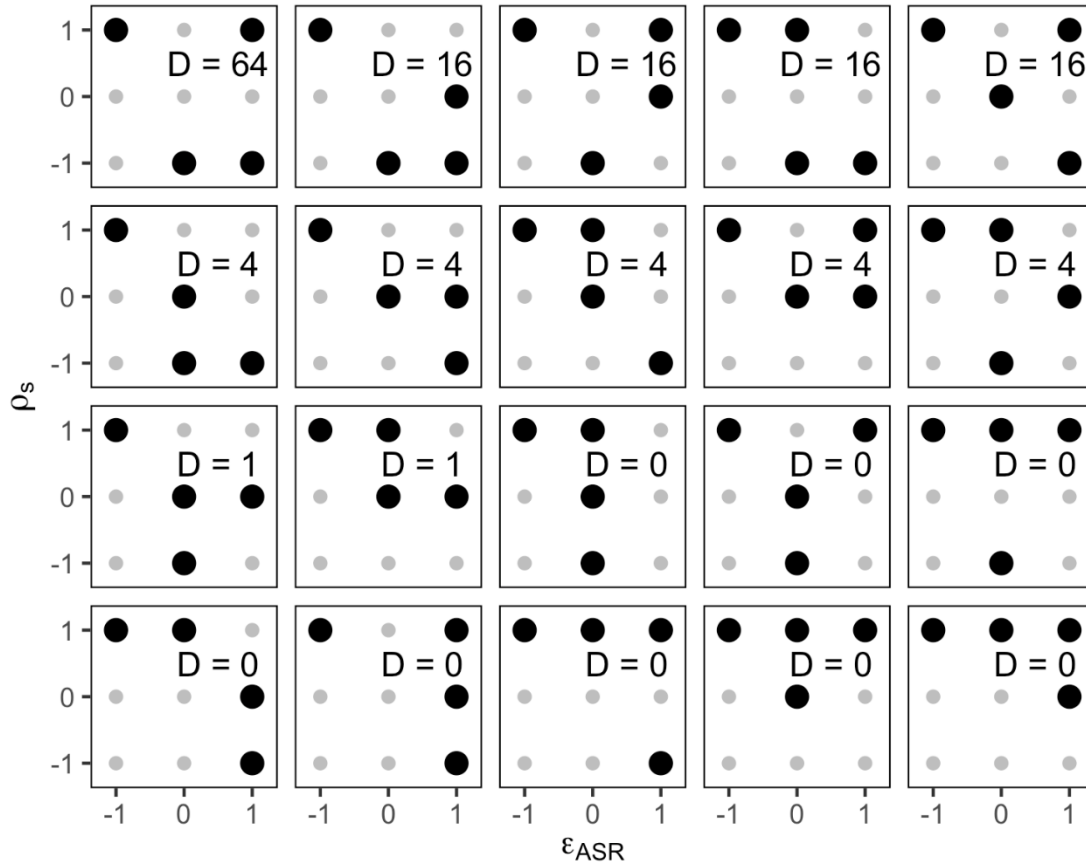


Figure 2.1: All 20 designs over the grid $\{-1, 0, 1\} \times \{-1, 0, 1\}$ meeting the experimental constraints. The designs are ordered from top left to bottom right according to their value of the D -criterion. The design in the top left panel is the D -optimal design selected for the experiment.

2.2 CONCRETE MIXTURE FOR WALL PANELS

Table 2.1 summarizes the mixture design used in the beam specimens. ASR Mix 3 concrete described in the Task 1 study (Sadek et al., 2021) was used for all 19 of the beam specimens. The target 28-day strength of the mixture was 5000 psi based on the measured strengths in the Task 1 study. The Placitas gravel and Jobe sand conformed to ASTM C33 (ASTM C33/C33M, 2018) gradation requirements #6 coarse aggregate and fine aggregate, respectively.

Wall 4's nonreactive panel was cast separately. For Wall 4, no sodium hydroxide was added to the mix and a 30 % lithium nitrate solution was added at a dosage of 3.2 gal/yd³ (15.8 L/m³). This corresponds to 110 % of the recommended dosage by the lithium nitrate manufacturer for the mix design (without the addition of sodium hydroxide) presented in Table 2.1.

Table 2.1. ASR Mix 3 Concrete Proportions

Constituent	Design proportions by weight
	lb/yd ³ (kg/m ³)
Type I/II, high alkali (0.89 % Na ₂ O _e) cement	588 (349)
Placitas coarse aggregate	1767 (1048)
Jobe fine aggregate	1185 (703)
Water	293 (174)
Sodium Hydroxide (NaOH)	4.0 (2.4)

2.3 DESIGN AND FABRICATION OF RC WALL SPECIMENS

To achieve the objectives of this task as described in Chapter 1, tests were conducted to investigate the cyclic performance of reinforced concrete shear walls that were made with reactive coarse and fine aggregates. The geometry and longitudinal reinforcement of the walls were selected to closely match walls previously tested by Oh et al. (2002), see Chapter 1. This test series was selected from the experimental database developed for ACI 445B (ACI Committee 445B, 2017), which included a large database of seismic testing of shear walls. Two criteria were used in selecting the test series for this project: (1) an aspect ratio of the wall (defined as the overall height, h_w , between the point of lateral load application and the top of the specimen footing divided by the length of the wall, l_w) in the range of 1.5 to 2.5 to exhibit a combined shear-flexural response during cyclic testing, see Figure 2.2, and (2) wall dimensions and lateral capacity not exceeding the experimental capabilities of the NIST Performance Engineering Research for Multi-hazards (PERFORM) Laboratory. The test series by Oh et al. (2002) met these two criteria. In addition, aligning the present experimental program to the tests by Oh et al. (2002) allowed for (1) comparison of the behavior of the ASR-affected walls to those with non-ASR-affected concrete and (2) augmenting the dataset of experimental results with data from walls with conventional concrete.

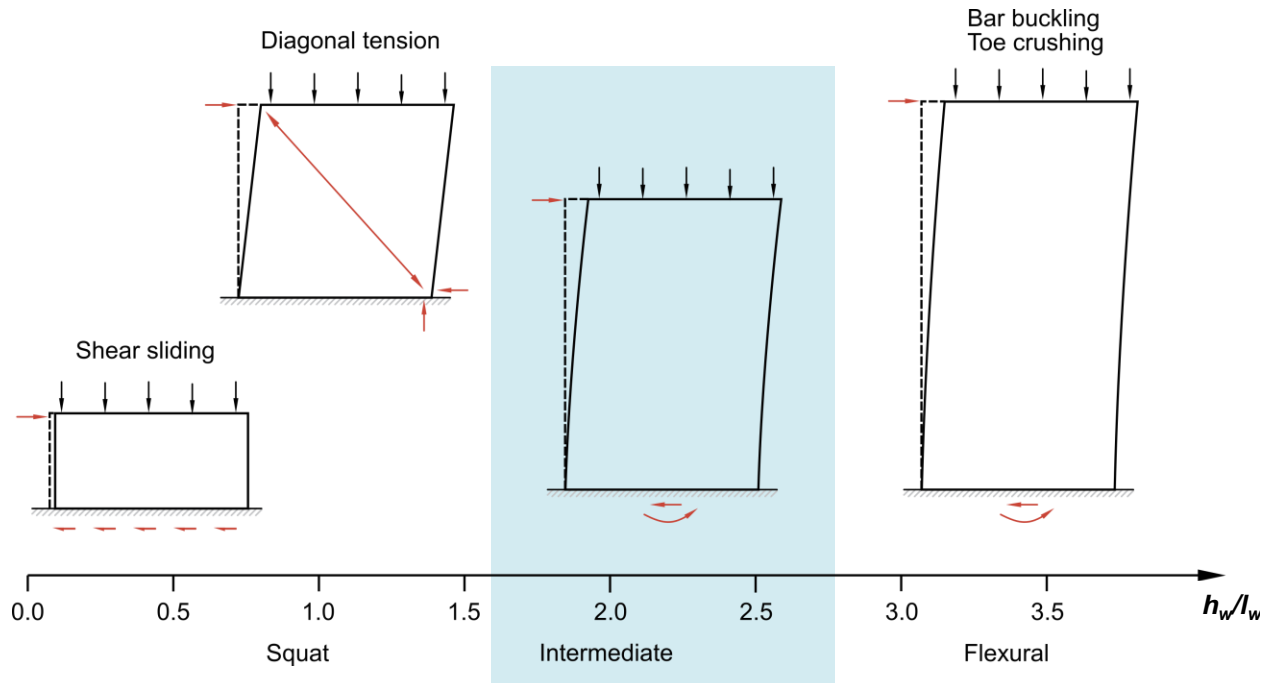


Figure 2.2: Schematic showing the effect of wall aspect ratio on predominant behavior and failure mode under lateral loading

The geometry and dimensions of the concrete shear wall specimens are shown in Figure 2.3. Each wall had a nominal thickness of 8.0 in (203 mm), a total length of 60.0 in (1520 mm), and a height between the footing and the top cap of 80.0 in (2030 mm). The footing had a length, width, and height of 89.0 in (2260 mm), 29.5 in (750 mm), and 30.0 in (762 mm), respectively, and was used to anchor the wall specimen to the steel reaction frame, which, in turn, was anchored to the strong floor of the laboratory (see Section 2.5). The top cap had a length, width, and height of 62.0 in (1570 mm), 29.5 in (749 mm), and 24.15 in (613 mm), respectively, and was used to anchor the wall to the upper steel loading beam, which in turn was connected to the hydraulic actuators applying vertical and lateral loading. The footings and top caps of the four shear wall specimens were cast with conventional concrete. The wall panels of wall specimens 1, 2, and 3 were cast with the reactive concrete mixture in accordance with Section 2.2, while non-reactive Wall 4 without sodium hydroxide per Section 2.2 used the same reactive mixture as the other three walls, but dosed with a lithium nitrate solution to mitigate the ASR effects.

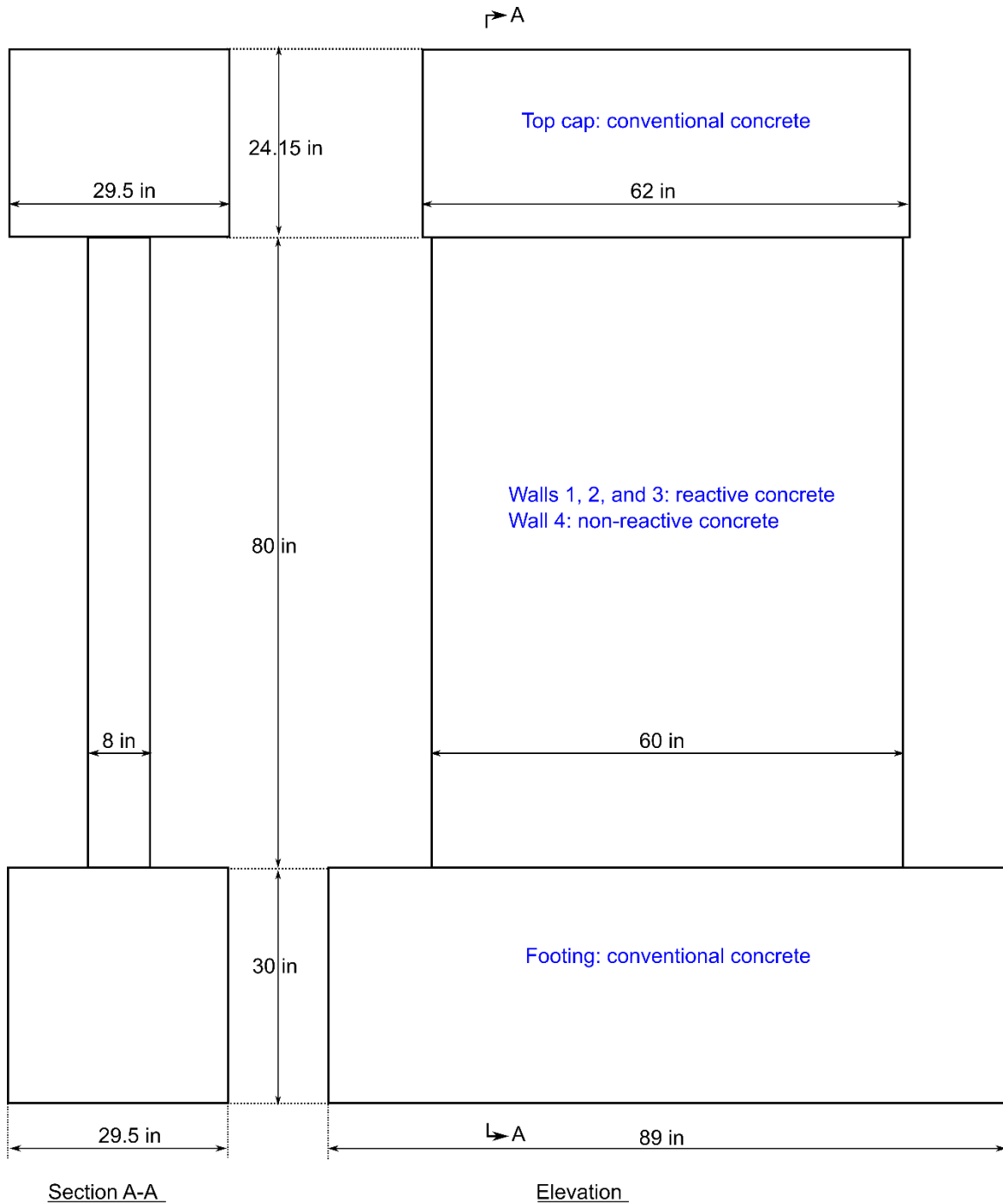


Figure 2.3: Geometry and overall dimensions of the shear wall specimens

All reinforcement in the shear wall specimens was ASTM A615/A615M Gr 60 (ASTM, 2020). The wall panel reinforcement, shown in Figure 2.4, consisted of the following:

- In each boundary element, four No. 4 (0.5 in [12.7 mm] diameter) longitudinal bars were used. As shown in Figure 2.4, the longitudinal bars extended from the bottom of the footing to the top of the top cap. Threaded mechanical anchorage devices (terminators) designed according to ACI 318-14 (2014) were used at the top of the longitudinal bars to avoid reinforcing bar congestion at the ends and to prevent slippage. In addition, transverse reinforcement consisting of closed No. 3 (0.375 in [9.5 mm] diameter) stirrups, with 135° hooks, was provided along the height of the boundary element. The spacing between the stirrups of Walls 2 and 4 was 4.0 in (102 mm) O.C., resulting in a transverse reinforcement ratio in the boundary element, ρ_t , of 2 % per the experimental design in Section 2.2. For Walls 1 and 3, however, the stirrups were used for only construction purposes and, as such, were spaced at 16.0 in (406 mm) O.C. resulting in ρ_t of 0.5 %.
- For the web between the two boundary elements, six No. 3 (0.375 in [9.5 mm] diameter) longitudinal bars, spaced at 8.80 in (224 mm) O.C. were used on each face of the wall. As shown in Figure 2.4, the longitudinal bars extended from the bottom of the footing to the top of the top cap. Transverse reinforcement consisting of No. 3 (0.375 in [9.5 mm] diameter) bars, spaced at 10.0 in (254 mm) O.C., was also provided on each side along the height of the wall.

The longitudinal reinforcement, eight No. 4 bars in the wall's two boundary elements and twelve No. 3 bars in the wall's web, amounted to a longitudinal reinforcement ratio, ρ_l , of 0.61 %.

The reinforcement cages for both the footing and top cap are shown in Figure 2.5. As shown in the figure, they were designed with a dense arrangement of reinforcing bars to avoid any possibility of their failure during testing. Their reinforcement cages consisted of two No. 4 (0.5 in [12.7 mm] diameter) stirrups, spaced at 10.0 in (254 mm) O.C., six (for the footing) and four (for the top cap), No. 8 (1.0 in [25.4 mm] diameter) U-shaped top and bottom longitudinal bars, four (for the footing) and three (for the top cap), and No. 6 (0.75 in [19.1 mm] diameter) U-shaped longitudinal bars distributed along the height.

Figure 2.6 shows the tie-downs for anchoring the footing and the top cap to the lower and upper steel beams of the steel reaction frame, respectively. This was achieved using twenty (for the footing) and ten (for the top cap) 1.0 in (25.4 mm) high-strength threaded rods, post-tensioned to 60.0 kip (267 kN) each. For this purpose, 2.5 in (63.5 mm) holes were created in the footing and top cap using PVC pipes inserted inside the formwork prior to concrete placement.

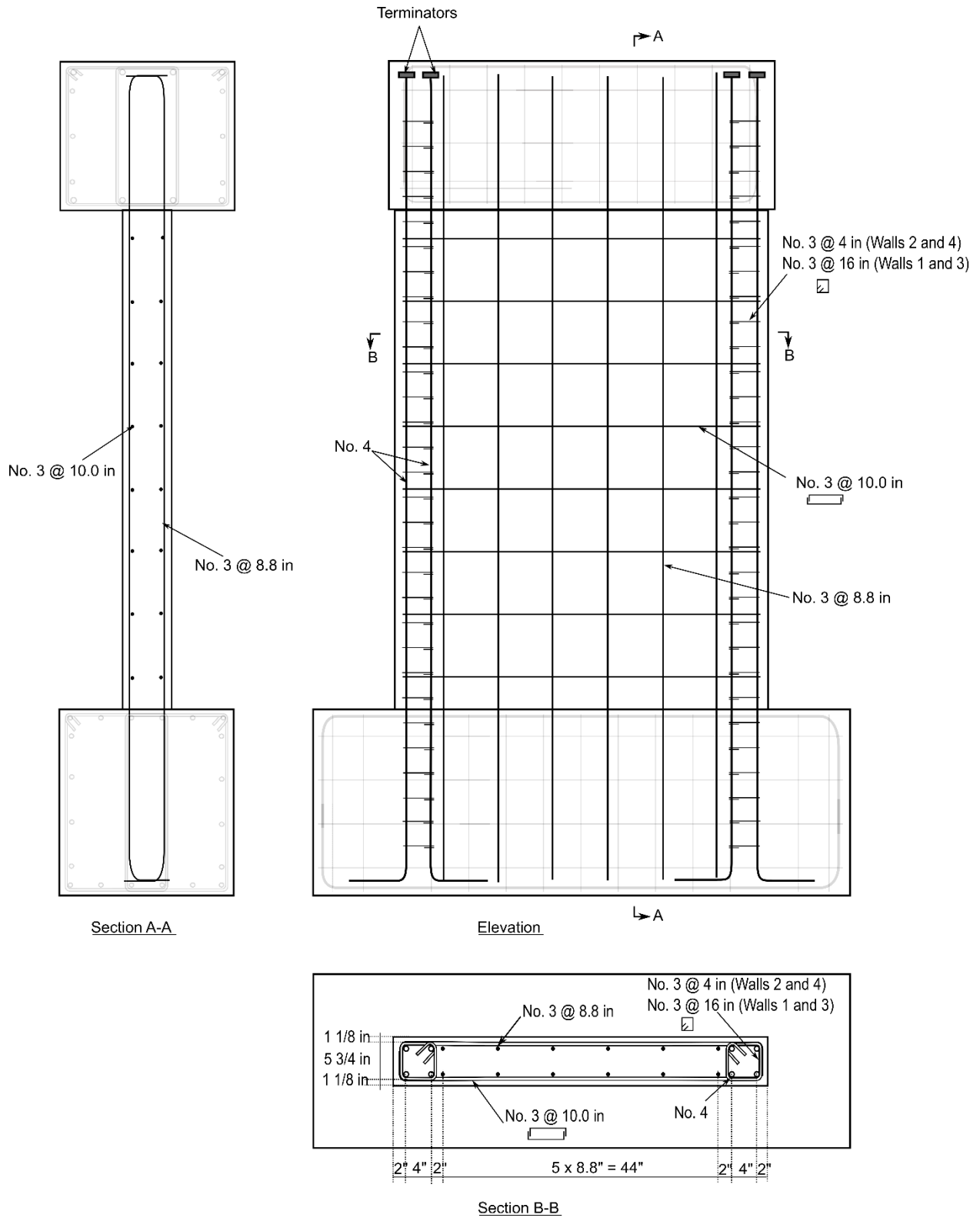


Figure 2.4: Typical reinforcement of wall panels. 1.00 in = 25.4 mm.

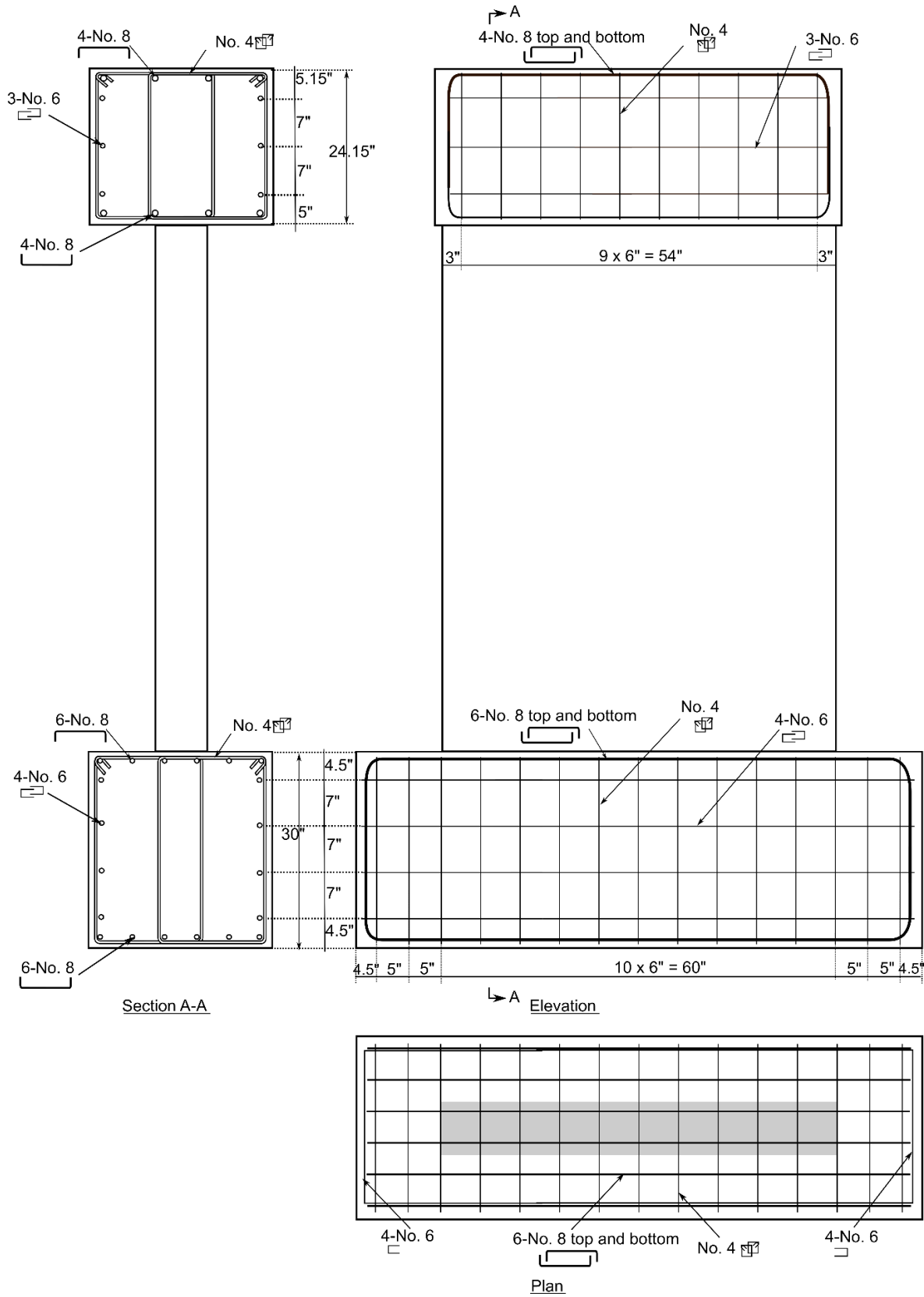


Figure 2.5: Reinforcement cage for footing and top cap. 1.00 in = 25.4 mm.

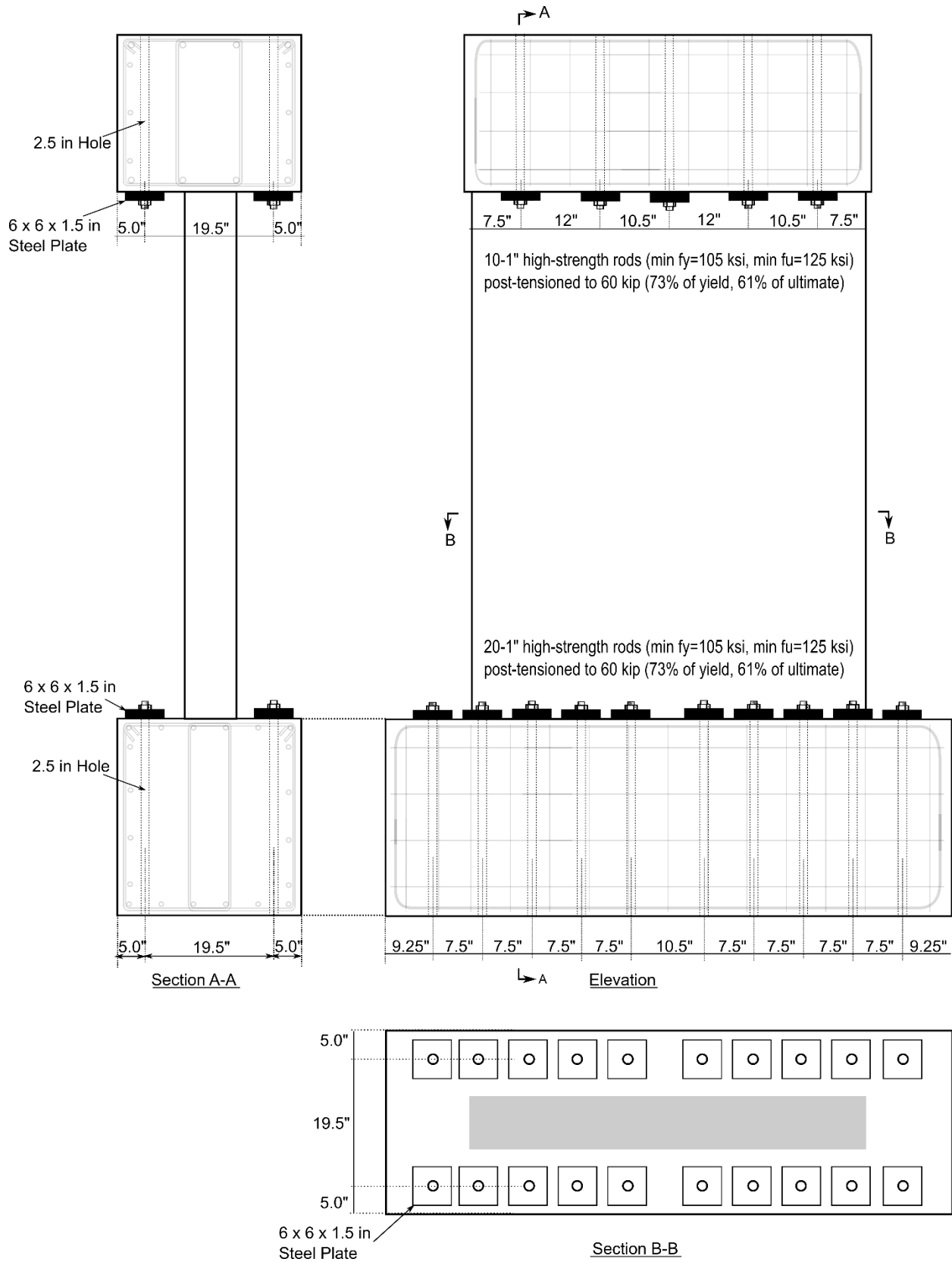


Figure 2.6: Tie-downs for footing and top cap. 1.00 in = 25.4 mm.

Figure 2.7 shows the reinforcement and formwork prior to casting of the (a) footings, (b) walls, and (3) top caps. The reinforcement cages were fabricated using jigs and placed into the formwork. To ensure consistent spacing between the bottom bars and formwork bottom in the footing and top cap, plastic-tipped slab bolsters were used to support the reinforcement cage. Prior to assembly of the reinforcing bars for the wall, strain gages were attached to the individual reinforcing bars which were then assembled to form the reinforcing bar cage based on the instrumentation plan in Section 2.6.



(a)



(b)





(c)

Figure 2.7: Formwork and reinforcement of (a) footing, (b) wall, and (c) top cap of the shear wall specimens.

The shear wall specimens were cast at different stages as follows:

- The footings of all four specimens were cast on November 14, 2018 using conventional, self-consolidating, concrete procured from a concrete mixing plant which batched the concrete in accordance with the NIST specifications (Figure 2.8).



Figure 2.8: Concrete placement into the footings formwork and consolidation using vibrators

- Wall panels 1 and 2 were cast on April 30, 2019 using the reactive concrete mix as specified in Section 2.2. Batching and mixing of concrete were carried out at NIST campus in Gaithersburg, MD. The coarse and fine aggregates, along with the cement and water, were loaded into a concrete volumetric truck mixer that was used as a batching plant (Figure 2.9). The volumetric truck contents were then loaded via a conveyer belt (telebelt) into a concrete mixer truck (Figure 2.10), where the sodium hydroxide was added. After mixing, the concrete was discharged from the concrete mixer onto a hopper, which was carried by an overhead crane. Concrete was then placed into the wall panel formwork using an elephant trunk. The concrete was consolidated using vibrators (Figure 2.11).



Figure 2.9: Loading of aggregates into volumetric truck mixer



Figure 2.10: Loading the volumetric truck contents to a concrete mixer truck via a conveyer belt (telebelt)



Figure 2.11: Concrete placement into wall's formwork and consolidation using vibrators

- Wall panel 3 was cast on May 09, 2019 using the reactive concrete mix as specified in Section 2.2. Batching, mixing, and placement of concrete were carried out at NIST campus in Gaithersburg, MD using a similar procedure to that used for Walls 1 and 2 except that the coarse and fine aggregates, along with the cement, water, and the sodium hydroxide solution were loaded directly into a concrete mixer truck using a telescoping forklift (Figure 2.12).



Figure 2.12: Loading of aggregates into concrete mixer truck

- The top caps for reactive Walls 1, 2, and 3 were cast on July 02, 2019 using conventional concrete procured from a concrete mixing plant which batched the concrete in accordance with NIST specifications. The concrete was discharged from the concrete mixer onto a concrete bucket, which was carried by an overhead crane. Concrete was then placed into the top cap formwork and consolidated using vibrators (Figure 2.13).



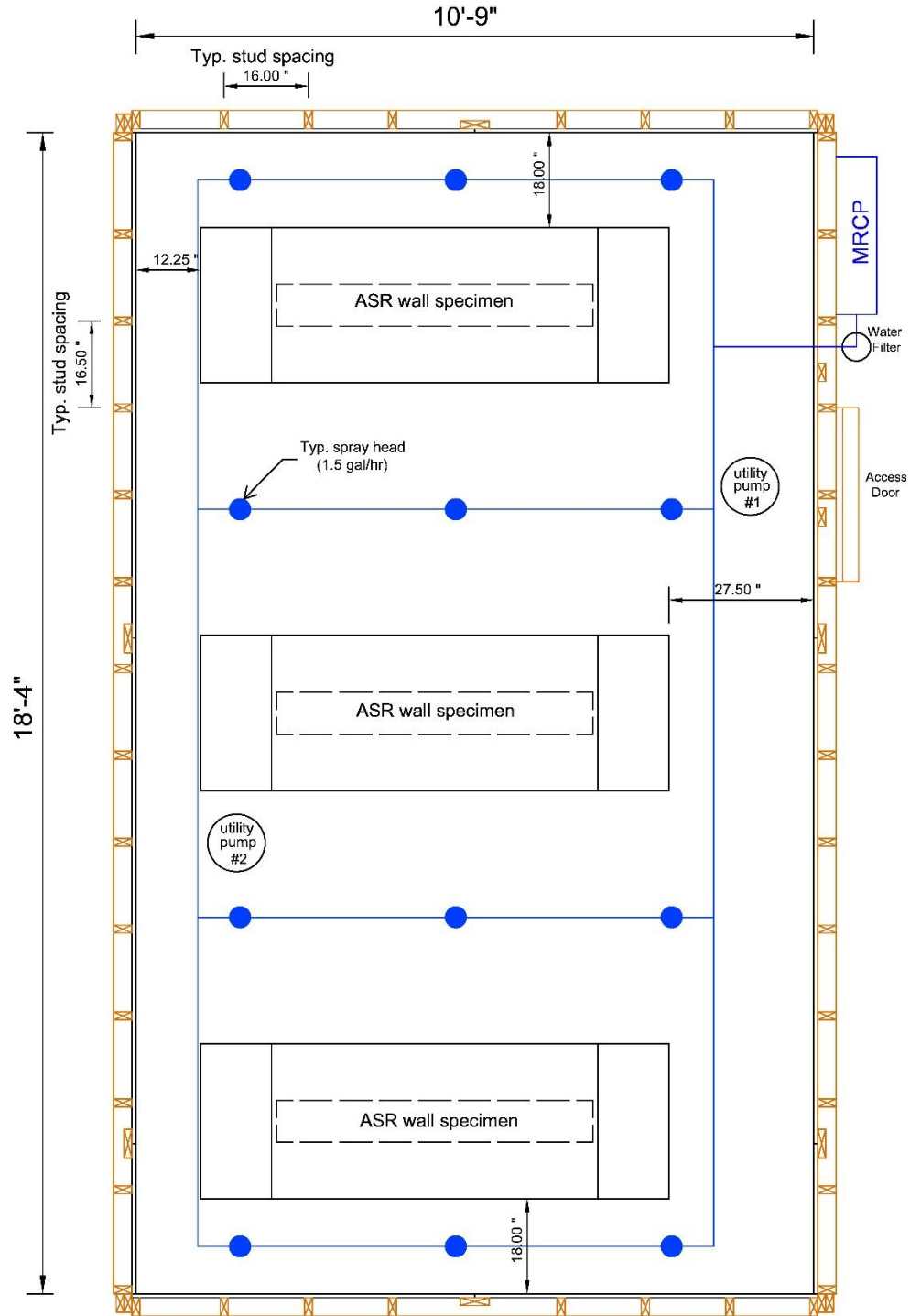
Figure 2.13: Concrete placement into the top cap formwork and consolidation using vibrators.

- Wall panel 4 was cast on August 23, 2019 using the reactive concrete mixture as specified in Section 2.2 (without the addition of sodium hydroxide) after adding lithium nitrate to render the concrete non-reactive. Batching, mixing, and placement of concrete were carried out at NIST campus in Gaithersburg, MD using a similar procedure to that used for Wall panel 3. As indicated earlier, Wall 4 was intended to serve as a control specimen and to be tested at 0 % of $\epsilon_{ASR-ult}$. As a result, a 30 % lithium nitrate solution was added to the mixture at a dosage of 3.2 gal/yd³ (15.8 L/m³). After additional mixing, the concrete was discharged from the mixer into a hopper, which was used to place concrete into the wall formwork. The concrete was consolidated using vibrators.
- The top cap for the control Wall 4 was cast on September 23, 2019 using conventional concrete procured from a concrete mixing plant and the same procedure for the top caps for the three reactive walls.

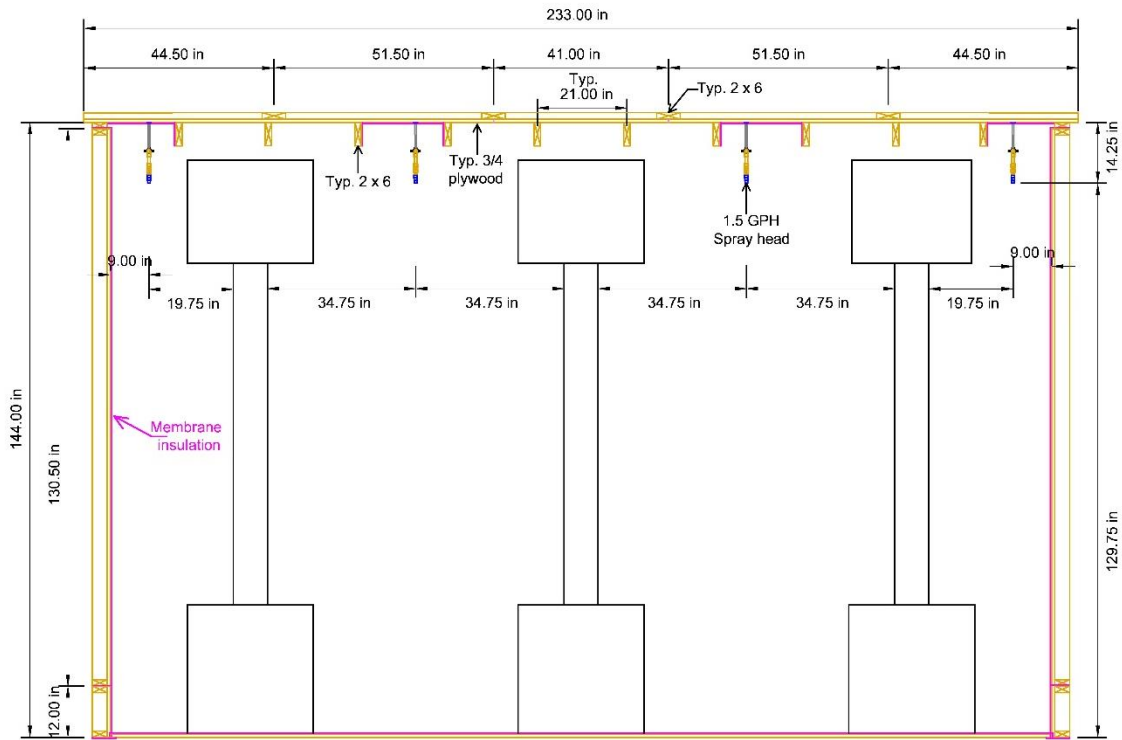
2.4 CURING OF RC WALL SPECIMENS

The reactive wall specimens were too large to be transported into a separate environmental chamber, so they were instead cured in-place on the strong floor to maintain overhead crane access. For that purpose,

a custom wood frame environmental chamber was constructed with interior dimensions: 18'-4" length × 10'-9" width × 12'-0" height (5.59 m length × 3.28 m width × 3.66 m height), see Figure 2.14.



(a)



(b)

Figure 2.14. Custom wood frame environmental chamber (a) top view, (b) sectional elevation. 1.00 in = 25.4 mm.

The construction of the environmental chamber was done in parallel with construction of the wall specimens. The elevated floor of the chamber was constructed first, which was lined with a self-adhesive, rubberized asphalt/polyethylene waterproofing membrane. After completion of the floor of the chamber, the footings of the reactive wall specimens were moved into the position shown in Figure 2.15, where they remained until the wall specimens were removed for testing.

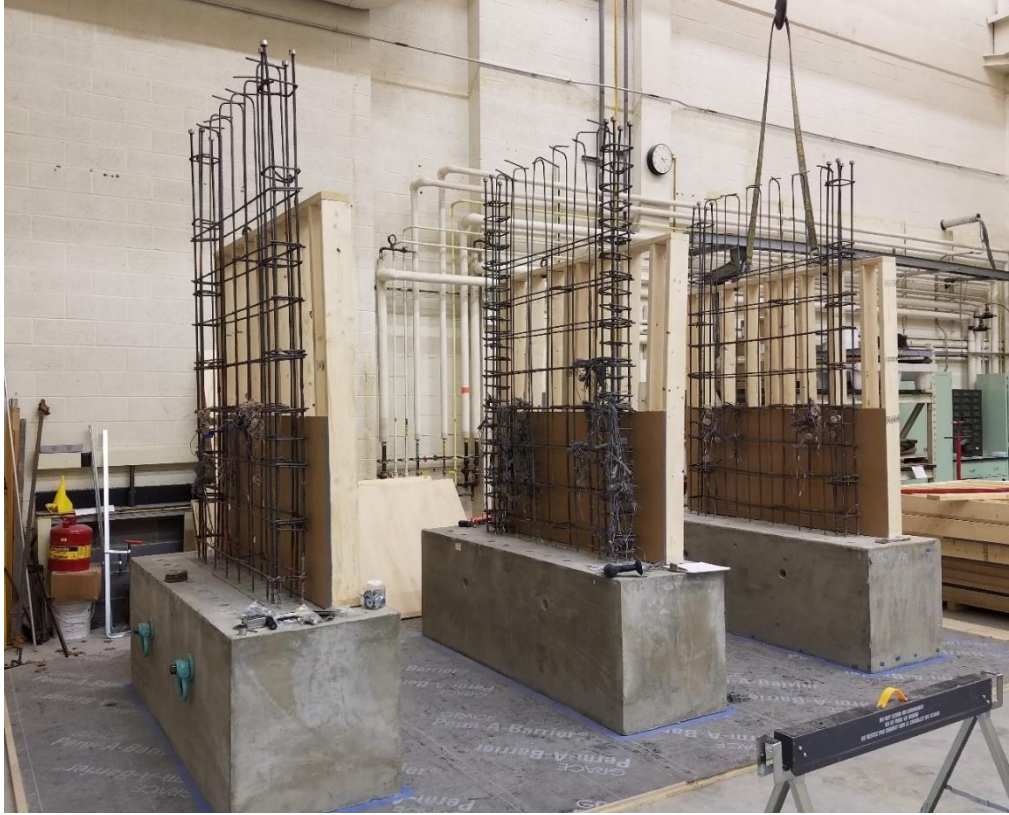


Figure 2.15. Bottom of the wood environmental chamber and the footings of wall specimens set in the final position

Wall panels of the chamber were installed around the perimeter as soon as the construction of the reactive specimens (including the top caps) was completed (Figure 2.16a). The chamber's wall panels were lined with the same asphalt/polyethylene membrane as was used for the floor of the chamber. Strain gages, used to monitor the ASR-induced expansion of specimen, were connected to the data acquisition system located outside of the chamber through PVC conduits that penetrated the exterior wall of the environmental chamber (see Figure 2.16a). The final construction step was the installation of the roof of the chamber using wood framing.

The temperature and relative humidity (RH) in the chamber were controlled by a commercially available wall-mounted Moisture Room Control Panel (MRCP), which automatically blended hot and cold water supplied in a closed-loop spraying system, based on the desired target temperature. The closed-loop spraying system, was attached by hangers to the chamber's roof (see Figure 2.14a, Figure 2.16b), and consisted of 12 spray heads, each with a flow rate of 1.5 gal/h (5.7 L/h). The spray heads were installed in the configuration recommended by the manufacturer's guidelines, to maintain a constant RH in the chamber. Figure 2.16c shows the assembled environmental chamber. The MRCP temperature/RH control probe was installed on the west wall chamber of the chamber (Figure 2.16d). Additionally, nine thermocouples were installed inside the chamber and within the wall specimens, for monitoring the chamber and specimen temperature during curing.



(a)



(b)



(c)



(d)

Figure 2.16. Construction of the environmental chamber: (a) exterior wall panels installed immediately after construction of wall specimens; (b) Closed loop spraying system attached to the chamber's roof; (c) Assembly of the custom environmental chamber completed; and (d) Moisture Room Control Panel (MRCP) + chamber access door (SW corner)

Two utility pumps were placed inside the chamber to pump the water that accumulated on the floor during curing (Figure 2.14a). The pumps were programmed to operate for a 5 min – 10 min duration at intervals of 30 min – 45 min, which was effective in removing any accumulated water from the floor of the chamber.

2.5 TEST SETUP AND LOADING PROTOCOL

This section describes the experimental setup for testing of ASR-affected concrete shear walls. The setup was designed to allow for application of 200 kip (890 kN) of constant vertical loading and lateral reversed cyclic loading based on a prescribed protocol to the shear wall specimens up to failure, while preventing out-of-plane displacements and maintaining safe operation throughout testing. The experimental setup included the NIST PERFORM Laboratory's structural reaction (strong) floor, hydraulic actuators, a primary reaction frame made up of a foundation frame and loading beam, a lateral bracing frame (LBF), and a Concrete Structural Reaction Block (CSRB) Wall (Figure 2.17). The strong floor consists of a 6.0 ft (1.83 m) thick heavily reinforced concrete slab. Both the foundation frame and the CSRB block wall were anchored to the strong floor using 1-1/2 in (38.1 mm) diameter UNF high-strength threaded rods connected into the sockets embedded in the strong floor. Each high-strength threaded rod was post-tensioned to its working capacity, or a load of approximately 100 kip (445 kN).

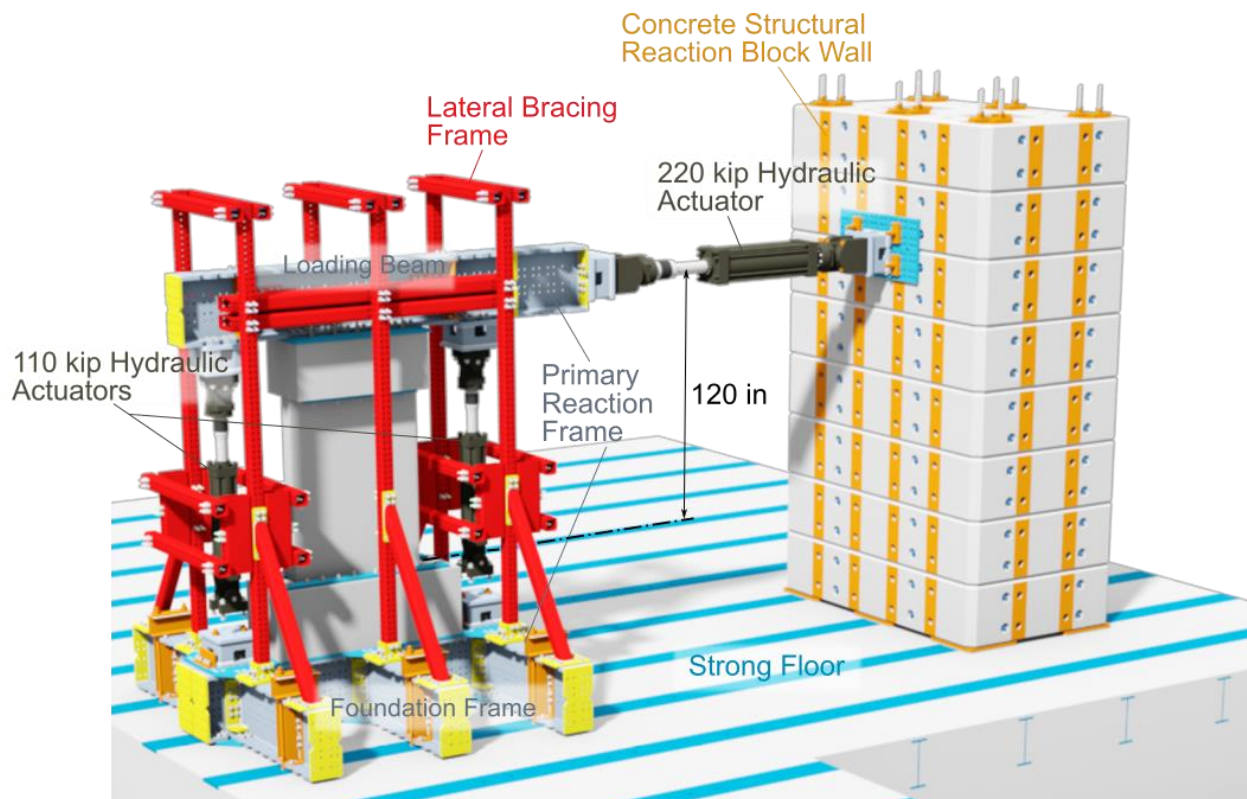


Figure 2.17. Experimental setup for testing ASR-affected concrete shear wall specimens (1.000 kip = 4.448 kN)

The foundation frame (see Figure 2.17) was erected as an assembly of structural steel reaction frame components. Two parallel W27×235 foundation beams, which were anchored to the strong floor near their ends where vertically-spanning actuators framed into them, provided a platform to mount the footing of the shear wall specimen. Six outriggers extended perpendicularly as cantilevers from the foundation beams to provide both stability to the overall foundation frame and additional tie-down

locations to post-tension the foundation frame to the strong floor. Similar to the foundation beams, the outriggers were W27×235 cross-sections. All connections between the outriggers and foundation beams were designed to be moment-resisting with each bolt tensioned to approximately 113 % of its minimum bolt pretension (i.e., a slip-critical condition, as specified in the AISC Steel Construction Manual [AISC, 2011]). In total, eight pairs of tie-down locations anchored the foundation frame to the structural reaction floor, ensuring that the foundation frame would remain stationary under the anticipated levels of lateral loading to be applied to the shear wall specimens. The load in the horizontally-spanning 220.0 kip (979 kN) capacity actuator (see Figure 2.17) that would be required to decompress the foundation frame from the strong floor was calculated as 293 kip (1300 kN), based on assuming a nominal post-tensioned load of 100 kip (445 kN) per anchor rod. This 293 kip (1300 kN) lateral load is substantially larger than the load required to fail the concrete shear wall specimen, so decompression of the foundation frame did not occur. Assuming a coefficient of friction of 0.30 between the foundation frame's steel surfaces and the concrete strong floor, the load that would be required to induce slip of the foundation frame was 480 kip (2135 kN), which was also substantially larger than the load required to fail the shear wall specimen.

In addition to the primary reaction frame, Fig. 2.17 shows a lateral bracing frame which was used to prevent out-of-plane displacements and rotations of the wall specimens. The lateral bracing frame was designed to remain elastic, and to deflect less than 1.00 in (25.4 mm) under the lateral loads that would be induced by wall specimen were it to fail in out-of-plane flexure or in torsion. Contact between the loading beam and lateral bracing frame was made by four 14.0 in (356 mm) long lengths W14×90 beam with 12.0 in × 12.0 in (305 mm × 305 mm) polytetrafluoroethylene (PTFE) sheets adhered to their exterior faces where they bore against the lateral bracing frame. The W14×90 sections were bolted through the loading beam's web such that one end (the end without the attached PTFE sheet) was flush against its faces. Large 48 in × 12 in (1220 mm × 305 mm) stainless steel sheets were mechanically bolted onto the opposite lateral bracing frame surfaces so that all contact areas between the loading beam and lateral bracing frame was by near-frictionless PTFE-polished stainless steel interface. A silicone-based lubricant was applied to the PTFE-stainless-steel interfaces just before beginning each test, to further reduce friction.

As shown in Figure 2.17, and further highlighted in Figure 2.18, three actuators applied structural loads to the shear wall specimen, which was mounted at its footing to the foundation steel frame by twenty 1.0 in (25.4 mm) diameter high-strength threaded rods. Two vertically-spanning 110 kip (489 kN) capacity hydraulic actuators pulled downward in force control to apply axial compression (100 kip [449 kN] each) to the wall panel of the concrete shear wall specimen, simulating the in-situ gravity loading condition of the wall. The axial load was equivalent to $0.093 A_g f'_c$ where A_g is the gross area of the wall panel cross section and f'_c is the 28-day compressive strength of concrete (4500 psi [31 MPa]). At the same time, one horizontally-spanning 220 kip (979 kN) capacity actuator applied reversed cyclic deformations in displacement control simulating the demands placed on the wall panel during an earthquake. As shown in Figure 2.17, the height of the horizontally-spanning 220 kip (979 kN) capacity actuator was 120.0 in (3048 mm) above the top of the footing.

The vertically-spanning actuators were aligned directly over pairs of embedded socket anchors in the strong floor, and were tied down by two 1-1/2 in (38.1 mm) diameter UNF high-strength threaded rods, so that they had a direct tension load path to the strong floor. The horizontally-spanning actuator was reacted at its base swivel by the Concrete Structural Reaction (CSRB) Block Wall, which was post-tensioned

down to the strong floor with twelve post-tensioned 1-3/8 in (34.9 mm) diameter DWIDAG Threadbars. The lateral load was transmitted to the concrete shear wall specimen via the loading beam, which was mounted on top of the specimen's top cap and connected by ten post-tensioned 1.00 in (25.4 mm) diameter high-strength threaded rods. All components of the primary reaction frame, including the steel loading beam, were designed to remain elastic under the maximum forces that the three actuators were capable of producing.

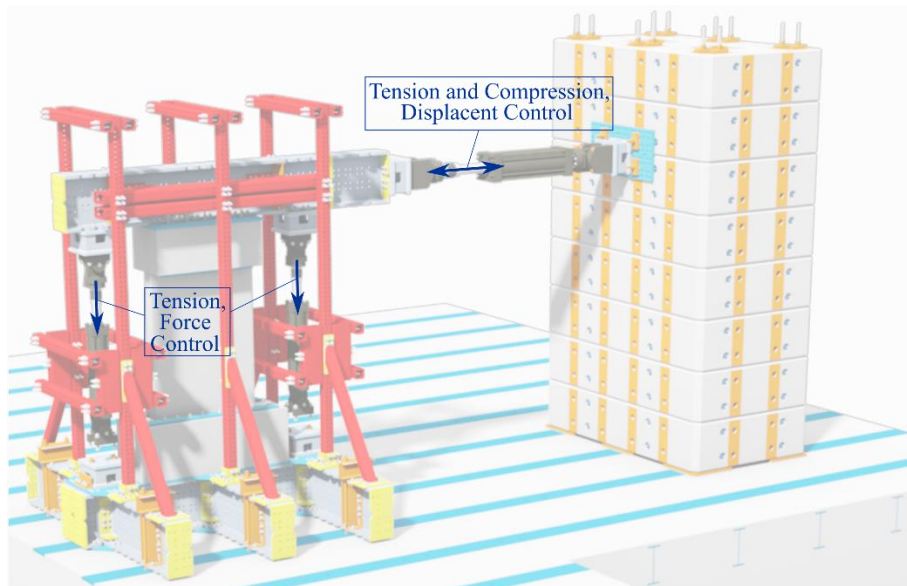


Figure 2.18. Partially transparent view of test setup for testing concrete shear walls, with applied actuator forces shown as arrows. The vertically spanning actuators apply tension in force control and the horizontally spanning actuator applies tension and compression in displacement control.

Five phases of reversed cyclic loading (Figure 2.19) represented the seismic loading protocol (Figure 2.20) to which each wall was subjected: an initial elastic phase, three phases corresponding to Immediate Occupancy (IO), Life Safety (LS), and Collapse Prevention (CP) performance objectives, and finally loading to failure. The purpose of the selected levels of cyclic loading was to cover a range of structural performance from elastic to failure, with measurements regularly interspersed throughout the intermediate stages. The drift ratios associated with each performance objective in Figure 2-19 were based on ASCE 41-17 (ASCE, 2017). For added clarity, each phase of the seismic loading protocol in Figure 2.19 is differentiated by color, and that same color scheme has also been mapped onto the plot of the loading protocol in Figure 2.20. Each phase was apportioned into cycles having multiple peak drift levels, that increased in magnitude within the phase. One cycle each at four levels of elastic drift (specified in Figure 2.19 and Figure 2.20 in percent drift) were followed by three cycles each at three drift ratios (peak displacement divided by a height of 120 in [3.05 m]) within the IO phase, three cycles each at two drift ratios within the LS phase, and three cycles each at two drift ratios within the CP phase. Following the CP phase, the shear wall specimen was loaded to failure by two cycles each at drift ratios increasing by 1 % increments from 2.0 % to 5.0 %. The loading rates were specified such that they were sufficiently slow to prevent dynamic effects, but loosely scaled along with the peak drift ratio of the wall for each phase so that cycle times (i.e., the time required to complete a full cycle) remained tractable to complete

testing of a wall specimen within a single working day. The gain factors for the vertically-spanning 110 kip (489 kN) actuators, which controlled the rate at which their Proportional, Integral, Derivative (PID) controls respond, were deliberately reduced as a safety precaution to prevent overly large squash deformations upon loss of axial load carrying capacity.

ASCE/SEI 41	Cycle No.	Cycle Name	Cycle Time (min)	Peak Disp (in)	Drift Ratio (%)	Load Rate (in/sec)
Elastic	1	01a	0.5	0.06	0.050	0.008
	2	01b	1.0	0.12	0.100	
	3	01c	1.5	0.18	0.150	
	4	01d	2.0	0.24	0.200	
Immediate Occupancy	5	02a-1	2.0	0.30	0.250	0.010
	6	02a-2	2.0	0.30	0.250	
	7	02a-3	2.0	0.30	0.250	
	8	02b-1	3.0	0.45	0.375	
	9	02b-2	3.0	0.45	0.375	
	10	02b-3	3.0	0.45	0.375	
	11	02c-1	4.0	0.60	0.500	
	12	02c-2	4.0	0.60	0.500	
	13	02c-3	4.0	0.60	0.500	
Life Safety	14	03a-1	4.0	0.90	0.750	0.015
	15	03a-2	4.0	0.90	0.750	
	16	03a-3	4.0	0.90	0.750	
	17	03b-1	5.3	1.20	1.000	
	18	03b-2	5.3	1.20	1.000	
Collapse Prevention	19	03b-3	5.3	1.20	1.000	
	20	04a-1	6.7	1.50	1.250	0.015
	21	04a-2	6.7	1.50	1.250	
	22	04a-3	6.7	1.50	1.250	
	23	04b-1	8.0	1.80	1.500	
To failure	24	04b-2	8.0	1.80	1.500	
	25	04b-3	8.0	1.80	1.500	
	26	05a-1	8.0	2.40	2.000	0.020
	27	05a-2	8.0	2.40	2.000	
	28	05b-1	12.0	3.60	3.000	
	29	05b-2	12.0	3.60	3.000	
	30	05c-1	16.0	4.80	4.000	
	31	05c-2	16.0	4.80	4.000	
	32	05d-1	20.0	6.00	5.000	
	33	05d-2	20.0	6.00	5.000	

Figure 2.19. Five phases of loading for ASR-affected concrete shear wall specimens: elastic loading, three phases corresponding to Immediate Occupancy, Life Safety, and Collapse Prevention performance objectives, and loading to failure. 1.0 in = 25.4 mm.

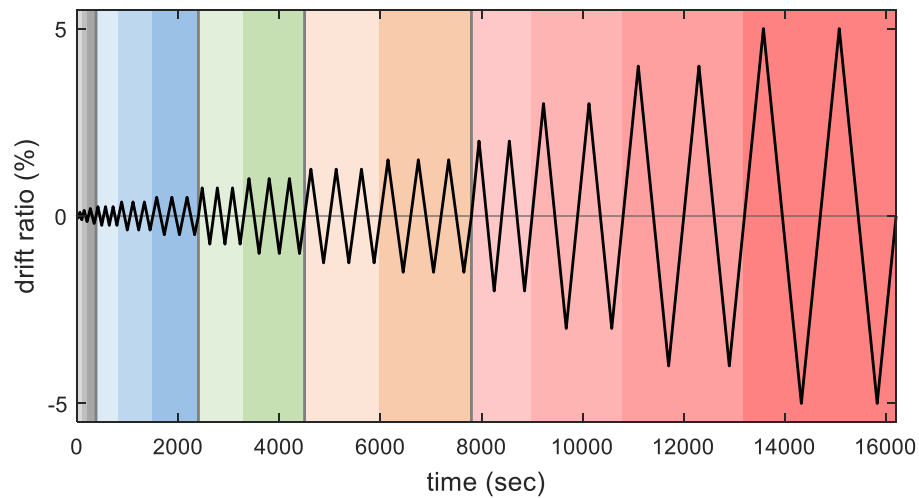


Figure 2.20. Loading protocol for testing ASR-affected concrete shear wall specimens. Colors denote the five phases of loading for ASR-affected concrete shear wall specimens: elastic loading, three phases corresponding to Immediate Occupancy, Life Safety, and Collapse Prevention performance objectives, and loading to failure

At the peaks and valleys of each loading cycles, the displacement of the horizontal actuator was paused (i.e., the actuators has stopped displacing), to allow making observations (e.g., of concrete spalling, rebar buckling), taking photographs, and tracing the initiation and propagation of wall cracking occurring within each cycle (see Chapter 3).

2.6 INSTRUMENTATION

The applied loads, lateral deflections, and wall deformations were monitored during testing. In addition, strain gages applied to the longitudinal and transverse reinforcement prior to placing the concrete monitored the development of strains in the reinforcement in the walls during both curing and testing.

Figure 2.21 shows the nominal location of displacement transducers that were used to measure the lateral wall displacements during testing. Wall displacements were measured at several heights along the wall relative to a fixed frame. Lateral displacements were measured on both sides of the wall specimen at each measurement location. The transducers spanned between an instrumentation column, fixed to the south wall of the laboratory, and threaded rods that were embedded in the wall specimen prior to casting.

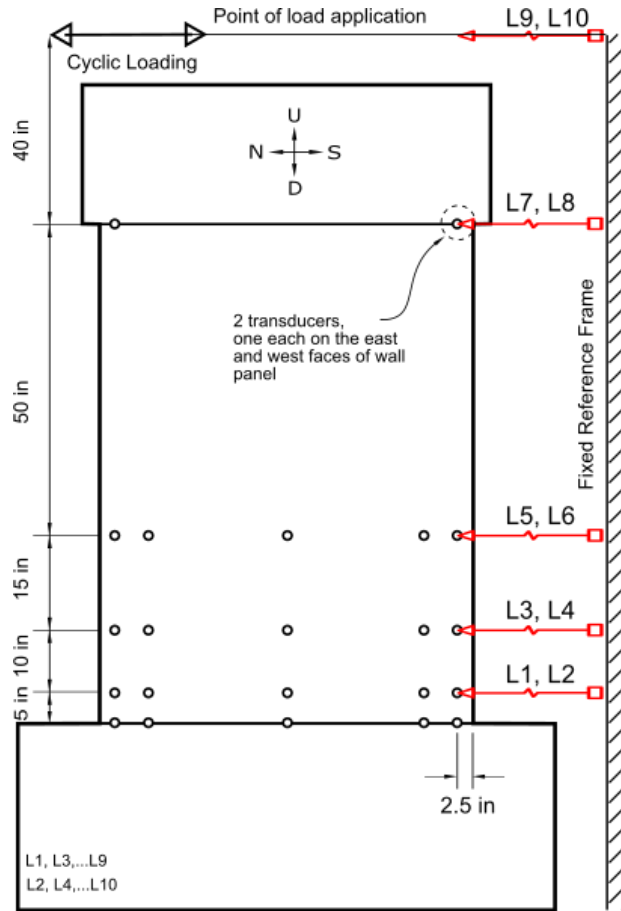


Figure 2.21. Wall displacement transducer locations (elevation view - West side). 1.0 in = 25.4 mm.

Figure 2.22 shows the nominal location of wall deformation measurements during the cyclic tests. Prior to casting the walls, threaded rods were passed, horizontally, through the formwork walls and the reinforcement cage. Displacement transducers, shown in Figure 2.22, were affixed to the rods and used to measure the relative deformation between successive rod locations during loading. Also shown in Figure 2.22 are the locations of transducers that were used to measure the relative displacements between the wall panel and the footing (shear sliding) and the footing and the reaction frame (footing sliding and rocking).

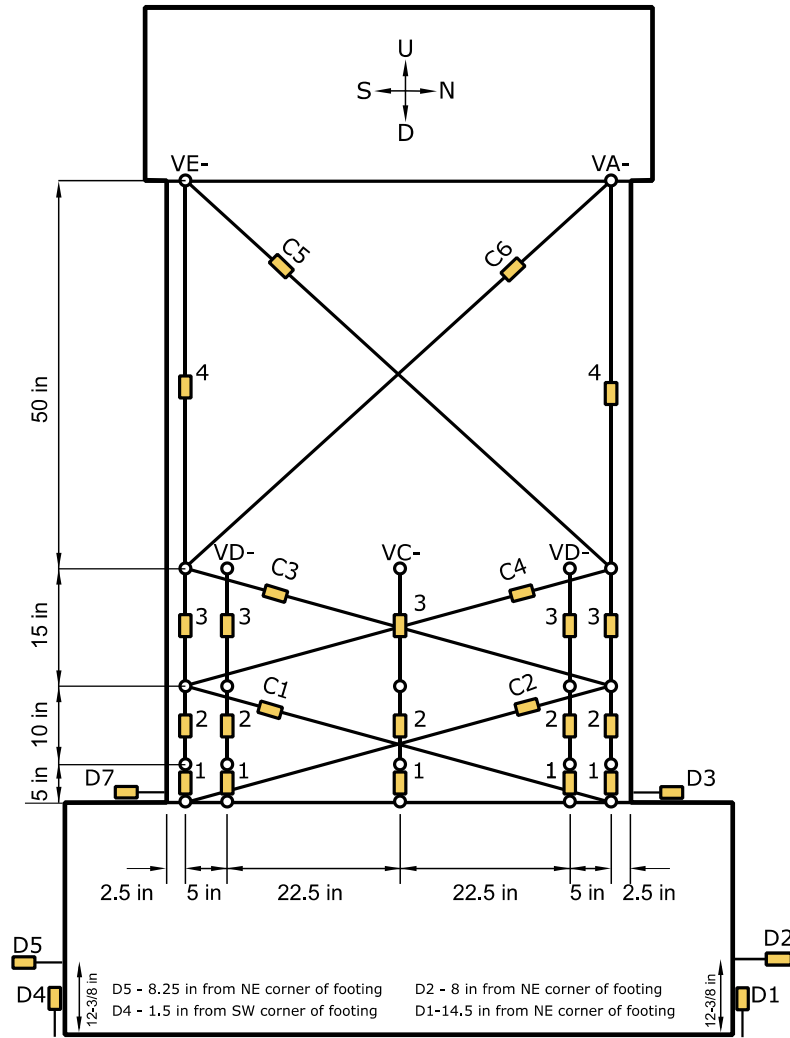


Figure 2.22. Wall deformation measurement locations (elevation view - East side). 1.00 in = 25.4 mm.

Figure 2.23 shows the nominal location of inclinometers that were used to measure the wall rotations during testing. Inclinometers were directly affixed to the wall surface using a hot melt adhesive.

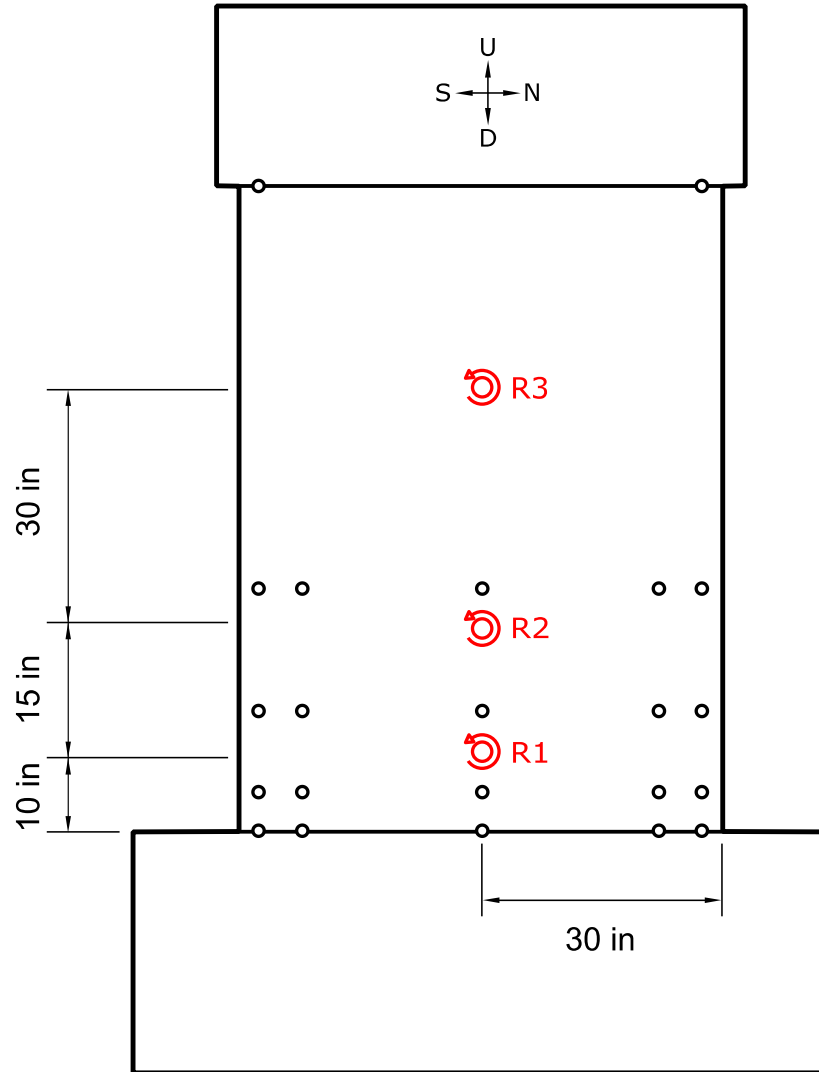


Figure 2.23. Nominal location of inclinometers used to measure wall rotations during testing (elevation view – East side). 1.00 in = 25.4 mm.

Figure 2.24 shows the nominal location and nomenclature for the strain gages on the west and east curtains for the walls with $\rho_t = 0.5\%$ (Walls 1 and 3). Similarly, Figure 2.25 presents the strain gages that were attached on the stirrups and crossties for Walls 1 and 3. In addition, Figure 2.26 shows the strain gages on the west and east curtains, while Figure 2.27 presents the strain gages on the stirrups and crossties for Walls 2 and 4 with $\rho_t = 2\%$. Strain gages were affixed to bars in the west reinforcement curtain; while gages were applied on the east reinforcement curtain only at the footing interface. Two gages per location were applied (on both sides of the bar) on the longitudinal and transverse reinforcement and crossties. Gages were also applied on all four legs of certain stirrups in the boundary elements.

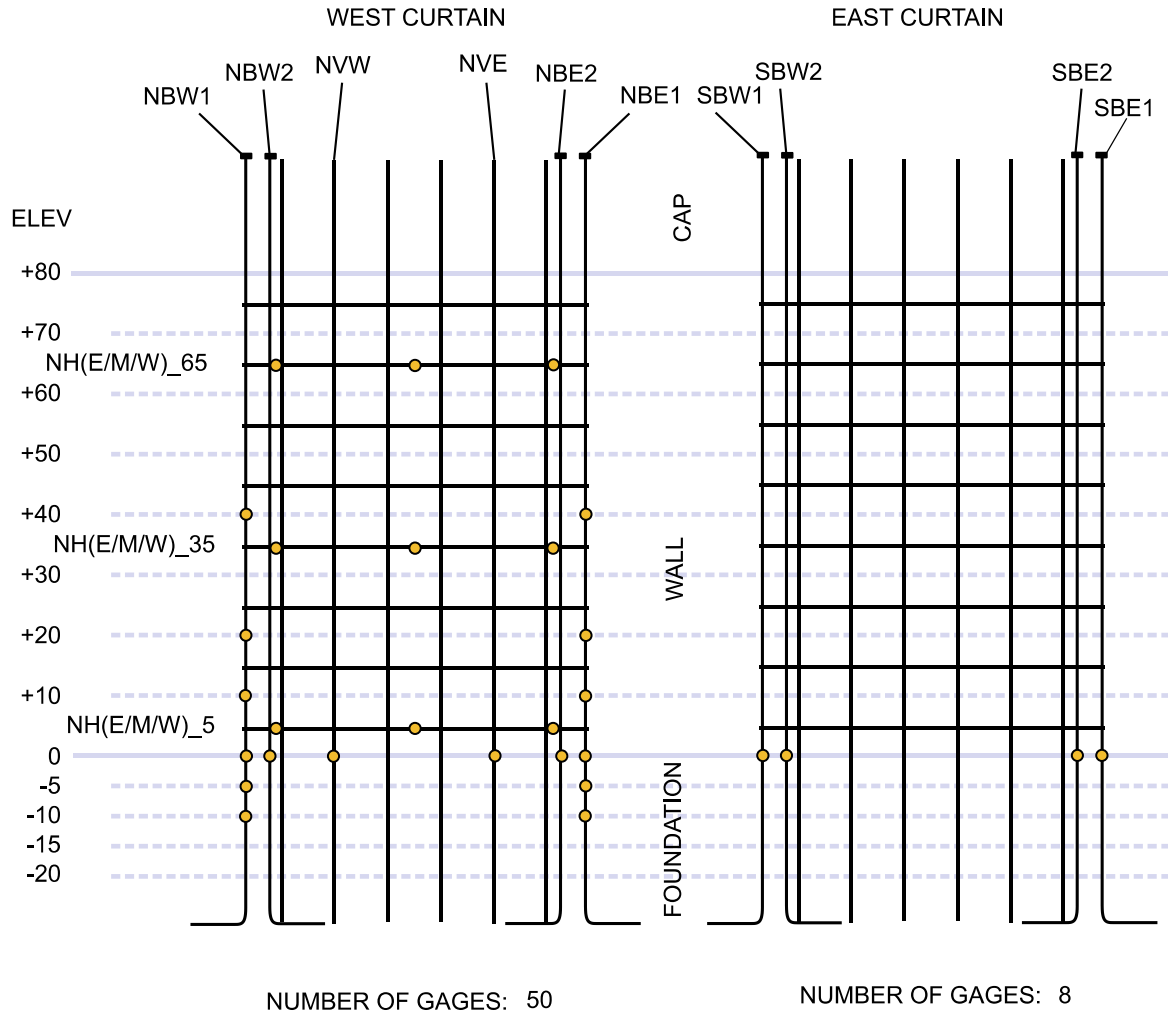


Figure 2.24. Location and nomenclature of strain gages (west and east curtains) for Walls 1 and 3. 1.00 in = 25.4 mm.

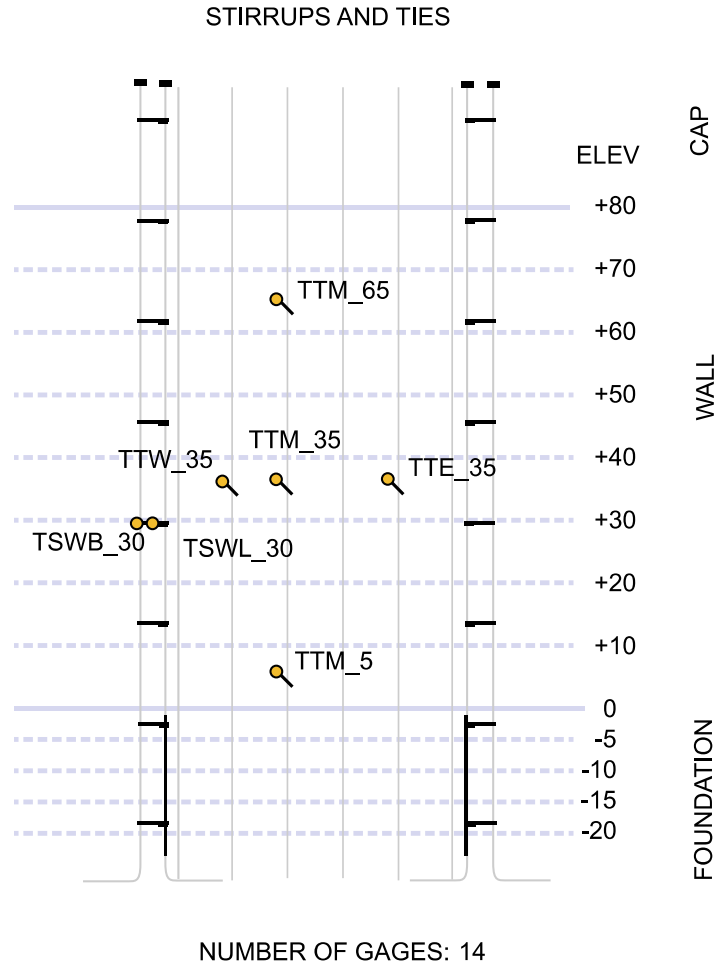


Figure 2.25. Location and nomenclature of strain gages (stirrups and ties) for Walls 1 and 3. 1.00 in = 25.4 mm.

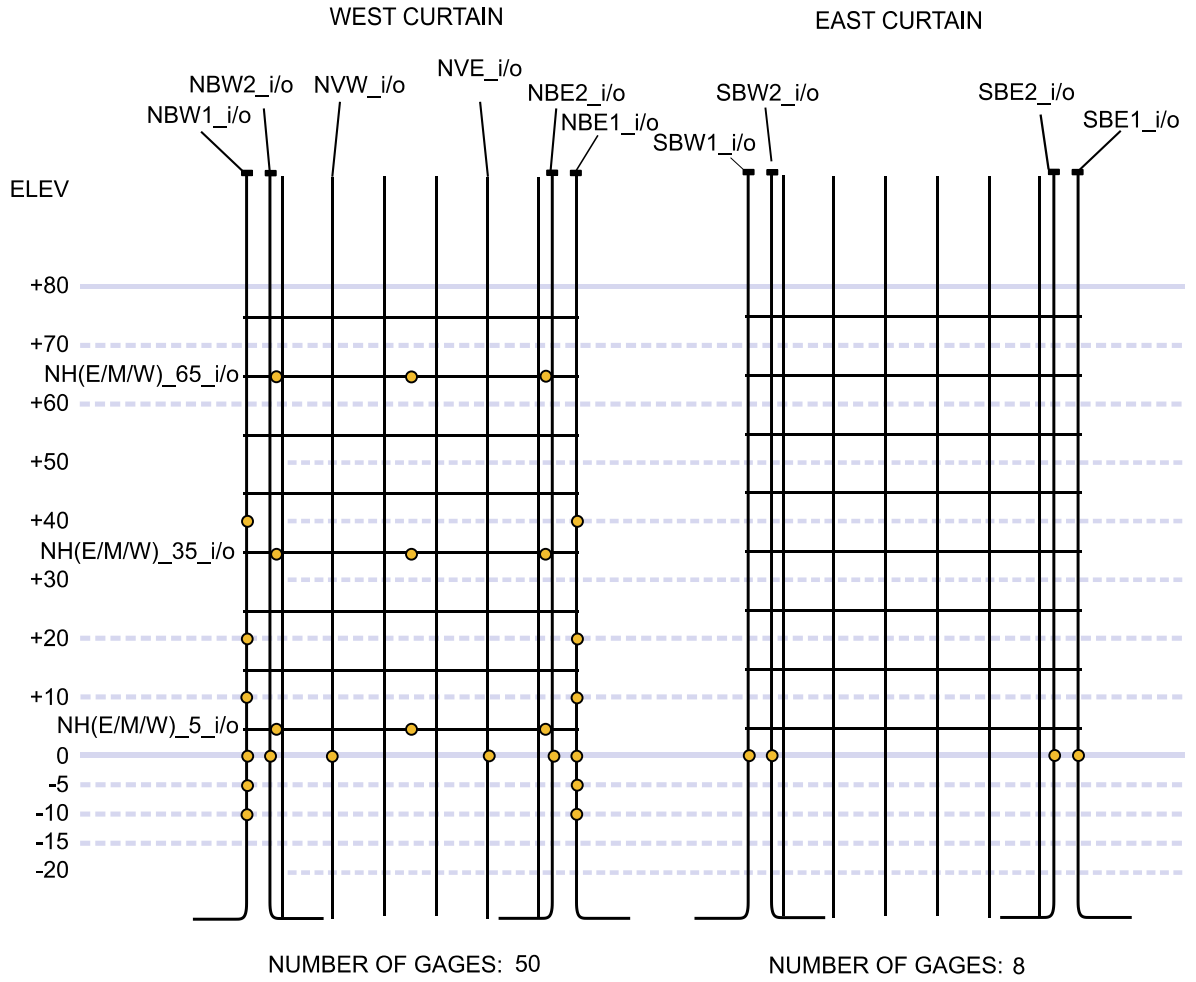


Figure 2.26. Location and nomenclature of strain gages (west and east curtains) for Walls 2 and 4. 1.00 in = 25.4 mm.

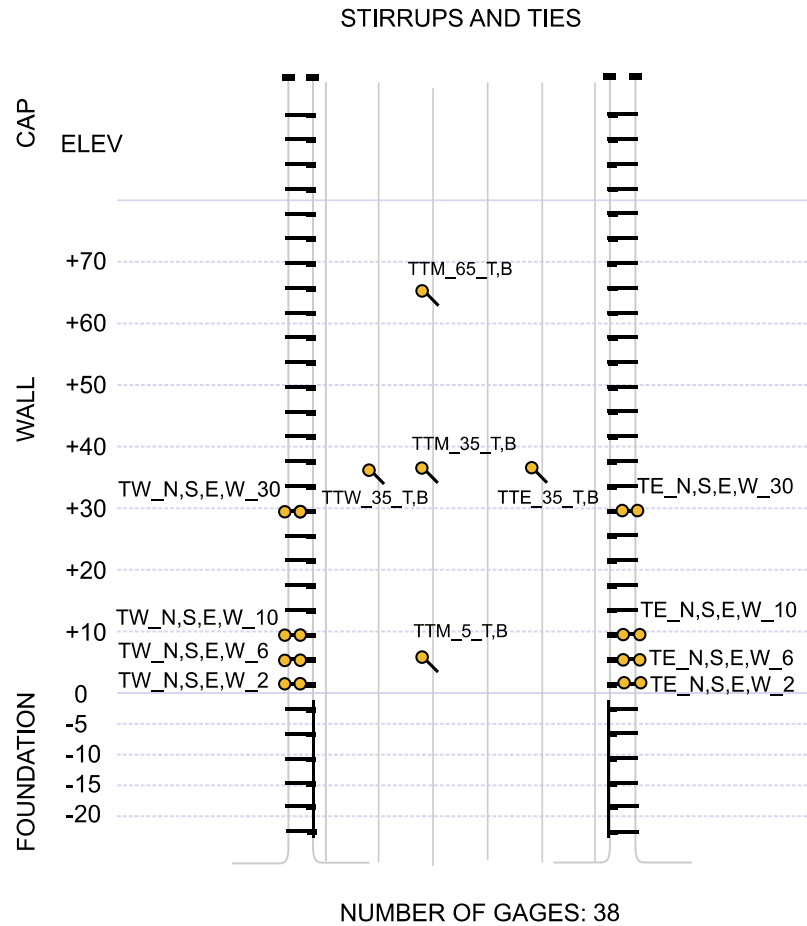


Figure 2.27. Location and nomenclature of strain gages (stirrups and ties) for Walls 2 and 4. 1.00 in = 25.4 mm.

Strains were monitored in the three reactive wall specimens during ASR-induced expansion. Figure 2.28 shows the nominal location of strain gages that were monitored during ASR-induced expansion for the three specimens.

The installation of foil resistance strain gages on the reinforcement bars followed the same procedure described in Sadek et al. (2020) and Thonstad et al. (2020). The bars were prepared using a belt sander to remove their mill scale and achieve the required flatness in the gage area. Bars were further prepared using a fine grit sandpaper and cleaned using a chemical degreaser, prior to gage installation. Gages were adhered to the bar using a two-component epoxy system and the gage installation was protected from the highly alkaline concrete environment using a two-part polysulfide liquid polymer compound.

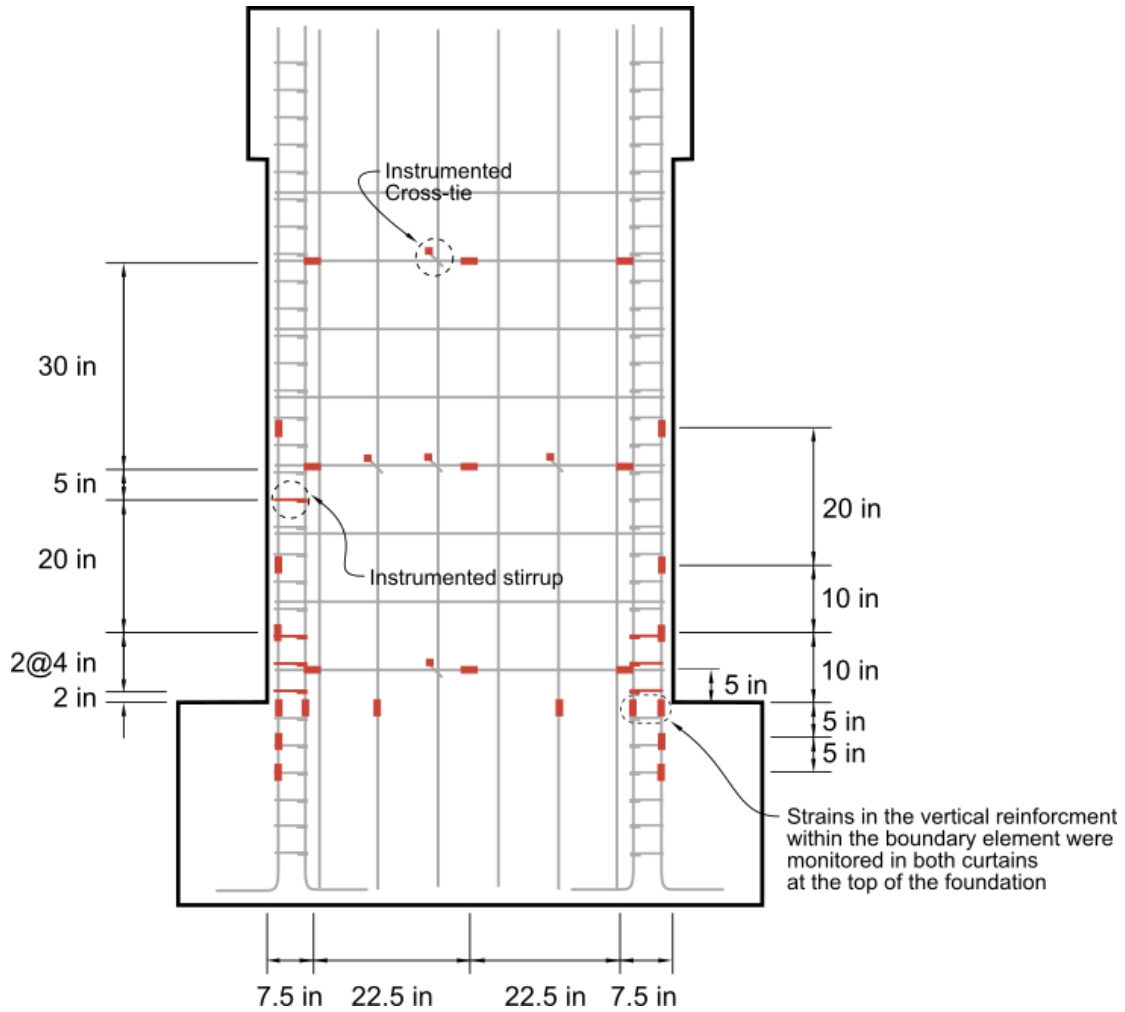


Figure 2.28. Location of strain gages on west reinforcement curtain of the three reactive walls that were monitored during curing. 1.00 in = 25.4 mm.

2.7 PROJECT TIMELINE

Table 2.2 presents a summary of the sequence and dates of key events for this experimental study including concrete placements, operations of environmental controls, and cyclic testing of wall specimens.

Table 2.2. Project timeline

Date	Event
November 14, 2018	Concrete placement for footings of all specimens
April 30, 2019	Concrete placement for reactive wall panels (Walls 1 and 2)
May 9, 2019	Concrete placement for reactive wall panel (Wall 3)
July 2, 2019	Concrete placement for top caps for Walls 1, 2, and 3
August 23, 2019	Concrete placement for non-reactive wall panel (Wall 4)
September 23, 2019	Concrete placement for top cap of Wall 4
August 30, 2019	Start of environmental controls in environmental chamber
March 16, 2020	Laboratory closure and environmental controls shut-down
July 16, 2020	Laboratory reopening and environmental controls restart
September 2, 2020	Cyclic testing of Wall 4 (376 d after wall panel placement)
September 16, 2020	Removal of Wall 1 from environmental chamber
October 28, 2020	Cyclic testing of Wall 1 (547 d after wall panel placement)
November 3, 2020	Removal of Wall 2 from environmental chamber
November 30, 2020	Cyclic testing of Wall 2 (580 d after wall panel placement)
December 7, 2020	Removal of Wall 3 from environmental chamber
December 18, 2020	Cyclic testing of Wall 3 (589 d after wall panel placement)

Chapter 3

OBSERVED RESPONSE

This chapter describes the cracking that was observed in the three reactive shear walls due to the effects of ASR-induced expansion prior to structural loading and the progression of cracking and damage that was observed in all four walls during cyclic testing. For the rest of this chapter, the sides or faces of the wall specimens are identified in terms of cardinal directions (north, east, south, west), which corresponded to the directions in the tested orientation as shown in Chapter 2.

3.1 ASR-INDUCED EXPANSION

Prior to testing, the three reactive walls (Walls 1, 2, and 3) remained in the environmental chamber, which was kept at a high relative humidity and temperature. Walls were removed from the chamber between 3 weeks and 6 weeks prior to performing the cyclic testing to allow for ASR-induced crack mapping, placement into the testing frame, and installation of instrumentation. Visual observations of the condition of the concrete were documented prior to testing.

No visible cracks were observed on the surfaces of the non-reactive wall panel (Wall 4). On the reactive walls panels (of Walls 1, 2, and 3), ASR-induced cracks were observed on all exterior faces. No cracks were found on the exterior faces of the footings or the top caps which were cast with conventional concrete. Outward evidence of widespread ASR-induced cracking in the wall panels consisted of randomly oriented surface cracks. The observed cracks did not appear to be preferentially aligned with the embedded reinforcement, and no discoloration was observed that would suggest corrosion of the embedded reinforcement cages. Furthermore, no discernable differences were found between the cracking patterns on the three reactive wall panels despite their differences in age (at the time of observation) and the amount of transverse reinforcement in the boundary elements.

ASR-induced cracks were mapped/traced using green permanent marker on the west face and north and south ends of each wall panel. Since large numbers of displacement transducers and inclinometers were placed on the east face of the walls, it was not practical to perform crack mapping on that face. Figure 3.1 presents an example of the cracks observed on Wall 2. Further, exudation of a white substance, from the cracks, was also observed as shown in Figure 3.2. It was presumed that this substance was ASR gel, however chemical analyses were not performed to confirm this assumption.



(a)



(b)



(c)

Figure 3.1. Wall 2 ASR-induced cracking: (a) north end, (b) south end, and (c) west face. Shown also in (c) is the 20.0 in × 20.0 in (508 mm × 508 mm) square drawn on the west face for cracking index calculation. Cracks highlighted using permanent marker.



Figure 3.2. Exudation of a white substance on the face of reactive walls. Cracks highlighted using permanent marker.

In addition, a visual crack mapping procedure was performed to quantify the degree of surface cracking present on the reactive walls prior to testing. This approach was based on the cracking index (CI) method that was developed, and is used extensively, by the Federal High Administration (Fournier et al., 2010). This method was also used to measure surface expansion on the reactive block specimens in the Task 1 study (Sadek et al., 2021) and the reactive beam specimens in the Task 2 study (Thonstad et al., 2021). The CI has been used to judge the extent of surface damage to the concrete due to ASR, based on the implicit assumption that external damage is proportional to internal damage; thus, the higher the CI, the higher the assessed level of damage of the concrete element under investigation.

The crack mapping procedure employed in the present study included measurement and summation of crack widths along the perimeter of a 20.0 in \times 20.0 in (508 mm \times 508 mm) square drawn on the west face of the reactive wall specimens. The process can be outlined as follows:

- Identify the location of the square as the area with the most intense cracking on the west face of the wall, see Figure 3.1.
- Each line on the square was scanned using a handheld optical microscope with 20 \times optical magnification and a measuring reticle graduated in 0.004 in (0.1 mm) increments. However, there were many instances where smaller crack width was detected. In these instances, “eyeballing” was used to approximate the crack width (e.g., 0.003 in [0.07 mm]).
- The CI was calculated for each line as the summation of all crack widths along a given line and then dividing by the original length of the line. Cracks smaller than 0.002 in (0.05 mm) were observed and recorded but were not used in calculation of the CI.

Table 3.1 presents the average CI over the horizontal and vertical lines of the square on the west face of each wall. In general, the cracking indices for Walls 1 and 2 (cast together) were similar and higher than those for Wall 3 (cast at a later date).

Table 3.1. Average cracking index for the reactive wall specimens prior to testing

Wall	Average Cracking Index (in/in [mm/mm])	
	Horizontal Lines	Vertical Lines
Wall 1	0.0018	0.0021
Wall 2	0.0018	0.0017
Wall 3	0.0014	0.0014

3.2 WALL CYCLIC TESTING

This section describes the visible cracking and damage to the wall specimens that were observed during the cyclic load testing of the shear walls. Throughout the testing to failure, no cracks or damage was observed for the footing and top cap of all walls. The section, thus, focuses on the observed damage to the wall panels.

3.2.1 Non-reactive Wall 4

Non-reactive Wall 4 served as a control specimen for the testing program with a stirrup spacing of 4.00 in (102 mm) in the boundary elements resulting in a transverse reinforcement ratio, ρ_t , of 2.0 %. As indicated in Section 3.1, this wall did not have pre-existing cracking prior to testing on September 2, 2020. As expected, no cracks were developed during the elastic cycles (Cycles 1 through 4). Also, no cracks were observed for the first three cycles in the immediate occupancy range at a drift ratio of 0.250 % (Cycles 5 to 7). Cracks started to develop at a drift ratio of 0.375 % (Cycles 8 to 10) and kept getting wider and longer with increased drift ratios. Initially, flexural cracks developed in the lower part of the tensile zone of the wall, characterized by horizontal cracks in the boundary elements. These cracks progressed into flexural-shear cracks characterized by horizontal-diagonal cracks, see Figure 3.3, at a drift ratio of 0.500 %. As the drift ratio increased, new cracks with the same pattern were developed in the upper portion of the wall as shown in Figure 3.4 at a drift ratio of 1.000 % in the life safety performance objective range. Figure 3.5 shows the maximum crack width observed and measured on the west face of the four walls, typically at the lower portion of the walls. For a given drift ratio, the crack with the largest width was visually identified and measured using a concrete crack ruler card. The uncertainty associated with the maximum crack width measurement is shown in Table 3.2. Figure 3.5 shows increased crack width with increased drift ratio for the four walls. For Wall 4, a steep rise in the maximum crack width could be observed between drift ratios of 1.000 % and 2.000 %.

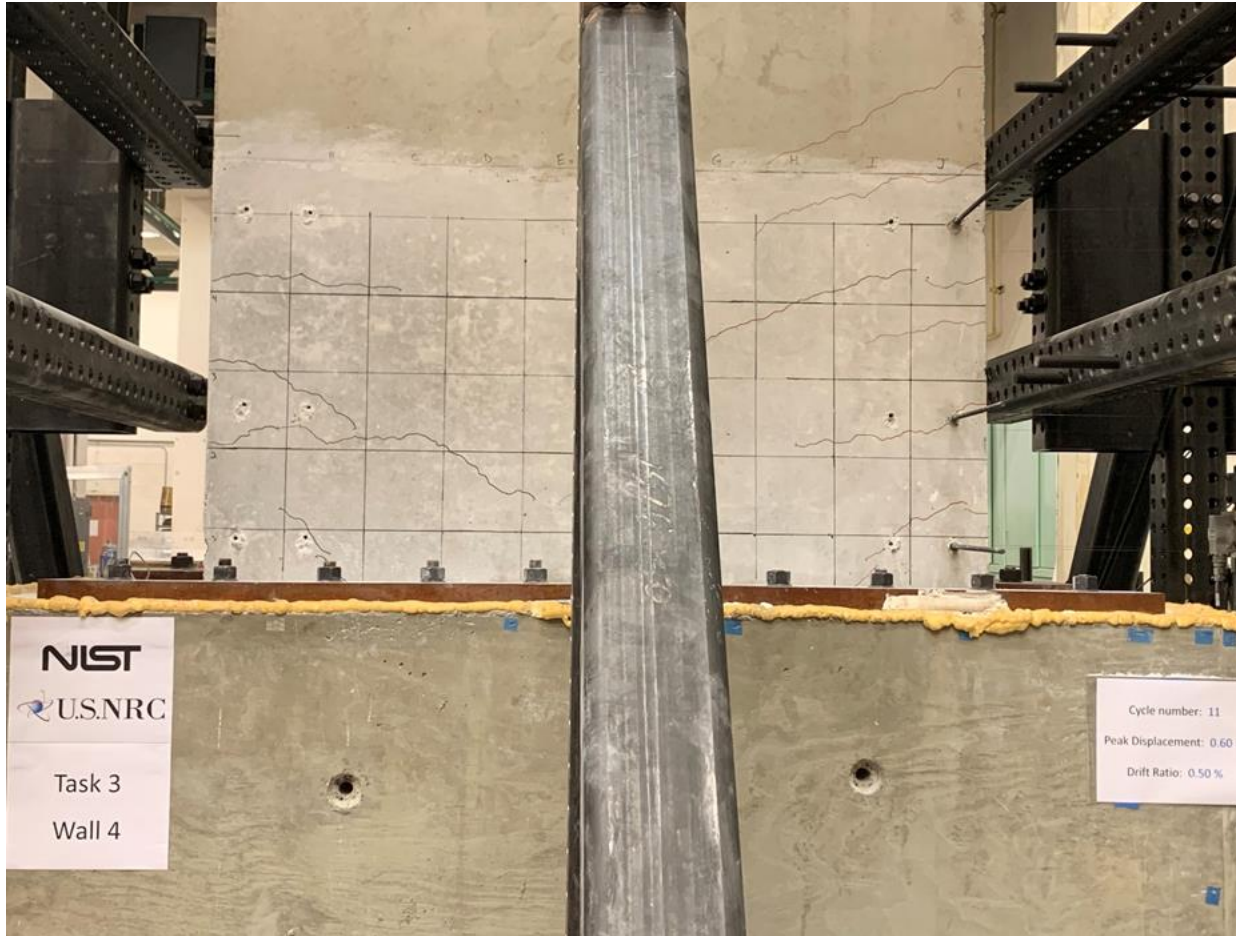


Figure 3.3. Cracks on the west face of Wall 4 at a drift ratio of 0.500 % (Cycle 11). Cracks highlighted using permanent marker.



Figure 3.4. Cracks on the west face of Wall 4 at a drift ratio of 1.000 % (Cycle 17). Cracks highlighted using permanent marker.

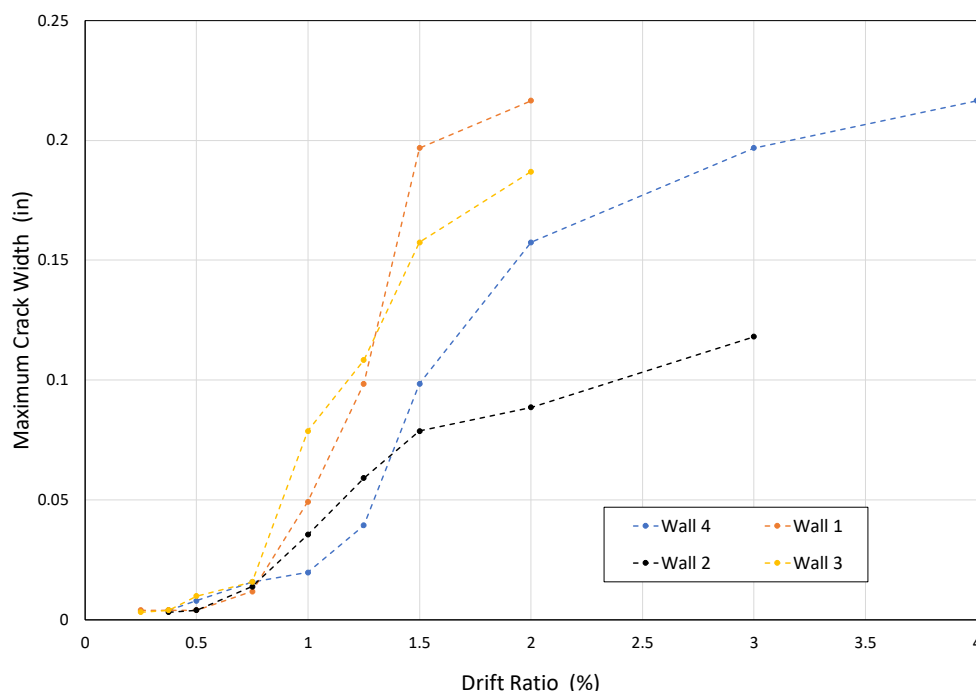


Figure 3.5. Maximum crack width versus drift ratio for the four walls during cyclic testing (1.00 in = 25.4 mm)

Table 3.2. Maximum crack width measurement uncertainty

Maximum Crack Width in (mm)	Measurement Uncertainty in (mm)
< 0.004 (< 0.1)	0.0008 (0.02)
0.004 to 0.025 (0.1 to 0.6)	0.002 (0.05)
0.025 to 0.040 (0.6 to 1.0)	0.008 (0.20)
0.040 to 0.060 (1.0 to 1.5)	0.010 (0.25)
> 0.060 (> 1.5)	0.020 (0.50)

Prior to failure (in the collapse prevention performance objective range and beyond), the wall primarily behaved in a flexural manner by means of yielding of the longitudinal reinforcement and suppressing of a premature shear failure. Ultimately, the wall failed by buckling of longitudinal reinforcement in the boundary element that resulted in spalling/crushing of concrete at the compression zone. The first sign of concrete spalling in the compression zone was observed at a drift ratio of 2.000 % (Cycle 27) as shown in Figure 3.6. At a drift ratio of 3.000 % (Cycle 29), extensive spalling occurred on the compression zone, exposing the buckled longitudinal reinforcement in the boundary element, see Figure 3.7. Increasing the drift ratio to 4.000 %, the wall could not sustain any further loading with longitudinal reinforcing bars

excessively yielding on the tensile zone and buckling on the compression zone. As shown in Figure 3.8(b), one longitudinal reinforcing bar at the boundary element fractured in the tensile zone.

The behavior, cracking pattern, and primary failure modes of non-reactive Wall 4 were consistent with those observed in specimen WR-20 in Oh et al. (2002) which had similar reinforcement and transverse steel ratio in the boundary element to those in Wall 4.



(a)



(b)

Figure 3.6. Damage to Wall 4 at a drift ratio of 2.000 % (Cycle 27): (a) spalling of concrete on compression zone and (b) cracks on the west face. Cracks highlighted using permanent marker.



Figure 3.7. Spalling of concrete in compression zone of Wall 4 at a drift ratio of 3.000 % (Cycle 29) exposing buckled reinforcement in the boundary element



(a)



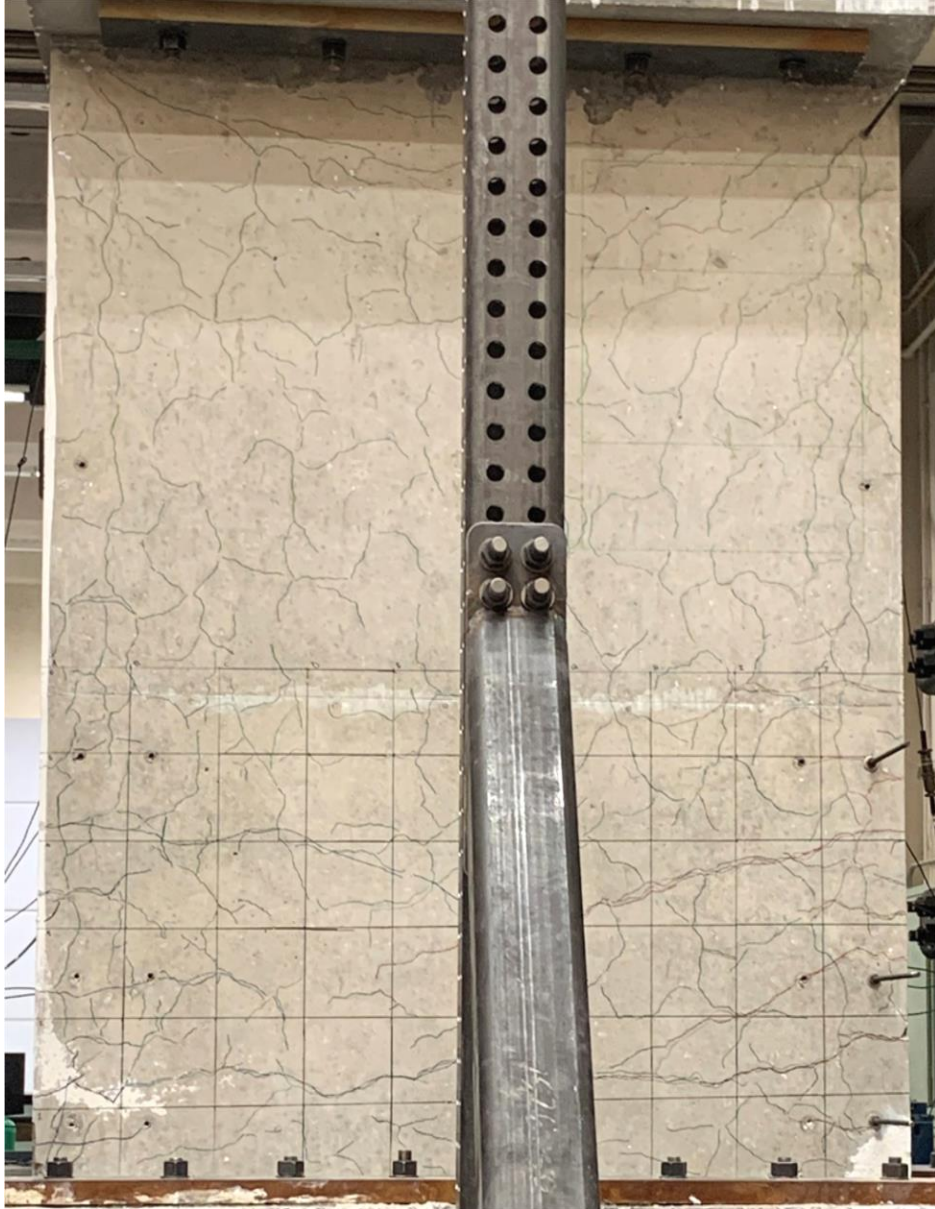
(b)

Figure 3.8. Wall 4 at failure at a drift ratio of 4.000 % (Cycle 31): (a) west face and (b) rupture of longitudinal reinforcing bar in the boundary element

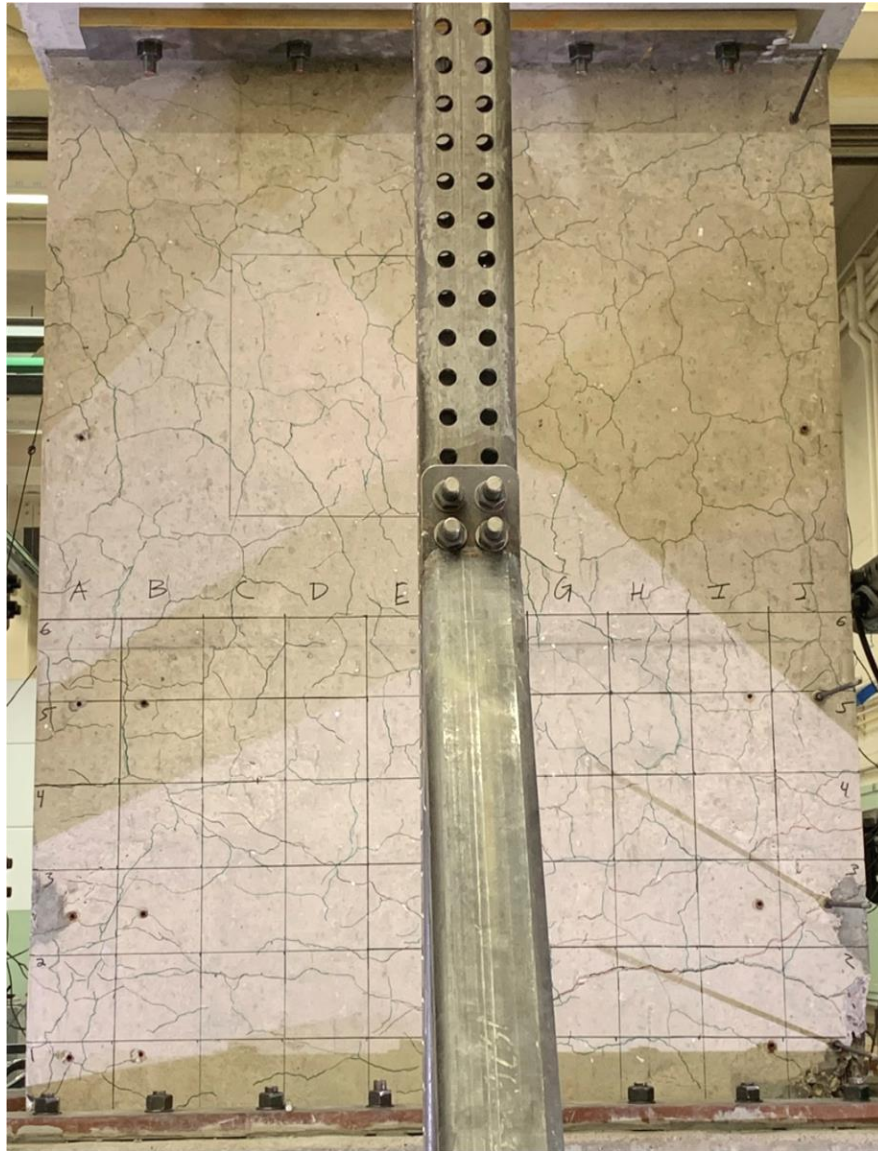
3.2.2 Reactive Walls 1 and 3

Reactive Walls 1 and 3 with identical reinforcement with a stirrup spacing of 16.0 in (406 mm) in the boundary elements resulting in ρ_t of 0.5 % were tested on October 28, 2020 and December 18, 2020, respectively, after being cured in the environmental chamber to accelerate ASR expansion and damage. As a result, both walls had pre-existing cracks at the time of testing as discussed in Section 3.1. In general, both walls demonstrated similar response characteristics and are presented together.

For the cyclic testing, no additional cracks were observed during the elastic cycles (Cycles 1 through 4). Widening and elongation of ASR-induced cracks were observed starting with the cycles in the immediate occupancy range at a drift ratio of 0.250 % (Cycles 5 to 7). Cracks kept getting wider and longer with increased displacements and drift ratios, see Figure 3.5. Figure 3.5 indicates that the maximum crack widths for Walls 1 and 3 were similar with a steep rise in the maximum crack width between drift ratios of 0.750 % and 1.500 %. The cracks were primarily flexural cracks developed in the lower part of the tensile zone of the wall, characterized by horizontal cracks in the boundary element and into the web of the walls. In contrast with Wall 4, no significant horizontal-diagonal cracks were observed. Figure 3.9 presents the cracking pattern at a drift ratio of 1.250 % for both walls (for all subsequent figures, green lines, black lines, and red lines signify pre-existing ASR-induced cracks, tensile cracks on north side, and tensile cracks on south side, respectively).



(a)



(b)

Figure 3.9. Cracks on the west face at a drift ratio of 1.000 %: (a) Wall 1 (Cycle 22) and (b) Wall 3 (Cycle 20). Cracks highlighted using permanent marker.

The two walls failed in a similar fashion to Wall 4, by buckling of the longitudinal reinforcement in the boundary element in the compressive zone and excessive yielding of the longitudinal reinforcement in the tensile zone, albeit at different drift ratios. Buckling of longitudinal bars was accompanied by spalling/crushing of concrete in the compression zone. The first sign of spalling in the compressive zone was observed at a drift ratio of 2.000 % (Cycle 26) and 1.250 % (Cycles 20-22) for Walls 1 and 3, respectively as shown in Figure 3.10. With repeated cycling at higher drift levels, damage to the walls became more intense until the test was stopped as the walls could not sustain further loading at a drift ratio of 3.000 % (Cycle 29) and 2.000 % (Cycle 27) for Walls 1 and 3, respectively as shown in Figure 3.11.

At the end of the test, both walls lost their axial capacity and collapsed in a “squash mode” under the effect of the 200 kip (890 kN) vertical load that was still in effect, see Figure 3.11(a).

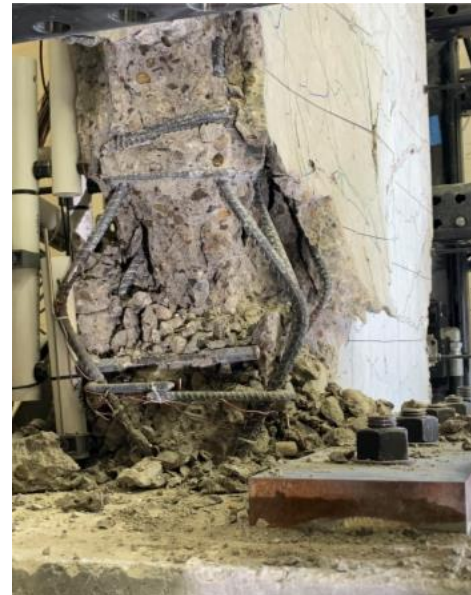
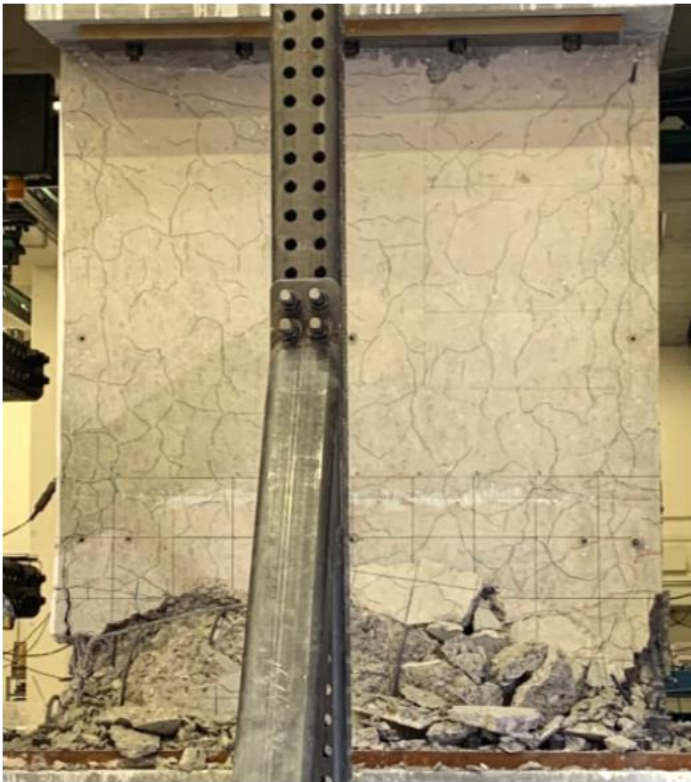


(a)



(b)

Figure 3.10. Buckling of longitudinal bars and concrete spalling in the compressive zone (a) Wall 1 at drift ratio of 2.000 % (Cycle 26) and (b) Wall 3 at drift ratio of 1.250 % (Cycle 22)



(a)



(b)

Figure 3.11. Failure of Walls 1 and 3: (a) Wall 1 west face and north end at drift ratio of 3.000 % (Cycle 29) and (b) Wall 3 west face and north end at drift ratio of 2.000 % (Cycle 27)

3.2.3 Reactive Wall 2

Reactive Wall 2 had an identical reinforcement to Wall 4 with a stirrup spacing of 4.00 in (102 mm) in the boundary elements resulting in ρ_t of 2.0 %. This wall was tested on November 30, 2020 after being cured in the environmental chamber to accelerate ASR expansion and damage. The wall had pre-existing cracks at the time of testing as discussed in Section 3.1.

For the cyclic testing, no additional cracks were observed during the elastic cycles (Cycles 1 through 4). Widening and elongation of ASR-induced cracks were observed starting with at a drift ratio of 0.375 % (Cycle 8) in the immediate occupancy range. Cracks kept getting wider and longer with increased displacements and drift ratios. The cracking pattern was for the most part similar to that observed in Wall 4 which was characterized by horizontal cracks in the boundary element that progressed into flexural-shear cracks characterized by horizontal-diagonal cracks in the web of the wall. Figure 3.12 presents the cracking pattern on the west face of Wall 2 at a drift ratio of 1.500 % (Cycle 23).

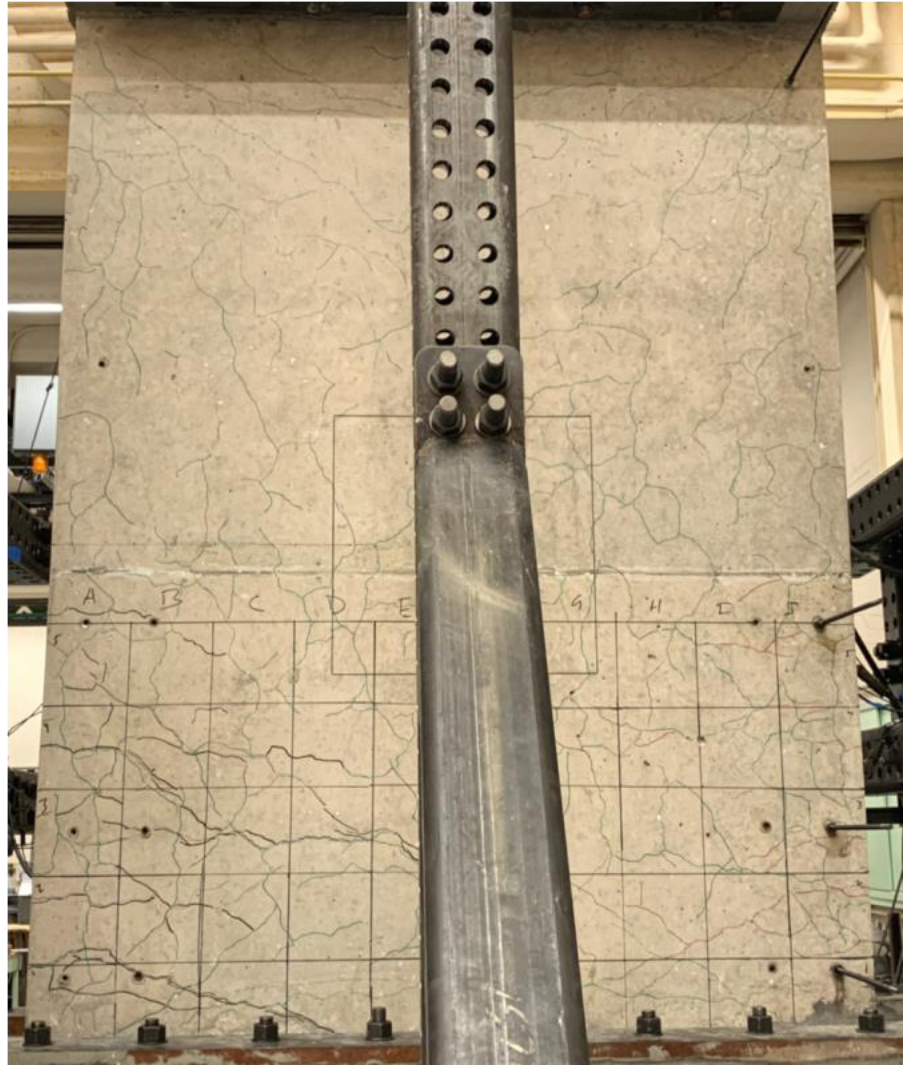
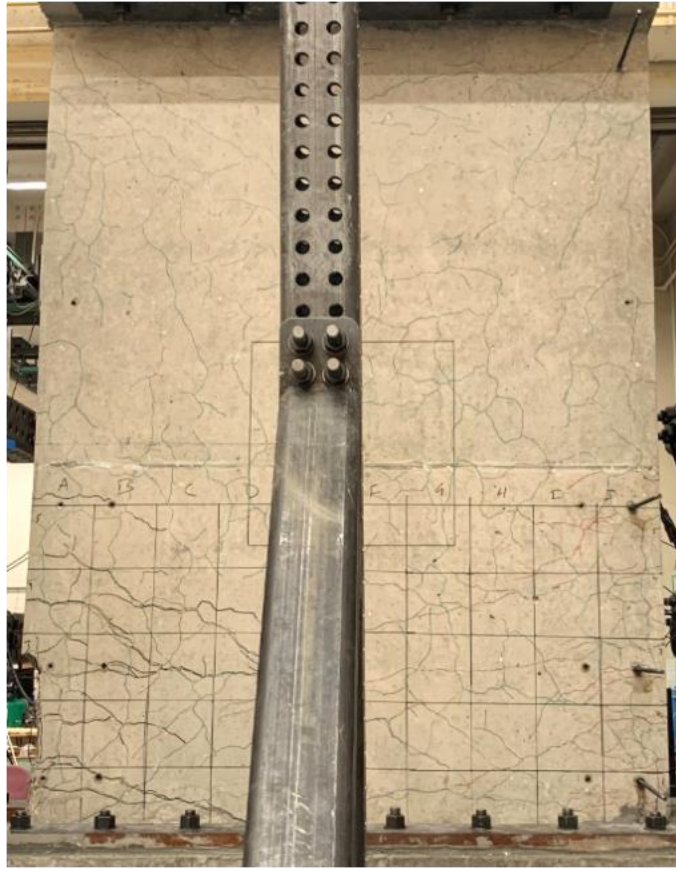


Figure 3.12. Cracks on the west face of Wall 2 at a drift ratio of 1.500 % (Cycle 23). Cracks highlighted using permanent marker.

In general, the failure mode of reactive Wall 2 was similar to that of non-reactive Wall 4. At a drift ratio of 2.000 % (Cycles 26-27), spalling of concrete was observed in the compressive zone, indicating buckling of longitudinal reinforced bars in the boundary elements, see Figure 3.13. At a drift ratio of 3.000 % (Cycle 29), extensive spalling occurred in the compression zone, exposing the buckled longitudinal reinforcement in the boundary element. Increasing the drift ratio to 4.000 %, the wall could not sustain any further loading with reinforcing bars excessively yielding on the tensile zone and buckling on the compression zone. As shown in Figure 3.14, similar to Wall 4, one longitudinal reinforcing bar at the boundary element fractured in the tensile zone.



(a)

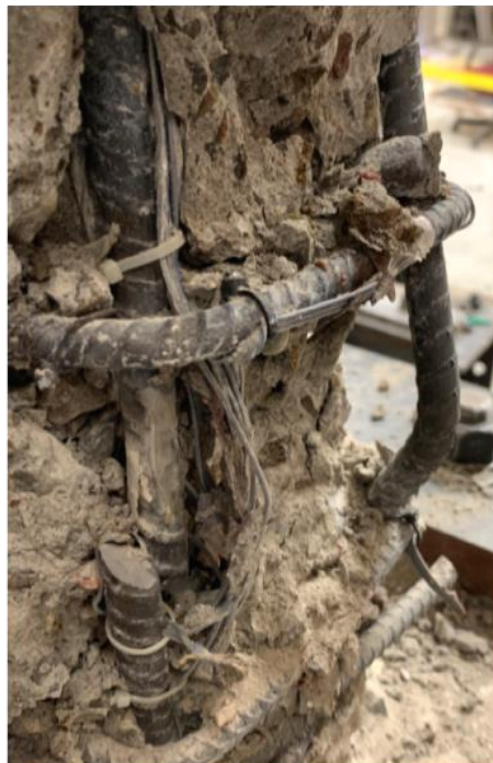


(b)

Figure 3.13. Damage to Wall 2 at a drift ratio of 2.000 % (Cycle 27): (a) cracks on the west face and (b) spalling of concrete on compression zone. Cracks highlighted using permanent marker.



(a)



(b)

Figure 3.14. Wall 2 at failure at a drift ratio of 4.000 % (Cycle 31): (a) west face and (b) rupture of longitudinal reinforcing bar in the boundary element

Chapter 4

MEASURED RESPONSE DURING ASR EXPANSION

This chapter describes the measured response of the wall specimens during curing. In addition, material tests performed on standard test specimens for concrete and reinforcement used in the shear walls are presented. The chapter includes the following sections:

- Section 4.1 gives the measured mechanical properties of concrete cylinders cast with the same concretes as those used in the various components of the wall specimens.
- Section 4.2 presents the measured mechanical properties of the steel reinforcement used to construct the wall panels.
- Section 4.3 describes the length change of standard expansion prisms cast with the same concrete as the wall panels throughout the testing program.
- Section 4.4 discusses the environmental conditions inside the chamber constructed to house the reactive wall specimens during curing.
- Section 4.5 presents the ASR-induced strains measured in the wall panel reinforcement during curing.

Each value reported in the following sections is denoted by mean value μ_c which was typically averaged from at least three independent measurements, followed by \pm uncertainty U . Unless otherwise noted, the reported uncertainty corresponds to the expanded uncertainty associated with the mean, which is determined for n independent measurements by $U = (k u_c)/\sqrt{n}$ from the combined standard uncertainty u_c (i.e., estimated standard uncertainty in the mean from an uncertainty analysis) with a coverage factor of k determined by the two-tailed Student's t distribution at probability $p = 95\%$ (i.e., at the 95th percentile) with $N = n - 1$ degrees of freedom. Assuming that the unknown true value being measured (for example, the compressive strength, elastic modulus, or tensile strength) is approximately normally distributed with standard deviation u_c , the reported mean value lies within the interval defined by $\pm U$ with a level of confidence of 95%. For each plot in this section, the markers correspond to mean values and the error bars correspond to $\mu_c \pm U$.

4.1 CONCRETE MECHANICAL PROPERTIES

The compressive strength, modulus of elasticity, and splitting tensile strength of the various components of the wall specimens including the footings, wall panels, and top caps were determined through tests on the 4.00 in \times 8.00 in (102 mm \times 203 mm) companion concrete cylinders prepared during casting of these components. Testing was conducted in accordance with ASTM C39-20 Standard Test Method for Compressive Strength of Cylindrical Concrete Specimens (ASTM C39, 2020), ASTM C469/469M-14 Standard Test Method for Static Modulus of Elasticity and Poisson's Ratio of Concrete in Compression (ASTM C469/469M, 2014), and ASTM C496/496M-17 Standard Test Method for Splitting Tensile Strength of Cylindrical Concrete Specimens (ASTM C496/496M, 2017).

For the reactive and non-reactive concretes used in the wall panels, the development of the mechanical properties over time was captured by testing their concrete cylinders at 7 d, 14 d, 28 d, 90 d, 180 d, and at the time of the respective wall cyclic testing. For the conventional concretes used in the footings and top caps, the cylinders were only tested at 28 d and at the time of each wall cyclic testing. In the following subsections, mechanical property values are presented as the average values for a given test date along with the expanded uncertainty as explained above. For the data presented in this section, time zero corresponds to the concrete casting date of the specific component of the wall specimens.

4.1.1 Uniaxial Compressive Strength

Conventional Concrete for Footings and Top Caps:

Figures 4.1 and 4.2 show the compressive strength of the concrete used for the footings and top caps, respectively, plotted against time measured in days after casting. In these figures, the solid circular marker represents the average value of the compressive strength, while the error band at each time corresponds to the expanded uncertainty. The concrete used in the footings had a 28-day compressive strength of 10 000 psi \pm 1480 psi (68.9 MPa \pm 10.2 MPa) and gained strength up to the range of 12 000 psi \pm 1450 psi (82.7 MPa \pm 10.0 MPa) to 13 800 psi \pm 1020 psi (95.1 MPa \pm 7.0 MPa) at the time of walls testing. The 28-day strength for the concrete used in the top caps of the reactive wall specimens (Walls 1, 2, and 3) was 5520 psi \pm 950 psi (38.1 MPa \pm 6.6 MPa) and gained strength up to the range of 6100 psi \pm 1360 psi (42.1 MPa \pm 9.4 MPa) to 7500 psi \pm 1810 psi (51.7 MPa \pm 12.5 MPa) at the time of walls cyclic testing. For the concrete used in the top cap of the non-reactive Wall 4, the 28-day strength was 5140 psi \pm 440 psi (35.4 MPa \pm 3.0 MPa) and gained strength up to 5640 psi \pm 1190 psi (38.9 MPa \pm 8.2 MPa) at the time of the wall testing.

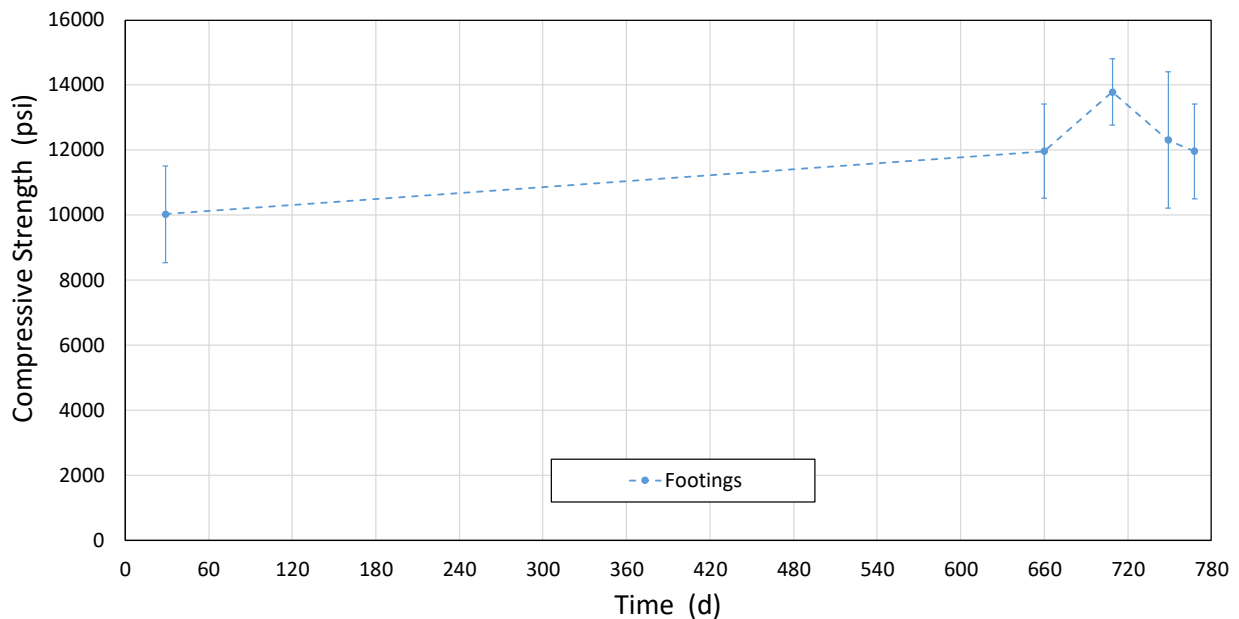


Figure 4.1. Compressive strength of concrete used in the footings (1.00000 psi = 0.00689 MPa)

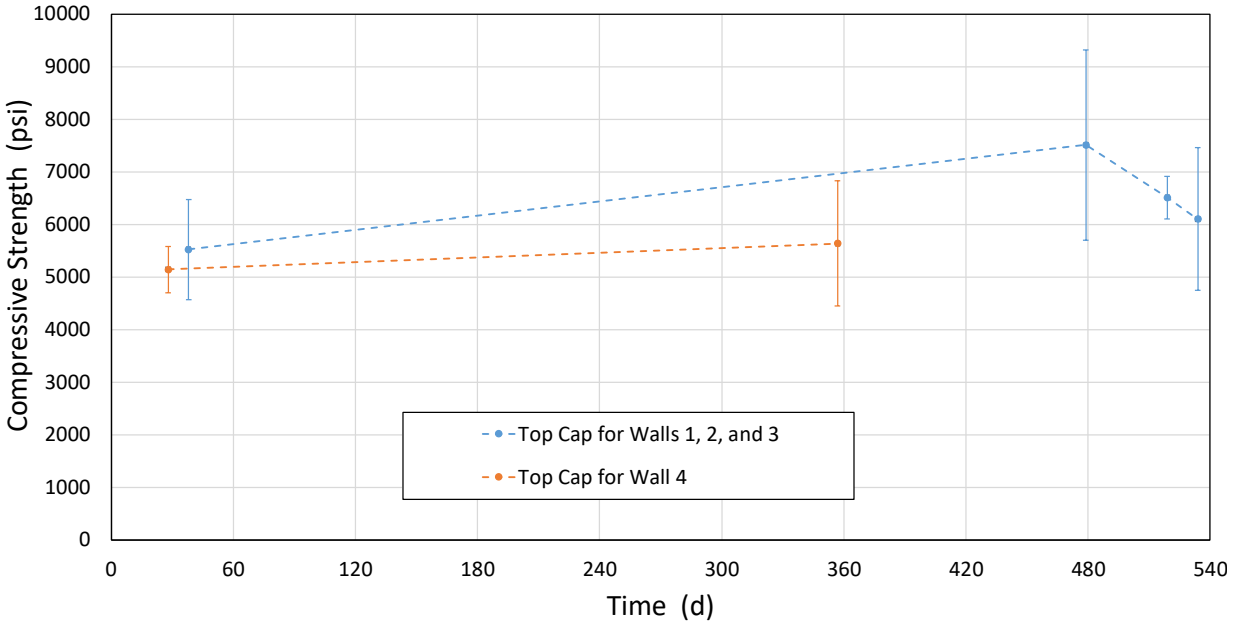


Figure 4.2. Compressive strength of concrete used in the top caps (1.00000 psi = 0.00689 MPa)

Reactive and Non-reactive Concrete for Wall Panels:

Figure 4.3 shows the compressive strength of the concrete used in reactive Walls 1 and 2, reactive Wall 3, and non-reactive Wall 4 (lithium-nitrate treated mixture) plotted against time. The reactive concrete cylinders continued to gain strength until roughly 90 d after casting. At 180 d and beyond, the compressive strength was roughly 20 % less than the 28-day compressive strength. Similar behavior was observed for the block specimens described in the Task 1 report (Sadek et al., 2021) and the beam specimens described in the Task 2 report (Thonstad et al., 2021). On the contrary, the non-reactive cylinders continued to gain strength until the Wall 4 cyclic testing, 378 d after casting. Table 4.1 provides the measured compressive strength of the 4.00 in × 8.00 in (102 mm × 203 mm) concrete cylinders from all wall panels throughout the testing period (see Section 2.7). The table shows increased uncertainty in the measured compressive strength of the reactive cylinders with increased ASR expansion and degradation.

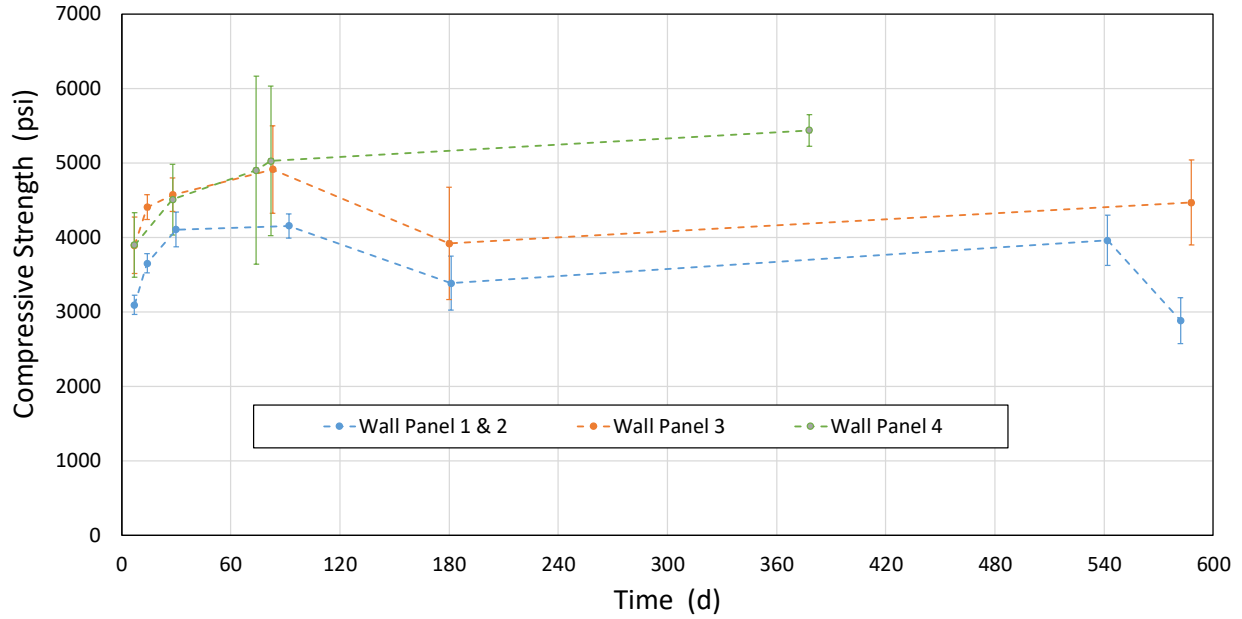


Figure 4.3. Compressive strength of reactive and non-reactive concrete used in the wall panels (1.00000 psi = 0.00689 MPa)

Table 4.1. Compressive strength of reactive and non-reactive concrete used in the wall panels

Time	Compressive Strength psi (MPa)		
	Walls 1&2	Wall 3	Wall 4
7 d*	3090 ± 130 (21.3 ± 0.9)	3890 ± 380 (26.8 ± 2.6)	3900 ± 430 (26.9 ± 3.0)
14 d*	3650 ± 130 (25.2 ± 0.9)	4410 ± 160 (30.4 ± 1.1)	
28 d*	4100 ± 240 (28.3 ± 1.7)	4570 ± 220 (31.5 ± 1.5)	4510 ± 470 (31.1 ± 3.2)
90 d*	4150 ± 160 (28.6 ± 1.1)	4910 ± 590 (33.9 ± 4.1)	5020 ± 1010 (34.6 ± 7.0)
180 d*	3380 ± 360 (23.3 ± 2.5)	3920 ± 760 (27.0 ± 5.2)	
Testing of Wall 1 at 542 d*+	3960 ± 340 (27.3 ± 2.3)		
Testing of Wall 2 at 582 d*+	2880 ± 310 (19.9 ± 2.1)		
Testing of Wall 3 at 588 d*+		4470 ± 570 (30.8 ± 3.9)	
Testing of Wall 4 at 378 d*+			5440 ± 210 (37.5 ± 1.4)

* Actual date might slightly differ

+ Test dates are relative to wall panel cast date

4.1.2 Modulus of Elasticity

The compressive modulus of elasticity was determined as the slope of the linear regression of the measured stress and strain up to 40 % of the compressive strength of the cylinder. This approach, unlike the ASTM C469 secant stiffness method, reduced the influence of the initial nonlinearity of the measured compressive stress-strain response that is often observed in ASR-affected concrete cylinders and cores. Calculation of the values of compressive modulus as the slope obtained from linear regression more robustly captured the basic features of this nonlinearity; however, as was described in the Task 1 report (Sadek et al., 2021), the choice of calculation method had only a minimal effect on the reported compressive modulus values.

Conventional Concrete for Footings and Top Caps:

Figures 4.4 and 4.5 show the compressive modulus of elasticity of the concrete used for the footings and top caps, respectively, plotted against time measured in days after casting. In the figures, the marker represents the average value of the modulus, while the error band at each time corresponds to the expanded uncertainty. The concrete used in the footings had a 28-day elastic modulus of 5700 ksi \pm 740 ksi (39.3 GPa \pm 5.1 GPa), and at the time of walls testing, the modulus was in the range of 6140 ksi \pm 1020 ksi (42.3 GPa \pm 7.0 GPa) to 6920 ksi \pm 330 ksi (47.7 GPa \pm 2.3 GPa). The 28-day elastic modulus for the concrete used in the top caps of the reactive wall specimens (Wall 1, 2, and 3) was 5690 ksi \pm 610 ksi (39.2 GPa \pm 4.2 GPa), and at the time of walls cyclic testing, the modulus was in the range of 5070 ksi \pm 2060 ksi (35.0 GPa \pm 14.2 GPa) to 6280 ksi \pm 650 ksi (43.3 GPa \pm 4.5 GPa). For the concrete used in the top cap of the non-reactive Wall 4, the 28-day modulus was 5760 ksi \pm 290 ksi (39.7 GPa \pm 2.0 GPa), and at the time of the wall testing, the modulus was 5260 ksi \pm 460 ksi (36.2 GPa \pm 3.2 GPa).

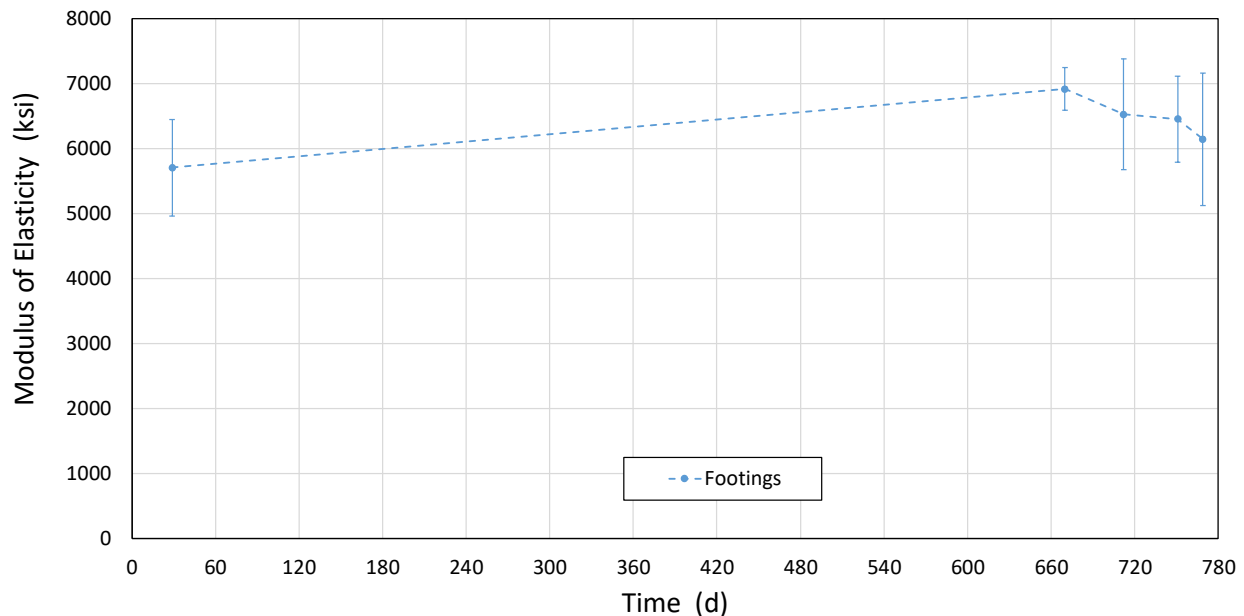


Figure 4.4. Compressive modulus of elasticity of concrete used in the footings (1.00000 ksi = 0.00689 GPa)

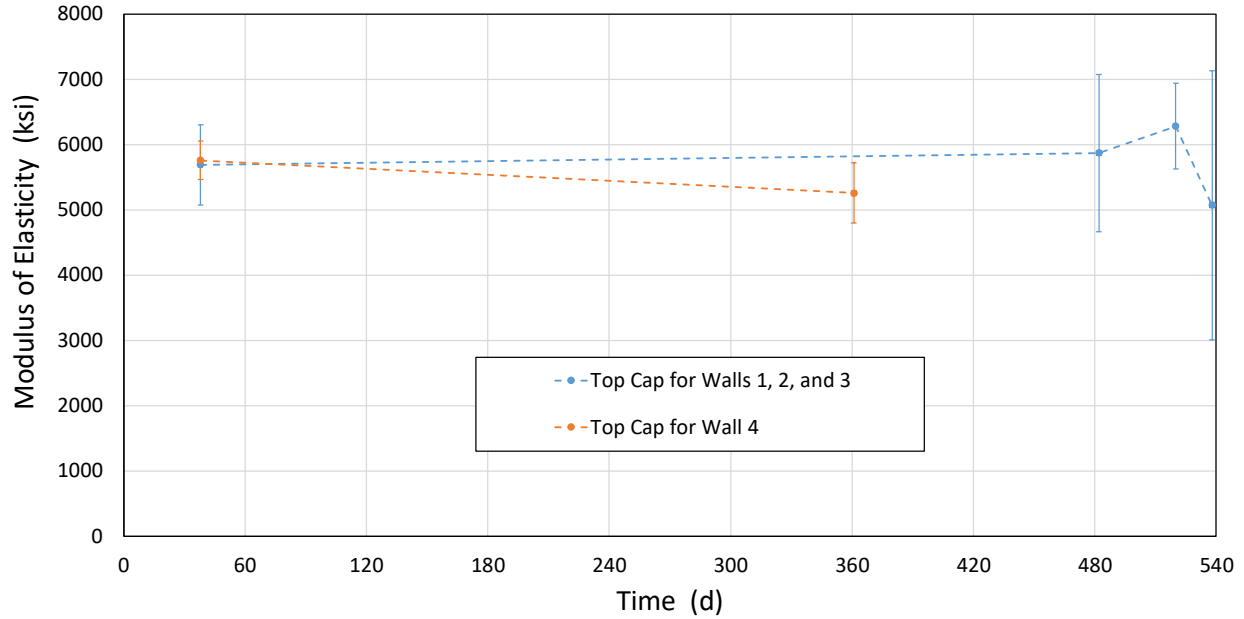


Figure 4.5. Compressive modulus of elasticity of concrete used in the top caps (1.00000 ksi = 0.00689 GPa)

Reactive and Non-reactive Concrete for Wall Panels:

Figure 4.6 shows the compressive modulus of elasticity of the concrete used in reactive Walls 1 and 2, reactive Wall 3, and non-reactive Wall 4 (lithium-nitrate treated mixture) plotted against time. The figure shows an increase in the elastic modulus of the reactive and non-reactive cylinders for the first 28 d after casting. At 90 d and beyond, the elastic modulus of the reactive cylinders significantly decreased, by up to 70 % for Walls 1 and 2, and by up to 50 % for Wall 3 when compared with their respective value of 28-day modulus. Similar behavior was observed for the block specimens described in the Task 1 report (Sadek et al., 2021) and the beam specimens described in the Task 2 report (Thonstad et al., 2021). On the contrary, the elastic modulus for the non-reactive cylinders of Wall 4 remained mostly flat until testing of the wall. Table 4.2 provides the measured compressive modulus of elasticity of the 4.00 in × 8.00 in (102 mm × 203 mm) concrete cylinders from all wall panels throughout the testing period. Similar to the compressive strength of reactive concrete samples, Table 4.2 shows increased uncertainty in the measured elastic modulus of the reactive cylinders with increased ASR expansion and degradation.

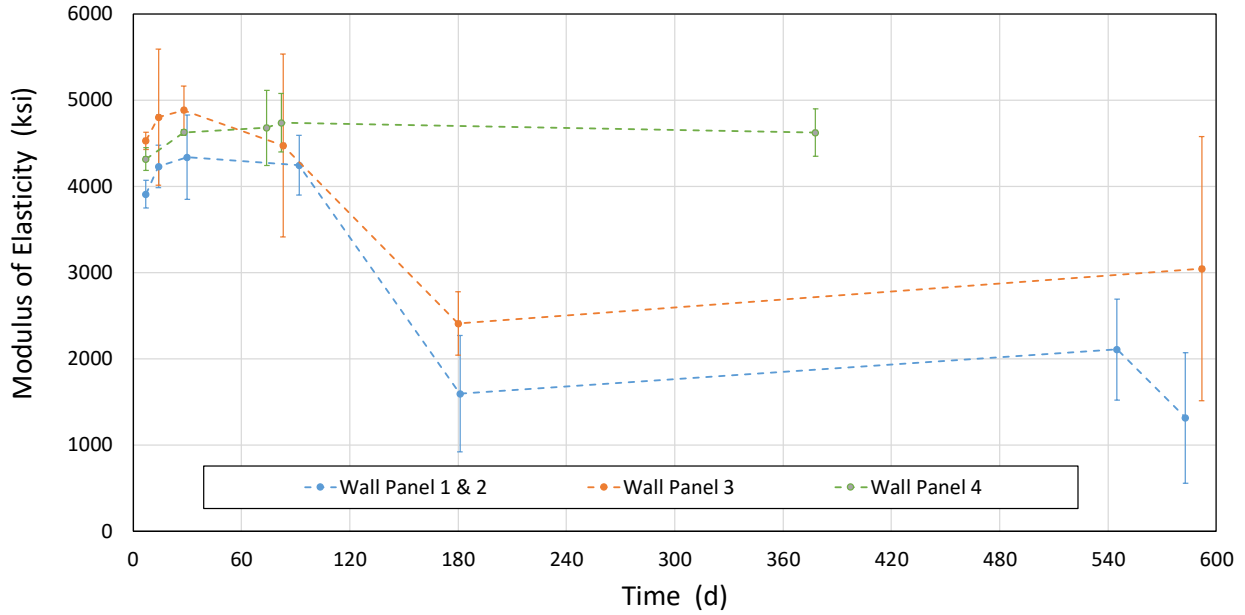


Figure 4.6. Compressive modulus of elasticity of reactive and non-reactive concrete used in the wall panels (1.00000 ksi = 0.00689 GPa)

Table 4.2. Compressive modulus of elasticity of reactive and non-reactive concrete used in the wall panels

Time	Compressive Modulus of Elasticity ksi (GPa)		
	Walls 1&2	Wall 3	Wall 4
7 d*	3910 ± 160 (27.0 ± 1.1)	4530 ± 100 (31.2 ± 0.7)	4310 ± 130 (29.7 ± 0.9)
14 d*	4230 ± 250 (29.2 ± 1.7)	4800 ± 790 (33.1 ± 5.4)	
28 d*	4340 ± 490 (29.9 ± 3.4)	4880 ± 280 (33.6 ± 1.9)	4630 ± 30 (31.9 ± 0.2)
90 d*	4240 ± 350 (29.2 ± 2.4)	4470 ± 1060 (30.8 ± 7.3)	4734 ± 340 (32.6 ± 2.3)
180 d*	1590 ± 680 (11.0 ± 4.7)	2410 ± 370 (16.6 ± 2.6)	
Testing of Wall 1 at 542 d*+	2100 ± 590 (14.5 ± 4.1)		
Testing of Wall 2 at 582 d*+	1310 ± 760 (9.0 ± 5.2)		
Testing of Wall 3 at 588 d*+		3040 ± 1530 (21.0 ± 10.5)	
Testing of Wall 4 at 378 d*+			4620 ± 280 (31.9 ± 1.9)

* Actual date might slightly differ

+ Test dates are relative to wall panel cast date

Figure 4.7 shows the mean value of modulus of elasticity versus the square root of the mean value of compressive strength at various ages of the cylinders from the four wall panels. In the figure, Walls 1 and 2, Wall 3, and Wall 4 are characterized by the circular, square, and triangular markers, respectively, while cylinders tested at or before 90 d of casting and those tested after 90 d of casting are characterized by the red and blue colors, respectively. The dashed line in the figure represents the modulus of elasticity calculated as a function of the compressive strength of concrete per ACI 318-14 (Section 19.2.2.1), while the two solid lines show $\pm 20\%$ deviations from the ACI equation. Section 19.2.2.1 of ACI 318-14 calculates the elastic modulus of concrete, E_c , as a function of the 28-day compressive strength, f'_c , as $E_c = 57000 \sqrt{f'_c}$ (in units of psi). Figure 4.7 shows that for the first 90 d after casting, the compressive modulus was within or exceeded the $\pm 20\%$ range of the ACI equation. After 90 d, the measured compressive modulus of the reactive cylinders (Walls 1, 2, and 3) became significantly lower, on average, than the modulus predicted by the ACI equation. This trend indicates that the compressive modulus of the reactive concrete degraded faster with ASR expansion than did the concrete's compressive strength. The non-reactive Wall 4 cylinders, on the other hand, remained within the $\pm 20\%$ range of the ACI equation. These observations are consistent with those from the Task 1 report (Sadek et al., 2021) and the Task 2 report (Thonstad et al., 2021).

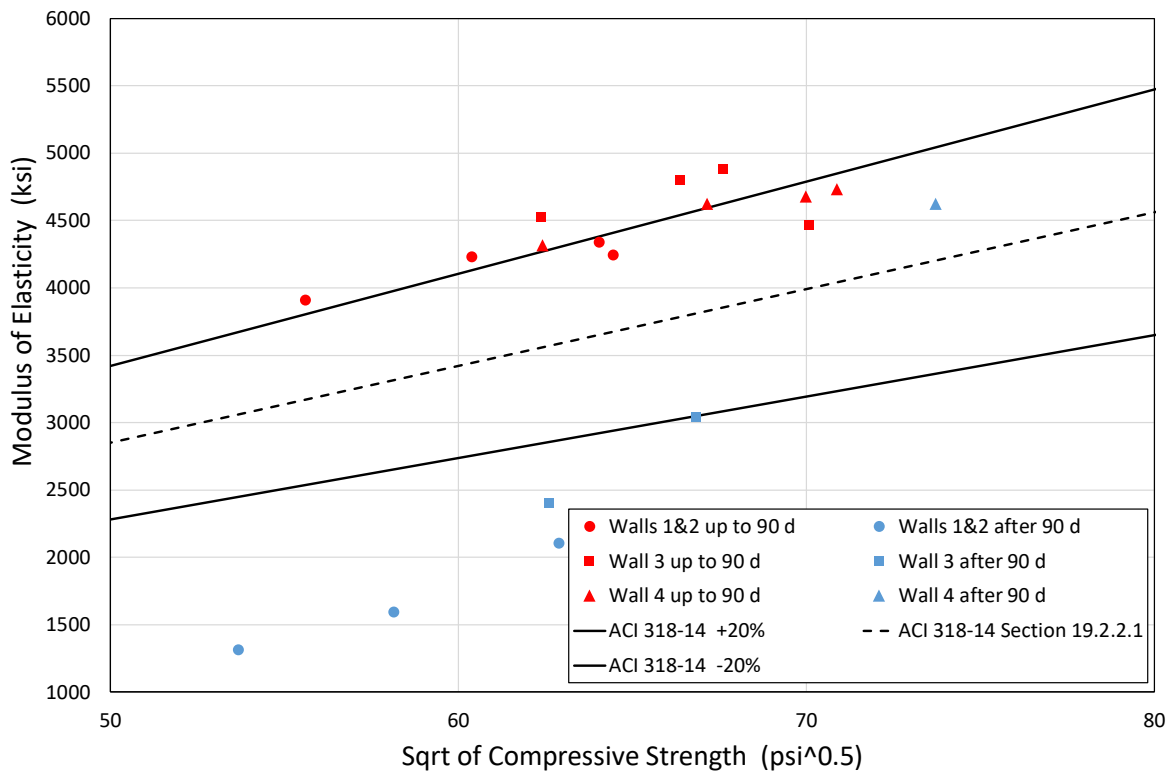


Figure 4.7. Compressive modulus of elasticity versus the square root of compressive strength for cylinders from all wall panels (1.00000 psi = 0.00689 MPa, 1.00000 ksi = 0.00689 GPa)

4.1.3 Splitting Tensile Strength

Conventional Concrete for Footings and Top Caps:

Figures 4.8 and 4.9 show the splitting tensile strength of the concrete used for the footings and top caps, respectively, plotted against time measured in days after casting. In the figures, the marker represents the average value of the compressive strength, while the error band at each time corresponds to the expanded uncertainty. The concrete used in the footings had a 28-day tensile strength of 800 psi \pm 300 psi (5.5 MPa \pm 2.1 MPa). At the time of wall testing, however, the tensile strength dropped to the range of 720 psi \pm 80 psi (5.0 MPa \pm 0.6 MPa) to 570 psi \pm 200 psi (3.9 MPa \pm 1.4 MPa). The 28-day splitting tensile strength for the concrete used in the top caps of the reactive wall specimens (Wall 1, 2, and 3) was 580 psi \pm 60 psi (4.0 MPa \pm 0.4 MPa) and at the time of wall testing, the tensile strength was in the range of 550 psi \pm 250 psi (3.8 MPa \pm 1.7 MPa) to 620 psi \pm 220 psi (4.3 MPa \pm 1.5 MPa). For the concrete used in the top cap of the non-reactive Wall 4, the tensile strength at 28 d was 520 psi \pm 60 psi (3.6 MPa \pm 0.4 MPa) and at the time of wall testing was 490 psi \pm 110 psi (3.4 MPa \pm 0.8 MPa).

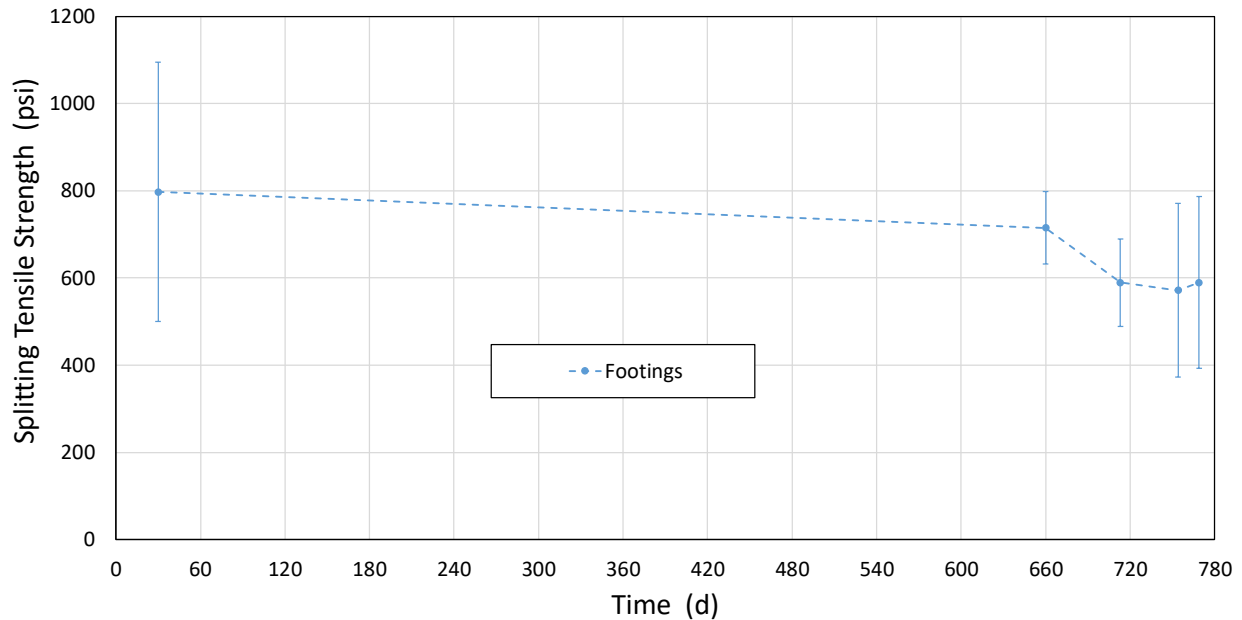


Figure 4.8. Splitting tensile strength of concrete used in the footings (1.00000 psi = 0.00689 MPa)

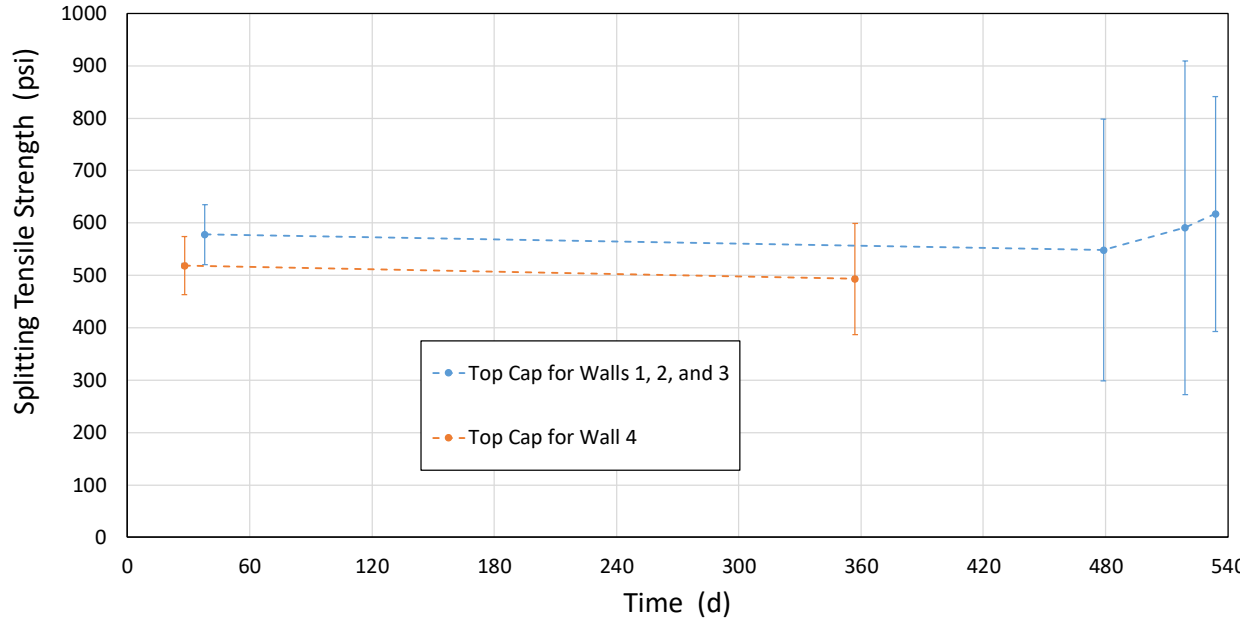


Figure 4.9. Splitting tensile strength of concrete used in the top caps (1.00000 psi = 0.00689 MPa)

Reactive and Non-reactive Concrete for Wall Panels:

Figure 4.10 shows the splitting tensile strength of the concrete used in reactive Walls 1 and 2, reactive Wall 3, and non-reactive Wall 4 (lithium-nitrate treated mixture) plotted against time. The figure shows that the reactive cylinders continued to gain strength until roughly 90 d after casting. After 90 d, the tensile strength was roughly 30 % to 33 % less than the 28-day tensile strength. Similar behavior was also observed for the block specimens described by the Task 1 report (Sadek et al., 2021) and the beam specimens described by the Task 2 report (Thonstad et al., 2021). On the contrary, the non-reactive cylinders continued to gain strength at a slow rate until the Wall 4 cyclic testing, 378 d after casting. Table 4.3 provides the measured splitting tensile strength of the 4 in × 8 in (102 mm × 203 mm) concrete cylinders from all wall panels throughout the testing period (see Section 2.7).

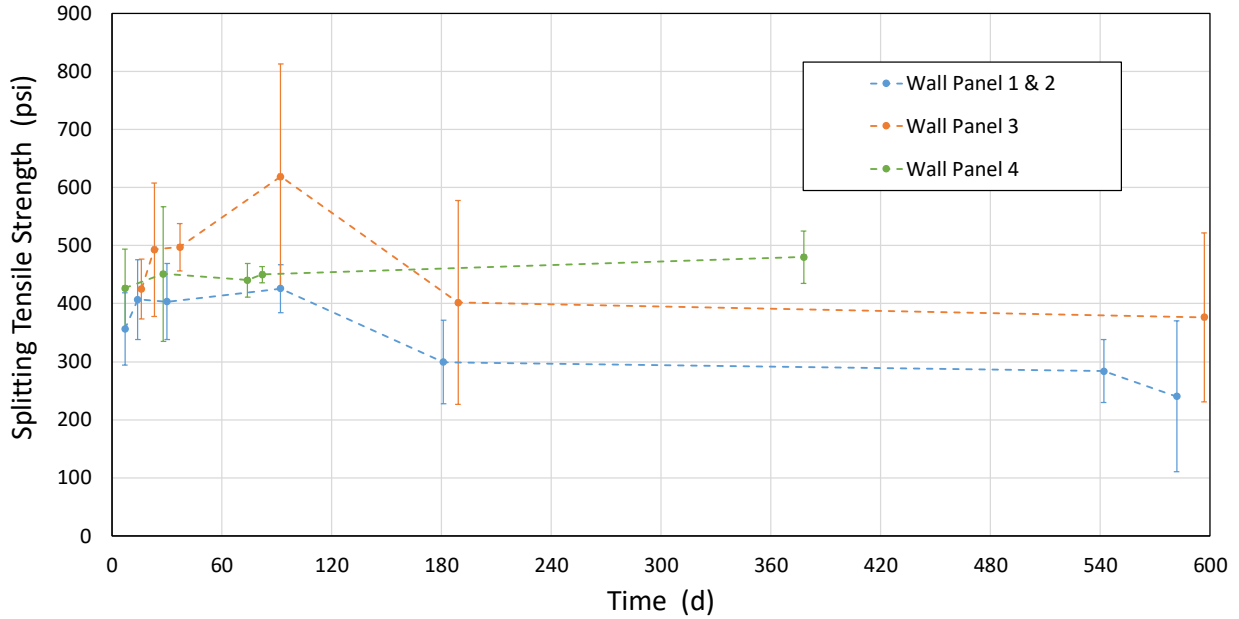


Figure 4.10. Splitting tensile strength of reactive and non-reactive concrete used in the wall panels (1.00000 psi = 0.00689 MPa)

Table 4.3. Splitting tensile strength of reactive and non-reactive concrete used in the wall panels

Time	Compressive Strength psi (MPa)		
	Wall 1&2	Wall 3	Wall 4
7 d*	360 ± 60 (2.48 ± 0.41)		430 ± 70 (2.96 ± 0.48)
14 d*	410 ± 70 (2.83 ± 0.48)	425 ± 50 (2.93 ± 0.34)	
28 d*	400 ± 70 (2.76 ± 0.48)	490 ± 120 (3.38 ± 0.83)	450 ± 120 (3.10 ± 0.83)
90 d*	430 ± 40 (2.96 ± 0.28)	620 ± 190 (4.27 ± 1.31)	450 ± 10 (3.10 ± 0.07)
180 d*	300 ± 70 (2.07 ± 0.48)	400 ± 180 (2.76 ± 1.24)	
Testing of Wall 1 at 542 d*+	280 ± 50 (1.93 ± 0.34)		
Testing of Wall 2 at 582 d*+	240 ± 130 (1.65 ± 0.90)		
Testing of Wall 3 at 588 d*+		380 ± 150 (2.62 ± 1.03)	
Testing of Wall 4 at 378 d*+			480 ± 45 (3.31 ± 0.31)

* Actual date might slightly differ

+ Test dates are relative to wall panel cast date

Figure 4.11 shows the measured mean value of splitting tensile strength versus the square root of the measured mean value of compressive strength at various ages of the cylinders from the four wall panels. In the figure, Walls 1 and 2, Wall 3, and Wall 4 are characterized by the circular, square, and triangular markers, respectively, while cylinders tested at or before 90 d of casting and those tested after 90 d of casting are characterized by the red and blue colors, respectively. The dashed line in the figure represents the splitting tensile strength calculated as a function of the compressive strength of concrete per ACI 318-14 (Section 19.2.4.3), while the two solid lines present $\pm 20\%$ deviations from the ACI equation. Section 19.2.4.3 of ACI 318-14 calculates the splitting tensile strength, f_{ct} , as a function of the measured average concrete compressive strength, f_{cm} , as $f_{ct} = 6.7\sqrt{f_{cm}}$ (in units of psi). The figure shows that the measured splitting tensile strength was, for the most part, within the $\pm 20\%$ range of the ACI equation with the exception of cylinders from Walls 1 and 2 tested between 180 d and 582 d, where the measured splitting tensile strength was, on average, lower than the ACI equation - 20 %.

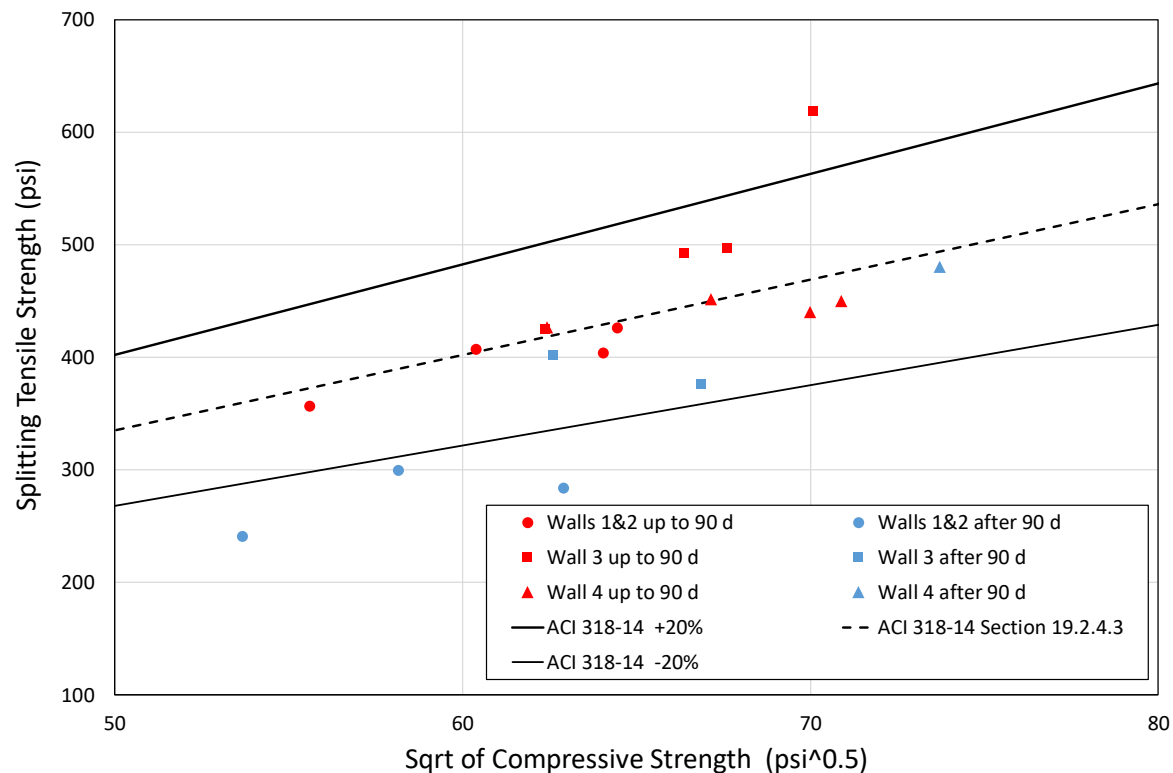
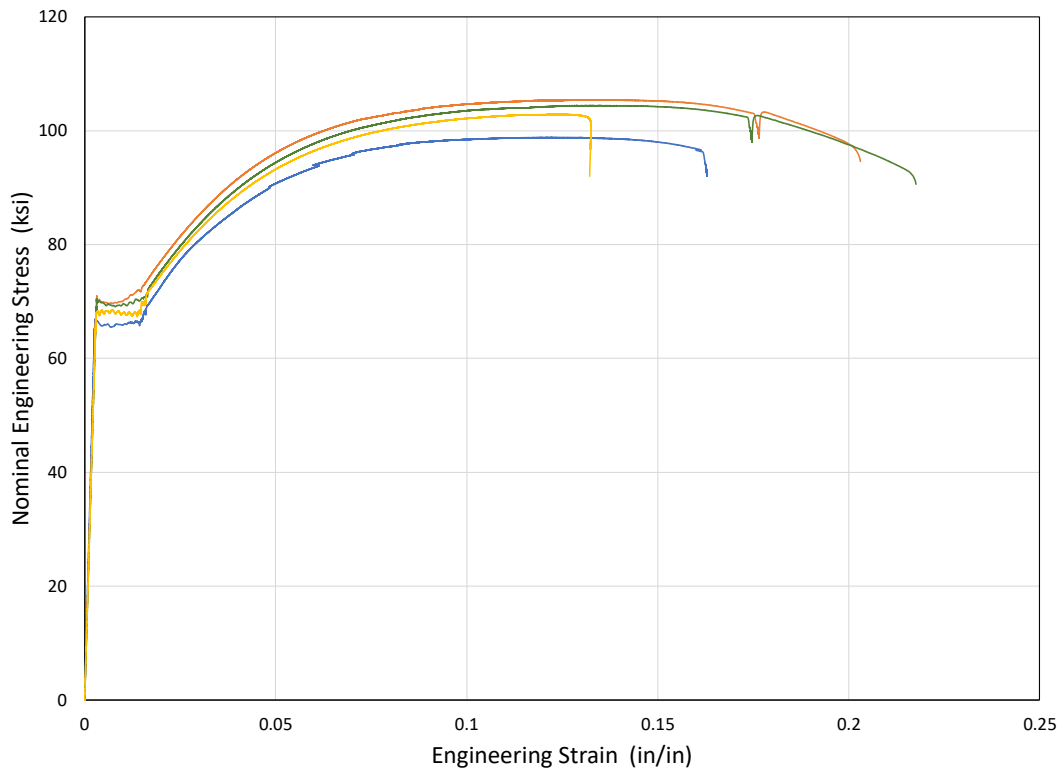


Figure 4.11. Splitting tensile strength versus the square root of compressive strength for cylinders from all wall panels (1.00000 psi = 0.00689 MPa, 1.00000 ksi = 0.00689 GPa)

4.2 REINFORCEMENT MECHANICAL PROPERTIES

Figure 4.12 shows the engineering stress-strain relationships for the No. 3 (0.375 in [9.5 mm] diameter) and No. 4 (0.5 in [12.7 mm] diameter) reinforcing bars used as reinforcement in the wall panels. The

curves were obtained in accordance with ASTM A370-20 Standard Test Methods and Definitions for Mechanical Testing of Steel Products (ASTM A370, 2020). For sample preparation, the deformed bars were ground flat and chemically etched at the midpoint of the sample prior to affixing strain gages using cyanoacrylate adhesive. In addition, engineering strains were recorded using an extensometer with a 2.00 in gage length that met ASTM E83 B2 classification (ASTM E83, 2016). No discernable differences were found between the strain readings from the two methods prior to reaching the strain capacity of the adhesive attaching the strain gage to the bar, which occurred at roughly 1 % strain. The engineering strains presented in Figure 4.12 are those measured by the extensometer. Engineering stresses were calculated by dividing the force recorded by the servohydraulic load frame's inline load cell by the nominal area of the reinforcing bar. It should be noted that this procedure leads to an estimated elastic modulus lower than the nominal modulus of the steel, since the area of the reinforcement sample has an effective area smaller than the nominal one. This is due to both the manufacturing process and gage installation. For example, the apparent modulus of the No. 4 bars, using the nominal bar area, was $24\,300 \pm 2\,700$ ksi (167.5 ± 18.6 GPa), 16 % lower than the nominal elastic modulus of 29 000 ksi (200 GPa).



(a)

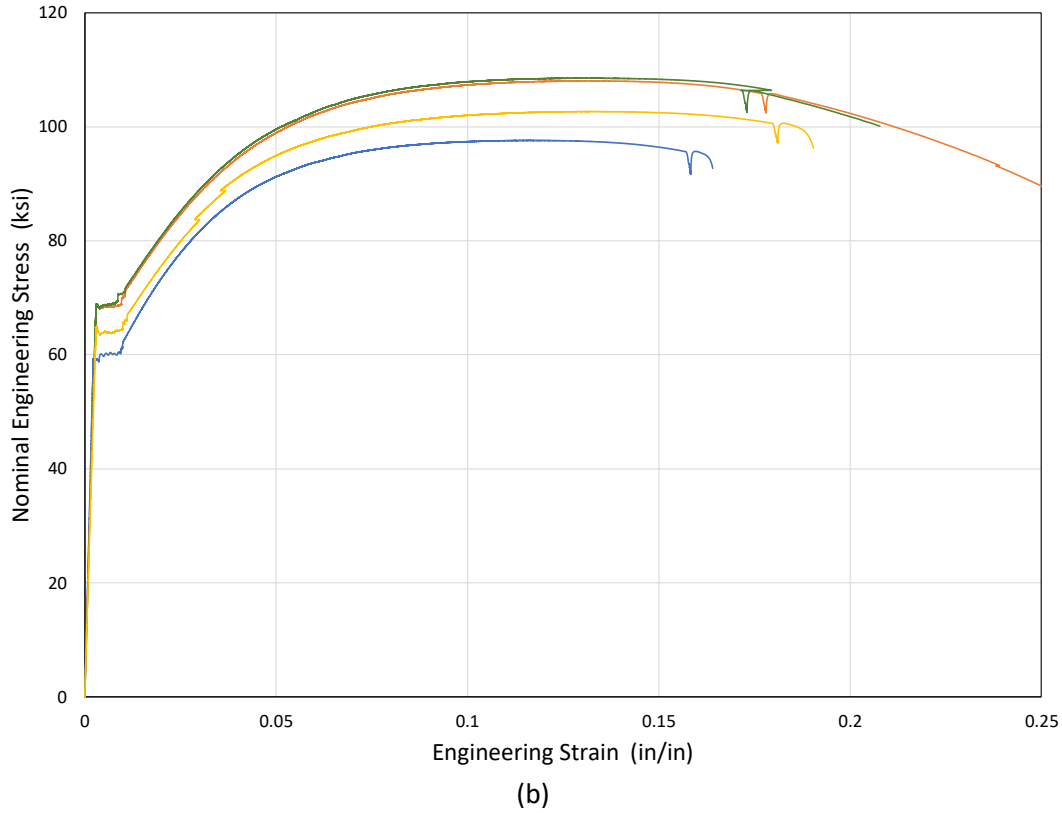


Figure 4.12. Engineering stress-strain curves for the reinforcing bars used in the wall panels: (a) No. 3 bars, (b) No. 4 bars (1.000 ksi = 6.894 MPa)

Table 4.4 presents a summary of the reinforcing bar tests. The yield strength, f_y , was calculated as the upper yield point stress between a strain of 0.2 % and 0.5 %, the tensile strength, f_u , was the recorded maximum stress, and the ultimate tensile strain (post-peak) was determined as the strain corresponding to a 5 % decrease in the tensile strength.

Table 4.4. Measured properties of reinforcement

	No. 3	No. 4
Yield Strength f_y ksi (MPa)	69.2 ± 2.9 (477 ± 20.0)	65.7 ± 6.5 (453 ± 44.8)
Tensile Strength f_u ksi(MPa)	102.9 ± 4.6 (709 ± 31.7)	104.2 ± 8.2 (718 ± 56.5)
Ultimate tensile strain (%)	17.0 ± 4.5	18.6 ± 2.4

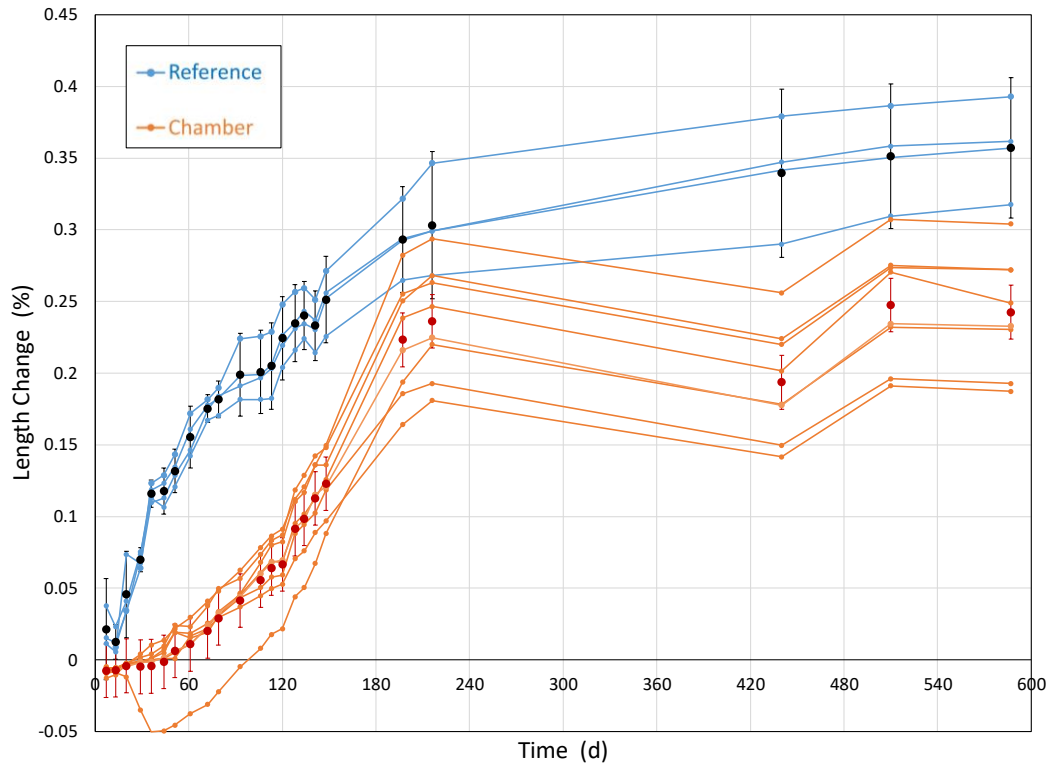
4.3 EXPANSION PRISMS

The rate of ASR-induced expansion of the unreinforced companion specimens was measured using the 3 in × 3 in × 11.25 in (76 mm × 76 mm × 286 mm) standard prisms, prepared per the ASTM C1293-20 specifications (ASTM C1293, 2020) using the same concrete as that used for the reactive Walls 1 and 2, reactive Wall 3, and non-reactive Wall 4, resulting in three sets of prisms. Similar to observations from the Task 1 report (Sadek et al., 2021) and Task 2 report (Thonstad et al., 2021), while the measured length change of these prisms was not representative of the restrained ASR-induced expansion in the walls, it was indicative of the potential expansion of the concrete mixture.

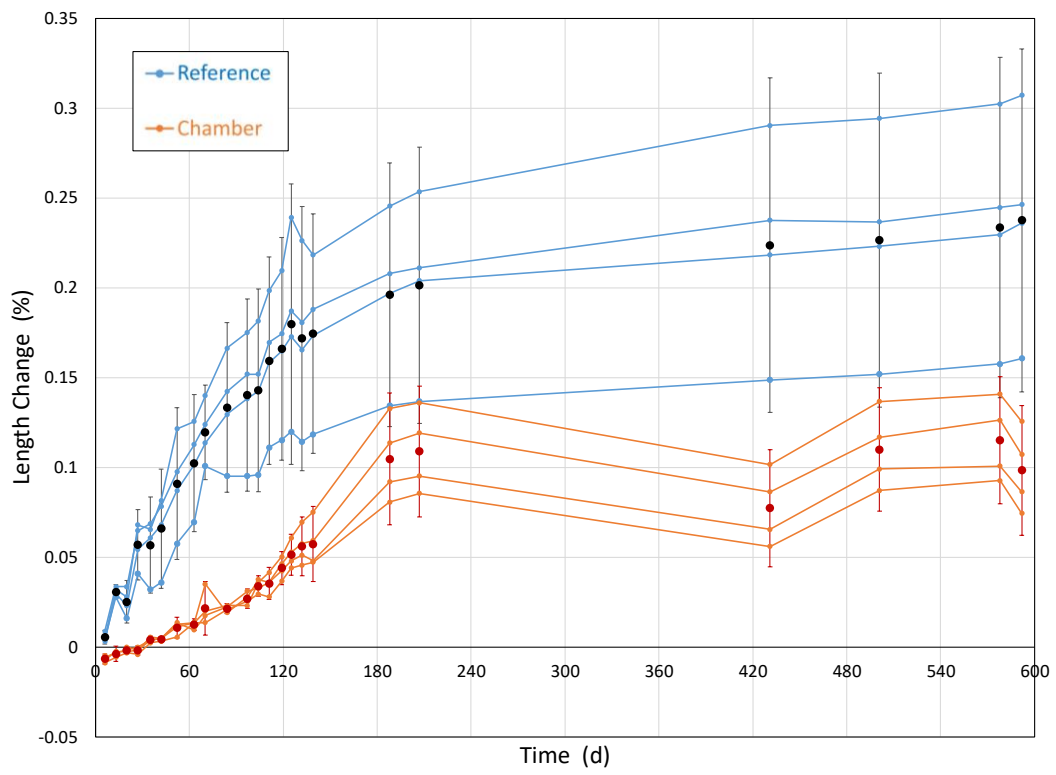
Figure 4.13 shows the length change versus time for the three sets of standard prisms: (1) Walls 1 and 2; (2) Wall 3, and (3) Wall 4. Each set included two groups of prisms. One group, labeled “Reference” in Figure 4.13, was suspended vertically over water in sealed containers and kept at a constant temperature of 100 °F (37.8 °C) throughout the duration of the study in accordance with ASTM C1293 (ASTM C1293, 2020). The second group was exposed to the same conditions as were the wall specimens. This group included prisms from:

- (1) reactive Walls 1, 2, and 3 that were kept in the environmental chamber, which had variations in temperature and humidity as described in Section 4.4. This group was labeled “Chamber” in Figure 4.13(a, b).
- (2) non-reactive Wall 4 that were kept outside the environmental chamber with the wall specimen. This group was labeled “Ambient” in Figure 4.13(c).

The plots in Figure 4.13 show the length change for each individual prism (blue lines for “Reference” and orange line for “Chamber” or “Ambient”) along with the average length change of each group (black circular markers for “Reference” and red circular markers for “Chamber” or “Ambient”) and associated expanded uncertainty (black error bars for “Reference” and red error bars for “Chamber” or “Ambient”).



(a)



(b)

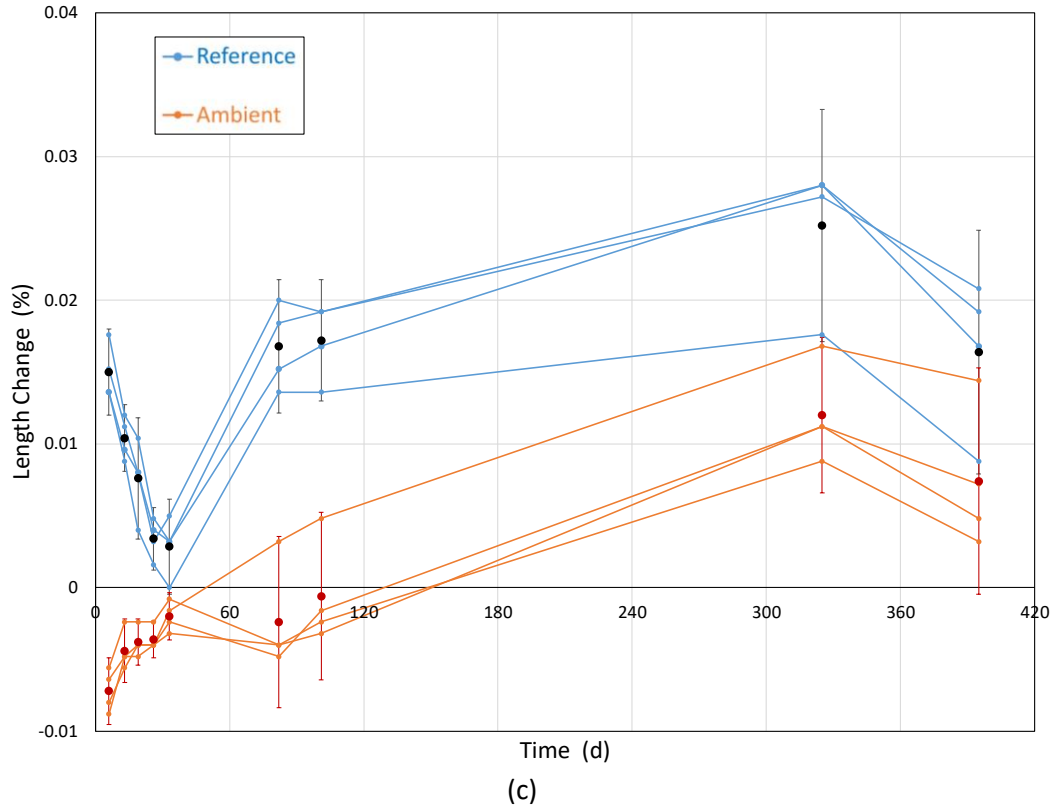


Figure 4.13. Measured length change for prisms for (a) reactive Walls 1 and 2, (b) reactive Wall 3, and (c) non-reactive Wall 4

For non-reactive Wall 4 prisms, plot (c) of Figure 4.13 shows that the measured expansions were less than 0.03 % during the duration of the study, indicating no significant ASR reactivity. For the reactive walls, plots (a) and (b) of Figure 4.13 show that the prisms kept within the environmental chamber tended to expand at a slower rate and achieved smaller ultimate expansions than did the “Reference” prisms. This was attributed to the lower initial temperature and relative humidity (RH) of the chamber. The “Reference” prisms exhibited a rapid increase in expansion over the first 216 d for Walls 1 and 2 and 125 d for Wall 3, followed by a period of slower rate of expansion and plateauing. The “Chamber” prisms followed a pattern consistent with the four curing phases presented in Section 4.4, including a slow rate of expansion over the first 119 d, followed by an increased rate of expansion with the increased humidity and temperature in the chamber. After the closure of the laboratory and shutting down the environmental controls at 321 d (see Section 4.4), the expansions decreased, but with the re-opening of the laboratory and the increased humidity and temperature at 442 d, expansions increased again, albeit at a slower rate. When comparing plots (a) and (b) of Figure 4.13, it is evident that both the “Reference” and “Chamber” prisms for Walls 1 and 2 had larger expansions than did those for Wall 3.

Based on expansion data from the “Chamber” prisms, it was concluded that cyclic testing of the reactive walls was conducted at ASR-induced expansion of up to 0.25 % based on standard prisms kept under the same environmental conditions as the wall specimens.

4.4 ENVIRONMENTAL CONDITIONS

Reactive Walls 1, 2, and 3 were cured in an environmental chamber that was capable of achieving a temperature of 100 °F (37.8 °C) and an RH approaching 100 %, see Chapter 2. Thermocouples were located around the chamber to measure the temperature for the duration of the test program. In addition, thermocouples were installed about 1.00 in (25.4 mm) into the walls at a height of 36.0 in (914 mm) above the footing to measure the below-surface concrete temperatures.

Figure 4.14 shows the measured temperatures based on the thermocouples that were installed around the environmental chamber. In the figure, four curing phases, which are delineated by red solid vertical lines, can be identified as follows (note that in this section, time is calculated relative to the date of concrete placement of Walls 1 and 2, which was April 30, 2019):

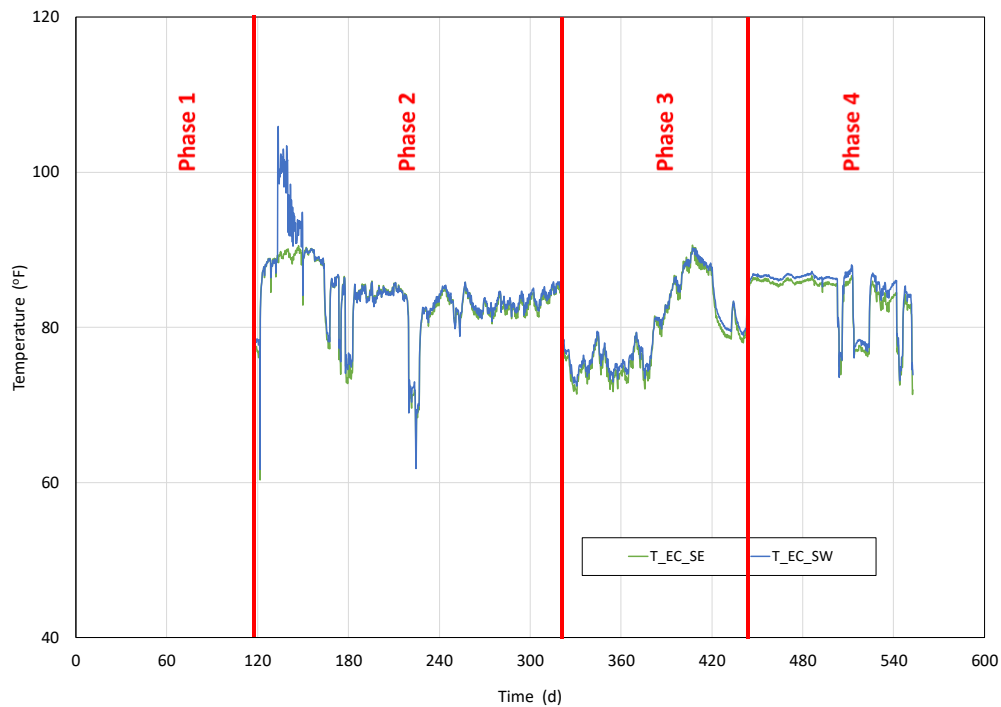


Figure 4.14. Temperature histories inside the environmental chamber ($^{\circ}\text{F} = 32 + 9^{\circ}\text{C}/5$)

Phase 1 (0 d to 119 d): During this period, the reactive walls were under ambient conditions (temperature range of about 75 °F [23.9 °C] to 80 °F [26.7 °C] and RH in the range of 50 % to 75 %). This phase allowed (1) the construction of the walls’ top caps and the environmental chamber, (2) the wall’s cover concrete to re-equilibrate after undergoing potentially significant drying, and (3) a smooth transition in the environmental conditions and as a result, the ASR expansion, to minimize the effects of creep of the newly cast concrete on the performance of the walls.

Phase 2 (119 d to 321 d): During this period, the RH was increased to the range of 95 % to 100 % and the temperature was maintained between 80 °F (26.7 °C) and 90 °F (32.2 °C), which allowed the ASR expansion to accelerate.

Phase 3 (321 d to 442 d): Due to the laboratory closure as a result of the COVID-19 pandemic, the environmental controls in the chamber (along with the HVAC system in the laboratory where the chamber was installed) were shut down from March 16, 2020 until July 15, 2020. During this period, the reactive walls were under ambient conditions (temperature range of about 75 °F (23.9 °C) to 90 °F (32.2 °C) and RH in the range of 50 % to 75 %).

Phase 4 (442 d to 552 d): On July 15, 2020, the laboratory was re-opened, and the environmental controls were restarted. During this period, the environmental chamber was under the same conditions as those for Phase 2.

The oscillations in recorded temperatures in Figure 4.14 were a result of shutting down the environmental controls in the chamber to allow for regular maintenance, inspection, and removal of walls from the chamber prior to testing.

Figure 4.15 shows the temperature histories inside the reactive walls. The internal temperature-time histories of the walls followed a pattern similar to that of the temperatures measured inside the environmental chamber, but with some time-lag (due to the wall concrete's large thermal mass).

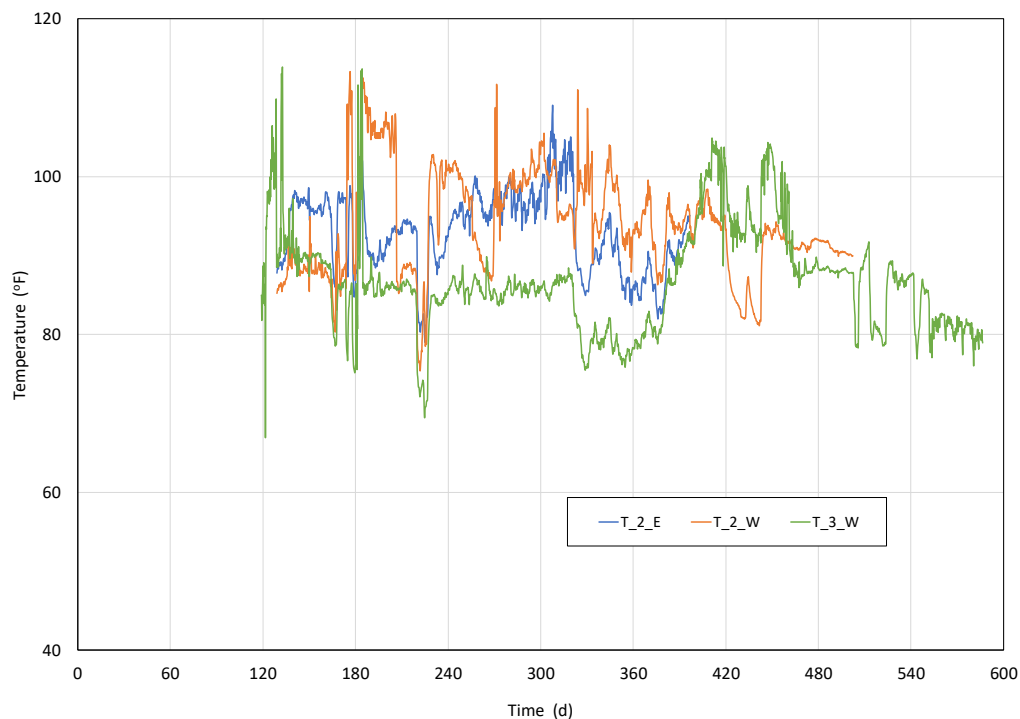


Figure 4.15. Measured temperatures inside the reactive walls ($^{\circ}\text{F} = 32 + 9^{\circ}\text{C}/5$).

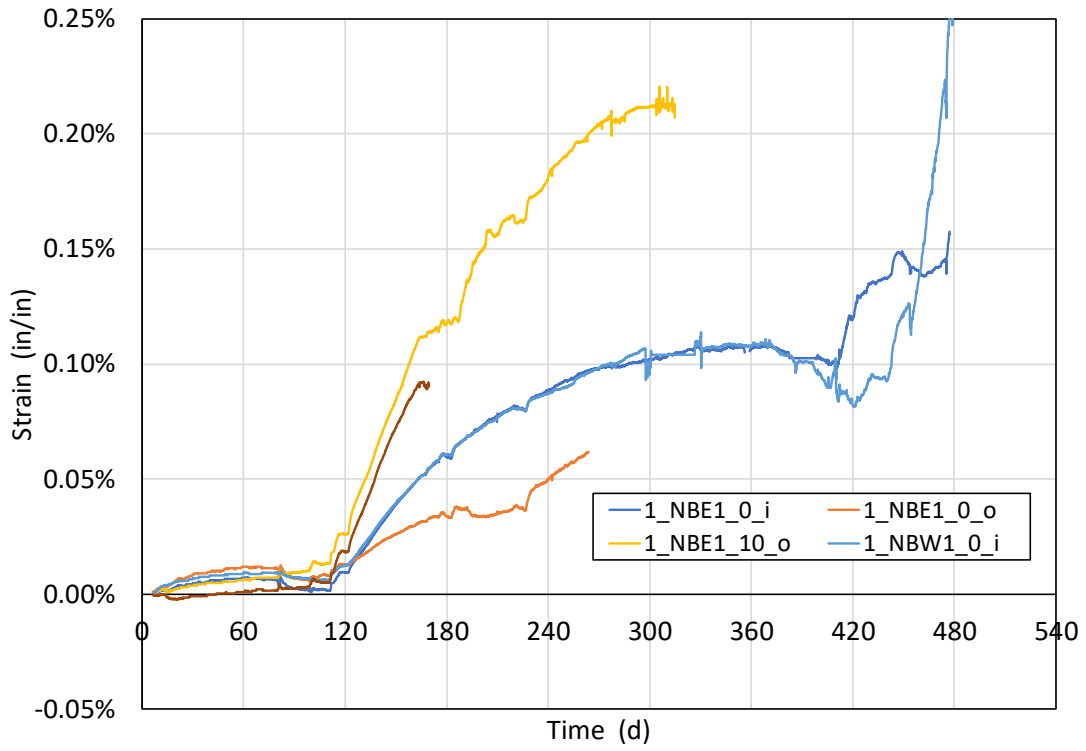
4.5 STRAINS IN THE REINFORCEMENT DURING ASR-INDUCED EXPANSION

Strains were monitored in the three reactive walls during ASR-induced expansion. During ASR-induced expansion, strains in the (1) longitudinal bars in the boundary elements, (2) transverse bars, and (3) crossties were measured and recorded every 12 min on average. These strain measurements provided ASR-induced expansion data in three directions. Strain data processing followed the procedure described in the Task 1 report (Sadek et al., 2021) and is summarized as follows:

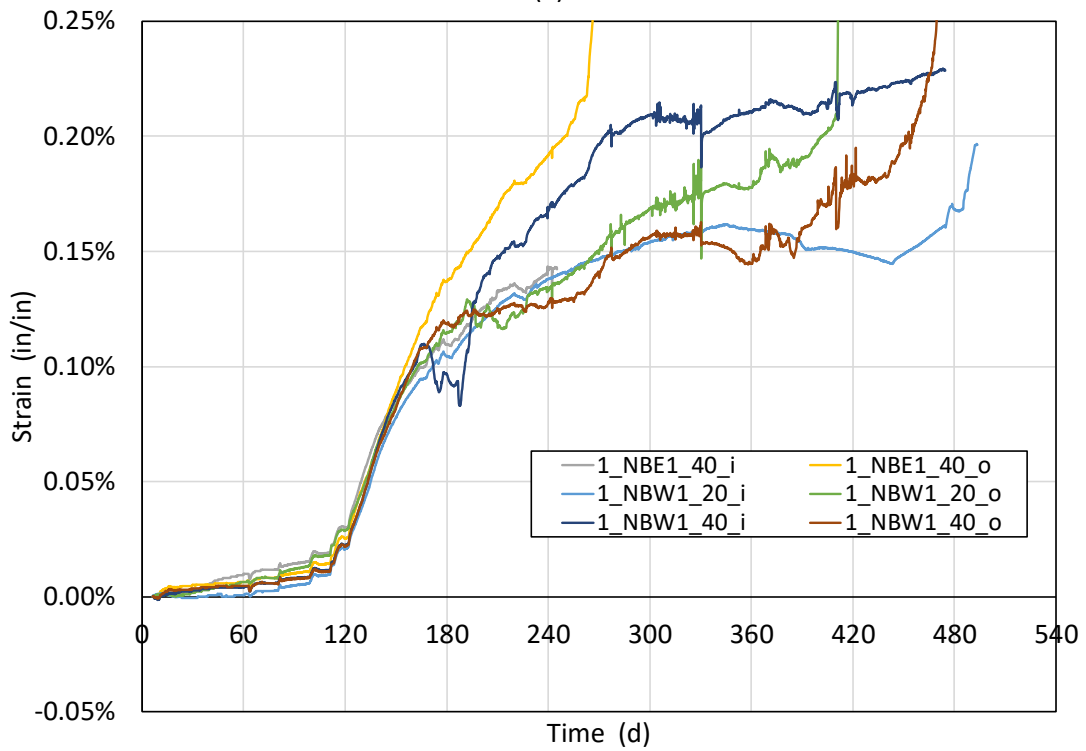
- (1) **Averaging:** To both reduce the amount of data for plotting and the high-frequency noise in the data, every 11 scans were averaged to produce a single strain datapoint, resulting in one strain reading per gage every 2.2 h.
- (2) **Stitching:** Data recording was periodically stopped and restarted to allow for system maintenance, or disconnection of gages that had malfunctioned. To ensure that strain data was continuous, the average top three strain values from the new scan (which generally started from zero strain values) were made equivalent to the average of the last three strain values from the previous scan. This resulted in continuous strain time-histories, without discontinuity due to the data acquisition stoppages.

In addition, visual inspection of the time-history of each strain gage measurement was also conducted to ensure that the gage produced meaningful data. Gages whose strain data showed erratic behavior (e.g., sudden upward or downward jumps, discontinuity, saturation, or behavior not consistent with surrounding gages) were removed from the plots starting from the onset of erratic behavior.

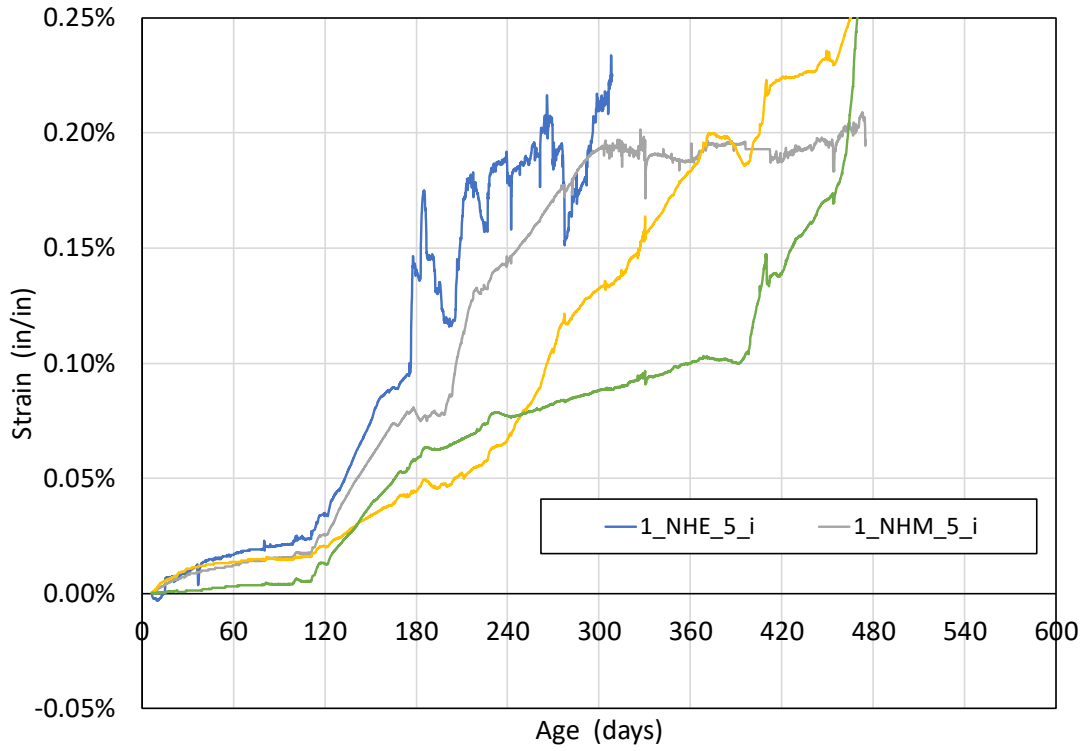
The measured ASR-induced strain developments in the reinforcing bars of the three reactive walls are shown in the Figures 4.16, 4.17, and 4.18 for Walls 1, 2, and 3, respectively. Each figure has the following plots depicting the strain development in the: (a) longitudinal bars in the boundary elements at low heights (0.00 in [0.00 mm] to 10.0 in [25.4 mm] above footing), (b) longitudinal bars in the boundary elements at intermediate heights (20.0 in [50.8 mm] to 40.0 in [1016 mm]), (c) transverse bars at low height (5.00 in [127 mm]), (d) transverse bars at intermediate height (35.0 in [889 mm]), (e) transverse bars at large height (65.0 in [1651 mm]), and (f) through-depth crossties. In all plots, positive strain values signify tensile strains (expansion), while negative strain values signify compressive strains (shrinkage). The location and nomenclature of the strain gages in the three reactive blocks are shown in Figures 2.24 to 2.28.



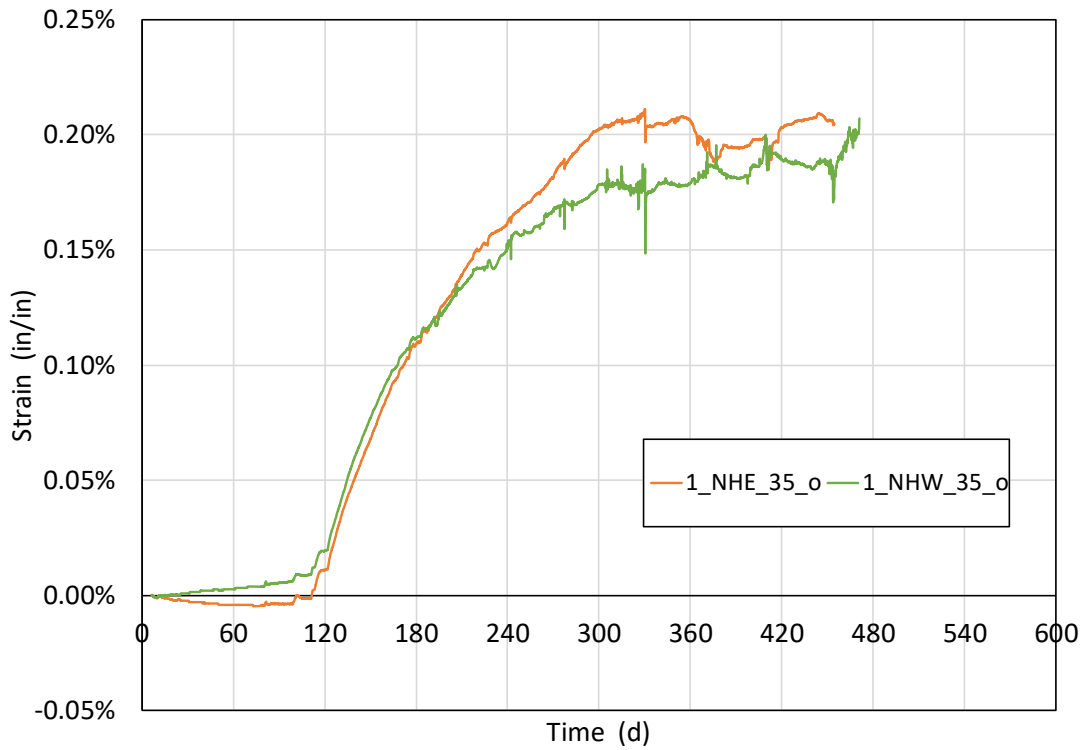
(a)



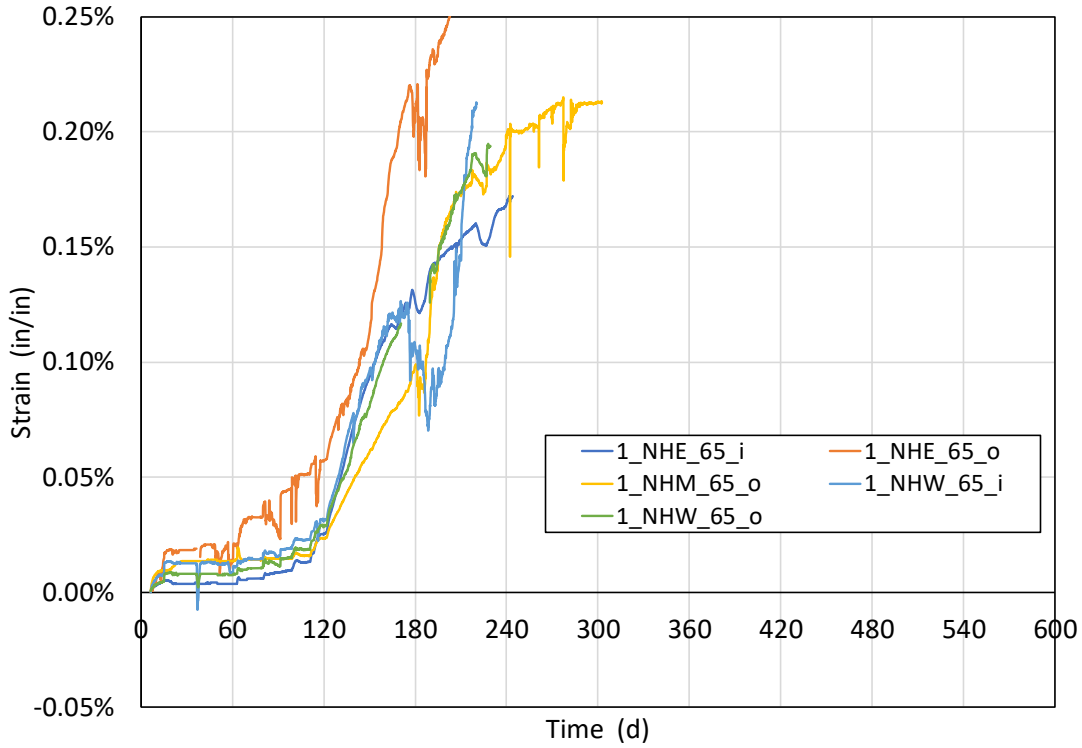
(b)



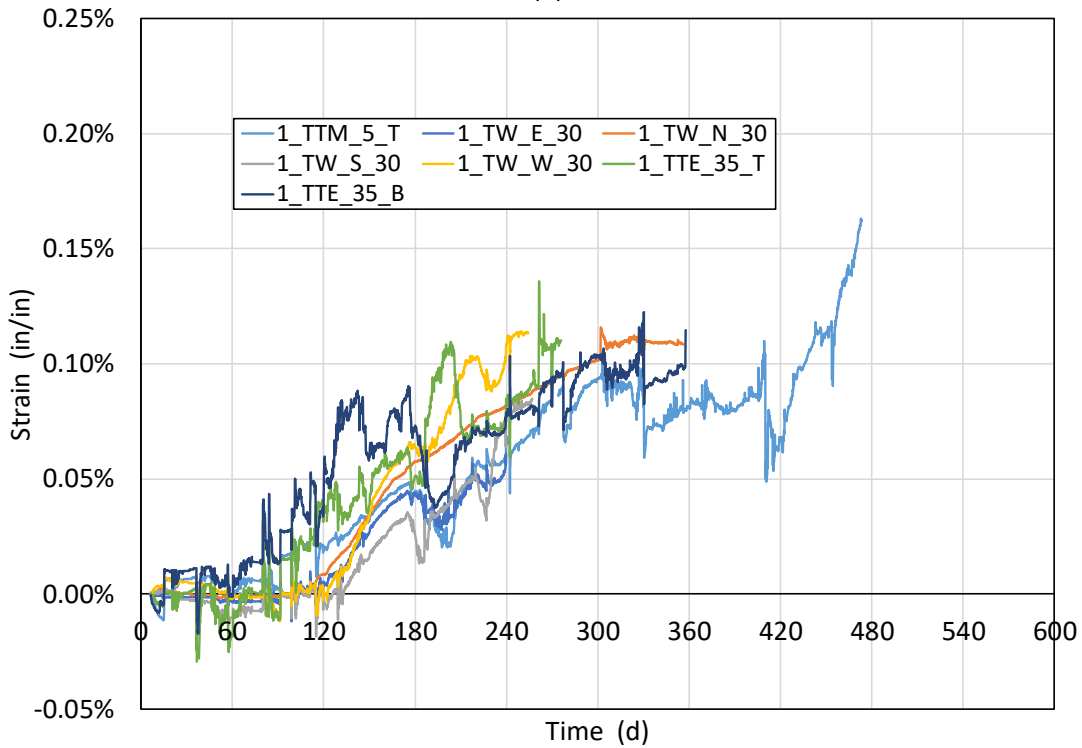
(c)



(d)

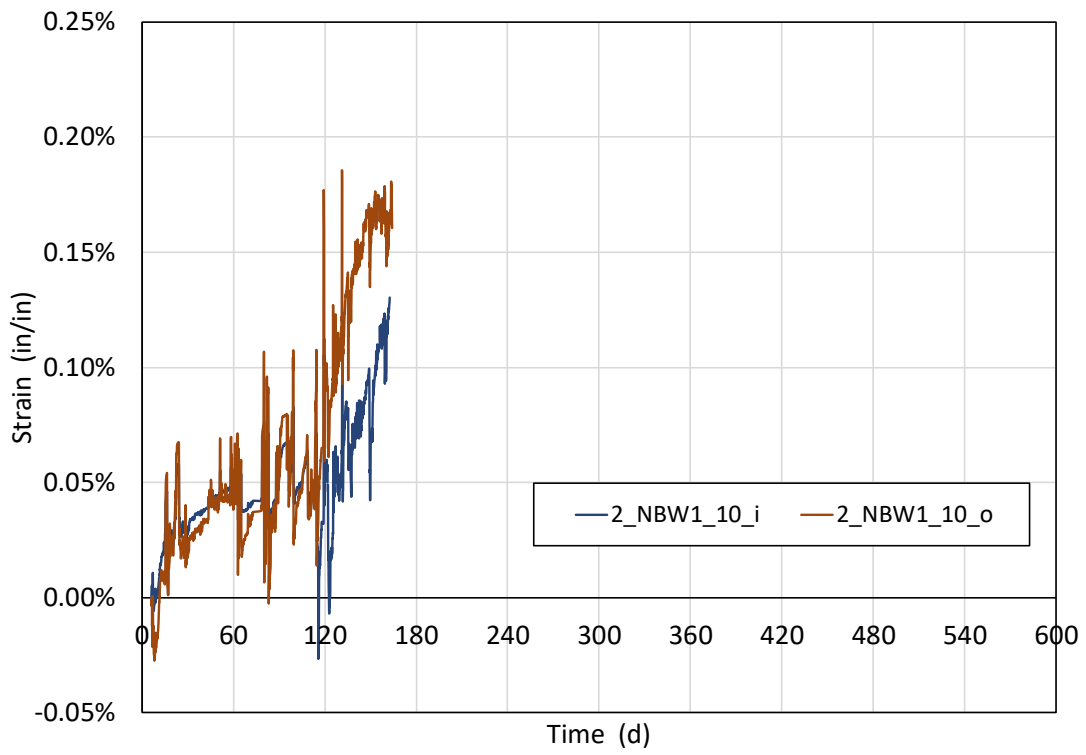


(e)

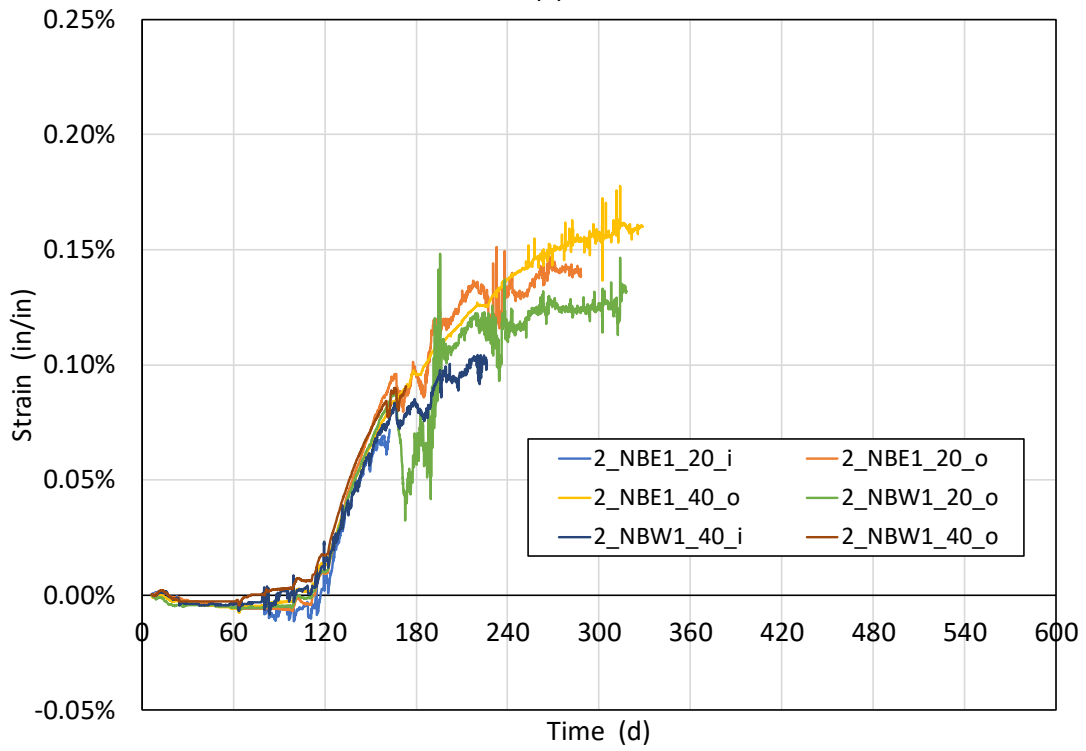


(f)

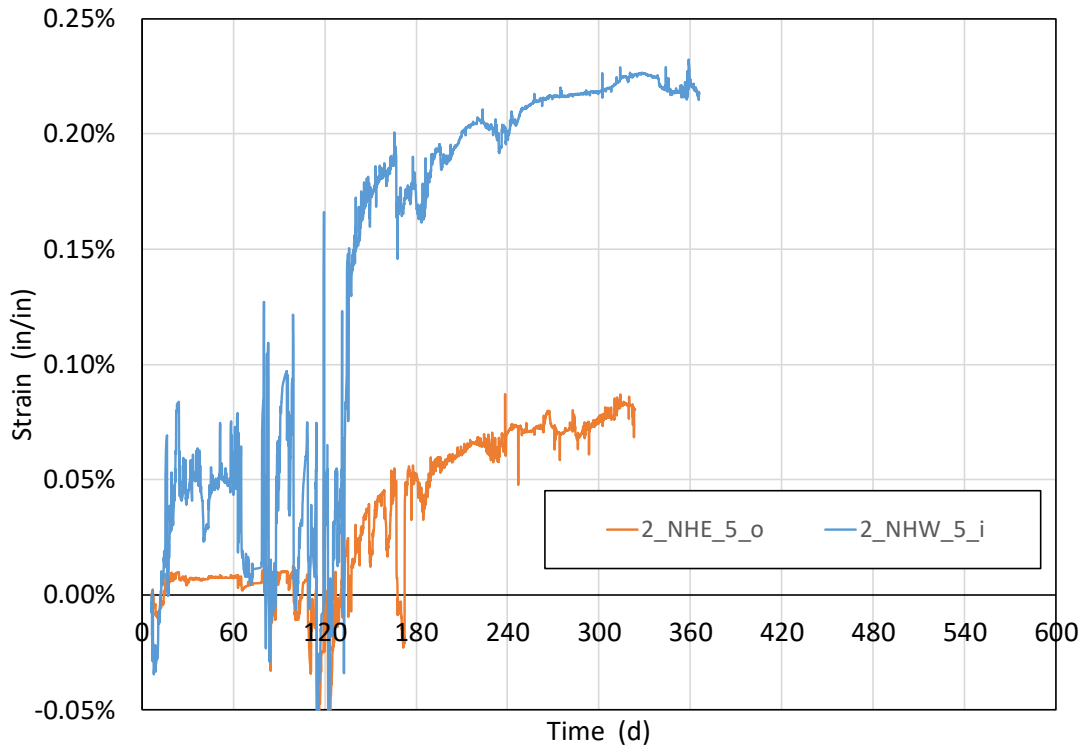
Figure 4.16. Measured strains on reinforcing bars of Wall 1: (a) longitudinal bars in the boundary elements at low heights, (b) longitudinal bars in the boundary elements at intermediate heights, (c) transverse bars at low height, (d) transverse bars at intermediate height, (e) transverse bars at large height, and (f) through-depth ties. 1.00 in/in = 1.00 mm/mm.



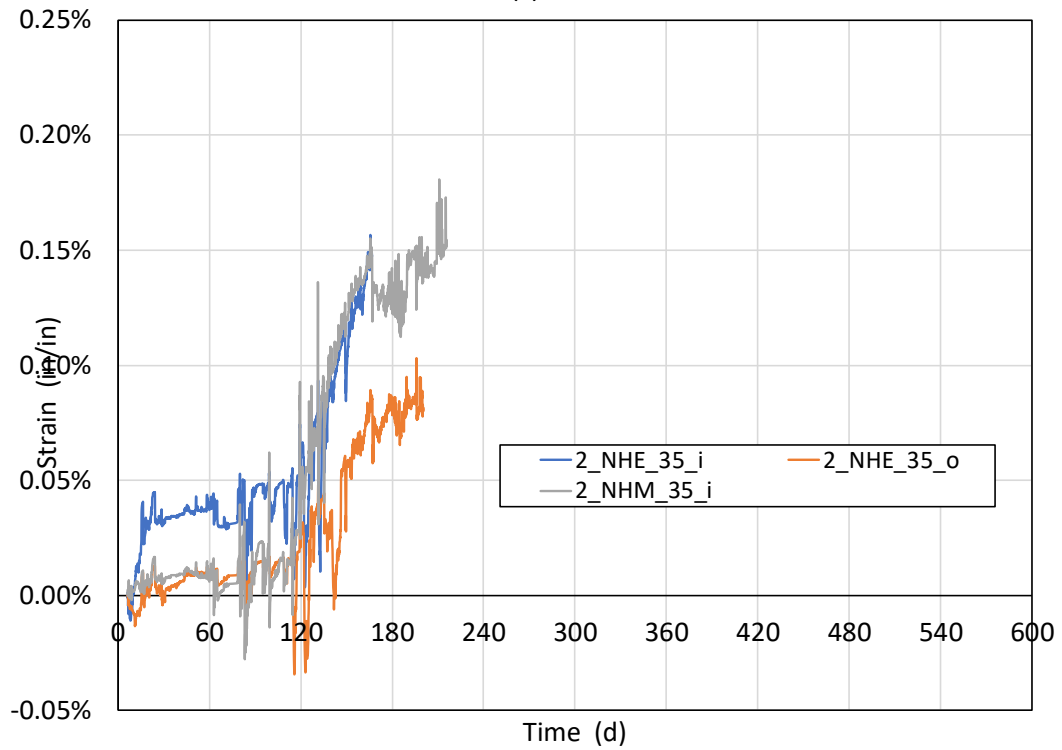
(a)



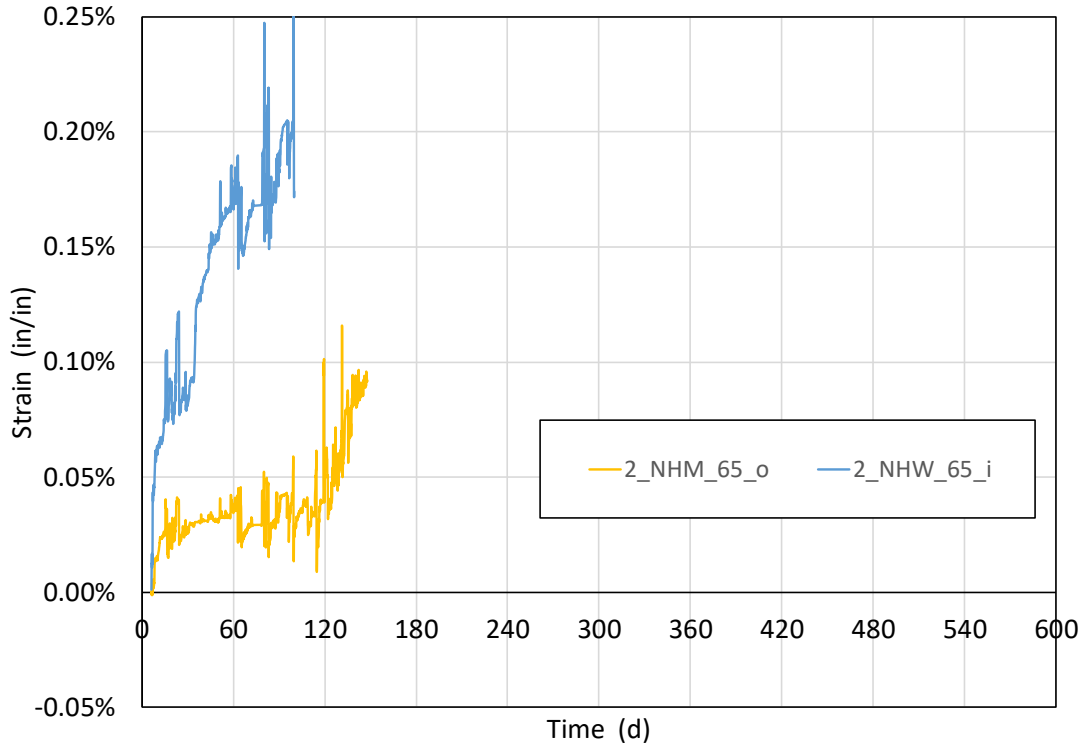
(b)



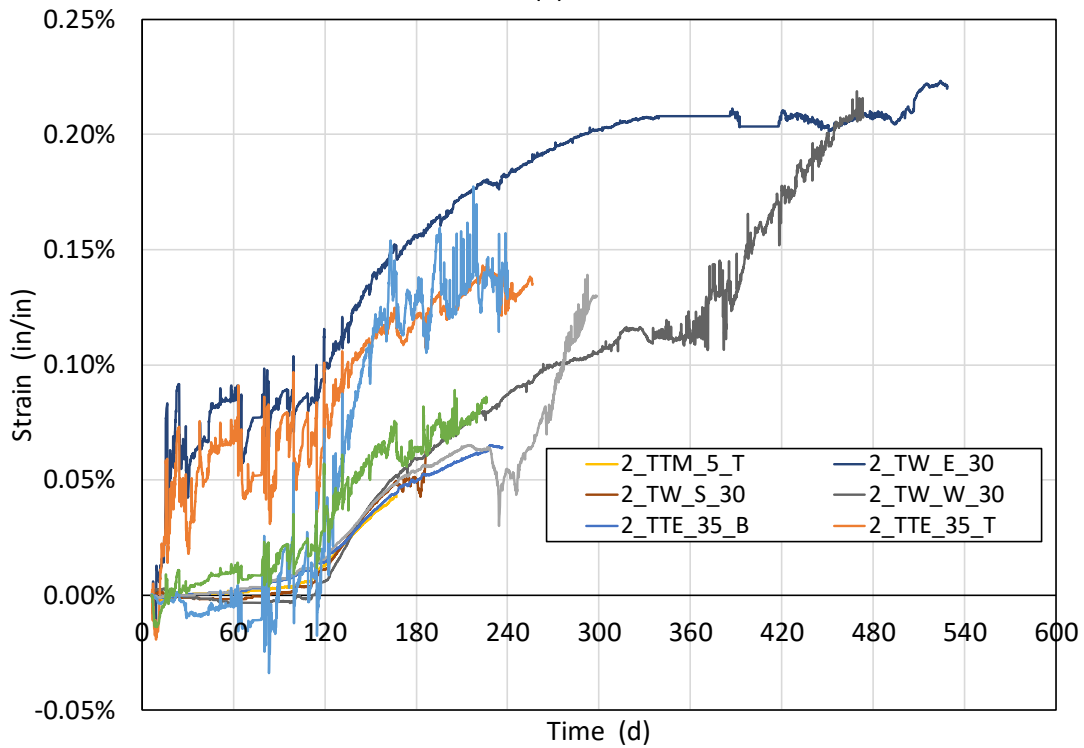
(c)



(d)

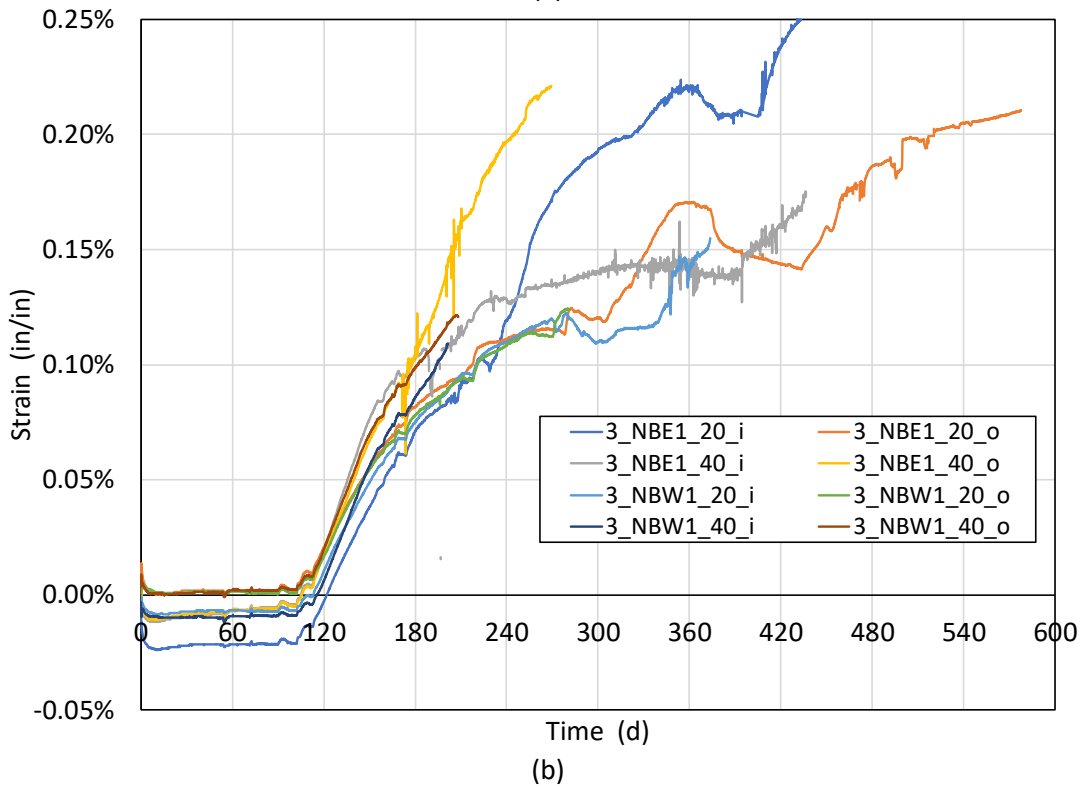
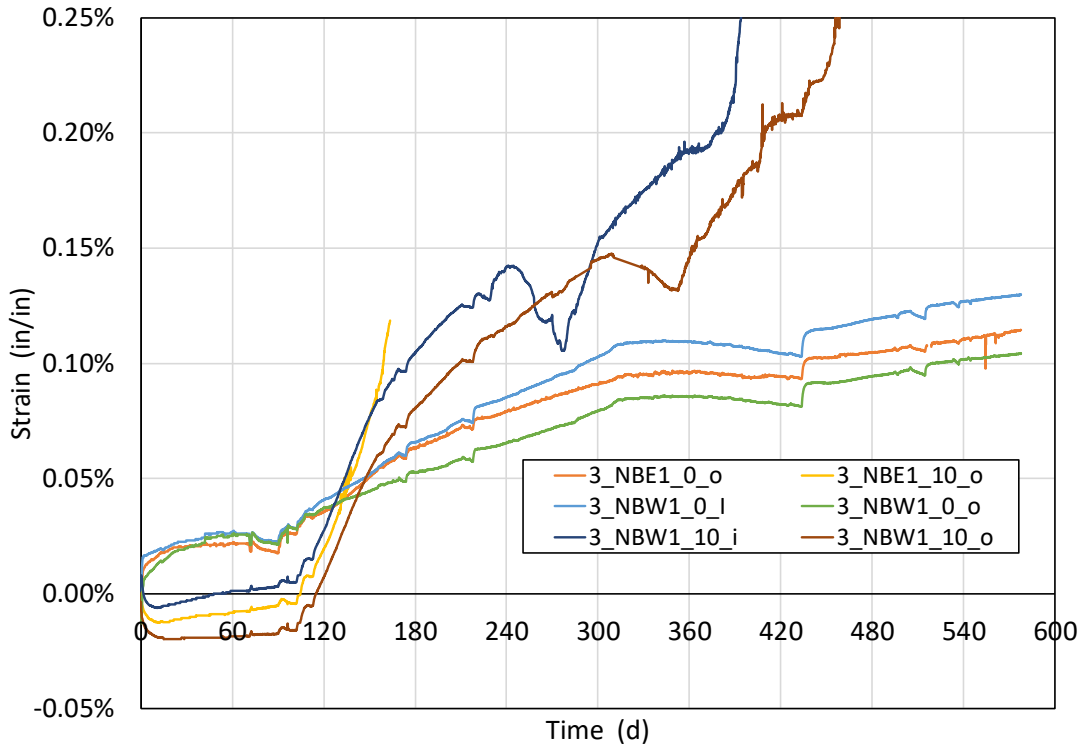


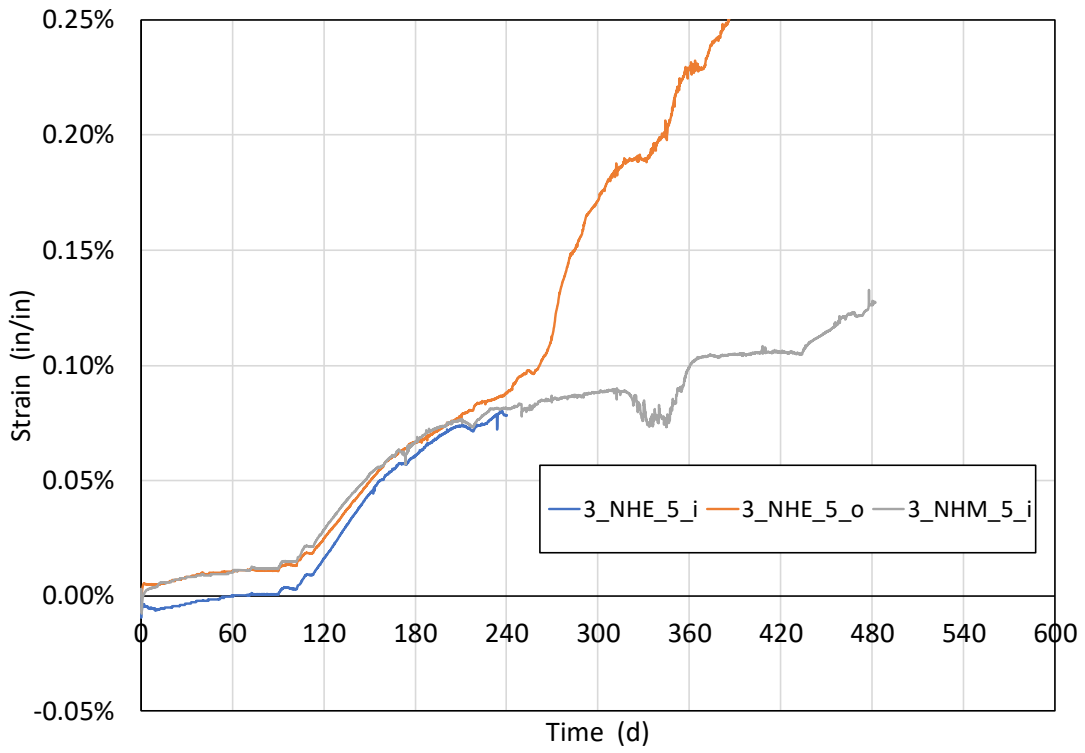
(e)



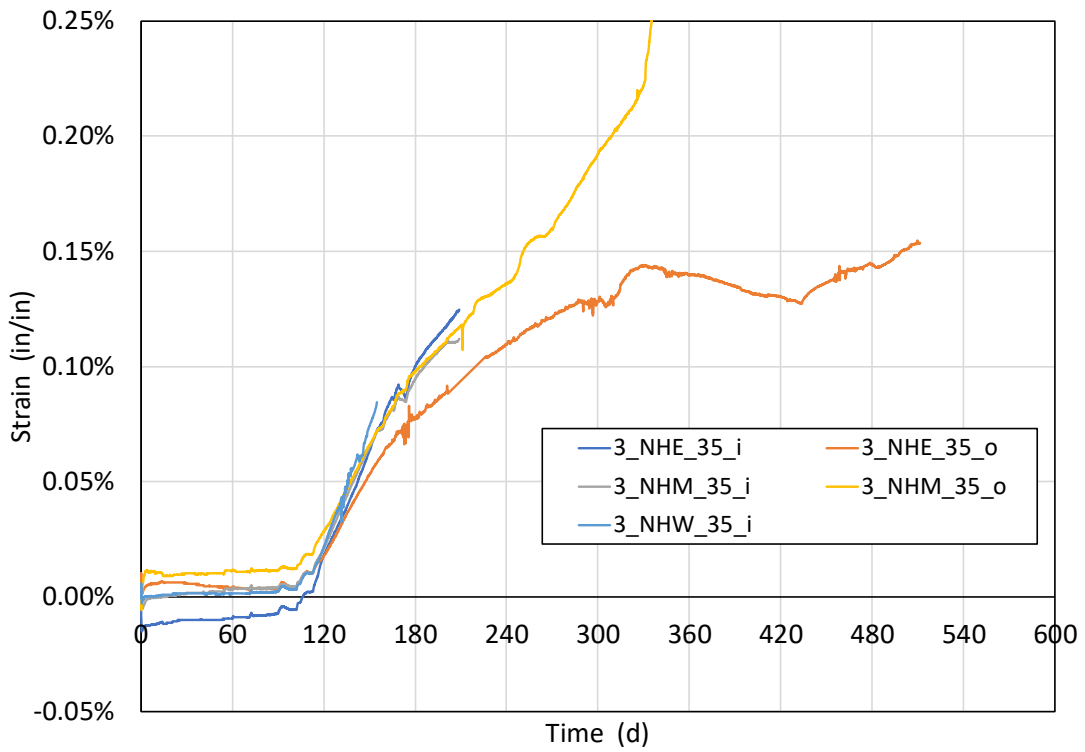
(f)

Figure 4.17. Measured strains on reinforcing bars of Wall 2: (a) longitudinal bars in the boundary elements at low heights, (b) longitudinal bars in the boundary elements at intermediate heights, (c) transverse bars at low height, (d) transverse bars at intermediate height, (e) transverse bars at large height, and (f) through-depth ties. 1.00 in/in = 1.00 mm/mm.

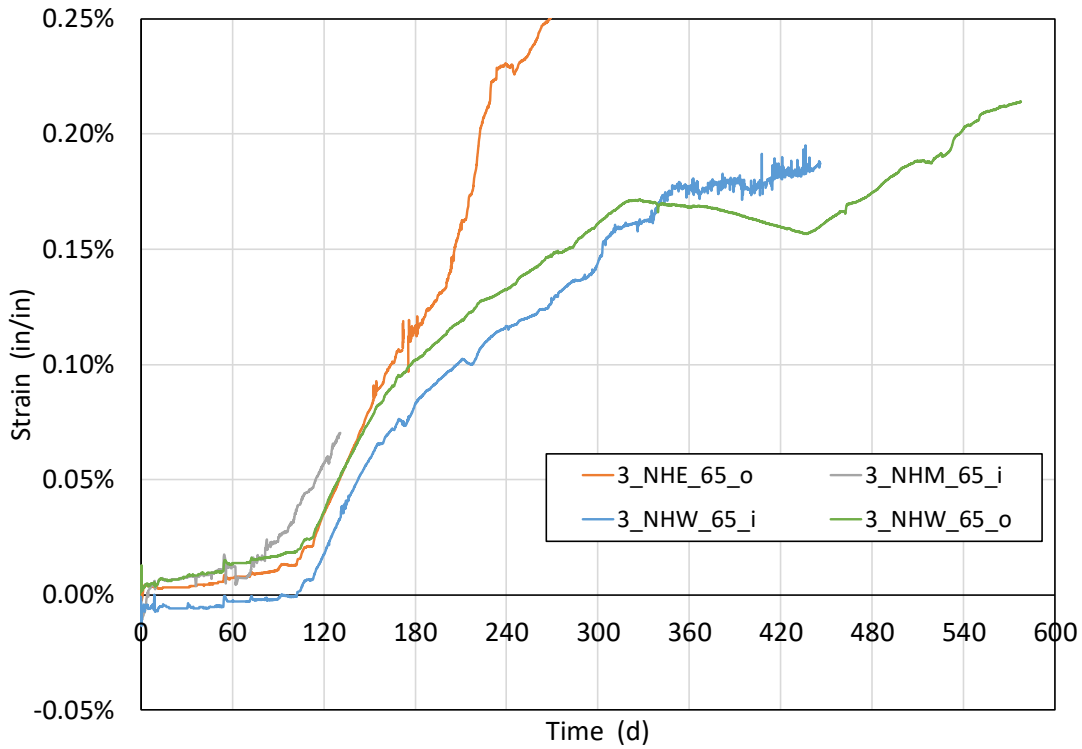




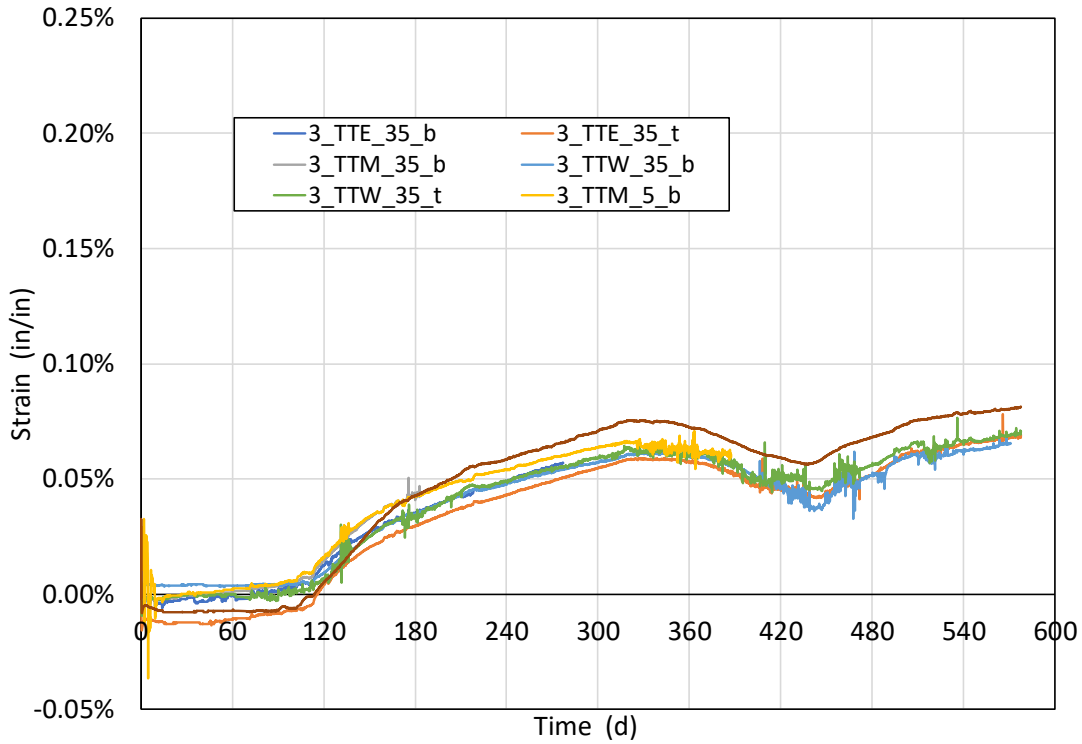
(c)



(d)



(e)



(f)

Figure 4.18. Measured strains on reinforcing bars of Wall 3: (a) longitudinal bars in the boundary elements at low heights, (b) longitudinal bars in the boundary elements at intermediate heights, (c) transverse bars at low height, (d) transverse bars at intermediate height, (e) transverse bars at large height, and (f) through-depth ties. 1.00 in/in = 1.00 mm/mm.

As is normal in data taken from strain gages embedded in concrete, several strain gages were damaged and lost during concrete placement, and others malfunctioned (e.g., loss of moisture protection causing short circuiting) over the duration of this study. Gages that malfunctioned can be recognized in the figures by their incomplete data through the more than 500 d of measurement. Despite these lost gages, due to the large redundancy in the layout of the strain gages, data from the surviving gages were sufficient to capture the strain distribution, especially for Walls 1 and 3. Based on the observed evolution of strain shown in Figures 4.16 through 4.18, the following general observations were made:

- Strain data showed an initial shrinkage characterized by negative strain values, which is typical of the concrete hydration and hardening process. Negative strains lasted for up to 120 d (curing Phase 1), particularly for Wall 3. With the acceleration of the ASR reaction, the strains became positive, signifying ASR-induced expansion evidenced by axial elongation of the reinforcing bars.
- The influence of the curing conditions on ASR-induced concrete expansion was evident; this effect can be observed in the strain-time histories of the reinforcing bars. The strains “took off” (i.e., the rate of accumulation of strains rapidly increased) after 120 d following the start of curing Phase 2 (RH in excess of 95 % and temperature of 80 °F [26.7 °C] to 90 °F [32.2 °C]). Strains seemed to plateau after about 330 d, consistent with the start of curing Phase 3 (ambient conditions due to laboratory closure). With the re-opening of the laboratory after 442 d, the measurements from the surviving strain gages were inconclusive; some gages showed an increase in strains while others did not.
- In general, no significant differences were observed among the expansions of the three reactive wall panels.
- In general, for the longitudinal reinforcing bars in the boundary elements, strain gages at lower heights (near the footings made from conventional concrete) measured lesser strains than did gages located higher (20.0 in [508 mm] to 40.0 in [1016 mm] above the footings); compare plot (a) versus plot (b) in Figures 4.3 to 4.5. This trend was expected due to the effect of the rigid non-expansive footings on the wall expansions. Similarly, transverse bars at mid-height of the wall (35.0 in [889 mm] above footing) exhibited, in general, the largest strains, being far removed from the footing and top cap compared with the transverse bars at heights of 5.00 in [127 mm] and 65.0 in [1651 mm] above the footing.
- Toward the end of the recorded strains prior to testing, several reinforcing bars might have yielded or were approaching yield ($\epsilon_y = 0.24 \% \pm 0.01 \%$ for the No. 3 bars and $= 0.23 \% \pm 0.02 \%$ for the No. 4 bars). These bars included the longitudinal bars in the boundary elements at heights between 10.0 in (254 mm) and 40.0 in (1016 mm) above the footings and the transverse bars at different heights.
- Of particular interest are the ASR-induced strains in the longitudinal bars in the boundary elements at the interface with the footings (height = 0.00 in [0.00 mm] above footing) prior to testing as these values determined the pre-existing strains at the location where failure was expected to initiate and propagate during cyclic testing. These strains can be found in plot (a) of Figures 4.16 through 4.18. Since Wall 2 did not provide meaningful data for these strains, an average of these strains from Walls 1 and 3 was taken at the end of the recorded strains prior to testing. The average ASR-induced strains in the longitudinal bars in the boundary elements at the interface with the footings was found to be approximately $0.113 \% \pm 0.013 \%$.
- Taken together, the strain data from the three reactive walls show that the largest recorded strain measurement was about 0.25 % for Walls 1 and 3 and 0.23 % for Wall 2 at the end of the curing

period prior to the cyclic testing. Note that these strain values might have been exceeded in the reinforcing bars that experienced yielding since no meaningful data was available after yielding.

Note that the measured strains on the reinforcing bars do not represent the unconfined (free) ASR expansion of concrete, but rather the structural response to the ASR-induced expansion at the locations of the reinforcement, with inherent accounting for confinement effects, stress condition and structural deformations, boundary conditions (footing and top cap), and possible degradation of bond between the concrete and the reinforcement (bond-slip behavior).

It is also important to note that while the original design of experiment, Section 2.1, specified testing of reactive Wall 1 at 50 % of the target ASR expansion and testing of reactive Walls 2 and 3 at 100 % of the target ASR expansion, closure of the laboratory caused by the pandemic (curing Phase 3) disrupted the planned sequence of curing and testing, and as indicated above, no discernable difference between the expansion of the three reactive walls was observed at the time of the structural testing of the three walls.

Chapter 5

MEASURED RESPONSE DURING CYCLIC TESTING

This chapter describes the measured response of the wall specimens during cyclic testing. The chapter includes the following sections:

- Section 5.1 describes evaluation of the accuracy of the experimental loading and control system;
- Sections 5.2 through 5.5 present the individual seismic responses of Walls 1 through 4, respectively;
- Section 5.6 shows the backbone response curve of each wall specimen along with its yield point and peak resistance in negative and positive flexure;
- Section 5.7 presents observations made by direct comparison between the responses of the wall specimens; and
- Section 5.8 presents key observations made by examining the data from each individual wall specimen, and by making direct comparisons between the responses of the wall specimens. These observations are reexamined in the context of their statistical design of experiments in Chapter 6.

5.1 EVALUATION OF EXPERIMENTAL CONTROL SYSTEM

The experimental setup for testing the ASR-affected concrete shear walls was described in Section 2.5. The setup allowed for simultaneous application of 200 kip (890 kN) of vertical loading and lateral cyclic displacements based on the prescribed loading protocol shown in Figure 2.19 and Figure 2.20, while preventing out-of-plane displacements. For each wall test, the accuracy of the applied loading relative to the target (specified) loading protocol was evaluated. Figure 5.1 shows the ratio of the applied (measured) to the target (specified) drift ratio of each half-cycle in the seismic loading protocol (shown in Figure 2.19 and Figure 2.20). The drift ratio is calculated as the applied drift divided by the overall height between the point of lateral load application and top of footing, h_w , of 120 in (3048 mm). The uncertainty in the measured actuator displacement, which is linearly related to applied drift, is shown in Appendix A. For Walls 1, 2, 3, and 4, the average ratio of applied to target drift ratio across all half-cycles was 1.0044, 1.0044, 1.0045, and 1.0017, respectively. Thus, the average error in the applied drift ratio for Walls 1, 2, 3, and 4 was 0.44 %, 0.44 %, 0.45 %, and 0.17 %, respectively. The calculated value of average error was skewed by the initial, low drift cycles (i.e., approximately the first 20 half-cycles in Figure 5.1), which consistently had the largest deviations in applied drift ratio from target drift ratio because their corresponding applied displacement was small – at or below 0.30 in (7.76 mm). For further evaluation of the accuracy of the applied drift relative to target specified by the loading protocol, a magnitude-consistent average error was determined by calculating each half-cycle's error on a per-unit-peak-drift basis, i.e., by weighting the ratio of applied to target drift ratio by the magnitude of drift relative to the total accumulated drift at the end of the test. The magnitude-consistent average error between the actual achieved drift ratio and target drift ratio of Walls 1, 2, 3, and 4 was 0.0039 %, 0.0032 %, 0.0039 %, and 0.0022 %, respectively.

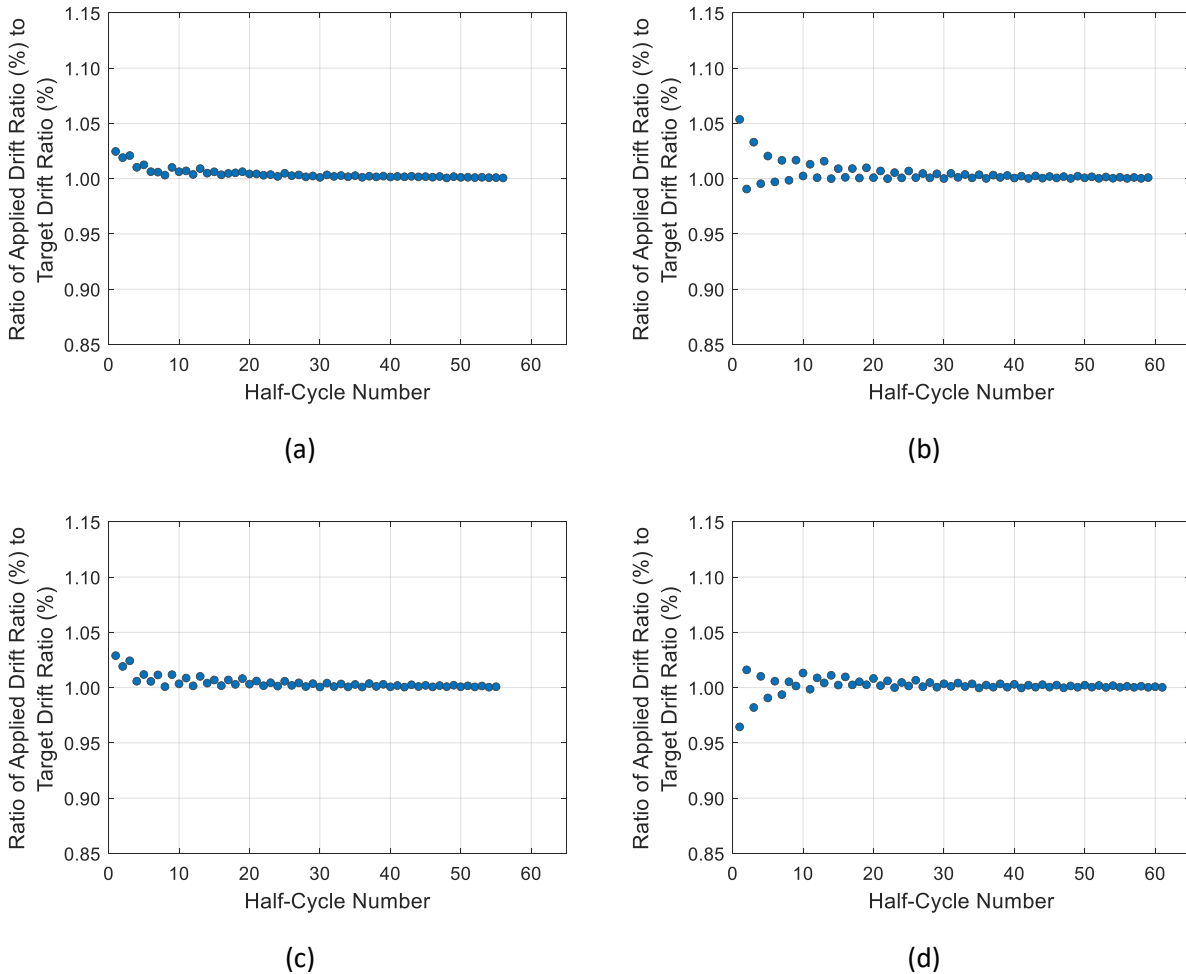


Figure 5.1: Ratio of applied (measured) to target (specified) drift ratio for (a) Wall 1, (b) Wall 2, (c) Wall 3, and (d) Wall 4

Figure 5.2 shows the axial loads measured by the two 110 kip (489 kN) capacity actuators throughout each of the four wall tests. In general, both the north (110 kip Struct #1) and south (110 kip Struct #2) actuators were able to maintain their applied axial load within a range of about (-3, +3) kip [-13, 13] kN of the target 100 kip (445 kN) per actuator throughout the duration of the cyclic loading protocol. The reason for the cyclicity of the actuator signals was that, as described in Chapter 2, their gain factors, which control the rate at which their proportional, integral, and derivative controls respond, were deliberately reduced as a safety precaution to prevent rapid squash deformations from occurring upon loss of axial load carrying capacity. Figure 5.3 shows the total axial load applied to each wall throughout the test. The total axial load was calculated by summing the measured axial loads in the two actuators at each time step. The average applied axial load for Walls 1, 2, 3, and 4 was 200.0 kip (889.6 kN), 199.8 kip (888.8 kN), 199.8 kip (888.8 kN), and 199.3 kip (886.5 kN), respectively. The uncertainties in the measurements taken by the load cells are quantified and shown in Appendix A. Relative to the target specified axial load of 200.0 kip (889.6 kN), the average error in the applied load (i.e., the average offset between the average applied load and target 200.0 kip [889.6 kN]) was 0.00 %, 0.12 %, 0.10 %, and 0.34 % for Walls 1, 2, 3, and 4, respectively.

4, respectively. The target axial load of 200.0 kip (889.6 kN) is depicted in the plots in Figure 5.3 by a horizontal dashed line. The square root of the sum of the average error squared, which represents the average deviation of the applied load from the 200.0 kip (889.6 kN) target axial load, was 0.24 kip (1.1 kN), 0.30 kip (1.3 kN), 0.31 kip (1.4 kN), and 0.76 kip (3.4 kN), respectively, for Walls 1, 2, 3, and 4.

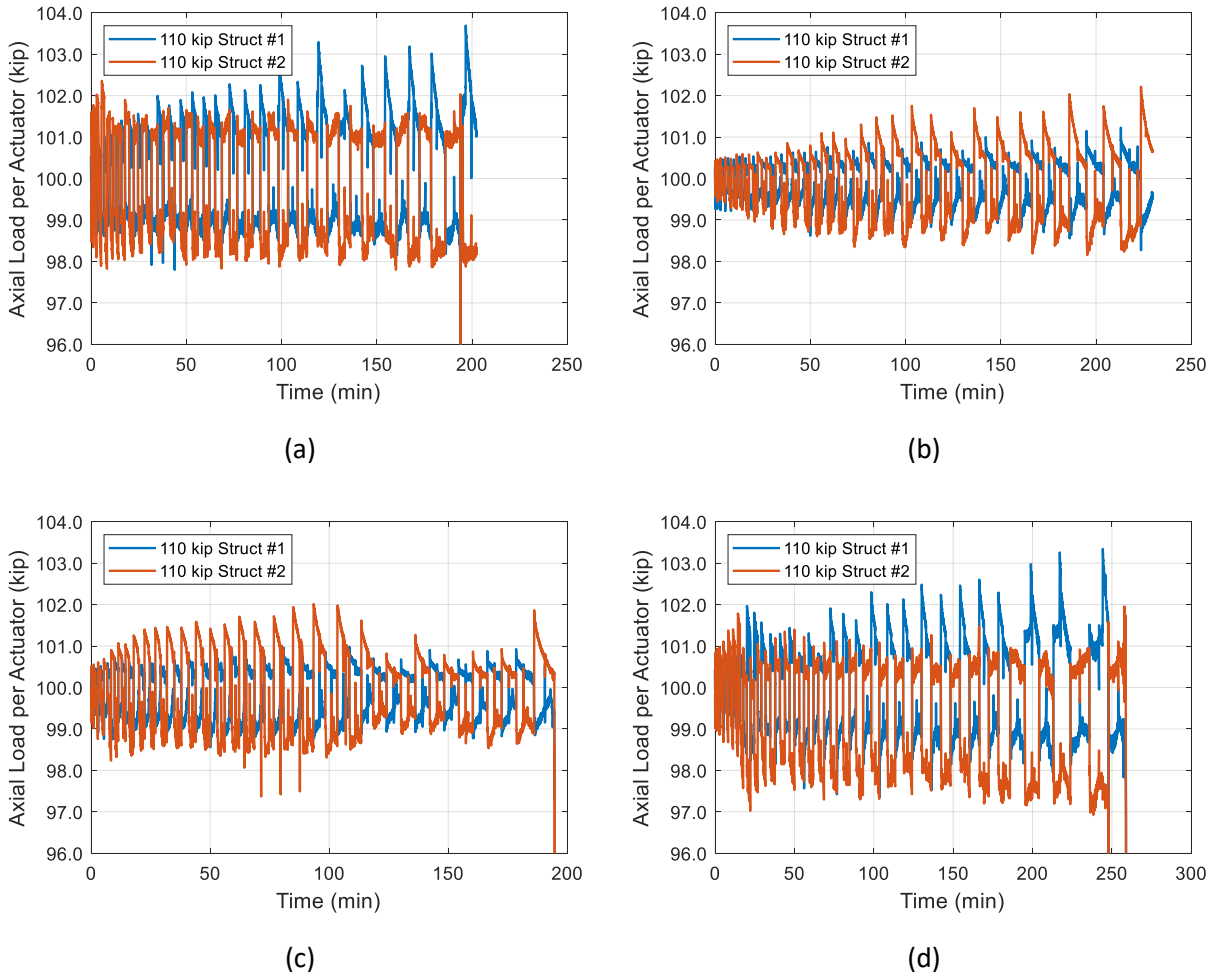


Figure 5.2: Measured axial load by the 110 kip (498 kN) capacity vertical actuators throughout duration of seismic loading protocol for (a) Wall 1, (b) Wall 2, (c) Wall 3, and (d) Wall 4 (1.000 kip = 4.448 kN)

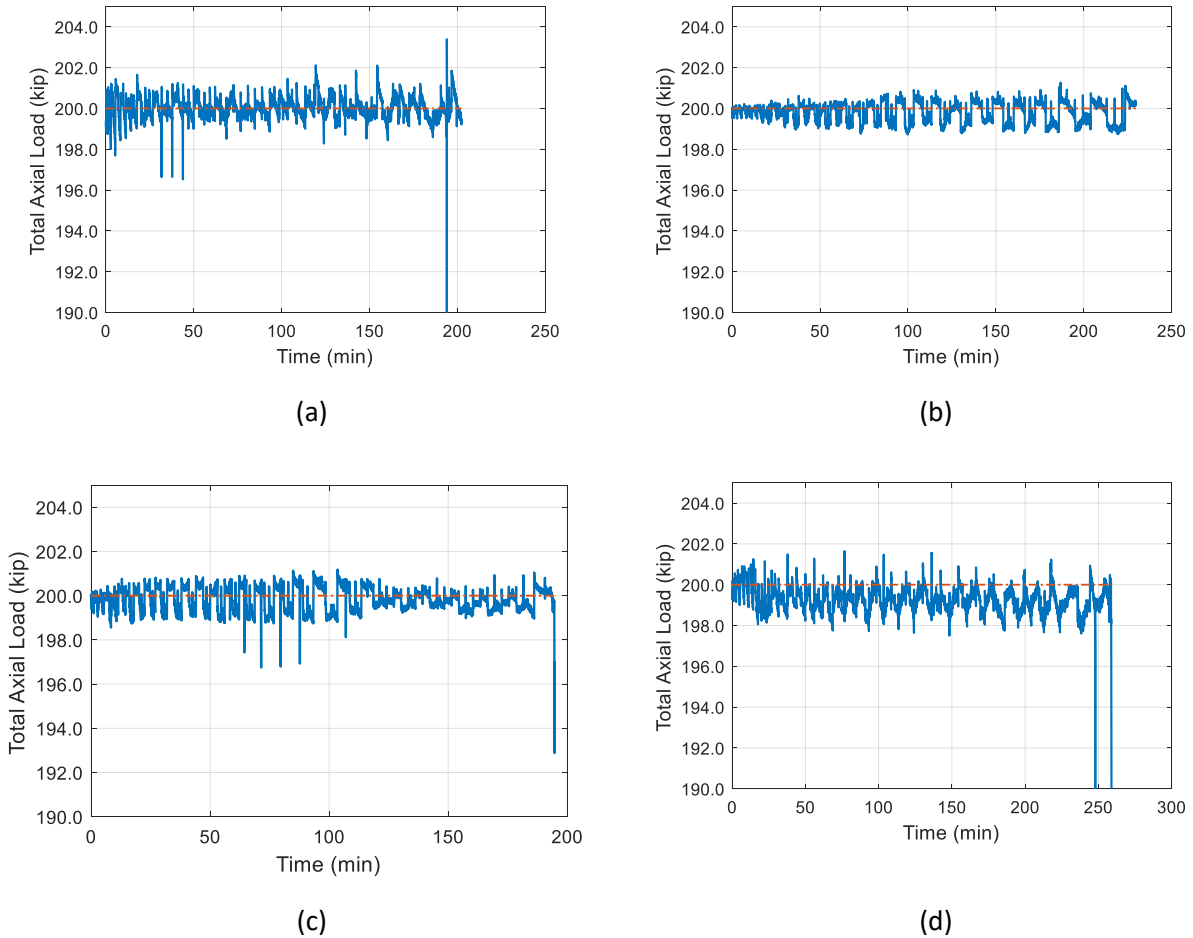


Figure 5.3: Total applied axial load throughout duration of seismic loading protocol for (a) Wall 1, (b) Wall 2, (c) Wall 3, and (d) Wall 4 (1.000 kip = 4.448 kN)

5.2 RESPONSE OF WALL 1

To This section presents the cyclic load test results for reactive Wall 1 with a stirrup spacing of 16 in (406 mm) in the boundary elements, resulting in a transverse reinforcement ratio ρ_t of 0.5 %, that was tested after being cured in the environmental chamber to accelerate ASR expansion and damage. Figure 5.4 shows the hysteretic response of Wall 1. Note that for ease of interpretation, although the test was repeatedly paused for data collection, the pauses were removed from the data presented in Figure 5.4 and other figures showing histories of the various measurements taken by the data acquisition system. The lateral displacement history of the wall, shown in Figure 5.4(a), mirrors the specified loading protocol defined in Figure 2.19 until failure of the wall occurred after about 200 min of applied loading. Lateral displacement was measured using the temposonics magneto-restrictive transducer sensor integral with the actuating cylinder of the horizontally-spanning 220 kip (979 kN) actuator. In Figure 5.4 and similar figures for the other wall specimens, positive lateral displacements were arbitrarily defined as moving the loading beam south (with the 220 kip [979 kN] horizontal actuator pushing the loading beam to the left in Figs. 2.17 and 2.18) while negative lateral displacements were defined as moving the loading beam north.

The text below also makes reference to positive and negative flexure, and positive and negative drift ratios. In the chosen sign convention, a positive drift ratio corresponded to a positive lateral displacement and positive flexure applied to the wall specimen.

Figure 5.4(b) shows the lateral force history of the specimen in time. The lateral force is calculated as

$$P_{\text{lat}} = P_{220 \text{ kip}} - (P_{110 \text{ kip N}} + P_{110 \text{ kip S}}) \sin \theta$$

where P_{lat} is the applied lateral force, $P_{220 \text{ kip}}$ is the force measured by the load cell of the 220 kip (979 kN) capacity horizontal actuator, and $P_{110 \text{ kip N}}$ and $P_{110 \text{ kip S}}$, respectively, are the forces measured by the load cells of the two vertical 110 kip (489 kN) capacity actuators on the north and south sides of the wall specimen (see Figure 2.17 for more information), and θ is the drift ratio.

The applied axial load does not impose a p-delta moment on the wall, because the wall specimen and vertically-spanning actuators, are all rigidly connected by the load beam, undergo the same imposed lateral drifts. Thus, the only imposed moment from the vertically-spanning actuators was due to the differences in the applied actuator loads shown in Figure 5.2. By the time the wall specimens reached yield, the contribution of the vertically-spanning actuators to the imposed moment on the wall was less than 1.00 % of the moment applied to the wall.

Figure 5.4(c) shows the lateral force-drift history of Wall 1. As previously indicated, drift ratio was linearly scaled from the wall lateral displacement by dividing by the nominal height from the base of the wall panel to the centerline of the loading beam (see Figure 2.17) of 120.0 in (3.048 m). The lateral force-drift history shows the peak negative and positive force was reached several cycles before the specimen failed, and the wall's cycle-to-cycle resistance to lateral loading had begun decreasing prior to failure of the wall at a drift ratio of -2.25 % during Cycle No. 28. Degradation in the wall's flexural resistance was due to buckling of the longitudinal reinforcement in the boundary element in the compressive zone and excessive yielding of the longitudinal reinforcement in the tensile zone. By a drift ratio of 2.00 % (Cycle 26), signs of concrete crushing and spalling in the compressive zone were observed. Continued cycling led to buckling of longitudinal bars accompanied by spalling/crushing of concrete in the compression zone.

Consistent with literature on the softening behavior of concrete shear walls (Pugh et al., 2015), failure was defined by occurrence of a failure mode leading to catastrophic strength loss, such as rupture of the longitudinal bars or compression failure of concrete associated with buckling of the longitudinal bars. Wall 1 failure was initiated by crushing failure of the concrete in the boundary elements, immediately followed by loss of vertical load carrying capacity resulting in axial collapse of the wall specimen. This type of failure is commonly termed "squash failure". However, to enable comparison with moment-curvature analysis approaches for softening systems in literature on seismic testing of concrete shear walls, in which a 20 % degradation in flexural strength is commonly used as an analogue for flexural failure, the drifts corresponding with 80 % of the peak flexural resistance, d_u (see Section 5.7), are reported in Tables 5.1 and 5.2. For Wall 1, d_u were -2.00 % and +3.00 %, respectively, in positive (positive displacement, or southward movement of the loading beam) and negative (negative displacement, or northward movement of the loading beam) flexure. The peak lateral load resistance of Wall 1 in negative flexure was -89.3 kip (397 kN) at a corresponding drift ratio d_{Mmax}^+ of -1.248 %, and peak lateral resistance in positive flexure was +90.3 kip (402 kN) at a d_{Mmax}^+ of +1.248 %.

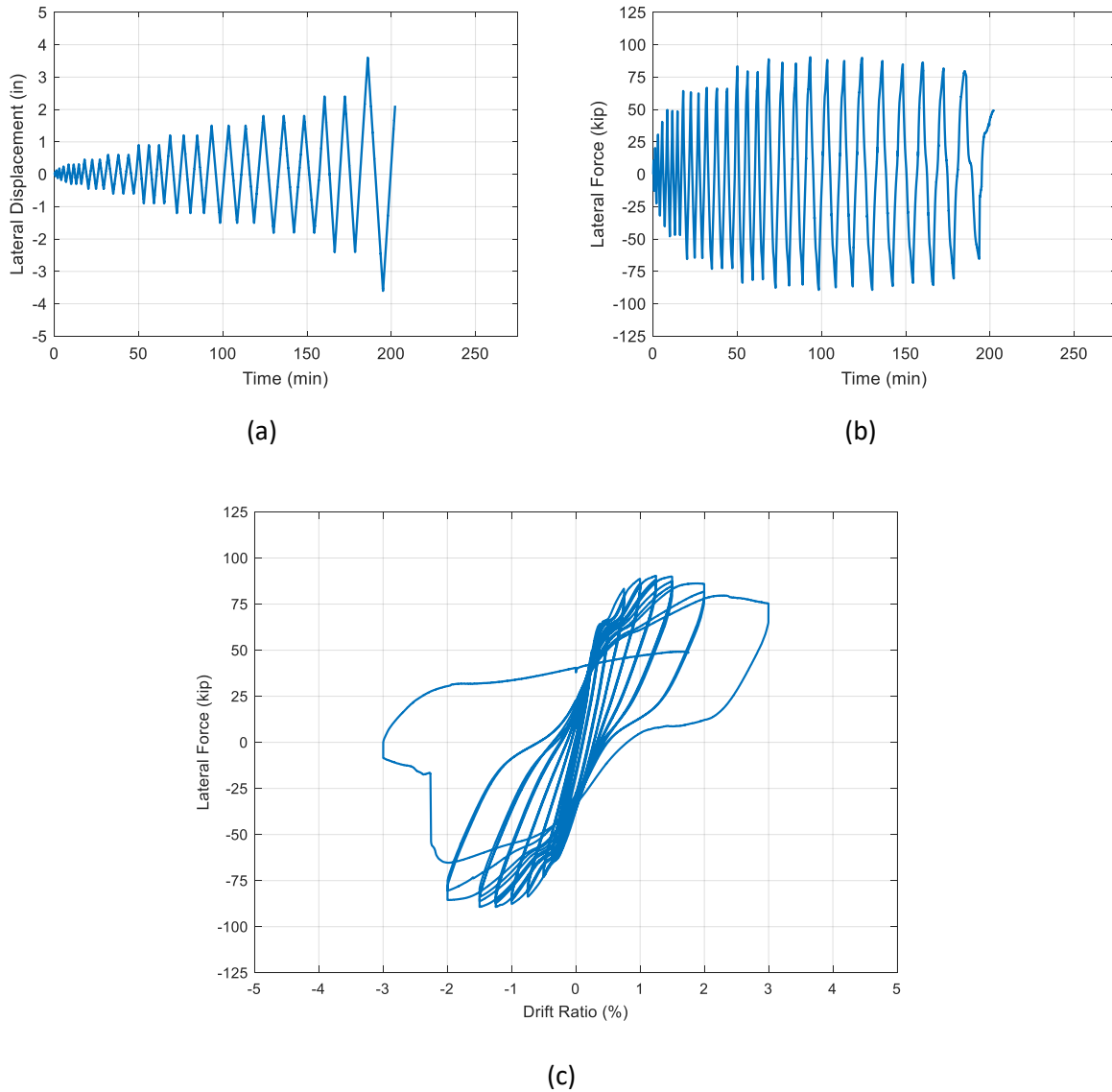


Figure 5.4: Response of Wall 1: (a) lateral displacement history, (b) lateral force history, and (c) force-drift hysteresis (1.00 in = 25.4 mm; 1.000 kip = 4.448 kN)

Figure 5.5 shows deformations and rotations measured by point sensors up the height of the wall. The measurement uncertainty of each type of point sensor, including string potentiometers, inclinometers, and linear variable differential transformers (LVDTs) is reported in Appendix A. As shown in Figure 2.22, displacement transducers were also used to measure relative displacements between the wall panel and the footing (indicative of shear sliding) and the footing and the reaction frame (indicative of footing sliding and rocking). The measurements of shear sliding and footing sliding/rocking were negligible in comparison to the lateral deformations of the wall panel, indicating that for the four tested specimens, the wall panel had sufficient anchorage in the footing and the footing was adequately anchored to the reaction frame, respectively.

The curves in Figure 5.5(a) correspond to in-plane lateral deformations measured with string potentiometers at heights of 5.0 in (127 mm), 15.0 in (381 mm), 30.0 in (762 mm), 80.0 in (2032 mm), and 120.0 in (3048 mm) above the footing of the wall (Figure 2.21 provides a schematic of wall displacement transducer locations). The subscript labels in the legend of Figure 5.5(a) specify the height, in inches (1.00 in = 25.4 mm), at which each deformation history was measured. Each deformation history in Figure 5.5(a) was averaged from the measurements of two string potentiometers collocated at the same height but aligned with opposite faces of the wall specimen. Figure 5.5(b) shows in-plane rotation histories taken at heights of 10.0 in (254 mm), 25.0 in (635 mm), and 55.0 in (1397 mm) from the base of the wall (Figure 2.23 provides a schematic of wall inclinometer locations). Figure 5.5(b) reveals that the measurements taken by R025 and R055 were within 12 % of one another, indicating that there was little differential rotation between heights of 25 in (635 mm) and 55 in (1397 mm) above the footing of the wall. A comparison of the relative magnitudes of measurements taken by R010, R025, and R055 (for example, taking as a reference their values at 134.5 min, at the peak of Cycle 23, in which $R010 = 0.341^\circ$, $R025 = 0.420^\circ$, and $R055 = 0.468^\circ$) shows that, as a proportion of the total rotation measured within the first 55 in (1397 mm) of wall height, 73 % occurred within the first 10.0 in (254 mm) of wall height and 90 % occurred within the first 25 in (635 mm) of wall height. Further quantification of the relative magnitudes of wall rotations at the peaks and valleys of each inelastic cycle is provided in Section 5.7.4, since it helps to facilitate comparisons of the degrees of damage localization among the four wall specimens.

Figure 5.5(c) shows in-plane lateral deformation profiles up the height of the wall for the first cycle of drift ratios ranging from 0.25 % to 3.00 %. These lateral deformation profiles are nearly linear with respect to height up to a drift ratio of 2.00 %. At Cycle 28 with a drift ratio of 3.00 %, wall deformation becomes more pronounced within the first 15.0 in (381 mm) of wall height. Such a concentration of deformation is indicative of damage at the bottom of the wall. Photos documenting the distribution of cracking on the west face of the wall specimen and spalling in the boundary elements are available in Chapter 3, Section 3.2.2.

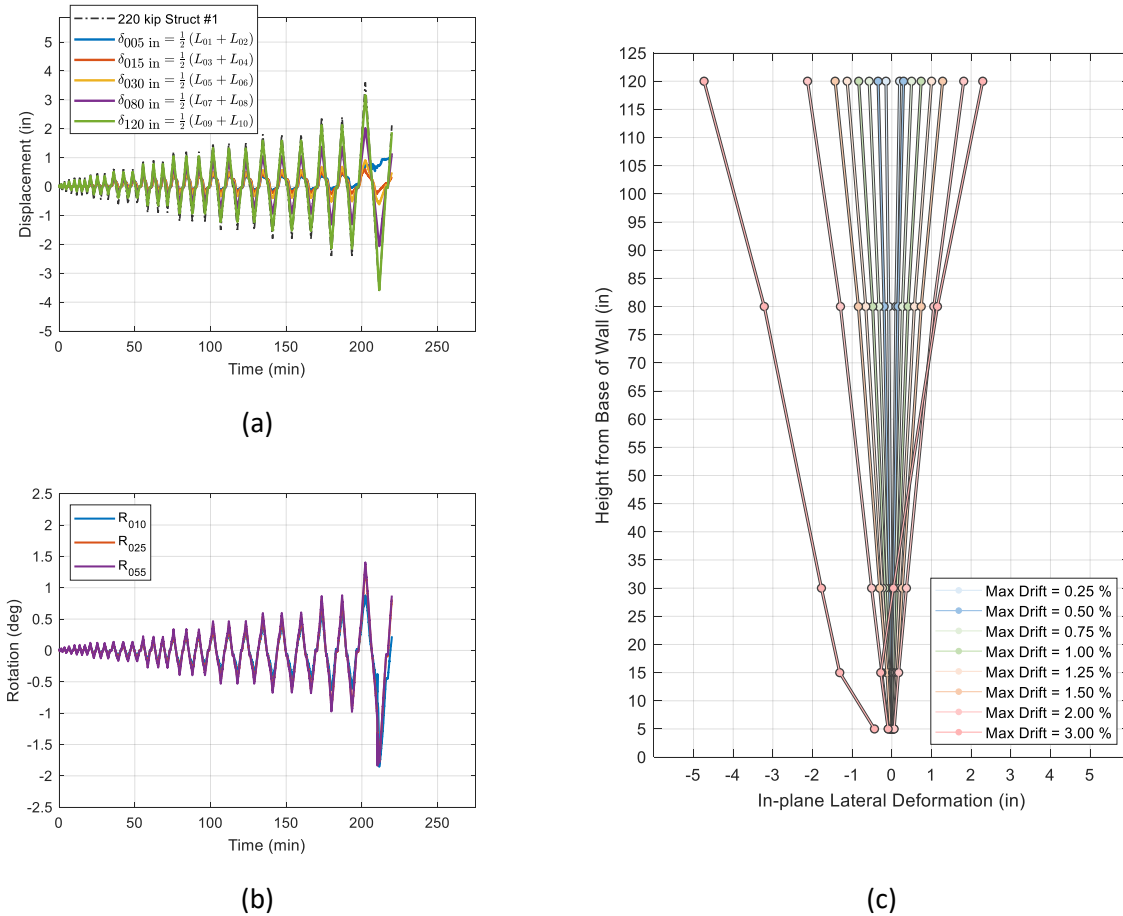


Figure 5.5: Point sensor measurements up the height of the Wall 1: (a) horizontal deformation history, (b) rotation history, and (c) in-plane lateral deformation profiles at peak/valley (1.00 in = 25.4 mm)

Figure 5.6 shows the measured strains in the west longitudinal bars at zero height (i.e., at the interface between the wall panel and footing), where the suffix “i” or “o” at the end of the gage name in the legend indicates that the gage was placed on the inside or outside of the bar, respectively (see Figures 2.24 to 2.27). The region shaded light grey corresponds to the strain range from zero to 0.0023 in/in (0.0023 mm/mm), which is the measured yield strain of the reinforcing bars. Consistent with the ASR Task 2 Report (Thonstad et al., 2021), the yield strain was determined as the ratio of the average measured yield stress of 65.7 ksi (453 MPa) (see Chapter 4) and an assumed nominal modulus of elasticity of rebar of 29,000 ksi (200 GPa). Measurements taken by the individual strain gages are shown in dark grey, and their average, which represents the average axial strain in the bar, is shown as a thinner red line. The initial offset in the strain values of 0.00113 in/in (0.00113 mm/mm) corresponds to the ASR-induced expansive strain of 0.113 % ± 0.013 % reported in Section 4.5 for the longitudinal bars at zero height above the footing.

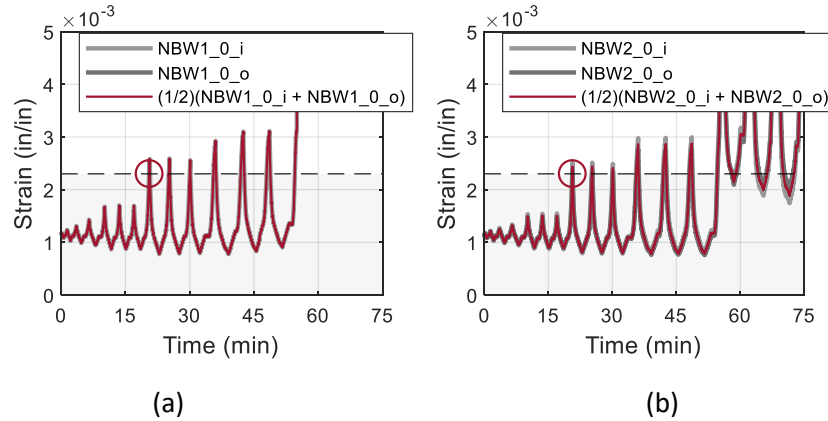


Figure 5.6: Measured strains in longitudinal bars of Wall 1 at height of 0.0 in (0.0 mm): (a) NBW1 (outer bar) and (b) NBW2 (inner bar)

Despite failure of the strain gages on the north longitudinal bar after Cycle 11, data collected was sufficient to determine flexural yield of the longitudinal bars in the boundary element. The drift ratio corresponding to yielding of longitudinal bars was determined by finding the drift ratio at which the average strain in the longitudinal bars first crossed the yield strain of 0.0023 in/in (0.0023 mm/mm), which is indicated by the black horizontal dashed line in the plots. The point at which the total average strain crosses the yield strain is also circled in Figure 5.6. The figure indicates that both the outer and inner longitudinal bars of the boundary elements yielded in the same cycle. Yield of the bars in Wall 1 in positive flexure was at 21.6 min corresponding to a drift ratio of +0.35 %, at a moment of 7584 kip-in (856.9 kN-m), or 79 % of the nominal moment capacity of the wall of 9572.9 kip-in (1081 kN-m) based on a sectional analysis of the wall that is further described in Section 5.6. The lateral force-drift point corresponding to yield the wall is shown on its backbone response curve of each wall below in Figure 5.27, because it is integral to the calculation of elastic and inelastic areas under the backbone curves as described in Section 5.7. The values of drift at yield and normalized yield moment are reported in Table 5.2.

The hysteretic energy of each cycle was calculated by numerically integrating the area bounded by the force-displacement curve for that cycle. All areas were calculated using the trapezoidal method, with nonuniform spacing determined by the measured drift coordinates of the curve. To illustrate the concept, Figure 5.7 shows an example of the hysteretic energy calculated for the first cycle of each inelastic phase of cyclic loading: i.e., for Cycle 05 (Immediate Occupancy), Cycle 14 (Life Safety), Cycle 20 (Collapse Prevention), and Cycle 26 (To Failure). This same approach was used to calculate the incremental hysteretic energy (i.e., energy dissipated by each individual cycle) of each of the four walls in this section and Sections 5.3 through 5.5.

The incremental hysteretic energy is plotted in Figure 5.8(a) and the accumulated, or cumulative, hysteretic energy, which is the sum of the energy dissipated from the first to each individual cycle, is plotted in Figure 5.8(b). The values along the x-axis (labeled "Cycle No."), correspond to the cycle numbers listed in the loading protocol in Figure 2.19. Figure 5.7 and Figure 5.8(a) show that earlier cycles in the loading protocol dissipate relatively less energy than later cycles, which had larger corresponding lateral

displacements/drifts. This trend can also be seen in Figure 5.8(b), in which the rate of accumulation of hysteretic energy increases with increasing cycle number.

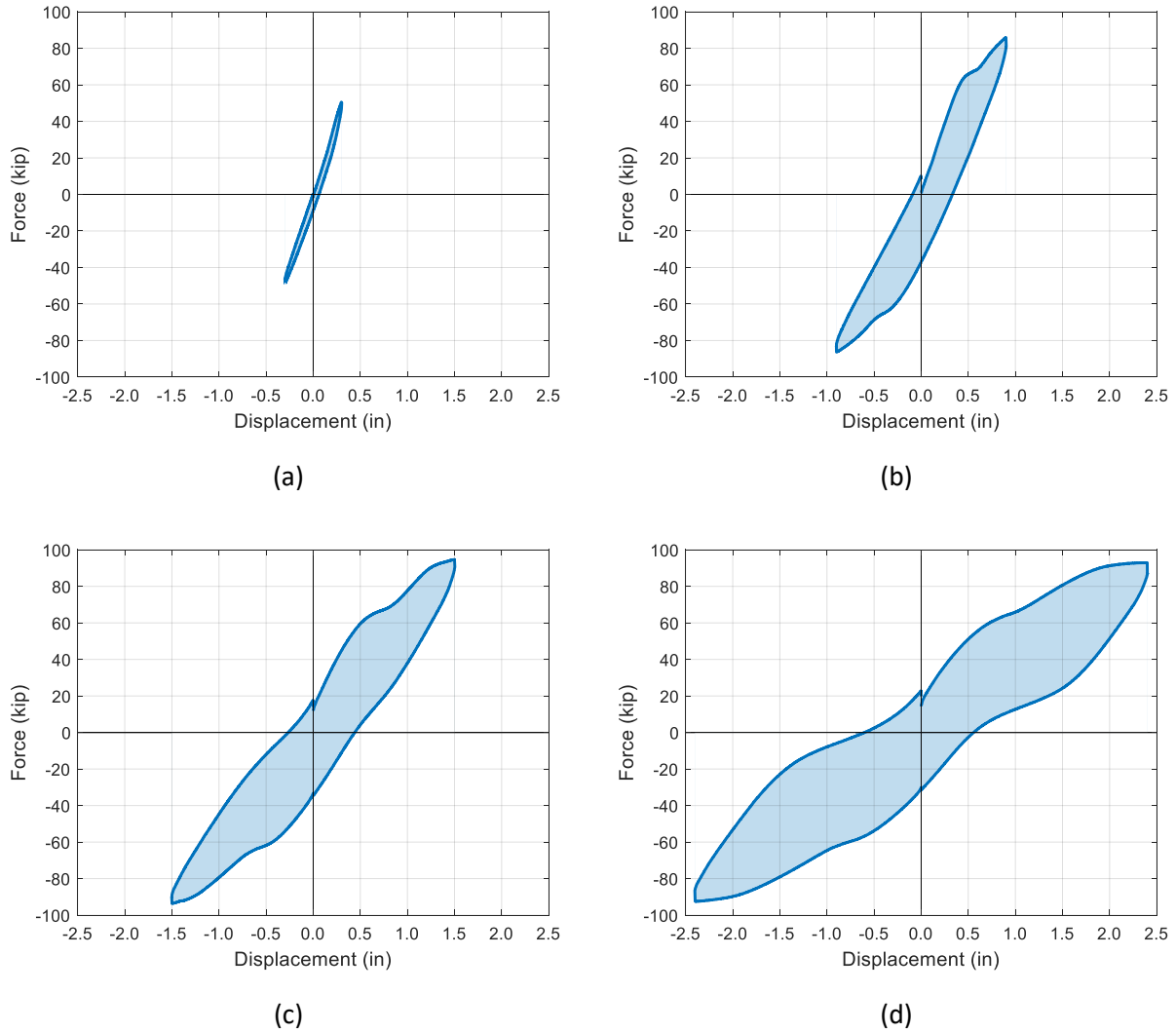


Figure 5.7: Hysteretic energy, shown as blue shaded area, of (a) Cycle 05 (Immediate Occupancy), (b) Cycle 14 (Life Safety), (c) Cycle 20 (Collapse Prevention), and (d) Cycle 26 (To Failure). 1.00 in = 25.4 mm; 1.000 kip = 4.448 kN.

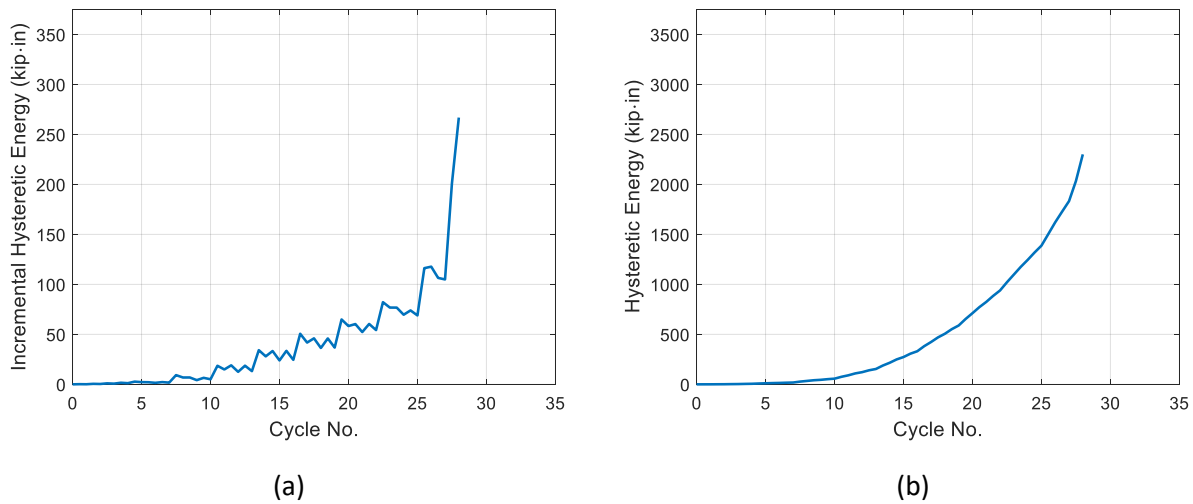


Figure 5.8: Cyclic hysteretic energy of Wall 1, calculated as area bounded by force-displacement curve for each cycle (a) incremental, and (b) cumulative (1.000 kip in = 0.113 kN m)

Two stiffness values were extracted near peak and valley of each cycle in the wall hysteretic force-displacement response to help characterize stiffness degradation with increasing level of drift. One stiffness value was measured while approaching the target drift at peak or valley and is designated as the “approach stiffness”, while the other stiffness value was measured while unloading immediately after reaching the target drift at peak or valley (Figure 5.9). The approach stiffness was calculated as the slope of the linear regression of cyclic force-displacement points approaching the peak displacement, and the unload stiffness was calculated as the slope of the linear regression of cyclic force-displacement points unloaded from the peak displacement. A total of 19 points (i.e., 19 force-displacement coordinate pairs) were used in calculating each linear regression so that the naturally-occurring high-frequency noise in the data had a minimal influence on the calculated stiffness value.

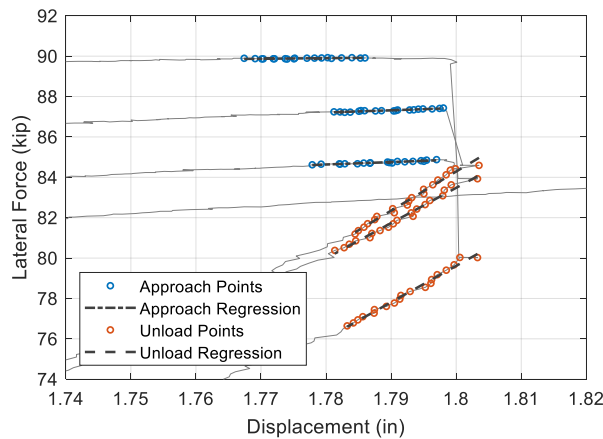


Figure 5.9: Magnified view of three cycles near peak displacement of 1.80 in (45.7 mm) showing points and regression lines used to extract approach and unload stiffness from cyclic force-displacement hysteresis. (1.000 kip = 4.448 kN, 1.00 in = 25.4 mm)

Figure 5.10 shows the measured values of approach and unload stiffness versus drift ratio. These values are reported because they are useful in calibrating computational models to capture the seismic behavior of concrete shear walls with an appropriate unload/reload stiffnesses and degrees of pinching. Each extracted value of approach stiffness or unload stiffness is represented in the plots by a single circular marker. Stiffness values in Figure 5.10(a) are shown in units of stiffness (i.e., in units of force divided by displacement), and values in Figure 5.10(b) were normalized by the initial stiffness of the wall's force-displacement response. The initial stiffness was calculated from the backbone (cyclic envelope) response of each wall specimen. The approach used in calculating the wall backbone responses and initial stiffnesses is described in Section 5.7. The shape of the relative changes in stiffness values with increasing positive or negative drift is the same in both plots because the normalization in Figure 5.10(b) is by a constant initial stiffness value.

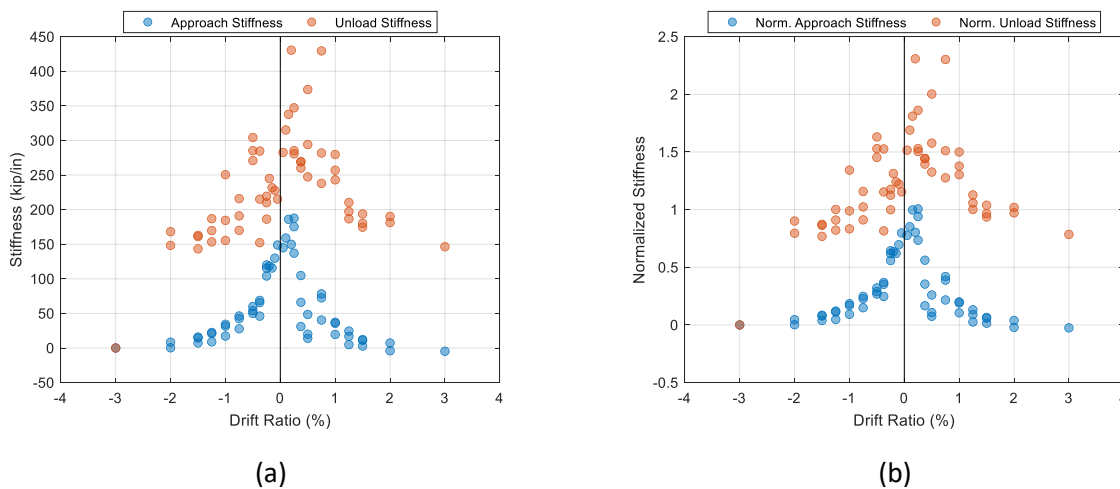


Figure 5.10: Approach and unload stiffness of Wall 1: (a) in units of kip/in (1.000 kip/in = 0.175 kN/mm), and (b) normalized by wall initial stiffness

Figure 5.10 shows that both the approach stiffness and unload stiffness generally decrease with increasing magnitude of peak drift. It is interesting to note that the approach stiffness decreases to less than zero at large peak drifts, indicating that the slope of force-displacement curve approaching peak was negative. For Wall 1, the approach stiffness first decreased below zero at a drift ratio of 2.00 % in positive flexure and -3.00 % in negative flexure. Because the loading protocol for the wall specimens in this study was applied pseudo-statically in displacement control (i.e., displacements were applied at a very slow rate), this transition of the wall's force-displacement response to a negative stiffness did not produce an in-plane instability; however, under force controlled actions, such a transition may lead either to snap-through, if forces could be effectively redistributed, or to collapse, if they could not be redistributed. For an isolated concrete shear wall tested in a structures laboratory, redistribution of forces may not be possible as no other structural components exist as part of the experimental specimen, so the transition

to negative stiffness can be interpreted as a predictor of incipient failure/collapse, rather than actual failure/collapse.

5.3 RESPONSE OF WALL 2

This section presents the cyclic load test results for reactive Wall 2 with a stirrup spacing of 4 in (102 mm) in the boundary elements, resulting in a ρ_t of 2.0 %, that was tested after being cured in the environmental chamber to accelerate ASR expansion and damage. Figure 5.11 shows the cyclic response of Wall 2 in terms of its lateral displacement history (Figure 5.11(a)), lateral force history (Figure 5.11(b)), and lateral force-drift ratio hysteresis (Figure 5.11(c)). The peak lateral resistance of Wall 2 in negative flexure was -91.0 kip (405 kN) and occurred at a drift ratio of -1.996 %. The peak lateral resistance in positive flexure was +85.3 kip (379 kN) at a drift ratio of +1.249 %. Spalling of concrete was first observed in the compressive zone at a drift ratio of 2.000 % (Cycles 26-27), and more extensive spalling, exposing the buckled longitudinal reinforcement in the boundary element, was observed at a drift ratio of 3.000 % (Cycle 29). The wall experienced tensile rupture of one longitudinal reinforcing bar in the boundary element at a drift ratio of +4.00 % along with compression failure in the compression zone of concrete. However, as is shown in Figure 5.11(a), the wall was then cycled back to 0.00 % drift ratio before the test was ended. The drift ratios corresponding to 80 % of the peak flexural resistance (i.e., a 20 % degradation in flexural strength) were -3.00 and +3.87 %, respectively, in negative and positive flexure. These values are reported in Table 5.1. At a drift ratio of +4.00 %, the wall's flexural resistance had degraded by 21.6 %.

The deformations and rotations measured by point sensors up the height of the wall are shown in Figure 5.12. Figure 5.12(a) shows lateral deformation measurements taken by string potentiometers and Figure 5.12(b) shows in-plane rotation measurements taken by inclinometers. The in-plane lateral deformation profiles up the height of the wall in Figure 5.12(c) shows that, throughout the entire test, the lateral deformations were nearly linear with respect to height.

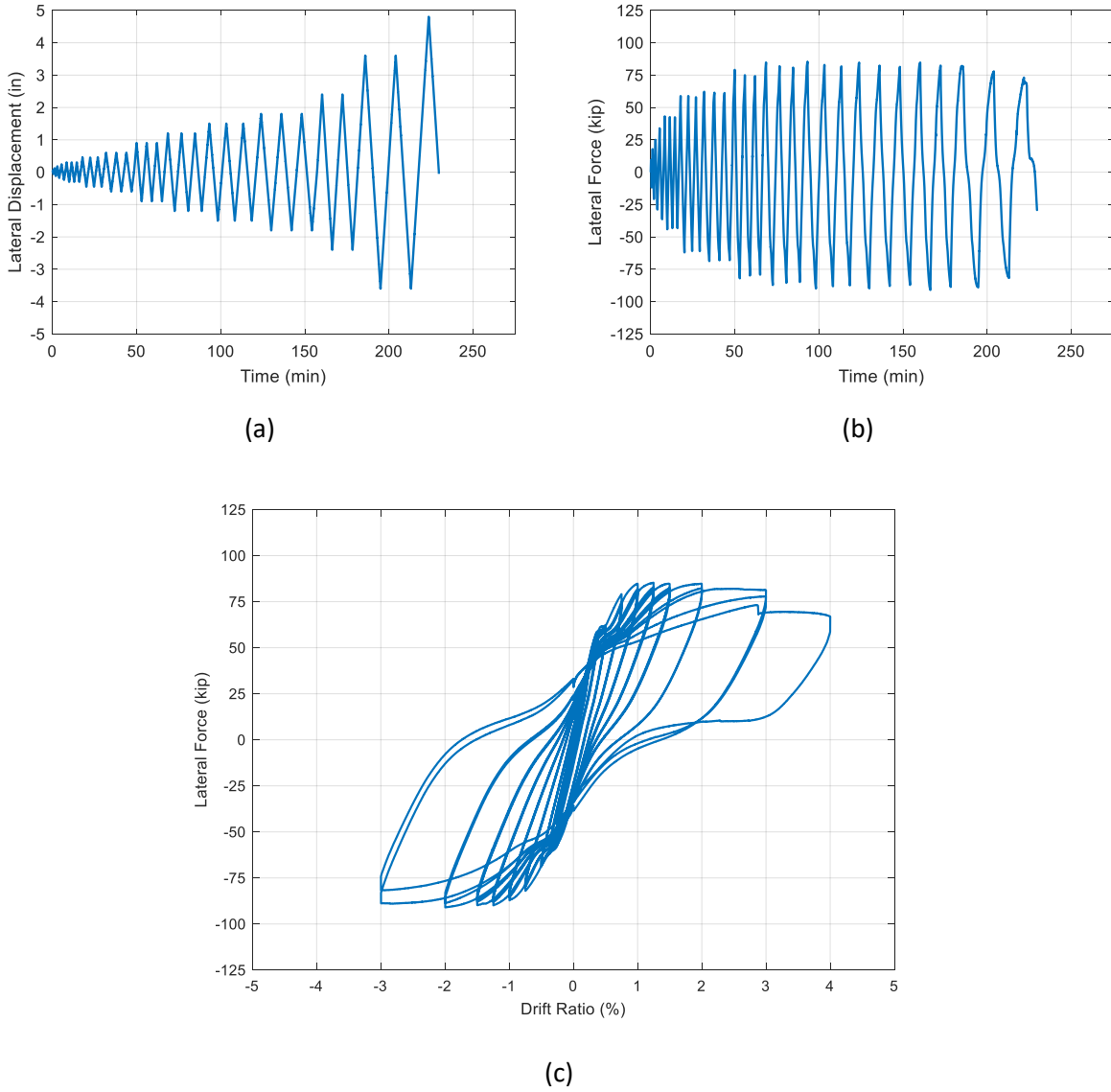


Figure 5.11: Response of Wall 2: (a) lateral displacement history, (b) lateral force history, and (c) force-drift hysteresis (1.00 in = 25.4 mm; 1.000 kip = 4.448 kN)

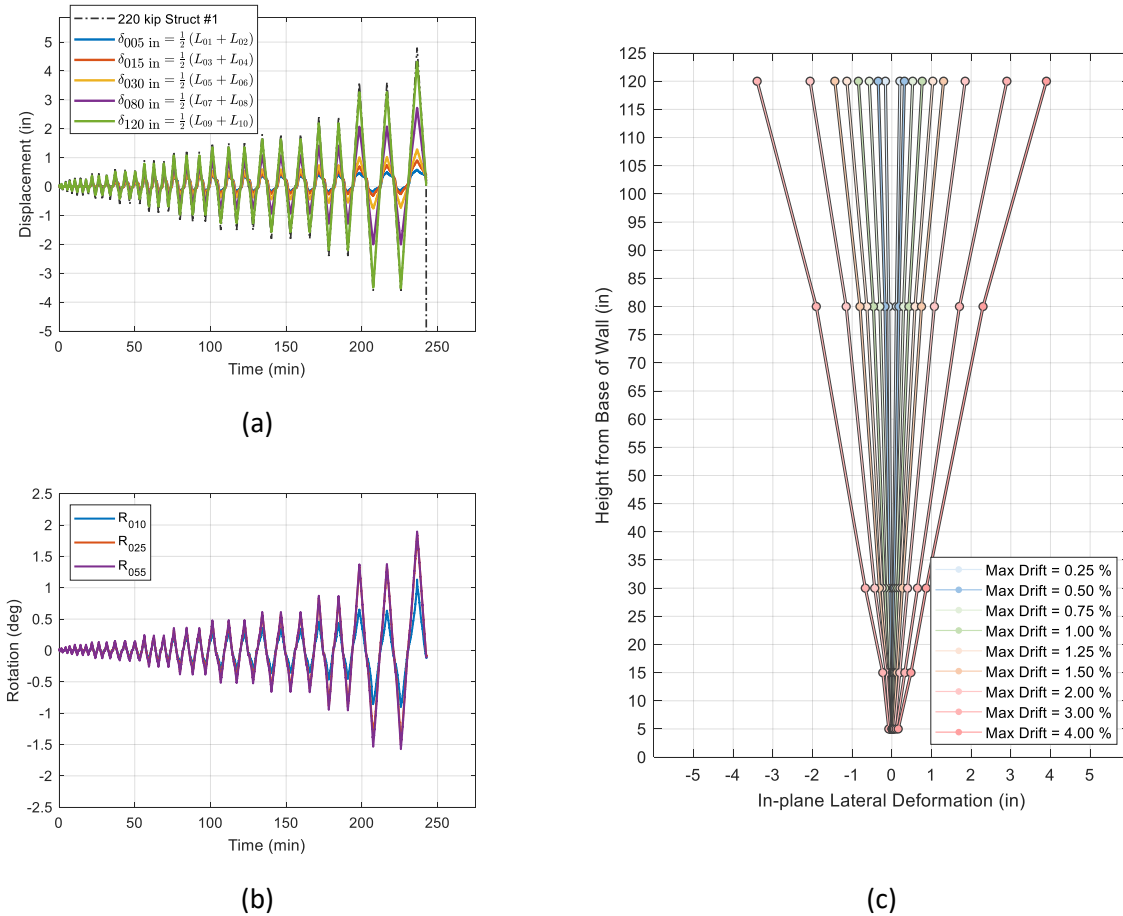


Figure 5.12: Point sensor measurements up the height of the Wall 2: (a) horizontal deformation history, (b) rotation history, and (c) in-plane lateral deformation profiles at peak/valley (1.00 in = 25.4 mm)

Figure 5.13 shows strain histories of the gages on the longitudinal bars in the boundary elements at zero height. Yield of the north longitudinal bar appeared to first occur at 6.8 min, in Cycle 04; however, little confidence was placed in these data because, during monitoring, gages NBW1_0_i and NBW1_0_o produced no meaningful data (had gages NBW1_0_i and NBW1_0_o produced reliable data, they would have been plotted in Figure 4.17(a)). Similar to Wall 1, the yield point of the bars was determined by finding the point at which the strain in all the longitudinal bars first crossed the yield strain of 0.0023 in/in (0.0023 mm/mm), so for Wall 2 yield of the wall was determined based on gages NBW2_0_i and NBW2_0_o. Wall 2 yielded at a drift ratio of 0.31 % and a moment of 6420 kip·in (725.4 kN·m) (67 % of the wall’s nominal moment capacity). The lateral force-drift ratio point corresponding to yield of Wall 2 is shown on its backbone response curve in Figure 5.27. The drift at yield and normalized yield moment are reported in Table 5.2.

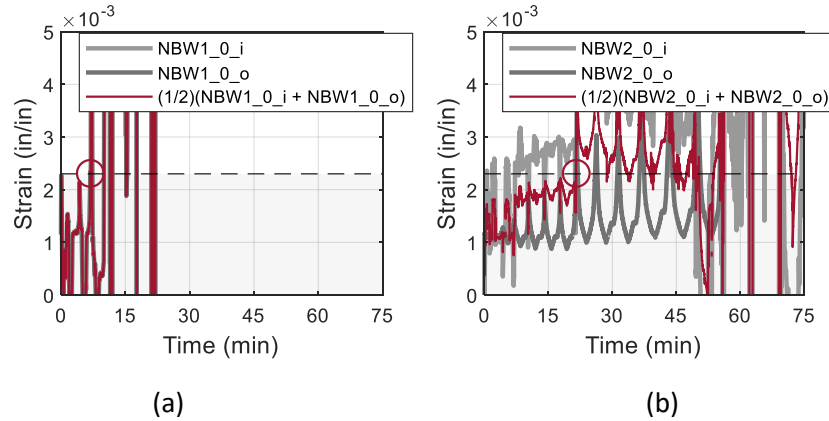


Figure 5.13: Measured strains in longitudinal bars of Wall 2 at height of 0.0 in (0.0 mm): (a) NBW1 (outer bar) and (b) NBW2 (inner bar)

Figure 5.14(a) and 5.14(b) show the incremental and cumulative hysteretic energy of Wall 2, respectively. Similar to observations from Wall 1, Figure 5.14(a) shows that earlier cycles in the loading protocol dissipate relatively less energy than later cycles which had larger lateral drifts. Relative comparisons between the energy dissipated by the four wall specimens are provided in Section 5.7.

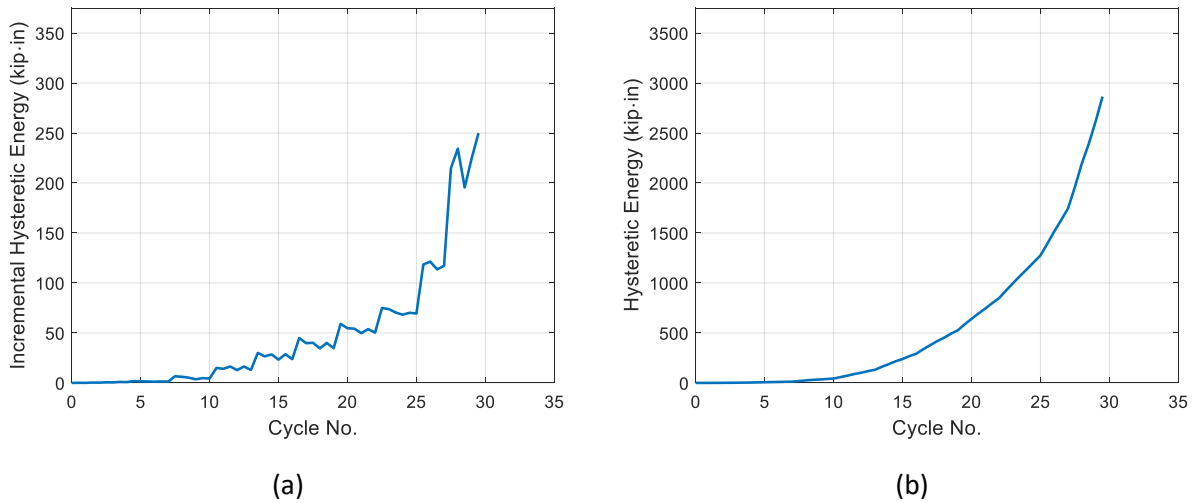


Figure 5.14: Cyclic hysteretic energy of Wall 2, calculated as area bounded by force-displacement curve for each cycle (a) incremental, and (b) cumulative (1.000 kip in = 0.113 kN m)

Figure 5.15 shows the wall’s approach and unload stiffness versus drift. Similar to Wall 1, the approach and unload stiffness values generally decreased with increasing drift. The approach stiffness had decreased to less than zero by Cycle 29, which had peak drift ratios of +3.00 % in positive flexure and -3.00 % in negative flexure.

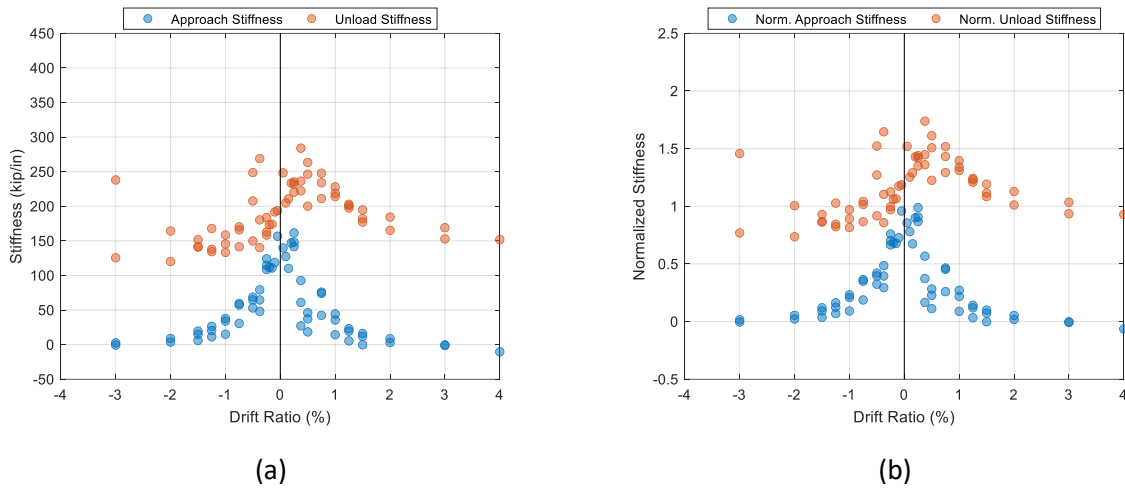


Figure 5.15: Cyclic stiffness response of Wall 2: (a) in units of kip/in (1.000 kip/in = 0.175 kN/mm), and (b) normalized by wall initial stiffness

5.4 RESPONSE OF WALL 3

This section presents the cyclic load test results for reactive Wall 3 with a stirrup spacing of 16 in (406 mm) in the boundary elements, resulting in a ρ_t of 0.5 %, that was tested after being cured in the environmental chamber to accelerate ASR expansion and damage. Figure 5.16 shows Wall 3's lateral displacement history in Figure 5.16(a), lateral force history in Figure 5.16(b), and lateral force-drift response of Wall 3 in Figure 5.16(c). The damage observed in the response of Wall 3 was similar to that of Wall 1 (see Chapter 3), with combined buckling of the longitudinal reinforcement in the boundary element in the compressive zone and yielding of the longitudinal reinforcement in the tensile zone. Spalling of the concrete in the compressive zone was first observed at a drift ratio of 1.250 % (Cycles 20-22). Wall 3 failed catastrophically during Cycle 28 in compression while cycling toward valley, after achieving +3.00 % drift ratio, i.e., a lateral displacement of +3.60 in (91.4 mm), in positive flexure. The drifts corresponding to 80 % of the peak flexural resistance (i.e., a 20 % degradation in flexural strength) were -2.00 and +2.00 %, respectively, in positive and negative flexure. These values are reported along with those of the other walls in Table 5.1. Wall 3 continued resisting lateral loading well beyond a 20 % degradation in flexural strength. Wall 3's flexural strength had degraded by 29.7 % relative to its peak flexural resistance in positive flexure, when a drift ratio of +3.00 % was first reached. The peak lateral resistance of Wall 3 in negative flexure was -88.0 kip at a drift ratio of -1.247 %, and peak lateral resistance in positive flexure was +85.5 kip at a drift ratio of +0.748 %.

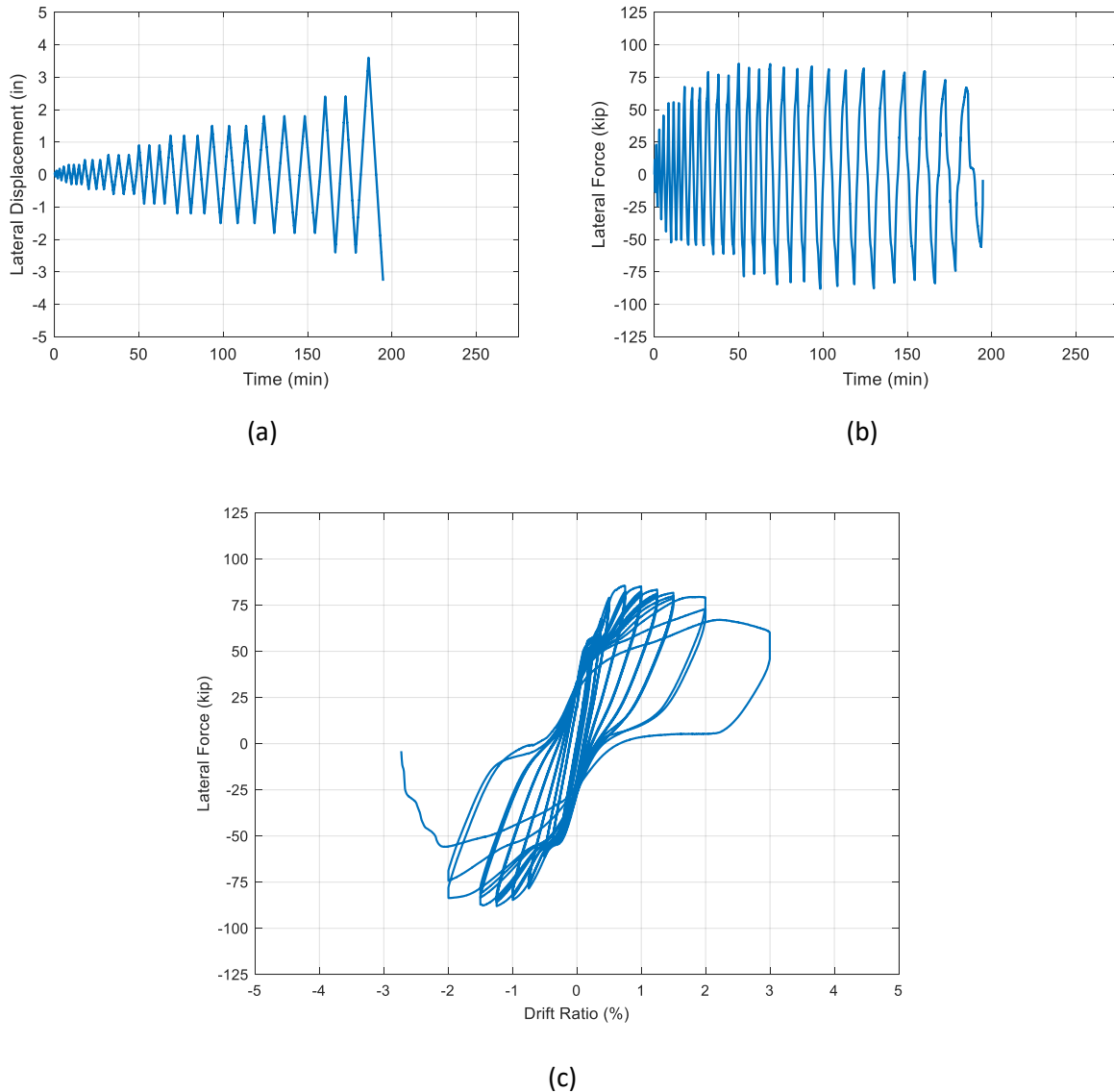


Figure 5.16: Response of Wall 3: (a) lateral displacement history, (b) lateral force history, and (c) force-drift hysteresis (1.00 in = 25.4 mm; 1.000 kip = 4.448 kN)

Figure 5.17 shows the deformations and rotations measured up the height of the wall by point sensors. Figure 5.17(a) shows lateral deformation measurements taken by string potentiometers and Figure 5.17(b) shows in-plane rotation measurements taken by inclinometers. The large apparent increase in the magnitude of the rotation at 194.3 min of loading corresponded to a dynamic shockwave induced by failure of the wall during its final cycle of loading.

The in-plane lateral deformation profiles up the height of the wall (Figure 5.17(c)) were nearly linear with respect to height until the final cycle of loading. The final snapshot of wall in-plane lateral deformations, in which the deformation was negative up to a wall height of about 62.0 in (1570 mm) and positive at the top of the wall, was taken at peak during Cycle 28. By then, lateral deformations concentrated within the

first 30.0 in (762 mm) of wall height became so concentrated that they were no longer recovered by the reversed cycle, indicating extreme localization of damage and impending failure. The lateral force-drift response in Figure 5.16(c) also shows a large decrease in lateral force while the lateral drift was paused at +3.00 % drift ratio before being cycled back toward valley, also indicating that the wall had begun to fail.

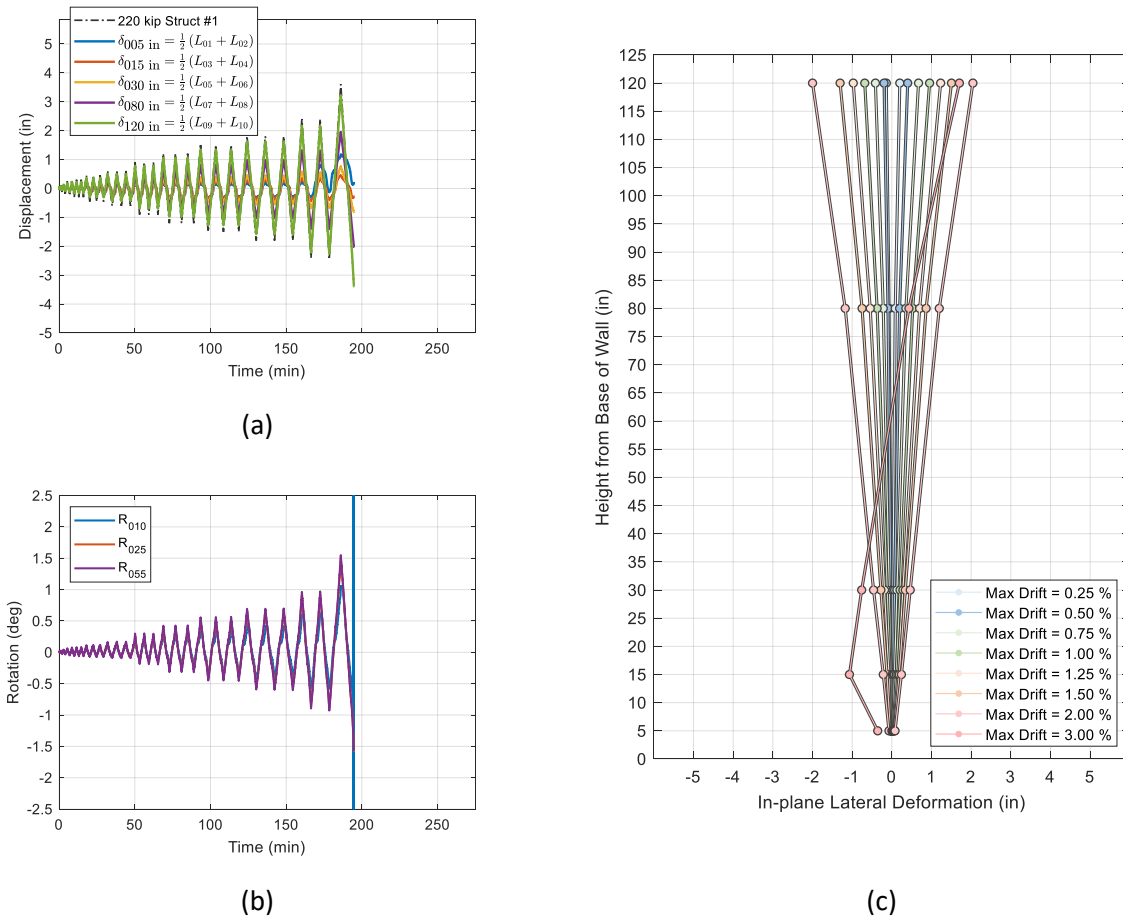


Figure 5.17: Point sensor measurements up the height of the Wall 3: (a) horizontal deformation history, (b) rotation history, and (c) in-plane lateral deformation profiles at peak/valley (1.00 in = 25.4 mm)

The point at which the average axial strain in the outer north bars exceeded the yield strain, which corresponded to flexural yield of the wall specimen, is shown circled in Figure 5.18(a). The yield moment of Wall 3 was 6468 kip-in (730.8 kN-m), which corresponds to 68 % of the nominal moment capacity. Wall 3 had the earliest yield point among the four tested wall specimens, at a drift ratio of only 0.24 %. The lateral force-drift point corresponding to yield of Wall 3 is shown on its backbone response curve in Figure 5.27, and the drift at yield and yield moment are reported in Table 5.2. Figure 5.18(b) shows that the strain gages on the inner longitudinal bars in the boundary element malfunctioned early and did not provide meaningful data.

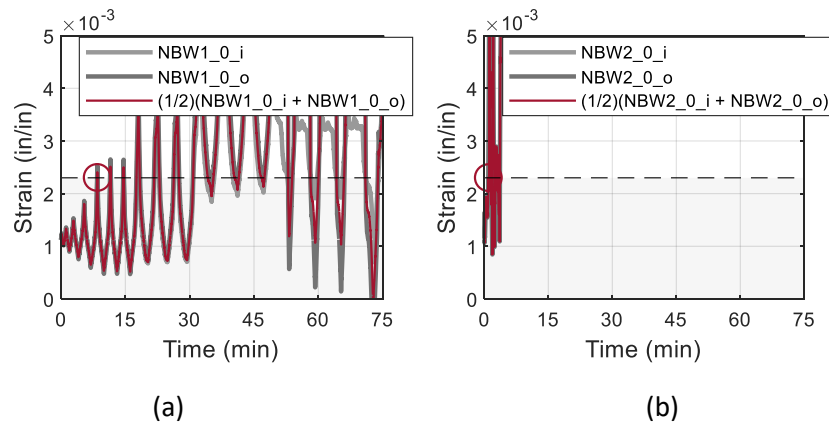


Figure 5.18: Measured strains in longitudinal bars of Wall 3 at height of 0.0 in (0.0 mm): (a) NBW1 (outer bar) and (b) NBW2 (inner bar)

The incremental and cumulative hysteretic energy of Wall 3 is shown in Figure 5.19(a) and 5.19(b), respectively. Of the four walls, Wall 3 had the most rapid per-cycle accumulation of hysteretic energy until its failure in Cycle 28. This observation is consistent with Wall 3 having the least drift at the yield moment among the four wall specimens. Because Wall 3 yielded earlier than did the other specimens, it began dissipating measurable amounts of hysteretic energy at earlier cycles than did the other specimens. Direct comparisons between the energy dissipated by Wall 3 and other wall specimens are provided in Section 5.7.

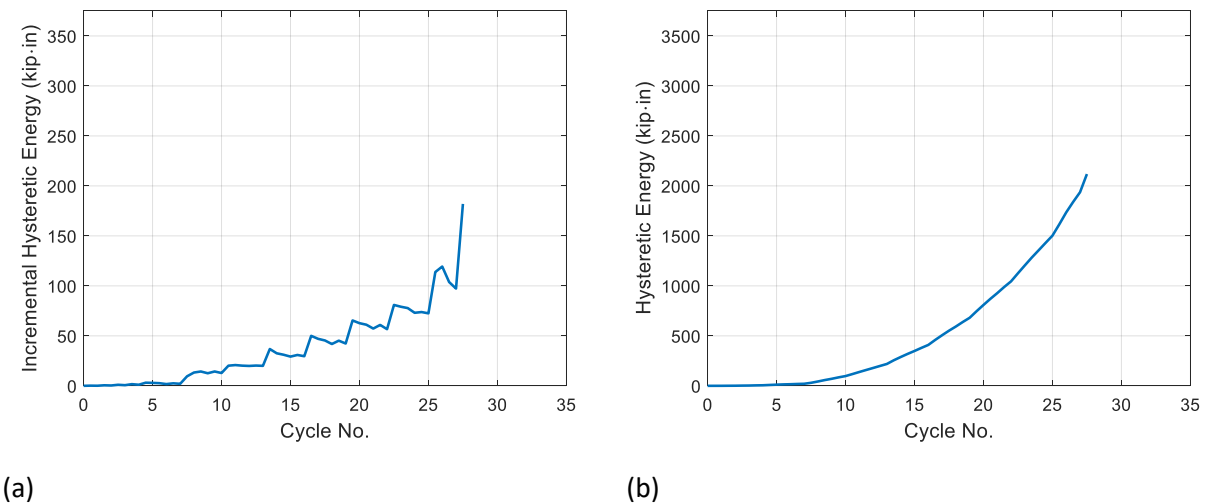


Figure 5.19: Cyclic hysteretic energy of Wall 3, calculated as area bounded by force-displacement curve for each cycle (a) incremental, and (b) cumulative (1.000 kip in = 0.113 kN m)

Figure 5.20 shows Wall 3's approach and unload stiffness versus drift. In positive flexure, the approach stiffness first decreased below a value of zero in Cycle 27 (the second cycle at 2.00 % drift ratio). By peak of the final cycle, Cycle 28 with a maximum drift ratio of 3.00 %, the approach stiffness had decreased to far below zero, indicating that failure was imminent. The approach stiffness did not decrease below zero in negative flexure, but the slope of the force-drift hysteresis was clearly negative when approaching valley in Cycle 28. However, no stiffness values were recorded for Cycle 28 in the plots in Figure 5.20 because the wall did not reach valley before failing.

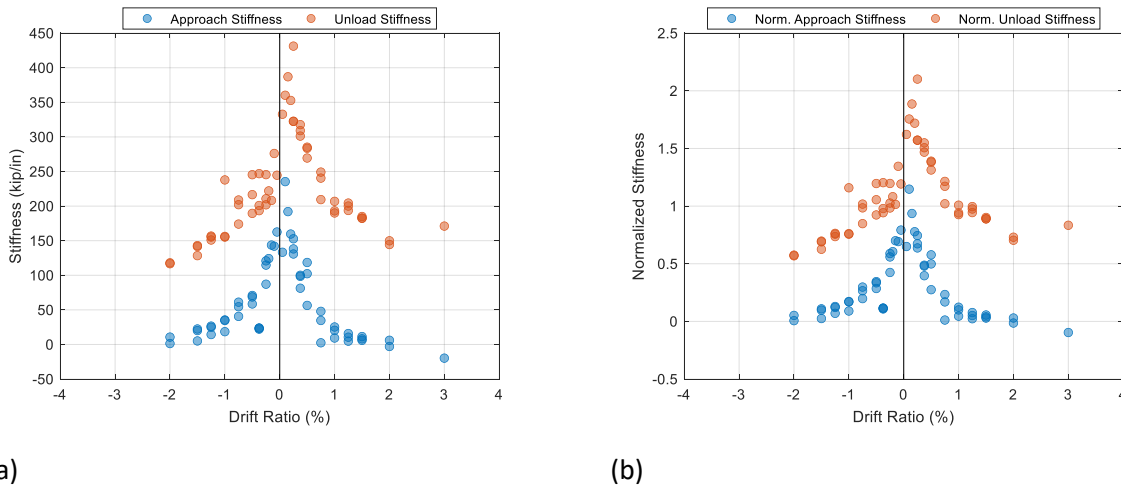


Figure 5.20: Cyclic stiffness response of Wall 3: (a) in units of kip/in (1.000 kip/in = 0.175 kN/mm), and (b) normalized by wall initial stiffness.

5.5 RESPONSE OF WALL 4

This section presents the cyclic load test results for non-reactive Wall 4 with a stirrup spacing of 4 in (102 mm) in the boundary elements, resulting in a ρ_t of 2.0 %, with no pre-existing ASR expansion or damage. Figure 5.21 shows the cyclic response of Wall 4; its lateral displacement history is plotted in Figure 5.21(a), its lateral force history is plotted in Figure 5.21(b), and its lateral force-drift response is plotted in Figure 5.21(c). The peak lateral resistance of Wall 4 in negative flexure was -104.5 kip (465 kN) at a drift ratio of -2.952 %, and its peak lateral resistance in positive flexure was +98.7 kip (439 kN) at a drift ratio of +1.903 %. As described in Chapter 3, buckling of longitudinal reinforcement in the compression zone, which was first observed at a drift ratio of 2.000 % (Cycle 27), followed by extensive spalling in the compression zone exposing the buckled longitudinal reinforcement in the boundary element, led to degradation in the wall's flexural resistance. Failure of Wall 4 was due to severe loss of flexural strength following rupture of the longitudinal bars, after achieving peak of the second cycle at 4.00 % drift and cycling back toward valley in Cycle 31. The drift ratios corresponding to 80 % of the peak flexural resistance (i.e., a 20 % degradation in flexural strength) were -4.00 and +4.00 %, respectively, in positive and negative flexure.

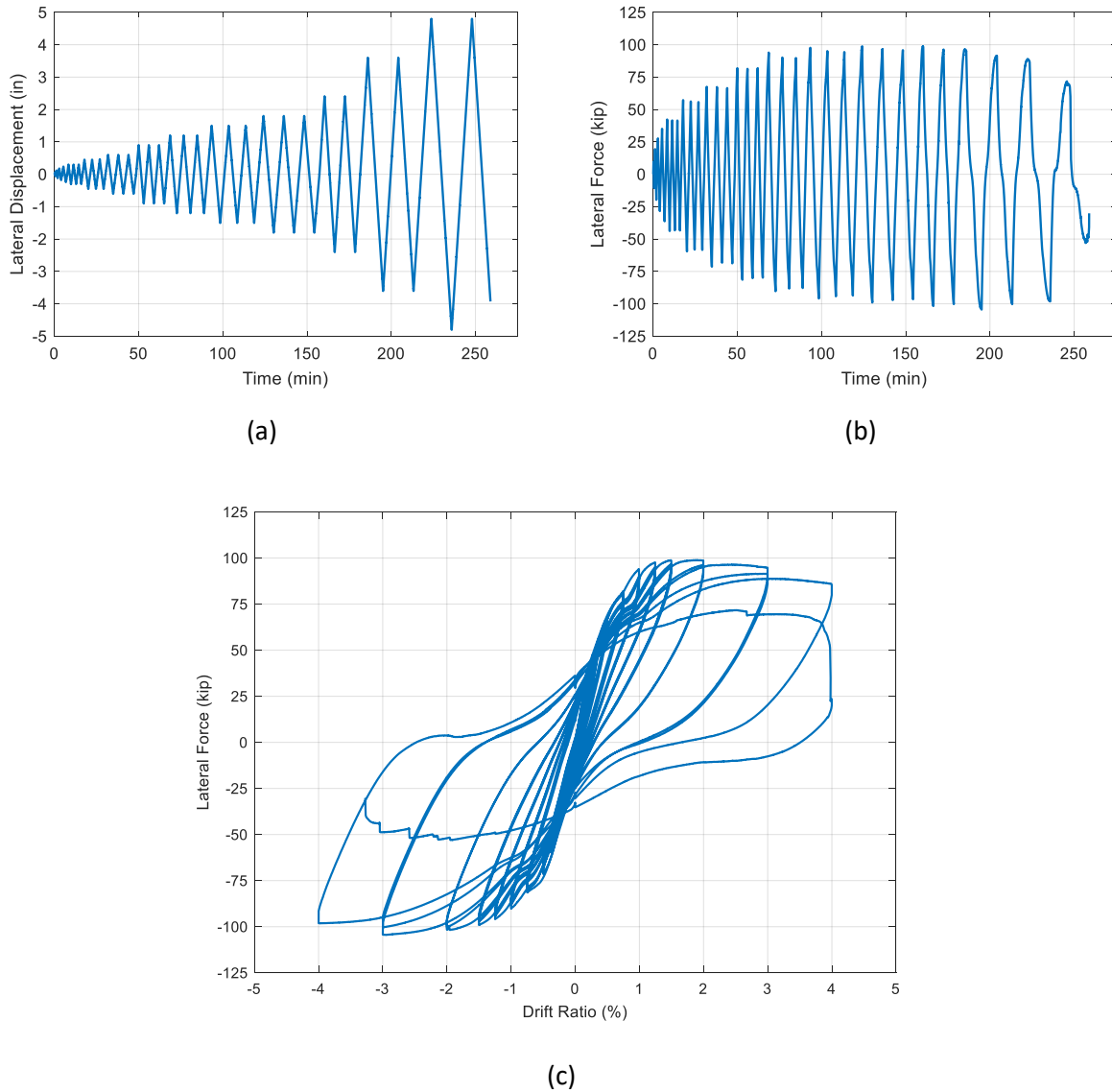


Figure 5.21: Response of Wall 4: (a) lateral displacement history, (b) lateral force history, and (c) force-drift hysteresis (1.00 in = 25.4 mm; 1.000 kip = 4.448 kN)

Figure 5.22 shows the deformations and rotations measured by point sensors up the height of the wall. Lateral deformation measurements taken by string potentiometers are shown in Figure 5.22(a), in-plane rotation measurements by inclinometers are shown in Figure 5.22(b), and in-plane lateral deformation profiles up the height of the wall are shown in Figure 5.22(c). The lateral deformation profiles in Figure 5.22(c) show that lateral deformations were nearly linear with respect to height throughout the entire test. Only at peak of the final cycle, at 4.00 % drift ratio, could a concentration of lateral deformation at the base of the wall be detected.

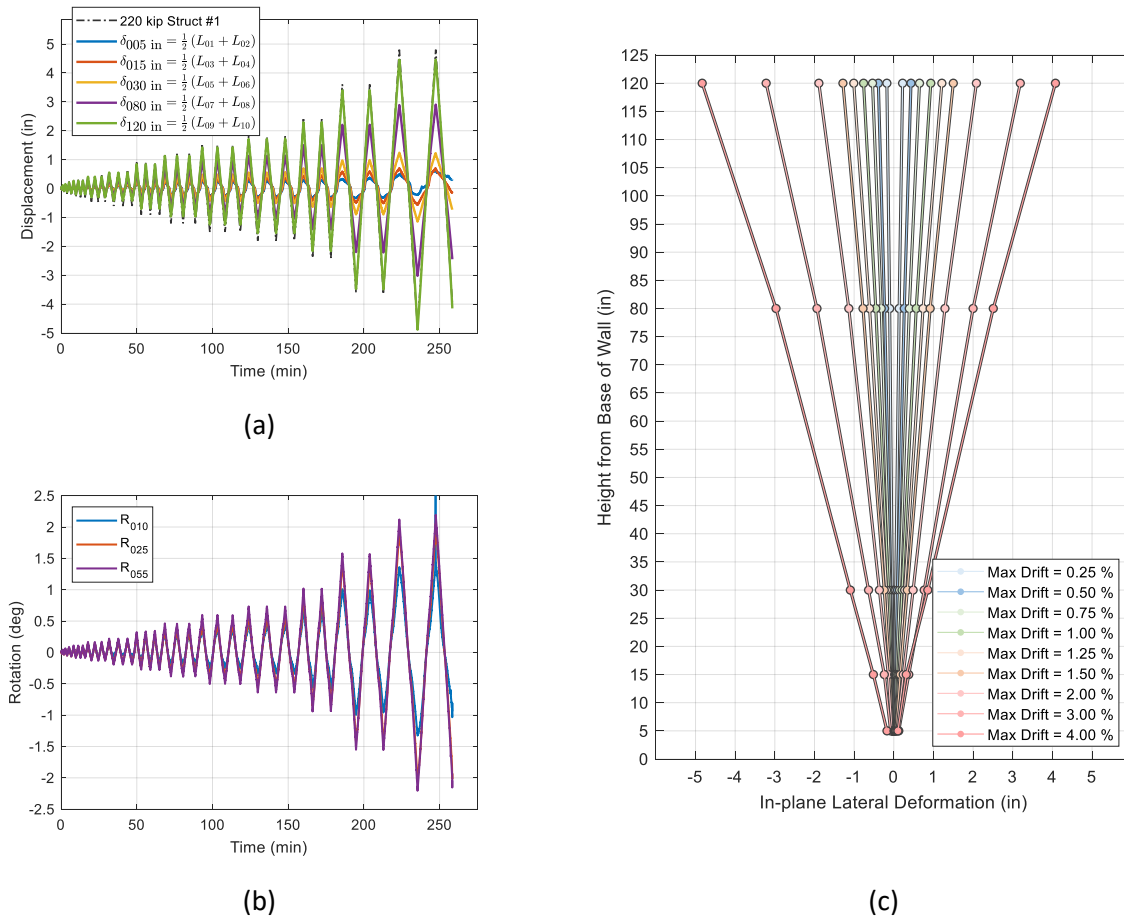


Figure 5.22: Point sensor measurements up the height of the Wall 4: (a) horizontal deformation history, (b) rotation history, and (c) in-plane lateral deformation profiles at peak/valley (1.00 in = 25.4 mm)

Figure 5.23 shows the average axial strain profiles for the longitudinal bars in the boundary elements of Wall 4. Axial strain profiles were not shown for Walls 1 through 3 because it was not possible to properly resolve the distribution of ASR-induced strains from the limited number of strain gages used to monitor wall expansion. Figure 5.23(a) shows that yielding of the north outside longitudinal bar first occurred in Cycle 14; this observation is verified in Figure 5.24(a), which shows strain histories of the gages placed on the longitudinal bars at zero height above the footing. Of the four wall specimens, Wall 4 had the most surviving strain gages at the beginning of the test and thus illustrates the clearest gradual progression of accumulated mechanical strains due to applied cyclic lateral loading. No pre-existing strain was added to the measured strain data during cyclic testing since Wall 4 was non-reactive. Like for the other wall specimens, yield was determined by finding the point at which the strain in all the longitudinal bars had first crossed the yield strain of 0.0023 in/in (0.0023 mm/mm), which for Wall 4 was in Cycle 15 (see Figure 5.24(b)). These points are circled in the plots in Figure 5.24. Yielding of the longitudinal bars in the boundary elements of the wall occurred at 55.9 min corresponding to a lateral drift ratio of 0.74 % and a moment of 9696 kip·in (1096 kN·m), or 101 % of the wall’s nominal moment capacity based on a sectional analysis of the wall. The lateral force-drift point corresponding to yield of Wall 4 is shown on its backbone

response curve in Figure 5.27, and the drift at yield and normalized yield moment are reported in Table 5.2.

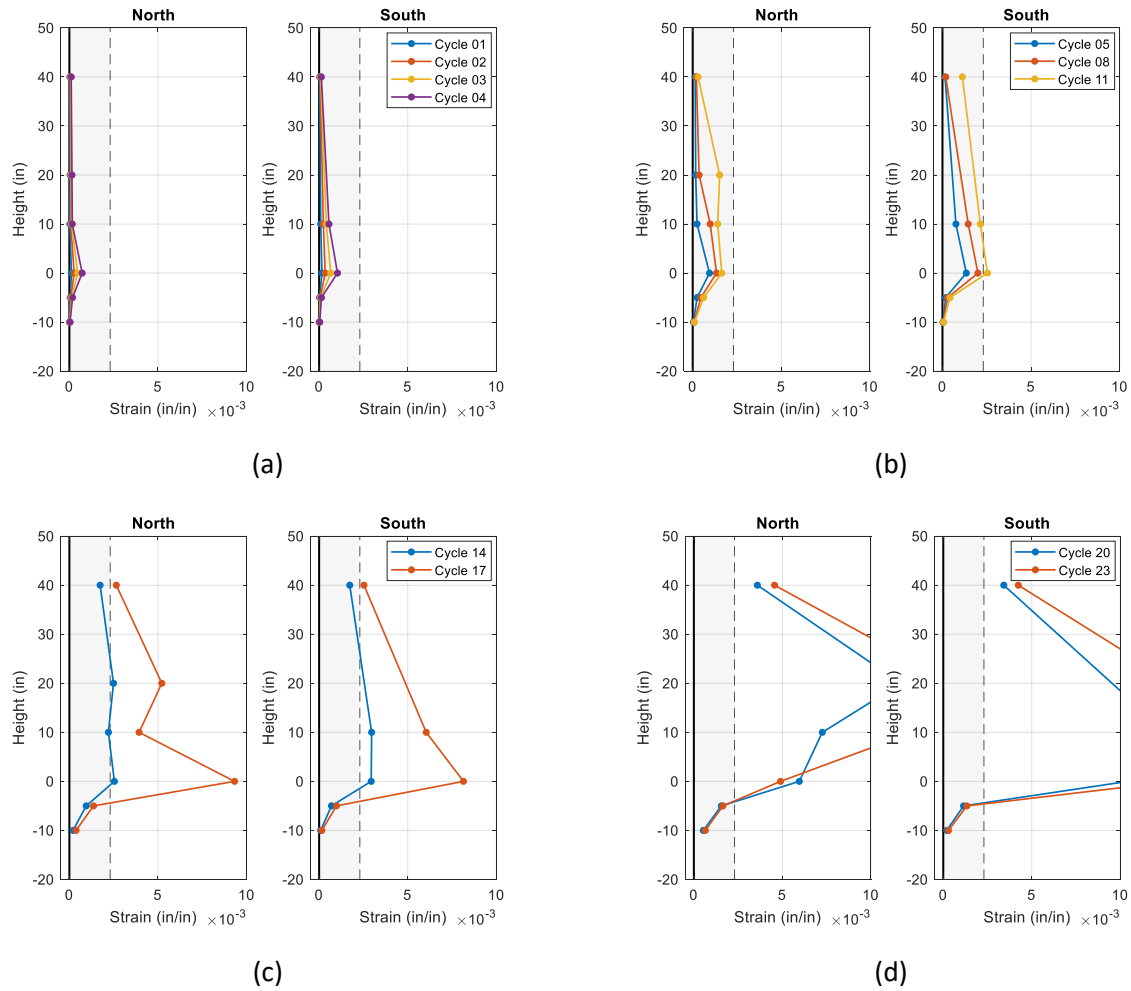


Figure 5.23: Distribution of total strains along length of north and south longitudinal rebar in boundary elements of Wall 4 at peaks/valleys during phases of loading protocol: (a) elastic, (b) immediate occupancy, (c) life safety, (d) collapse prevention (1.00 in = 25.4 mm)

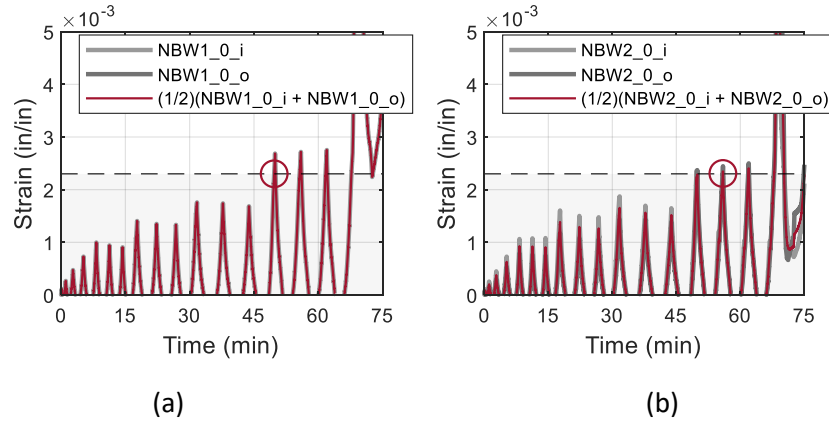


Figure 5.24: Measured strains in longitudinal bars of Wall 4 at height of 0.0 in (0.0 mm): (a) NBW1 (outer bar) and (b) NBW2 (inner bar)

Figure 5.25(a) and Figure 5.25(b) show the incremental and cumulative hysteretic energy of Wall 4, respectively. Wall 4 generally had the least per-cycle accumulation of hysteretic energy of the four walls, but achieved the highest ductility, which allowed it to dissipate the largest total amount of hysteretic energy. This observation is consistent with Wall 4 having the largest drift at yield among the four wall specimens, which meant that it began dissipating measurable amounts of hysteretic energy at later cycles than did the other specimens. This aspect of Wall 4's performance was due to its lack of ASR-induced damage and prestressing in the longitudinal bars. Direct comparisons made between the energy dissipated by the four wall specimens, provided in Section 5.7, further strengthen this observation.

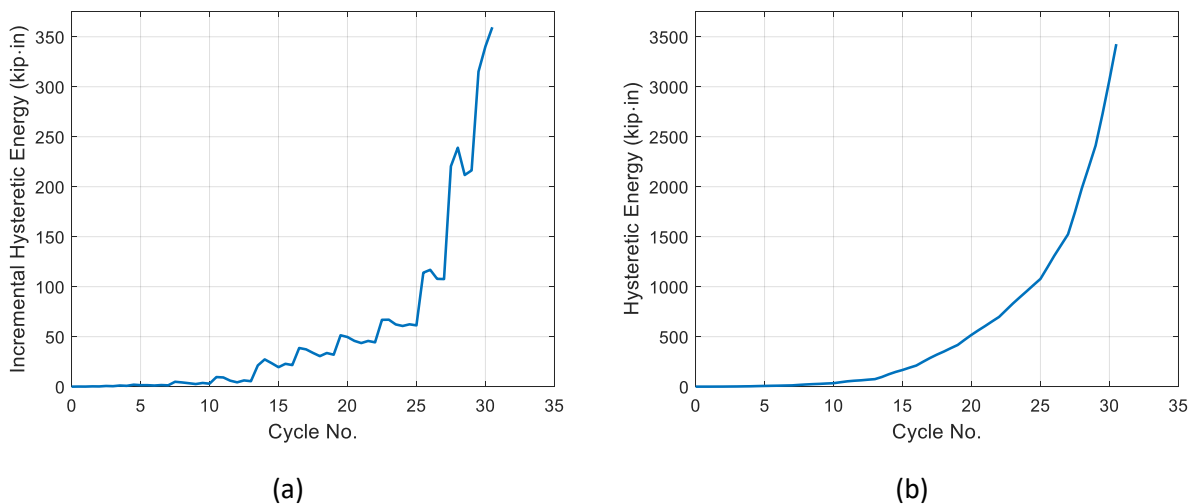


Figure 5.25: Cyclic hysteretic energy of Wall 4, calculated as area bounded by force-displacement curve for each cycle (a) incremental, and (b) cumulative (1.000 kip in = 0.113 kN m)

Figure 5.26 shows the approach and unload stiffness of Wall 4 with respect to drift ratio. Both the approach and unload stiffness generally decreased with increasing drift level. In positive flexure, the approach stiffness first decreased to below zero at peak of its second cycle at 2.00 % drift ratio (i.e., at Cycle 27) and remained negative at peak throughout the rest of the test. In negative flexure, the approach stiffness first decreased to below zero at valley of its second cycle at -3.00 % drift ratio (i.e., at Cycle 29). The approach stiffness remained negative at valley throughout the rest of the test until failure of the wall in Cycle 31.

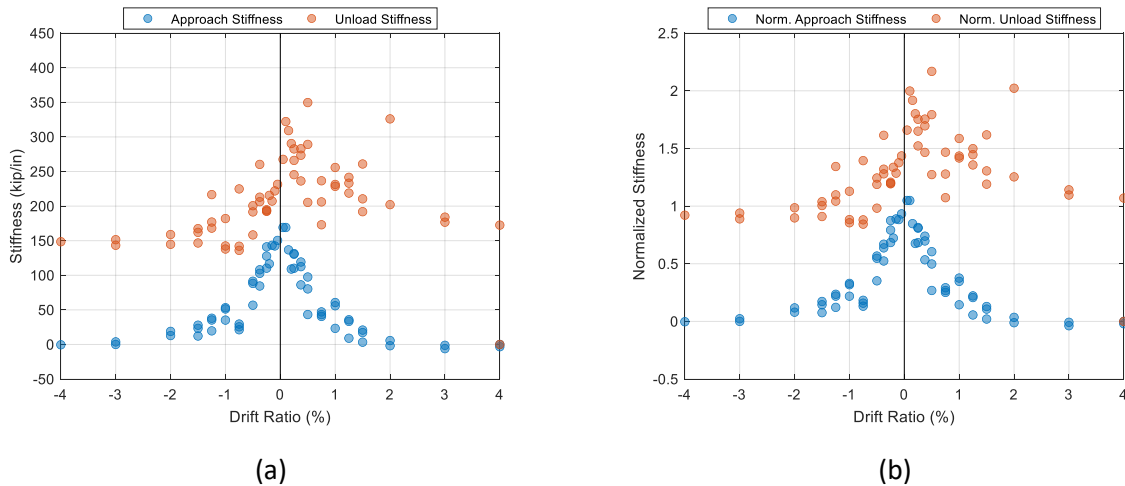


Figure 5.26: Cyclic stiffness response of Wall 4: (a) in units of kip/in (1.000 kip/in = 0.175 kN/mm), and (b) normalized by wall initial stiffness

5.6 BACKBONE RESPONSES

To facilitate comparisons between the overarching moment-drift behaviors of the four concrete shear wall specimens, a backbone response curve was calculated for each wall from its moment-drift hysteresis response in coordinates of drift ratio (%) and normalized moment M / M_n , where M_n is the nominal flexural strength calculated using sectional analysis based on ACI 318-19, 28-day concrete strength (4500 psi [31 MPa]), and nominal yield strength of reinforcement (60 ksi [413.7 MPa]). Consistent with the approach described in PEER/ATC (2010), the backbone response curves of the walls were taken as the cyclic envelopes enclosing the forces and deformations, under cyclic loading protocol (Figure 5.27). In each plot in Figure 5.27, the backbone response curve is shown as a thick solid blue line overlaying the wall's normalized hysteresis, which is depicted as a thin light grey line. The backbone response curve bounds the wall's hysteretic response and defines the peak flexural resistance of each wall at a given drift ratio. For each wall specimen the absolute peak flexural resistance in negative and positive flexure is depicted by a purple and green circular marker, respectively. Also shown in each of the plots in Figure 5.27, by the red solid circular marker, is the yield point of each wall specimen. Each yield point corresponds to a coordinate pair of drift at yield and yield moment. The notation used for the coordinates of the yield point, peak flexural resistance in negative and positive flexure, ultimate flexural resistance

and drift ratio, and ductility was adapted from ACI 318-19 (see Figure 5.28); their values are reported in Table 5.1.

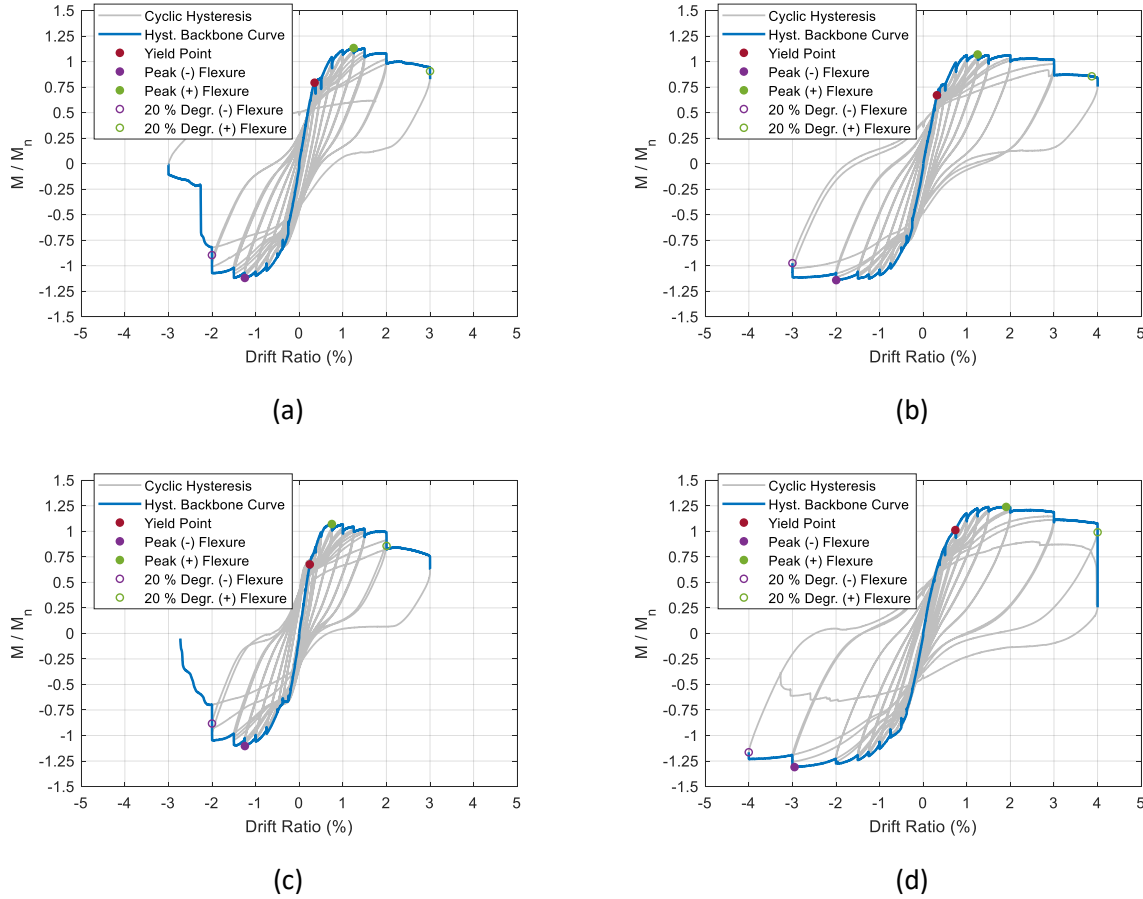


Figure 5.27: Backbone response curves (M/M_n versus drift ratio) for: (a) Wall 1, (b) Wall 2, (c) Wall 3, and (d) Wall 4.

As shown in Figure 5.28, the yield point of the wall has coordinates $(d_y, M_y/M_n)$, where d_y is the drift ratio at yield, M_y is the yield moment, and M_n is the nominal flexural capacity of the wall using sectional analysis of the wall according to ACI 318-19. Yield always first occurred in positive flexure (i.e., at a positive value of drift ratio), because the positive-flexure portion of each cycle was applied first in the loading protocol. The peak flexural resistance of the wall in negative and positive flexure has coordinates $(d_{M_{max}^-}, M_{max}^-/M_n)$ and $(d_{M_{max}^+}, M_{max}^+/M_n)$ where $d_{M_{max}^-}$ and $d_{M_{max}^+}$ are the drift ratio at the maximum moment in negative and positive flexure, respectively, and M_{max}^- and M_{max}^+ are values of maximum moment negative and positive flexure, respectively. A value of $0.80M_{max}^-/M_n$ or $0.80M_{max}^+/M_n$ corresponds to a 20 % loss of flexural strength in negative or positive flexure, respectively. The drift ratios corresponding to a 20 % strength loss in negative and positive flexure are denoted as d_u^- and d_u^+ , respectively. As previously described, failure of the walls was defined by occurrence of a failure mode leading to catastrophic strength loss. The value d_{fail} refers to the drift at failure (i.e., the ductility of the wall). Also schematically shown in Figure 5.28 is

calculation of the initial stiffness according to ACI 318-19 (i.e., taking the initial stiffness as the slope of the linear regression of the backbone response curve data below a value of $0.25M_{\max}^+ / M_n$).

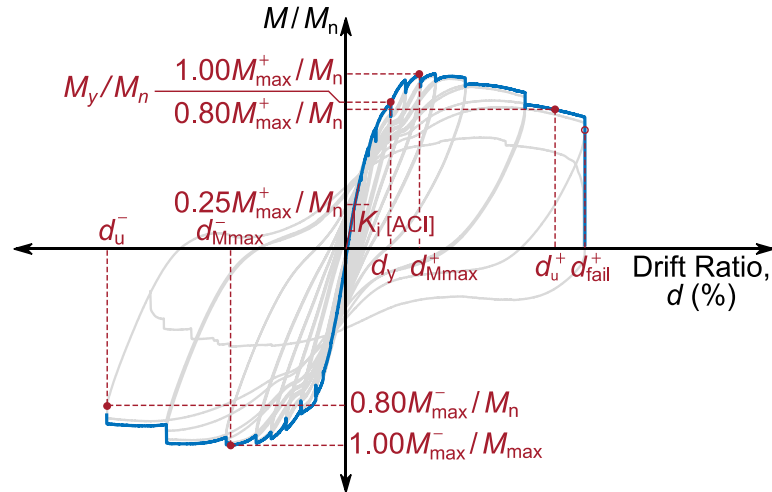


Figure 5.28: Adopted notation for coordinates of key points on wall backbone response curve.

5.7 SUMMARY QUANTITIES AND DIRECT COMPARISONS BETWEEN WALL RESPONSES

A number of useful observations can be made by direct comparisons of the responses of two or more wall specimens. These initial observations are further supported by the statistical analyses presented in Chapter 6, which are used to quantify trends based on simultaneous consideration of the responses of all four wall specimens. Table 5.1 presents a summary of key wall response variables, including e.g., peak drift (i.e., ductility), cumulative drift capacity (calculated as the sum of all drift ratios applied to the wall up to the point of wall failure), peak flexural capacity in both positive and negative flexure, yield moment, and cumulative hysteretic energy. Wall 4 had the largest normalized flexural resistance in both positive and negative flexure, achieving moments in positive and negative flexure that were 23.8 % and 31.1 % larger, respectively, than its nominal flexural capacity M_n . Wall 4 also had the largest yield moment among the four walls, achieving 101 % of its nominal flexural capacity at yield, and the largest cumulative hysteretic energy.

Table 5.1. Summary of wall response quantities in negative (-) and positive (+) flexure

Summary Quantity	Wall 1	Wall 2	Wall 3	Wall 4
d_y , %	0.35	0.31	0.24	0.74
M_y , kip·ft (kN·m)	632.5 (857.5)	534.7 (724.9)	539.3 (731.2)	807.6 (1095)
M_y/M_n	0.79	0.67	0.68	1.01
d_{Mmax}^+ , %	1.248	1.249	0.748	1.903
M_{max}^+ , kip·ft (kN·m)	903.0 (1224) ¹	852.7 (1156) ¹	854.5 (1159) ¹	987.3 (1339) ¹
M_{max}^+/M_n	1.132 ²	1.069 ²	1.071 ²	1.238 ²
d_u^+ , %	3.00	3.87	2.00	4.00
d_{Mmax}^- , %	-1.248	-1.996	-1.247	-2.952
M_{max}^- , kip·ft (kN·m)	893.4 (1211) ¹	910.4 (1234) ¹	880.3 (1194) ¹	1045.6 (1418) ¹
M_{max}^-/M_n	1.120 ²	1.141 ²	1.104 ²	1.311 ²
d_u^- , %	-2.00	-3.00	-2.00	-4.00
d_{fail} , %	3.00	4.00	3.00	4.00
Cumulative drift capacity, %	97.5	117.5	91.5	133.5
Total hysteretic energy, kip-in (kN·m)	2300.6 (259.9)	2864.4 (323.6)	2118.6 (239.4)	3426.6 (387.2)

¹ The peak flexural resistance was calculated as the peak lateral load multiplied by the height of the wall from its base to the point of application of lateral loading which was 10 ft (3.05 m).

² Calculated as the ratio of moment at peak load to wall nominal moment capacity M_n of 797.7 kip ft (1081.5 kN m)

Among the three reactive walls (Walls 1, 2, and 3), Wall 2 with the higher transverse reinforcement ratio ρ_t of 2.0 % (relative to the smaller transverse reinforcement ratio of 0.5 % in Walls 1 and 3) had the largest ductility (peak drift, d_{fail}), cumulative drift capacity, and cumulative hysteretic energy. These results show the key performance advantages of having a higher degree of confinement in the boundary elements. The flexural capacities of Walls 1, 2, and 3 were somewhat similar, their peak flexural resistances falling within 5 % of one another.

Walls 2 and 4 both had a ductility of 4.00 %. Even though Walls 2 and 4 achieved the same level of ductility, it is important to note that non-reactive Wall 4 failed during the second cycle at 4.00 % drift ratio, while reactive Wall 2 failed in the first cycle. This difference is observable by comparing their cumulative drift capacity, in which Wall 4 had the larger value between the two specimens. A Similar observation can be made with respect to Walls 1 and 3, which both had a ductility of 3.00 %. Wall 1 had a larger cumulative drift capacity because it failed farther into Cycle 28 than did Wall 3.

Table 5.1 indicates that the normalized yield moment, M_y/M_n , for the three ASR-affected walls (Wall 1, 2, and 3), were significantly less than unity (the values ranged from 0.67 to 0.79). This indicates that none of the ASR-affected walls met the ACI 318-19 design criteria, which is based on yielding of the longitudinal bars. ACI determines yield by sectional analysis, Using f'_c of 4500 psi and $f_y = 60$ ksi. Note that the sectional analysis of the walls indicated successive yielding of the longitudinal bars in the boundary elements in addition to some of the longitudinal bars in the web between the boundary elements. The yield moments, M_y , presented in Table 5.1 corresponded to yielding of the bars in the boundary elements only as no strain

gages were installed in the web. Thus, the values of the normalized yield moment, M_y/M_n might be slightly higher than those reported in Table 5.1, but will undoubtedly remain significantly smaller than unity.

To further facilitate comparisons between the responses of the four walls, Table 5.2 presents a similar summary table as was shown in Table 5.1, but with the value in each cell divided by the measured value from the reference, non-reactive Wall 4. Since Wall 4 generally had the largest value of each of the measured response quantities, the values in Table 5.2 can be thought of as representing the percentage of each summary quantity achieved, divided by 100, relative to the response of Wall 4. For example, by looking at their values of cumulative drift capacity, Walls 1, 2, and 3 would be observed to have reached 73.0 %, 88.0 %, and 68.5 % of the cumulative drift achieved by Wall 4. By examining the values associated with their yield points (yield moment and drift at yield moment), this format facilitates making a key observation of the influence of the ASR-induced pre-strain in the longitudinal bars on the flexural response of the reactive specimens. ASR-induced pre-strain in the longitudinal bars led to flexural yield at lower drift levels and lower yield moments. The average drift at yield of Walls 1 through 3 was only 40.5 % of that of Wall 4 and their average yield moment was only 70.4 % of that of Wall 4.

Table 5.2. Summary of wall response quantities in negative (-) and positive (+) flexure, normalized by the responses of the Wall 4, which did not have ASR

Summary Quantity	Wall 1	Wall 2	Wall 3	Wall 4
d_y	0.473	0.419	0.324	1.000
M_y	0.783	0.662	0.668	1.000
d_{Mmax}^+	0.656	0.656	0.393	1.000
M_{max}^+	0.915	0.864	0.865	1.000
d_u^+	0.750	0.968	0.500	1.000
d_{Mmax}^-	0.423	0.676	0.422	1.000
M_{max}^-	0.854	0.871	0.842	1.000
d_u^-	0.500	0.750	0.500	1.000
d_{fail} , %	0.750	1.000	0.750	1.000
Cumulative drift capacity	0.730	0.880	0.685	1.000
Total hysteretic energy	0.709	0.882	0.653	1.000

Non-reactive Wall 4 had the largest drift at its peak flexural capacity in both negative and positive flexure. This implies that, at a given drift ratio, damage at the base of the wall and in the boundary elements was less severe in the non-reactive Wall 4 than in the reactive Walls 1 through 3 because it did not lead to degradation in flexural resistance until cycles at larger drift ratios. This observation is corroborated by Figure 5.39, which compares the relative rotations of the four walls up their heights and is indicative of the ASR-induced damage that pre-existed in the reactive walls prior to seismic testing. The peak flexural resistance of Wall 4 in positive flexure was reached just before nearly 90 % of the rotation became localized below a height of 55.0 in (1397 mm) above the base of the wall.

The backbone response curves of the walls, described in Section 5.6, further facilitate consideration of two key wall response variables: their initial (i.e., elastic) flexural stiffness and the areas under the elastic

and inelastic portions of their envelopes. For consistency with the methodology used to measure the elastic stiffness of concrete materials in the Task 1 report (Sadek et al., 2021) and the initial flexural stiffness of ASR-affected reinforced concrete beams in the Task 2 report (Thonstad et al., 2021), the initial stiffness of the walls was calculated as the slope of the least-squares linear regression of the wall lateral force-displacement data between 10 % and 40 % of the load at peak of the initial elastic cycle (i.e., Cycle 01). These values of initial stiffness are shown in Table 5.3 under the heading “Initial Flexural Stiffness.” The initial stiffness of the walls was also calculated following the convention used in the ACI wall database, in which the initial stiffness is fitted as the slope of the linear regression of the lateral force-displacement envelope below $0.25M_{max}^*$. The ACI definition of initial stiffness is also reported in Table 5.3 under the column heading “Initial Flexural Stiffness [ACI].”

Table 5.3. Concrete shear wall specimen initial stiffness (in units of lateral force divided by lateral displacement) and elastic and inelastic areas in negative (-) and positive (+) flexure

Wall Specimen	Initial Flexural Stiffness	Initial Flexural Stiffness [ACI]	Elastic Area		Inelastic Area	
			(- Flexure)	(+ Flexure)	(- Flexure)	(+ Flexure)
	kip/in (kN/m)	kip/in (kN/m)	kip-ft (kN·m)	kip-ft (kN·m)	kip-ft (kN·m)	kip-ft (kN·m)
Wall 1	186.5 (32660)	193.5 (33890)	128.1 (173.6)	121.1 (164.2)	1624.4 (2202.4)	2150.3 (2915.5)
Wall 2	163.4 (28620)	171.7 (30070)	96.6 (130.9)	84.2 (114.1)	2283.5 (3096.0)	2832.5 (3840.3)
Wall 3	205.2 (35940)	217.3 (38060)	68.9 (93.4)	65.9 (89.4)	1657.1 (2246.7)	2042.8 (2769.6)
Wall 4	161.3 (28250)	191.7 (33570)	393.7 (533.8)	376.9 (510.9)	3186.3 (4320.0)	3037.5 (4118.4)

Table 5.3 shows no clear distinction between the initial stiffness values of reactive Walls 1 through 3 and non-reactive Wall 4. However, the initial stiffness of reactive Walls 1 through 3 was not less, on average, than that of non-reactive Wall 4. Using either (this report’s or ACI’s) measure of wall initial flexural stiffness, Wall 3 had the highest initial stiffness among the four wall specimens and Wall 1 had the second highest. The ranking between the initial stiffness of Walls 2 and 4 depended on which measure was used.

The elastic and inelastic areas under the backbone curve are also reported in Table 5.3 because they are also useful in formulating reduced-order models of concrete shear wall flexural behavior. As is shown in Figure 5.29 by the example backbone curve with and elastic and inelastic areas calculated in both negative (-) and positive (+) flexure, the value of drift at the yield moment delineates the elastic drift from the inelastic drift. Each of the four areas in Figure 5.29 was calculated by numerical integration using the trapezoidal method with nonuniform spacing determined by the drift coordinates of the backbone response curve.

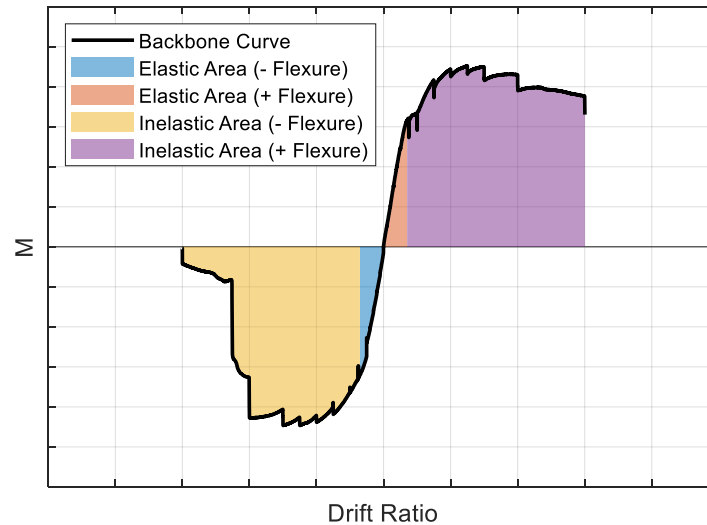


Figure 5.29: Example of backbone curve with elastic and inelastic areas calculated in both negative (-) and positive (+) flexure. 1.000 kip·ft = 1.356 kN·m.

The elastic and inelastic areas under the backbone curve of each of the four wall specimens in both negative (-) and positive (+) flexure are shown in Figure 5.30, and their corresponding values are reported, in units of force multiplied by length, in Table 5.3. Inspection of the elastic areas in Table 5.3 reveals that reactive Walls 1 through 3 consistently had less elastic area in either negative or positive flexure. This is consistent with observations made in Sections 5.2 through 5.4 that the onset of inelasticity in reactive Walls 1 through 3 was earlier than in non-reactive Wall 4 – an effect which was attributed to the ASR-induced pre-strain in reactive Walls 1 through 3, that led to yielding in the longitudinal bars at lower magnitude drift ratios. Table 5.3 also shows that non-reactive Wall 4 had the largest inelastic area in negative and positive flexure among the four wall specimens. This was due both to it having the greatest flexural resistance among the four walls specimens and the larger ductility (Walls 1 and 3 had a ductility of 3.000 % drift ratio while Walls 2 and 4 had a ductility of 4.000 % drift ratio).

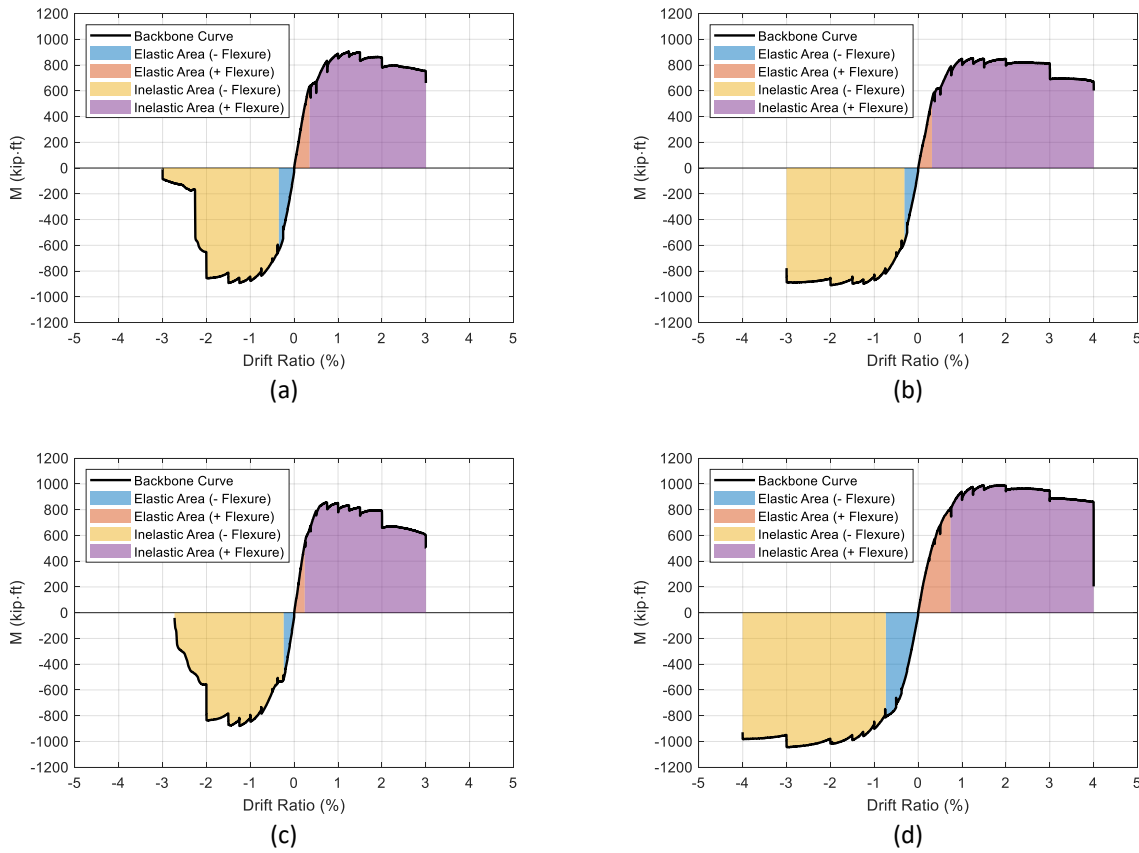


Figure 5.30: Comparison of backbone curve with and elastic and inelastic areas calculated in both negative (-) and positive (+) flexure for (a) Wall 1, (b) Wall 2, (c) Wall 3, and (d) Wall 4. 1.000 kip-ft = 1.356 kN-m.

5.7.1 Wall 2 and Wall 4 – Isolated Influence of ASR

Figure 5.31(a) shows a comparison between the normalized moment-drift hysteresis of Walls 2 and 4, while Figure 5.31(b) presents the backbone curve for both walls. Walls 2 and 4 differed only in that Wall 2 had ASR-affected concrete while Wall 4 had non-reactive concrete. Both walls had a transverse reinforcement ratio ρ_t of 2.0 %, corresponding to a nominal hoop spacing in their boundary elements of 4.00 in (102 mm).

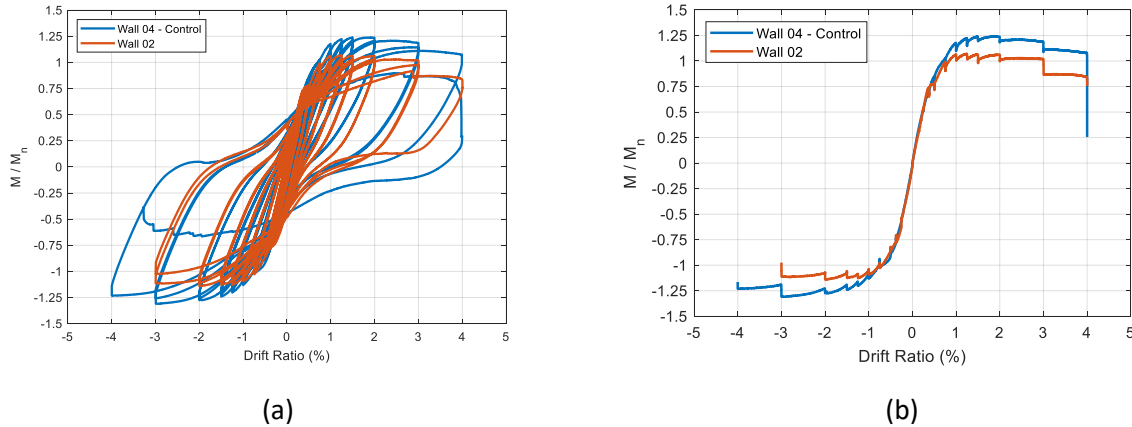


Figure 5.31: Comparison between normalized responses of Walls 2 and 4 (a) cyclic hysteresis, and (b) backbone curves

At relatively small drift ratios, the backbone responses of Walls 2 and 4 were similar, with their initial stiffnesses nearly the same at respective values of 163.4 kip/in (28.62 kN/mm) and 161.3 kip/in (28.25 kN/mm). The observation that the initial stiffness of Wall 2 was not less than that of Wall 4 further supports a key conclusion made by the ASR Task 2 report (Thonstad et al., 2021) – that, provided there is adequate confinement, the presence of ASR does not adversely affect the stiffness of structural components such as beams or walls despite the significant reduction in the concrete’s elastic modulus (see Section 4.1.2), due likely to the prestressing effect as a result of the confining reinforcement. After reaching drift ratios of 0.25 % (i.e., at the onset of inelasticity in the wall flexural response), the flexural backbone response of Wall 2 began to diverge from that of Wall 4. The normalized moments (in the inelastic range of their flexural backbone responses) of Wall 2 were, on average, about 20 % less than those of Wall 4. The average value of the measured compressive strength of Wall 2 on the day of testing (582 days for Wall 2 and 378 days for Wall 4, see Table 4.1) was only 52.9 % of that of Wall 4, and may have contributed to the decrease in flexural strength observable in Figure 5.31.

Several interesting observations can also be made by comparing the incremental and cumulative hysteretic energy between the two specimens. The incremental hysteretic energy of the two specimens followed similar trends (Figure 5.32(a)), with reactive Wall 2 consistently dissipating more hysteretic energy per cycle than non-reactive Wall 4 up to Cycle No. 27. Within the cumulative hysteretic energy plot (Figure 5.32(b)) this trend is seen as a widening gap between the curves up to Cycle No. 27. However, Wall 2 dissipated less hysteretic energy near the end of the loading protocol, failing partway through Cycle 29, while its additional ductility allowed Wall 4 to dissipate additional hysteretic energy up partway through Cycle 30. This single cycle of additional ductility capacity permitted the cumulative hysteretic energy dissipated by Wall 4 to surpass that of Wall 2; the total cumulative hysteretic energy dissipated by Wall 2 and Wall 4 was 2864.4 kip·in (323.6 kN·M) and 3426.6 kip·in (387.2 kN·M), respectively.

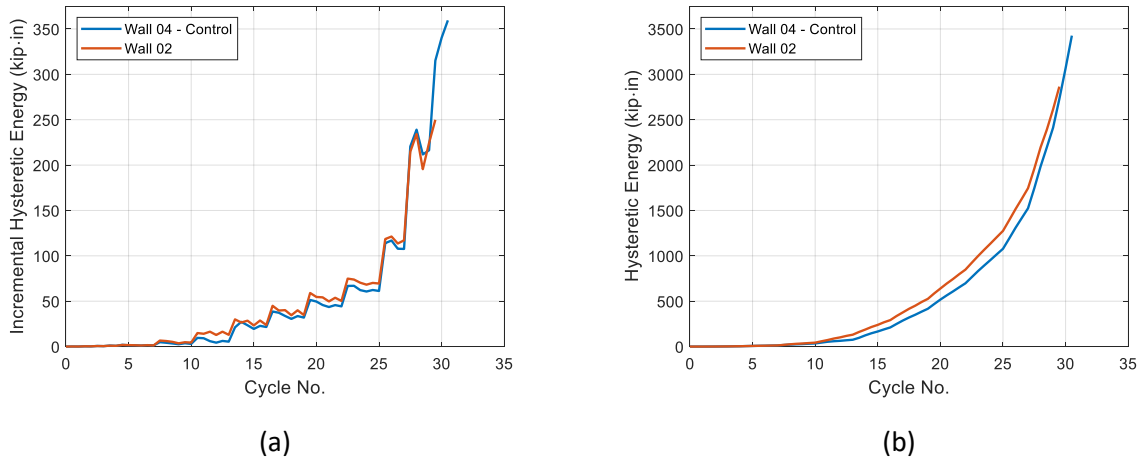


Figure 5.32: Comparison of hysteretic energy between Walls 2 and 4 (a) incremental, and (b) cumulative (1.000 kip in = 0.113 kN m)

5.7.2 Wall 1 and Wall 2 – Isolated Influence of Transverse Reinforcement Ratio

Figure 5.33(a) shows a comparison between the normalized moment-drift hysteresis of reactive Walls 1 and 2. Wall 1 had a lesser transverse reinforcement ratio ρ_t of 0.5 %, corresponding to a nominal hoop spacing in their boundary elements of 16.0 in (406 mm), while Wall 2 had a larger transverse reinforcement ratio ρ_t of 2.0 %, corresponding to a nominal hoop spacing in their boundary elements of 4.00 in (102 mm). Although barely noticeable in their backbone response curves, the initial stiffness of Wall 1 (of 186.5 kip/in [32.66 kN/mm]), was 14 % larger than that of Wall 2 (of 163.4 kip/in [28.62 kN/mm]). Following the onset of flexural inelasticity at about 0.25 % drift, the backbone curves were within 7 % of one another until the capacity of Wall 1 began degrading faster than that of Wall 2 beginning at 1.50 % drift. Taken together, the difference between the hysteresis response and the backbone curve of the two walls was relatively minor.

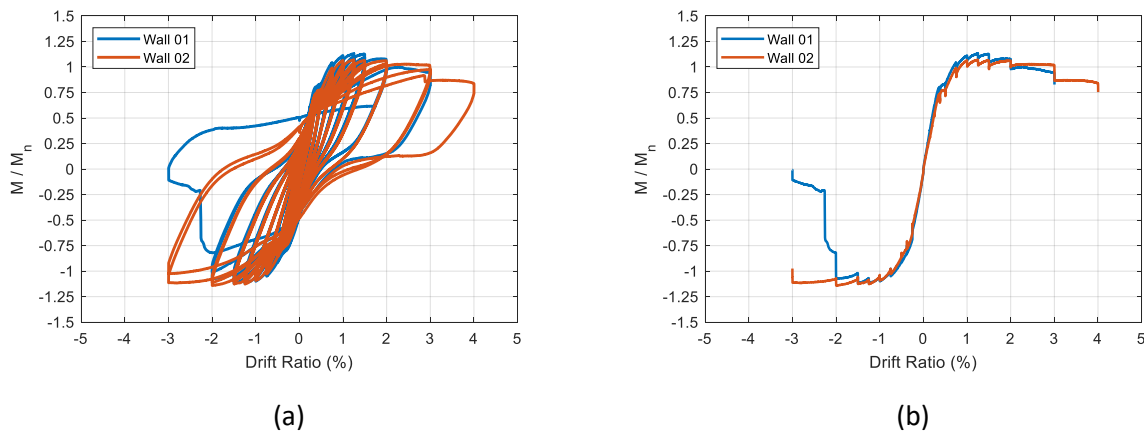


Figure 5.33: Comparison between normalized responses of Walls 1 and 2 (a) cyclic hysteresis, and (b) backbone curves

Direct comparison of the incremental hysteretic energy of Walls 1 and 2 (Figure 5.34(a)) shows that the per-cycle energy dissipated by the two specimens was also similar. Wall 1, on average, dissipated only slightly more hysteretic energy than did Wall 2, at least up until the beginning of Cycle No. 25. The cumulative hysteretic energy curves of these two specimens, shown in Figure 5.34(b), were again similar. Wall 1 dissipated slightly more cumulative hysteretic energy than did Wall 2 up until it failed at the end of Cycle 28. Because Wall 2 had a larger cumulative drift capacity, and did not fail until partway through Cycle 30, it dissipated more hysteretic energy overall than did Wall 1.

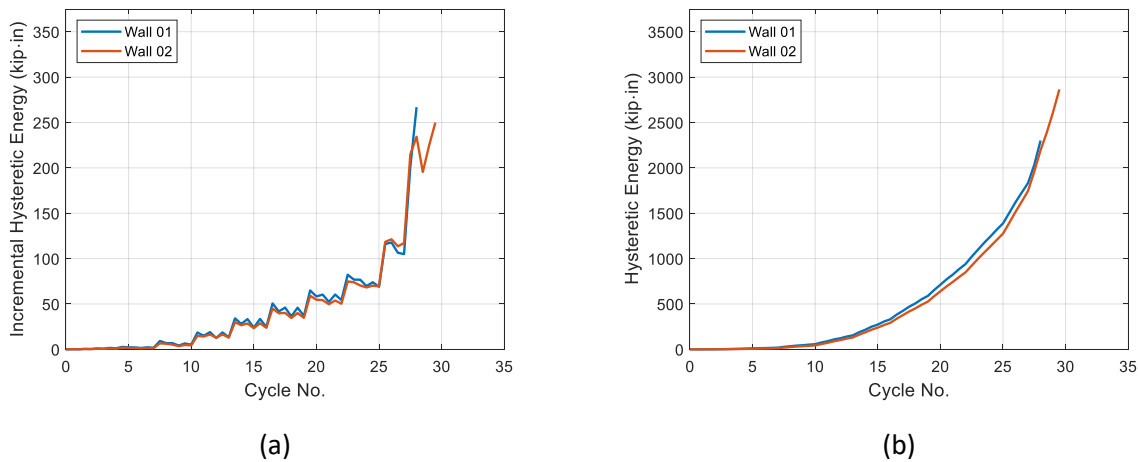


Figure 5.34: Comparison of hysteretic energy between Walls 1 and 2 (a) incremental, and (b) cumulative (1.000 kip in = 0.113 kN m)

Based on the data shown in Table 5.1, the most significant difference between the performance of reactive Walls 1 and 2 was in their ductility and cumulative drift capacity, where Wall 2 exhibited larger ductility (4 % for Wall 2 versus 3 % for Wall 1) and higher cumulative drift capacity (117.5 % for Wall 2 versus 97.5 % for Wall 1). The more ductile behavior of Wall 2 is attributed to its larger confinement in the boundary element.

5.7.3 Wall 1 and Wall 3 – Replicate Specimens

Walls 1 and 3 are considered to be replicate specimens, i.e., both have the presence of ASR and a transverse reinforcement ratio ρ_t of 0.5 %. Figure 5.35(a) shows a comparison between the normalized moment-drift hysteresis of reactive Walls 1 and 3, and Figure 5.31(b) shows a comparison of their backbone response curves. The initial stiffness of Walls 1 and 3 differed by about 10 %; their respective initial stiffness values were 186.5 kip/in and 205.2 kip/in. Between drift ratios of ± 2.00 %, the specimens' peak flexural responses, represented by their backbone curves, differed by as much as 18 %, with Wall 1 having the larger strength. Both walls showed signs of substantial damage resulting from spalling of

concrete in the compression zone beginning at drift ratios of $\pm 2.00\%$, after which their flexural resistance substantially decreased. Both walls achieved a ductility of 3.00% , but Wall 1 had a larger cumulative drift capacity of 97.5% compared with 91.5% for Wall 3.

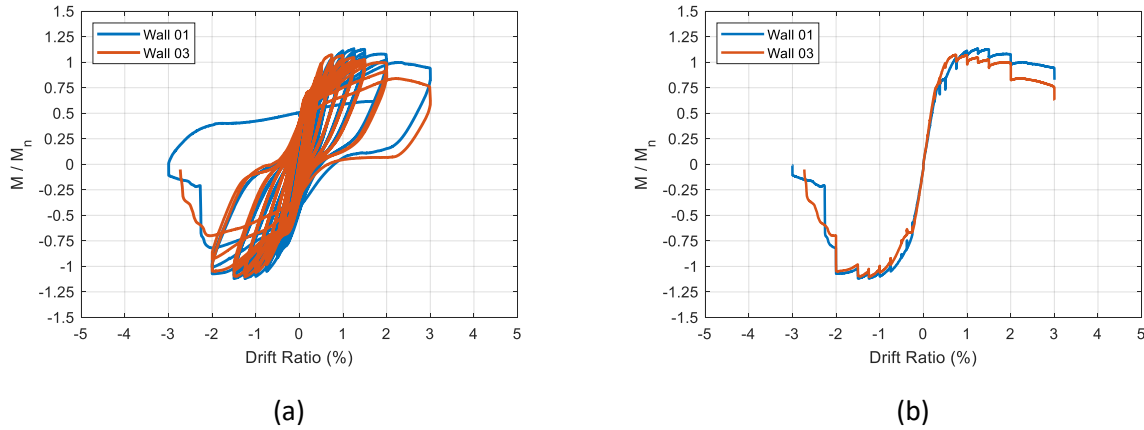


Figure 5.35: Comparison between normalized responses of Walls 1 and 3 (a) cyclic hysteresis, and (b) backbone curves

As might be expected for replicate specimens, a comparison of the incremental hysteretic energy of Walls 1 and 3 in Figure 5.36(a) shows that their per-cycle dissipated hysteretic energy was similar, with Wall 3 dissipating, on average, only slightly more hysteretic energy than Wall 1. Their cumulative hysteretic energy curves (Figure 5.38(b)) were also similar. Wall 3 dissipated slightly more hysteretic energy than did Wall 1 up until their final cycle (Wall 3 failed partway through Cycle 28 while Wall 1 failed at the end of Cycle 28), when the cumulative hysteretic energy dissipated by Wall 1 surpassed that of Wall 3. This demonstrates the strong correlation between cumulative drift capacity and total hysteretic energy dissipated: although Wall 3 generally had larger per-cycle hysteretic energy in nearly every cycle throughout their loading histories, Wall 1 still dissipated a larger total hysteretic energy because it completed Cycle 28 prior to failure, while Wall 3 failed before completion of Cycle 28.

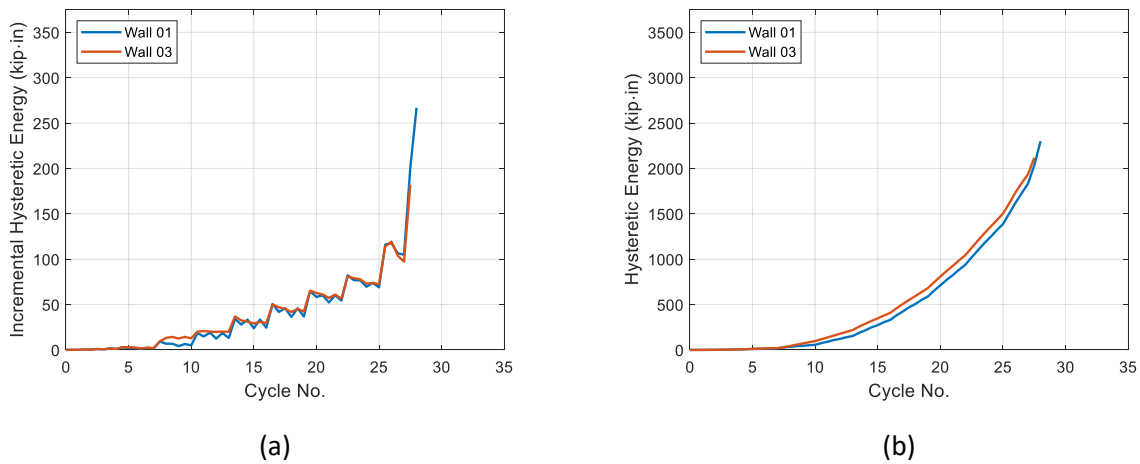


Figure 5.36: Comparison of hysteretic energy between Walls 1 and 3 (a) incremental, and (b) cumulative (1.000 kip in = 0.113 kN m)

5.7.4 Walls 1, 2, 3, and 4

A final set of direct comparisons includes all four wall specimens. Figure 5.37 shows (a) the normalized moment-drift hysteresis and (b) the backbone curves for reactive Walls 1, 2, and 3 along with non-reactive Wall 4. Walls 1 and 3 had a transverse reinforcement ratio ρ_t of 0.5 % (with corresponding hoop spacing in their boundary elements of 16.0 in [406 mm]), while Walls 2 and 4 had a transverse reinforcement ratio of 2.0 % (with corresponding hoop spacing in their boundary elements of 4.00 in [101 mm]). As shown by Figure 5.37(b), non-reactive Wall 4 clearly had the highest flexural resistance beyond a drift ratio of ± 1.00 % with a peak normalized flexural resistance near ± 1.25 , while the backbone response curves of the three reactive walls were somewhat grouped together nearer a peak normalized flexural resistance of ± 1.00 .

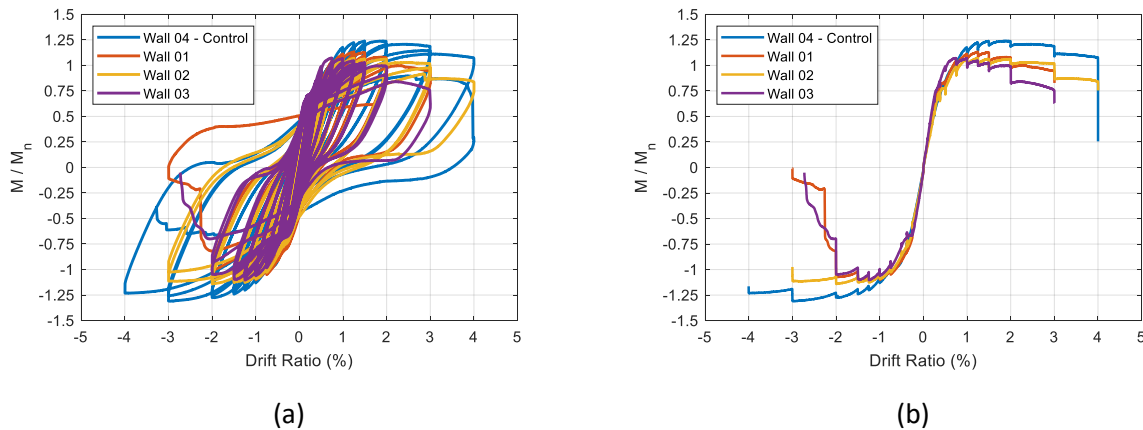


Figure 5.37: Comparison between normalized responses of Walls 1, 2, 3, and 4 (a) cyclic hysteresis, and (b) backbone curves

Figure 5.38(a) shows a comparison of the incremental hysteretic energy of all four wall specimens, and Figure 30(b) shows a comparison of their cumulative hysteretic energy curves. The most interesting observations can be made by comparing the curves of non-reactive Wall 4 to those of reactive Walls 1 through 3. On a per-cycle basis, Wall 4 generally dissipated the least energy among the four wall specimens, as is shown by Figure 5.40(a). However, Wall 4's larger ductility, in which it achieved a second cycle at 4.00 % drift ratio (Cycle 31) prior to failure, led to the wall achieving the largest amount of total hysteretic energy dissipated.

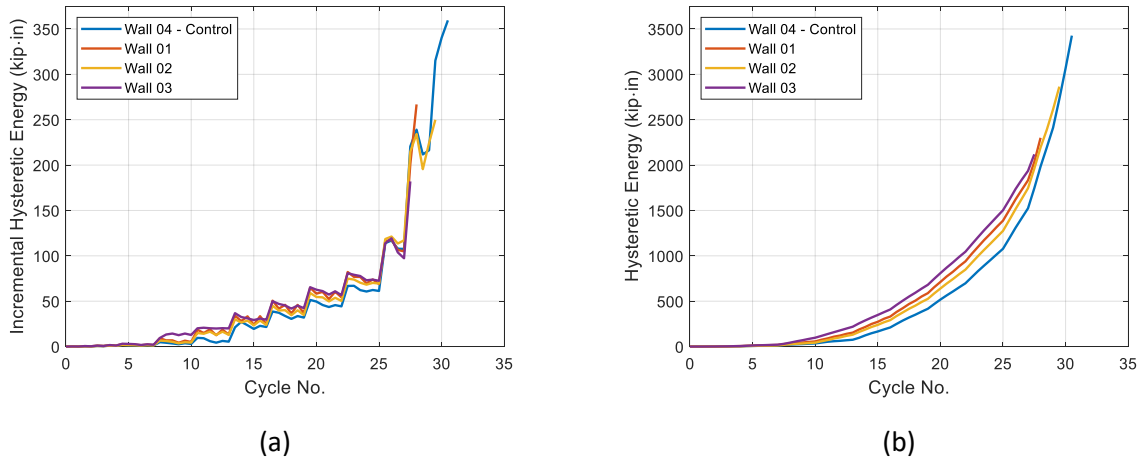


Figure 5.38: Comparison of hysteretic energy between Walls 1, 2, 3, and 4 (a) incremental, and (b) cumulative (1.000 kip in = 0.113 kN m)

The relative rotation of the four walls is shown in Figure 5.39. In each plot, the blue markers correspond to the relative magnitude of measurements taken by R010 and R025 relative to R055. The interpretation of these relative magnitudes is as follows: assuming that nearly all wall rotation has occurred by 55.0 in (1397 mm) of height above the base of the wall, which is a reasonable assumption for a concrete shear wall configured as a cantilevered flexural element, the value of the blue markers represents the percentage of the total rotation occurring below a height of 10.0 in (254 mm) and the value of the red markers represents the percentage of the total rotation occurring below a height of 25.0 in (635 mm). Consistently, for all four walls, by the end of the testing more than 90 % of the wall rotation was concentrated within the first 25 in (635 mm) of wall height. During peak or valley of their last cycle before failure, the percentage of the total rotation occurring below a height of 25.0 in (635 mm), which can be extracted as the larger of the values of the final two data points, was 98.8 %, 96.9 %, 95.8 %, and 92.9 % for Walls 1, 2, 3, and 4, respectively.

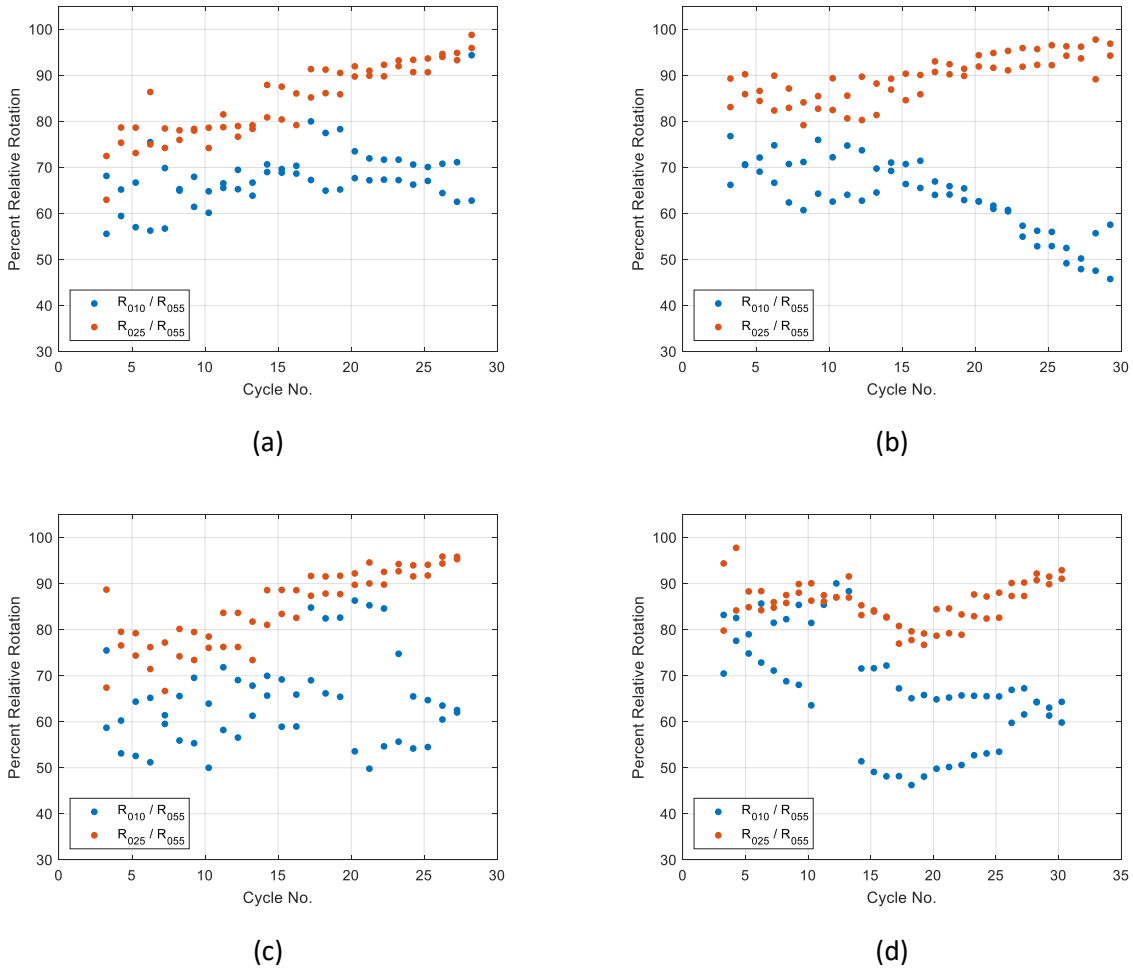


Figure 5.39: Percent relative rotation by height for (a) Wall 1, (b) Wall 2, (c) Wall 3, and (d) Wall 4

The plots in Figure 5.39 also allow for determination of the time and/or cycle in which measurements taken at 25 in (635 mm) up the height of the wall first crossed certain threshold values, for example, 90 % of the total wall rotation: Wall 1 at 79.5 min (in Cycle 20), Wall 2 at 62.5 min (in Cycle 18), Wall 3 at 68.8 min (in Cycle 19), and Wall 4 at 29.1 min (in Cycle 11). Interestingly for Wall 4, the relative rotation occurring below a height of 25.0 in (635 mm) reached a local maximum at 46.9 min (in Cycle 15) before decreasing in the subsequent cycles. After Cycle 15, the relative rotation occurring below a height of 25.0 in (635 mm) did not again reach 90 % until 166.1 min (in Cycle 29). Although anecdotal, this trend implies that, after the onset of inelasticity, Wall 4 was more effective at distributing inelastic damage farther up the height of the wall than were Walls 1 through 3.

5.8 SUMMARY AND KEY OBSERVATIONS

This chapter described seismic testing of four reinforced concrete shear wall specimens under combined axial (gravity) and lateral cyclic loading. The behavior of the walls was presented in terms of their measured lateral force-drift hysteresis, strain development beyond yield in the longitudinal bars in the boundary elements, and degree of localization of damage at the base of the wall which was estimated using measurements of relative rotation up the heights of the walls. The performance of the wall specimens was evaluated by the walls' peak flexural capacity in both positive and negative flexure, including the drift ratios at which the peak flexural capacities were achieved, ductility, cumulative drift capacity, and the amount of hysteretic energy dissipated.

Three of the wall panels (Wall 1, Wall 2, and Wall 3) had ASR-induced expansion and damage prior to testing, while in the fourth wall (Wall 4) with no sodium hydroxide added, the ASR reaction was mitigated by dosing the wall panel with a lithium nitrate solution. Pre-strains in the longitudinal bars of the boundary elements of Walls 1 through 3, due to ASR-induced expansion (see Chapter 4), notably led to flexural yielding (i.e., the onset of flexural inelasticity) at lower drift levels than in Wall 4. This earlier activation of inelasticity generally led Walls 1 through 3 to dissipate more hysteretic energy at a given drift ratio than did Wall 4; however, Wall 4 ultimately dissipated the largest hysteretic energy among the four specimens because of its larger cumulative drift capacity. The key observations from cyclic testing of the walls were as follows:

- The average drift ratio at the onset of yielding of reactive Walls 1 through 3 was 40.5 % of that of non-reactive Wall 4. This decrease in drift ratio at yield for Walls 1 through 3 is attributed to the ASR-induced pre-strain in the longitudinal bars, which led to the onset of inelasticity at lower drift ratios. As a result, none of the ASR-affected walls met the ACI 318-19 design criteria, which is based on yielding of the longitudinal bars in the boundary elements.
- The presence of ASR did not decrease the initial stiffness of the wall's force-drift flexural response.
- The average peak flexural resistance in negative and positive flexure of reactive Walls 1 through 3 were 85.6 % and 88.1 %, respectively, relative to those of non-reactive Wall 4.
- The average drift ratio at peak flexural resistance in negative and positive flexure of reactive Walls 1 through 3 were 50.7 % and 56.8 %, respectively, relative to those of non-reactive Wall 4.
- Ductility was not adversely affected by the presence of ASR; however, ductility was influenced by the amount of transverse reinforcement within the boundary elements. Both specimens with a transverse reinforcement ratio of 0.5 % achieved a ductility of 3.00 % while both specimens with a transverse reinforcement ratio 2.0 % achieved a ductility of 4.00 %.
- Non-reactive Wall 4 dissipated the largest total hysteretic energy, not because it dissipated more energy per cycle, but because it achieved the largest cumulative drift capacity. Non-reactive Wall 4 also had the largest drift at peak flexural capacity in both negative and positive flexure.
- The presence of ASR generally increased the amount of hysteretic energy dissipated in a given cycle, because walls with ASR yielded at lower drift ratios, due to the ASR-induced pre-strain in the longitudinal bars of their boundary elements, leading to increased inelasticity and energy dissipation at lower magnitudes of peak drift.

These observations are further strengthened by the statistical analyses presented in Chapter 6, which consider simultaneously for all four concrete shear wall specimens these key characteristics of the response.

Chapter 6

STATISTICAL ANALYSIS OF MEASURED DATA

The statistical analyses in this chapter aim to quantify the effects of two predictor variables: ASR-induced expansion (ε_{ASR}), and the transverse reinforcement ratio in the concrete shear wall's boundary elements, ρ_t , (as a measure of confinement) on the following response variables (indicators of wall cyclic performance):

- Deformation capacity variables: including cumulative drift capacity, drift ratio at yield moment, drift ratio at peak flexural capacity, drift ratio at 20 % reduction in peak flexural capacity, and peak drift capacity (or ductility), and
- Flexural capacity variables: including normalized yield moment, M_y/M_n , and normalized peak flexural capacity, M_{max}^*/M_n , and
- Energy dissipation capacity variables: including hysteretic energy by stage (at a given level of drift ratio corresponding to a certain performance objective), and total cumulative hysteretic energy.

For each response variable, two questions are addressed:

1. Which predictor variables have the largest impact on the response variable?
2. What is the direction and magnitude of the response variable change with a change in the predictor variables that were identified to be most important?

As indicated in Sections 4.4 and 4.5, the laboratory closure due to the pandemic in 2020 resulted in a difference between the planned experiment and the data that were eventually obtained. A wall at an intermediate value of ε_{ASR} with $\rho_t = 0.5\%$ was originally planned to be tested. Since the walls continued to expand during the closure period, the final data set contained three walls with essentially the same amount of ASR-induced expansion, two of which had $\rho_t = 0.5\%$, and no walls with an intermediate amount of ASR-induced expansion. This can be viewed both positively and negatively: on one hand the replication provided an estimate of pure error, but on the other it precluded the estimation of an interaction between ε_{ASR} and ρ_t .

Section 6.1 presents an overview of the statistical methods used in the analyses and Section 6.2 provides the results of the statistical analysis based on the four cyclic tests of concrete shear walls in this study. Data from these four walls is termed "the NIST data". A similar statistical analysis is presented in Section 6.3 using the NIST data augmented by relevant data from testing by Oh et al. (2002). A summary of the chapter is provided in Section 6.4.

6.1 METHODOLOGY

To estimate the effects of the ASR and confinement on measured responses of the shear walls, regression models of the form

$$y_i = \alpha + \beta_\varepsilon \cdot \varepsilon_{ASR,i} + \beta_\rho \cdot \rho_{t,i} + \beta_{\varepsilon\rho} \cdot \varepsilon_{ASR,i} \cdot \rho_{t,i} + \delta_i \quad (6.1)$$

are considered, where y_i is the measured response of wall i , $\varepsilon_{ASR,i}$ is wall i 's level of ASR expansion (0 for absent and 1 for present), and $\rho_{t,i}$ is the level of confinement in wall i 's boundary elements (0 for 2.0 % and 1 for 0.5 %). The term $(\varepsilon_{ASR,i} \cdot \rho_{t,i})$ represents an interaction between the two predictor variables. The coefficients β_ε , β_ρ , and $\beta_{\varepsilon\rho}$ represent the effects of ASR, confinement, and their interaction, respectively. When $\beta_{\varepsilon\rho}$ is non-zero, ASR and ρ_t are said to interact, and in that case, the magnitude of the effect of ASR depends on the level of ρ_t and similarly the magnitude of the effect of ρ_t depends on the presence or absence of ASR. The symbol α represents the intercept. A baseline parameterization was used, so the intercept, α , is the predicted value for the baseline factor combination. The choice of parameterization is discussed in Section 6.1.3. The term δ_i represents a random error.

The least absolute selection and shrinkage operator (LASSO) (Tibshirani 1996) was used to estimate the effects of ASR and confinement on the response variables. The use of the LASSO may seem unintuitive and techniques based on ordinary least squares (OLS) may seem more natural given the small sample size of four shear walls and number of predictor variables (two) with two levels each. However, the LASSO was chosen for two reasons:

1. The sample size and number of combinations of predictor variables grows very quickly when the measured values of hysteretic energy at each performance objective in the experiment (see Section 2.5 and Figure 2.19) are considered.
2. To have a single unifying statistical methodology in this report that is also consistent with the statistical methods used in the companion Task 1 report (Sadek et al., 2021) and Task 2 report (Thonstad et al., 2021).

The LASSO may be described as a penalized version of OLS; that is, OLS in which the estimated predictor variable effects are decreased (reduced toward zero) according to a penalty. The penalty balances the trade-off between bias and variance for the estimated effects. When the penalty is zero, the LASSO estimates are unbiased and match the OLS estimates. For very large penalties, all predictor variable effects would be estimated to be exactly zero. Thus, they would have low variance, but potentially, high bias. By properly selecting the penalty, it is possible to estimate predictor variable effects with simultaneously low bias and low variance. The intercept of the regression model is typically not penalized, and that convention was followed here.

6.1.1 Choosing the LASSO Penalty

It is common to choose the LASSO penalty using cross-validation (Hastie et al., 2015). However, with only four concrete shear wall specimens, even leave-one-out cross validation was infeasible. Since only one of the walls was non-reactive ($\varepsilon_{ASR,i} = 0$), if that wall was left out of the data set, the effect of ASR could not

be estimated. As a result, the Bayesian Information Criterion (BIC) for the LASSO, described by Zou et al. (2007), was used in selecting the LASSO penalty.

6.1.2 Statistical Significance

Given a chosen value for the LASSO penalty, some of the coefficient estimates may be exactly zero. The ability of LASSO-penalized regression to force certain coefficient estimates exactly to zero may be used in place of hypothesis tests for statistical significance. If a coefficient is estimated to be exactly zero, the effect or interaction associated with the zero coefficient has no influence on predictions made by the regression model and may thus be deemed unimportant from the perspective of prediction. This is not to say that the variable is unimportant from an engineering perspective. It only means that, for the variable combinations in the experiment, the effect of that variable is not discernible from noise. In this report, a predictor variable is said to have a statistically significant effect on the response variable when the estimated coefficient for that predictor variable is not zero.

6.1.3 Baseline Parametrization

There are many ways to parameterize a regression model. A baseline parameterization was chosen for this study, with the baseline combination of predictor variables being non-reactive ($\epsilon_{ASR} = 0\%$) and high confinement ($\rho_t = 2.0\%$). That variable combination is represented by the value of α in the regression model. The coefficient β_ϵ then represents the average effect of changing from ASR being absent to being present. The coefficient β_ρ represents the average effect of ρ_t changing from its high value (2.0%) to its low value (0.5%). The coefficient $\beta_{\epsilon\rho}$ represents the interaction between ASR and confinement, which may be interpreted as modifying the average effect of one predictor variable (ASR or ρ_t) according to the level (or magnitude) of the other. It is possible, with the LASSO, to estimate $\beta_{\epsilon\rho}$, where it would not be with OLS since the ASR absent condition is paired only with high confinement. However, while it was technically possible to estimate $\beta_{\epsilon\rho}$ using the LASSO, in this parameterization, it was aliased with β_ρ , the main effect of ρ_t . It was included in the analyses only for completeness, and if estimated to be non-zero, its interpretation would need to account for the aliasing.

6.1.4 Uncertainty in Effects Estimates

Even though the LASSO is used here to replace hypothesis tests of statistical significance, it remains useful to consider the range of estimated effects (and mean values) that might be observed if the experiment were to be repeated. The bootstrap algorithm described in Chapter 6 of Hastie et al. (2015) was used for this goal.

6.2 RESULTS OF STATISTICAL ANALYSIS

As described previously, the response variables that together constitute wall performance include:

- Deformation capacity variables: including cumulative drift capacity, drift at yield moment, drift at peak flexural capacity, drift at 20 % reduction in peak flexural capacity, and peak drift capacity (or ductility), and
- Flexural capacity variables: including normalized yield moment, M_y/M_n , and normalized peak flexural capacity, M_{\max}^*/M_n ,
- Energy dissipation capacity variables: including hysteretic energy by stage (at a given drift level corresponding to a certain performance objective), and total cumulative hysteretic energy.

With the exception of hysteretic energy by stage, the test (predictor) variables (ASR and ρ_t) and the measured wall performance data considered in this chapter are given in Table 6.1.

6.2.1 Cumulative Drift Capacity

Figure 6.1 depicts the estimated regression coefficients for cumulative drift capacity as a function the LASSO penalty. For small values of the LASSO penalty, the estimated regression coefficients would be similar to their OLS counterparts. As the penalty increases, the magnitude of the regression coefficients is decreased toward zero, and the coefficients eventually become identically zero. To automate model selection (or statistical inference or hypothesis testing), the value of the penalty must be chosen. Cross-validation is a common strategy employed for choosing the penalty term (e.g., see Sadek et al., 2021 and Thonstad et al., 2021). However, with only four observations, cross-validation could not be employed here.

Table 6.1. Measured performance data for NIST wall specimens

ϵ_{ASR}	ρ_t (%)	Cumulative drift capacity (%)	Drift ratio at yield moment, d_y (%)	Drift ratio at peak flexural capacity, d_{Mmax}^* (%)	Drift ratio at 80% peak flexural capacity, d_{80}^* (%)	Peak drift capacity, d_{fail} (%)	Normalized peak flexural capacity (M_{max}^*/M_n)	Normalized Yield Moment (M_y/M_n)	Cumulative hysteretic energy, kip-in (kN.m)
Present (≥ 0.25 %)	0.5	97.5	0.35	1.248	3.00	3.0	1.132	0.79	2300.6 (259.9)
Present (≥ 0.23 %)	2.0	117.5	0.31	1.249	3.87	4.0	1.141	0.67	2864.4 (323.6)
Present (≥ 0.25 %)	0.5	91.5	0.24	0.748	2.00	3.0	1.104	0.68	2118.6 (239.4)
Absent (0.0 %)	2.0	133.5	0.74	1.903	4.00	4.0	1.311	1.01	3426.6 (387.2)

To choose the LASSO penalty, the BIC was used instead of cross-validation (see Section 6.1.1). Figure 6.2 shows the BIC values plotted against the LASSO penalty. It is ideal, for a plot such as Figure 6.2, to have a clearly unique minimum. That was not the case for Figure 6.2, most likely because of the small sample size and small number of predictor variables. In cases where no clear minimum BIC exists, the BIC associated with the “elbow” (i.e., domain of maximum curvature) of the plot is typically selected, which represents the point of diminishing returns. Values of the LASSO penalty between e^1 and $e^{1.5}$ are considered.

The large dark-colored points in Figure 6.3 display the estimated regression coefficients for two LASSO penalties, e^1 and $e^{1.5}$. The small light-colored points depict bootstrap replicates of those estimates. In both cases, the qualitative conclusion is clear, ASR and ρ_t both affected cumulative drift capacity. The presence of ASR and decreasing ρ_t both had a negative impact on (i.e., both resulted in a reduction in) cumulative drift capacity. The presence of ASR was estimated to reduce the mean cumulative drift capacity by about 10 %. When $\rho_t = 2.0\%$, this is 8 % relative, and when $\rho_t = 0.5\%$, it is 9 % relative. Decreasing ρ_t from 2.0 % to 0.5 % was estimated to reduce the mean cumulative drift capacity by 20 %. When ASR is absent, this is 16 % relative, and when ASR is present, this is 17 % relative. From Figure 6.3 it was also concluded that there was no evidence that the presence of ASR and ρ_t interacted, i.e., there was no evidence that the effect of ASR depended on ρ_t and similarly there was also no evidence that the effect of ρ_t depended on the presence or absence of ASR.

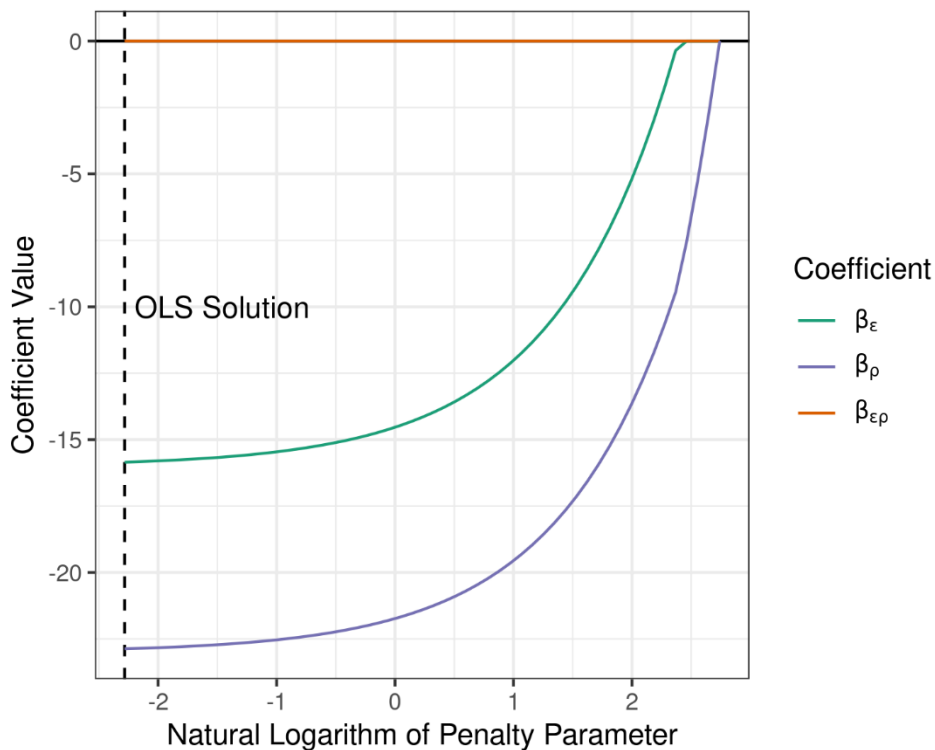


Figure 6.1: Estimated regression coefficients as a function of the LASSO penalty. The color indicates the coefficient.

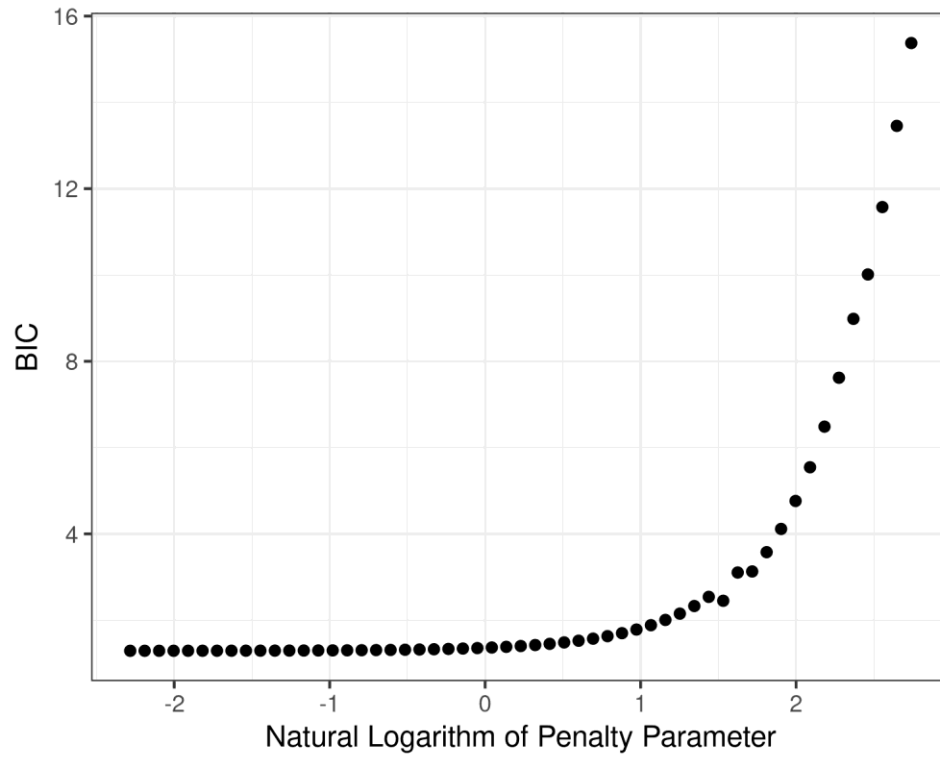


Figure 6.2: BIC plotted versus the LASSO penalty

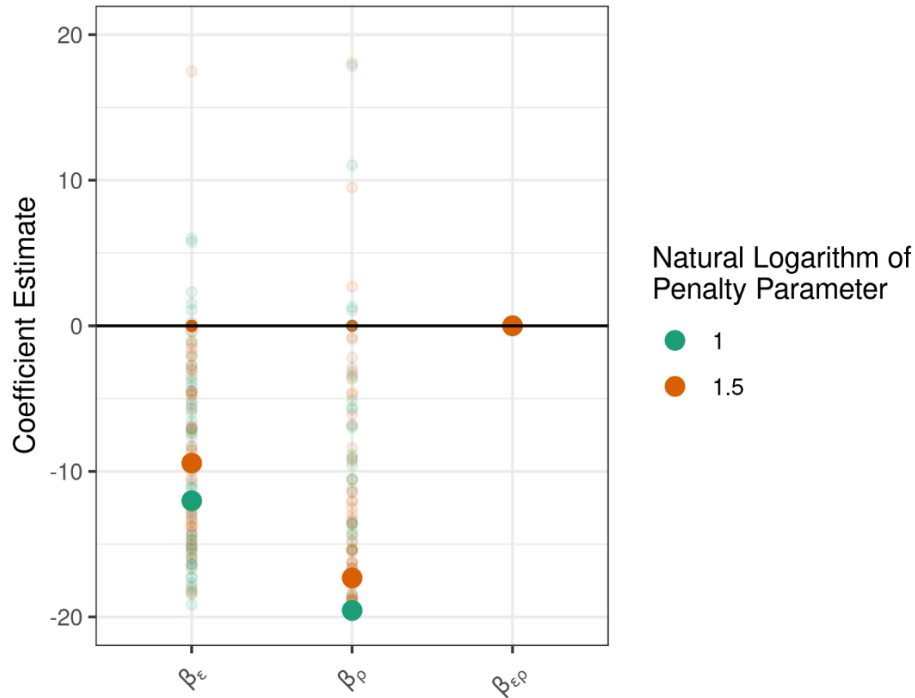


Figure 6.3: Estimated regression coefficients for two LASSO penalties (large dark-colored points) and bootstrap replicates of them (small light-colored points) for cumulative drift capacity

Figure 6.4 shows the estimated mean cumulative drift capacity at four combinations of ρ_t and ε_{ASR} . The decrease in the estimated mean cumulative drift capacity when ASR is present and as ρ_t decreases is evident. At the combination ASR absent and $\rho_t = 2.0\%$, the estimated mean is 128%, and when ASR is present and $\rho_t = 0.5\%$ the estimated mean is 97%, for a decrease of 24%. In Figure 6.4, we also observe a large amount of uncertainty in the estimated means since the bootstrap replicates are spread over a wide range of values. The broad uncertainty is attributable to the low sample size. It should also be noted in Figure 6.4 (and all similar figures henceforth) that the combination ASR absent and $\rho_t = 0.5\%$ represents extrapolation since there are no data for that combination. If, for example, the interaction term between ε_{ASR} and ρ_t was important, even though it was not found to be important given the available data, the estimated mean for the missing combination would be biased.

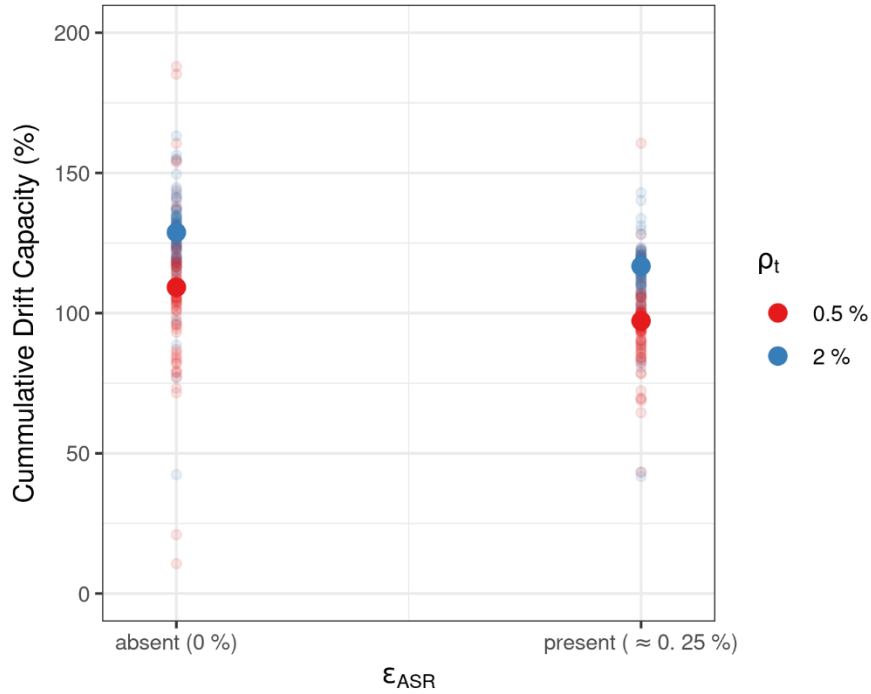


Figure 6.4: Estimated mean cumulative drift capacity for four combinations of ε_{ASR} and ρ_t (large dark-colored points), and 100 bootstrap replicates of the estimated mean cumulative drift capacity (small light-colored points).

6.2.2 Drift Ratio at Yield Moment d_y

The statistical methodology for drift ratio at yield moment, d_y , was the same as for cumulative drift capacity, so only the estimated coefficients and the bootstrap replicates are shown in Figure 6.5. Note in Figure 6.5 that the best estimates of the LASSO penalty parameter for d_y are e^{-4} and $e^{-3.5}$, which differ from those in Figure 6.3 for cumulative drift capacity of e^1 and $e^{1.5}$. This is expected because the best penalty parameter can be affected by the respective units of the response variable and predictor variables, the signal to noise ratio, and the size of the regression model (i.e., the number of regression terms). The estimated regression coefficients (large dark-colored points) for d_y are shown in Figure 6.5, along with 100 bootstrap replicates (small light-colored points). Figure 6.5, shows that the presence of ASR negatively affects d_y (the presence of ASR decreased d_y), but there is no evidence that decreasing ρ_t affected d_y . It is estimated that for the level of ε_{ASR} in this study the mean d_y decreased by about 0.40 %, depending on the choice of the LASSO penalty.

The estimated mean d_y is shown in Figure 6.6 (large red points) for the ASR absent and present conditions with $\rho_t = 0.5\%$. The estimated means for $\rho_t = 2\%$ would not change since the effect of ρ_t is estimated to be zero. The bootstrap replicates of the estimated means in Figure 6.6 (small grey points) would change slightly for the for $\rho_t = 2\%$. As expected, based on Figure 6.5, the estimated negative effect of the presence of ASR is evident. With the LASSO penalty $e^{-3.5}$, for the ASR absent condition, the estimated mean is 0.69 %, and for the ASR present condition it is 0.32 %, which is a decrease of 54 %. The range of the

bootstrap replicates is again broad, from almost 1 % for the ASR absent condition to almost 0 % for the ASR present condition.

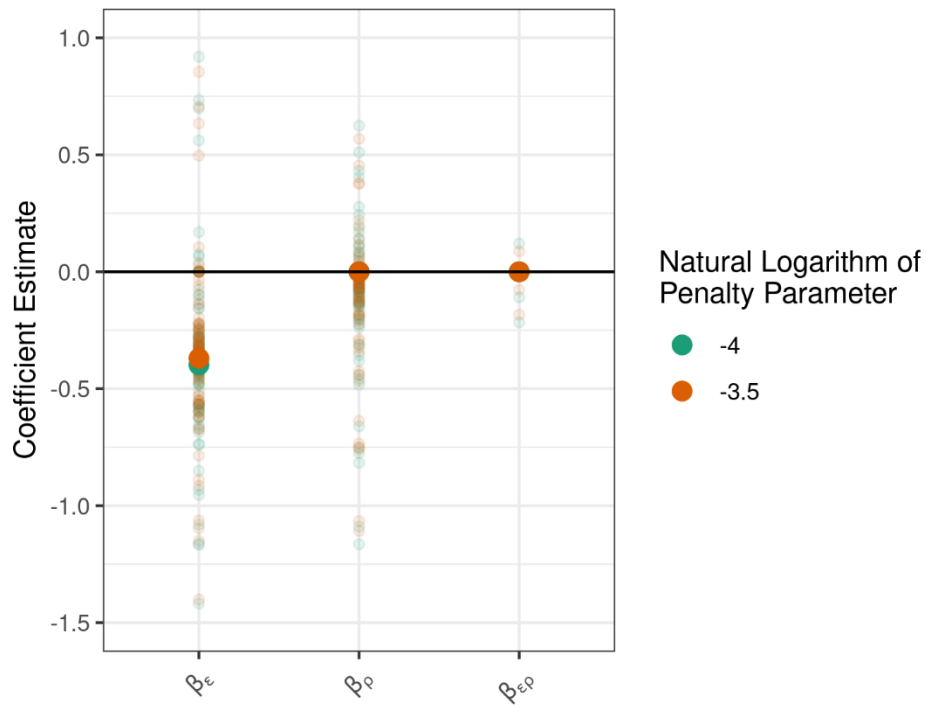


Figure 6.5: Estimated regression coefficients for two LASSO penalties (large dark-colored points) and bootstrap replicates of them (small light-colored points) for drift at yield moment.

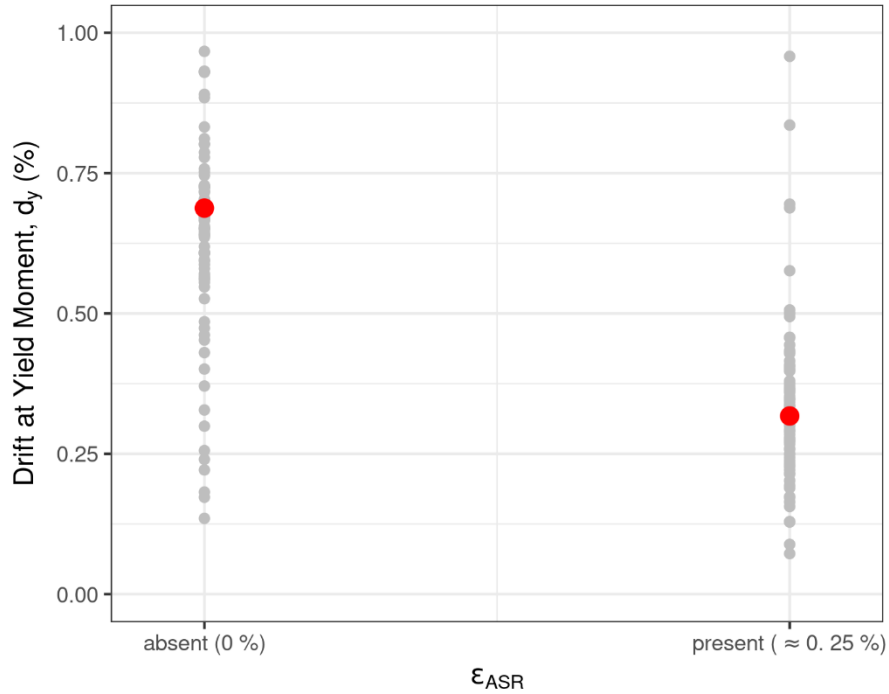


Figure 6.6: Estimated mean drift at yield moment at the ASR present and absent conditions and $\rho_t = 0.5\%$ (large red circles), and 100 bootstrap replicates of the estimated mean drift at yield moment (small grey circles).

6.2.3 Drift Ratio at Peak Flexural Capacity, d_{Mmax}^+

The estimated regression coefficients (large dark-colored points) for drift ratio at peak flexural capacity, d_{Mmax}^+ , are shown in Figure 6.7, along with 100 bootstrap replicates (small light-colored points). As with drift at yield moment, Figure 6.7 shows that the presence of ASR negatively affected d_{Mmax}^+ (the presence of ASR decreased d_{Mmax}^+), but there is no evidence that decreasing ρ_t affected d_{Mmax}^+ . It was estimated that for the level of ϵ_{ASR} in this study, the mean value of d_{Mmax}^+ decreased by about 0.35 %.

The estimated mean value of d_{Mmax}^+ is shown (by large red points) in Figure 6.8 for the ASR absent and present conditions with $\rho_t = 0.5\%$. The estimated means for $\rho_t = 2.0\%$ would not change since the effect of confinement is estimated to be zero. The bootstrap replicates of the estimated means in Figure 6.8 (shown by small grey points) would change slightly for the high level of ρ_t . As expected, based on Figure 6.7, the estimated negative effect of the presence of ASR is evident. For the ASR absent condition, the estimated mean was 1.55 %, and for the ASR present condition it was 1.20 %, which is a decrease of 23 %. The range of the bootstrap replicates was again broad, ranging as high as 7.5 % and as low as 0 % for the ASR absent condition.

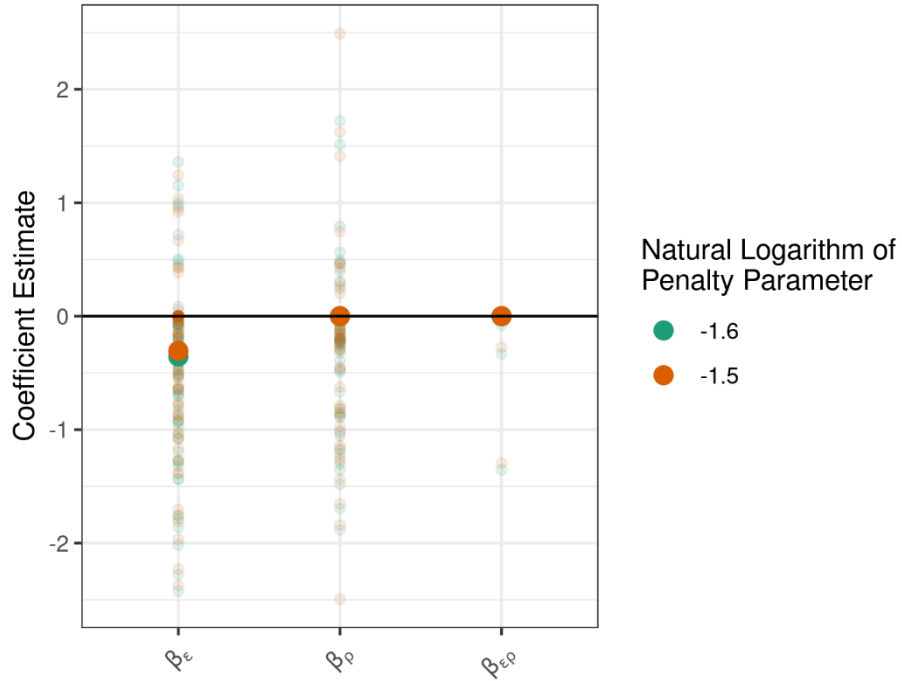


Figure 6.7: Estimated regression coefficients for two LASSO penalties (large dark-colored points) and bootstrap replicates of them (small light-colored points) for drift at peak flexural capacity.

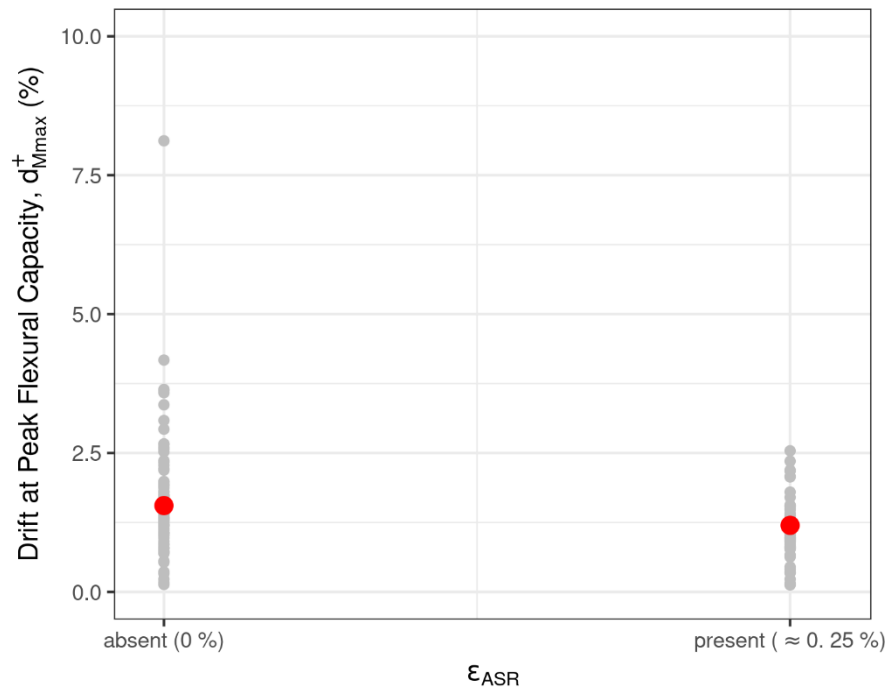


Figure 6.8: Estimated mean drift at peak flexural capacity at the ASR present and absent conditions and $\rho_t = 0.5\%$ (large red points), and 100 bootstrap replicates of the estimated mean drift at peak flexural capacity (small grey points).

6.2.4 Drift Ratio at 20 % Reduction in Peak Flexural Capacity, d^*_u

In contrast to d_y and d^*_{Mmax} , Figure 6.9 shows that decreasing ρ_t negatively affected the drift at 20 % reduction in flexural capacity d^*_u (as ρ_t decreases, d^*_u decreases), but there was no evidence that the presence of ASR affected d^*_u . It is estimated that decreasing ρ_t from 2.0 % to 0.5 % decreases the mean value of d^*_u by about 0.7 %, depending on the value of the LASSO parameter.

The estimated mean value of d^*_u is shown (by large red points) in Figure 6.10 for the two values of ρ_t in the study with ASR absent. The estimated means at the ASR present condition would not change since the effect of ASR is estimated to be zero. The bootstrap replicates of the estimated means in Figure 6.10 (shown by small grey points) would change slightly for the ASR present condition. As expected, based on Figure 6.9, the estimated negative effect of decreasing ρ_t was evident. With the LASSO penalty $e^{-1.1}$, for $\rho_t = 0.5$ %, the estimated mean was 3.6 %, and for $\rho_t = 2.0$ % the estimated mean was 2.83 %, which was a decrease of 21 %. The range of the bootstrap replicates again indicate broad uncertainty, almost spanning the range 1 % to 10 %.

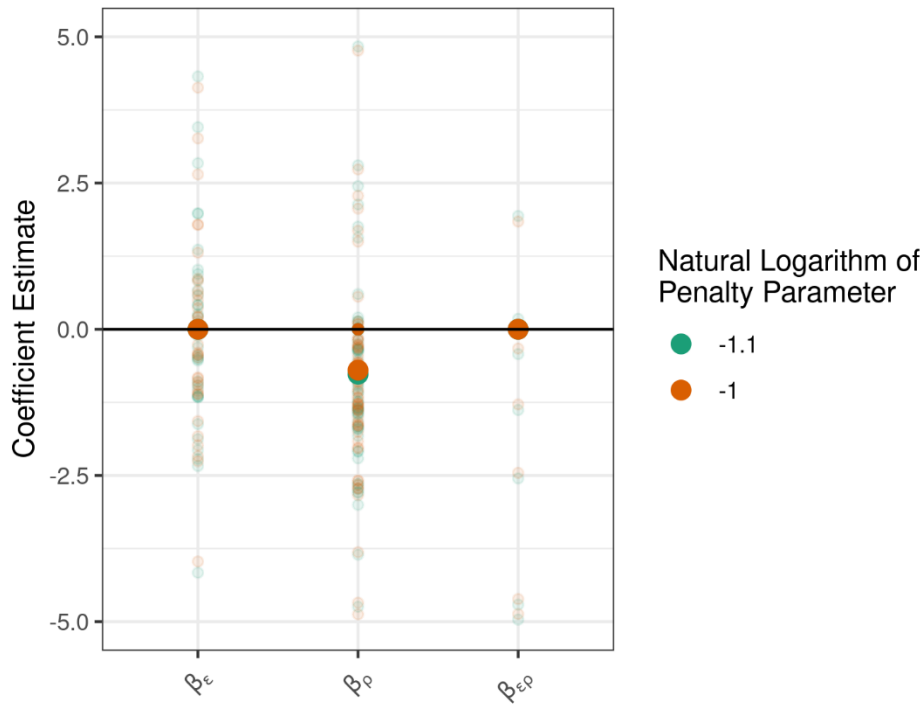


Figure 6.9: Estimated regression coefficients for two LASSO penalties (large dark-colored points) and bootstrap replicates of them (small light-colored points) for drift at 20 % reduction in flexural capacity.

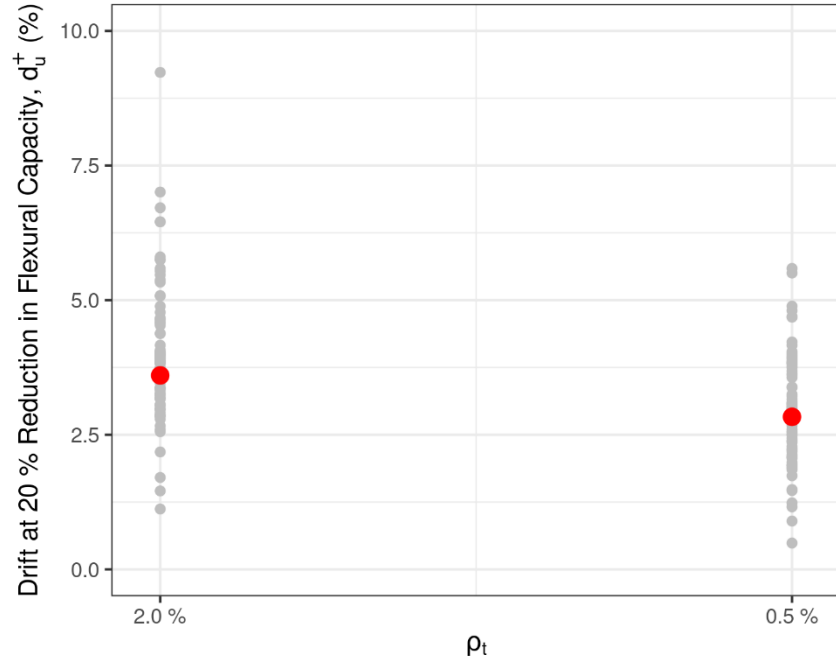


Figure 6.10: Estimated mean drift at ultimate flexural capacity at $\rho_t = 2.0\%$ and 0.5% and ASR absent (large red points), and 100 bootstrap replicates of the estimated mean drift at 20% reduction in flexural capacity (small grey points).

6.2.5 Peak Drift Capacity, d_{fail}

Figure 6.11 shows the maximum drift ratios, d_{fail} , observed for each wall. circles were slightly moved horizontally and vertically so that all four points are visible; otherwise, only two points would be visible. The methods of Section 6.1 were not applied here because they rely on continuous measurements, and d_{fail} may only take on the discrete drift ratio values 2.0%, 3.0%, or 4.0%. Instead, we notice that d_{fail} for walls with $\rho_t = 2.01\%$ and 0.5% were 4.0% and 3.0%, respectively. This suggests a negative effect of decreasing ρ_t on d_{fail} (as confinement decreases, d_{fail} decreases). On the other hand, a direct comparison of the two walls at the high confinement level, one reactive and one not, provides no evidence that the presence of ASR at the level considered in this study affected the wall's value of d_{fail} . Again, these remarks are based only on the raw data. No statistical procedures were applied. Thus, no claim is being made that they would replicate if the experiment were repeated because variability is not quantified.

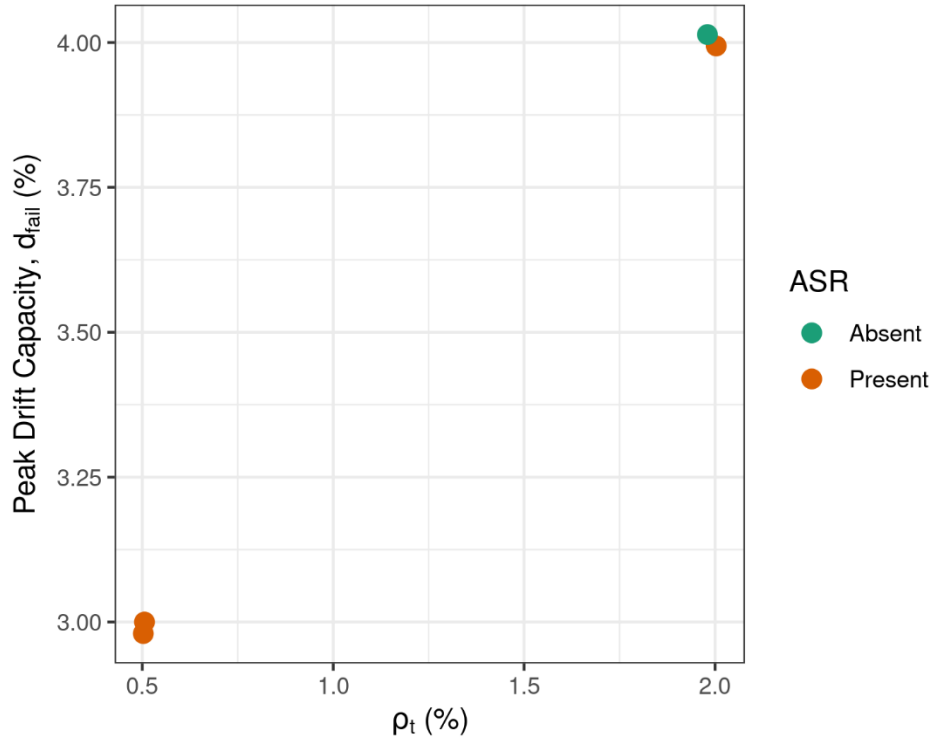


Figure 6.11: Peak drift capacity for the four walls, circles slightly moved horizontally and vertically so that the four circles are visible.

6.2.6 Normalized Peak Flexural Capacity, M_{max}^+/M_n

The estimated regression coefficients (shown by large dark-colored points) for normalized peak flexural capacity M_{max}^+/M_n are shown in Figure 6.12, along with 100 bootstrap replicates (shown by small light-colored points). Similarly to d_{Mmax}^+ and d_y , Figure 6.12 shows that the presence of ASR negatively affected M_{max}^+/M_n (the presence of ASR decreased M_{max}^+/M_n), but there is no evidence that decreasing ρ_t affected normalized peak flexural capacity. It is estimated that for the level of ϵ_{ASR} in this study the mean normalized peak flexural capacity, M_{max}^+/M_n , decreases by about 0.13 depending on the choice of LASSO penalty.

Figure 6.13 depicts the estimated mean peak flexural capacity (shown by large red points) for the ASR absent and present conditions with $\rho_t = 0.5\%$, and 100 bootstrap replicates of the estimated mean peak flexural capacities (small grey circles). Since estimated effect of ρ_t is zero, the estimates (red circles) would remain the same for $\rho_t = 2.0\%$, but the bootstrap replicates (shown by grey circles) would shift slightly. With the LASSO penalty e^{-4} , for the case where ASR is absent, the estimated mean peak flexural capacity is 1.28, and for the ASR present condition, the estimated mean peak flexural capacity is 1.14, which is a decrease of 11%. For the ASR absent and present conditions, almost all of the bootstrap replicates (94% for the present condition) are also larger than one.

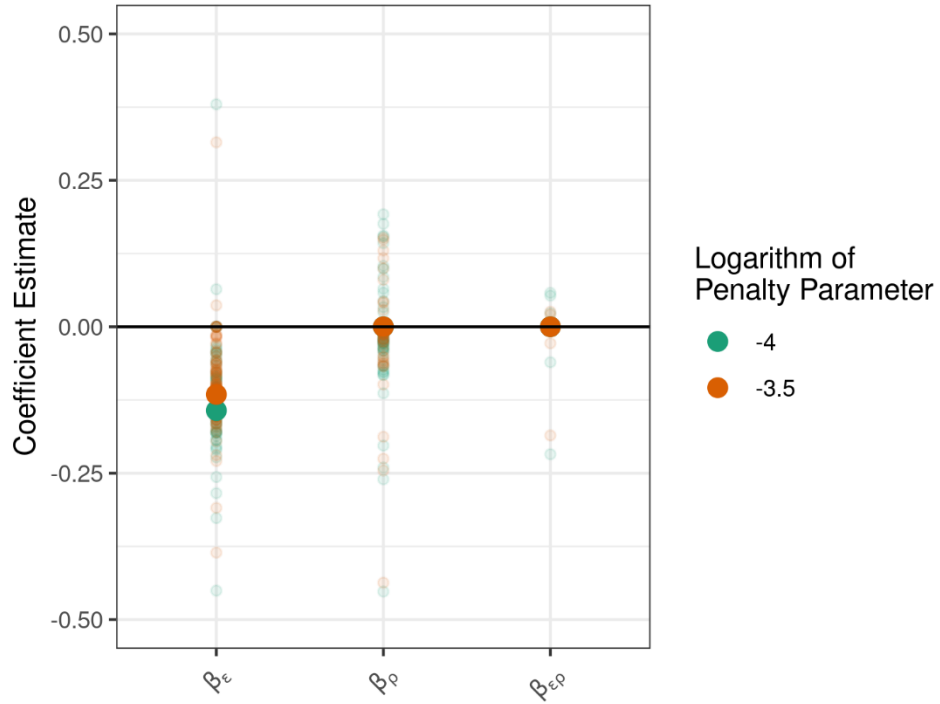


Figure 6.12: Estimated regression coefficients for two LASSO penalties (large dark-colored points) and bootstrap replicates of them (small light-colored points) for M^*_{\max}/M_n

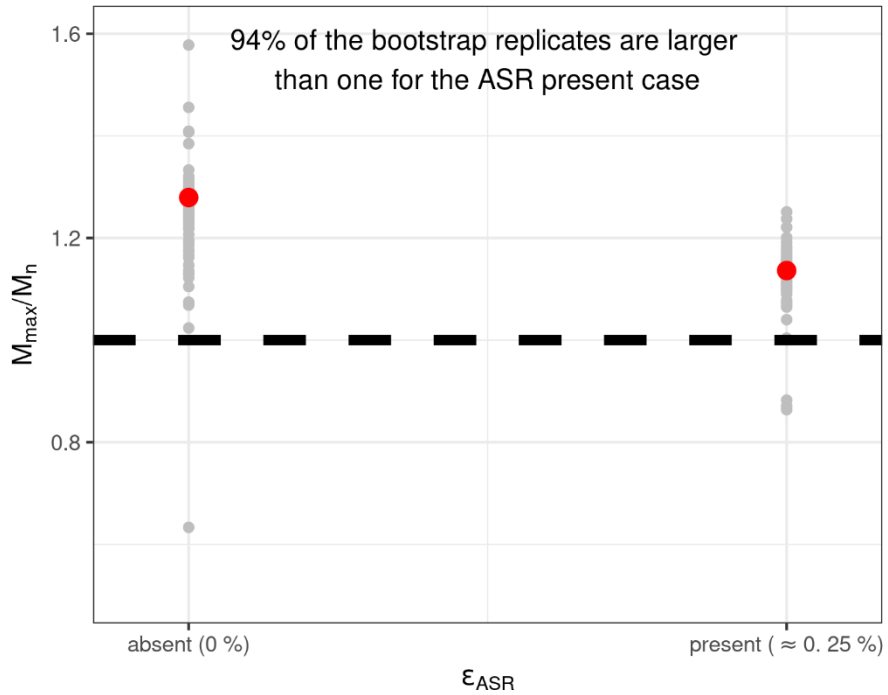


Figure 6.13: Estimated mean normalized peak flexural capacity at the ASR present and absent conditions and $\rho_t = 0.5\%$ (large red circles), and 100 bootstrap replicates of the estimated mean M^*_{\max}/M_n (small grey circles).

6.2.7 Normalized Yield Moment, M_y/M_n

The estimated regression coefficients (shown by large dark-colored points) for normalized yield moment are shown in Figure 6.14, along with 100 bootstrap replicates (shown by small light-colored points). Similar to M_{\max}^+/M_n , Figure 6.14, shows that the presence of ASR negatively affected M_y/M_n (the presence of ASR decreased M_y/M_n), but there was no evidence that decreasing ρ_t affected M_y/M_n . It was estimated that for the level of ϵ_{ASR} in this study the mean M_y/M_n decreases by about 0.25 depending on the chosen LASSO penalty.

Figure 6.15 depicts the estimated mean M_y/M_n (shown by large red points) for the ASR absent and present conditions with $\rho_t = 0.5\%$, and 100 bootstrap replicates of the estimates (shown by small grey circles). Since estimated effect of ρ_t is zero, the estimates (shown by red circles) would remain the same for $\rho_t = 2.0\%$, but the bootstrap replicates (shown by grey circles) would slightly shift. With the LASSO penalty $e^{-3.75}$, for the case where ASR was absent, the estimated mean normalized yield moment was about one (0.97%), and 44% of the bootstrap replicates were larger than one (56% are below one). For the case where ASR is present, the estimated mean normalized yield moment was 0.73, and 89% of the bootstrap replicates of it, were less than one.

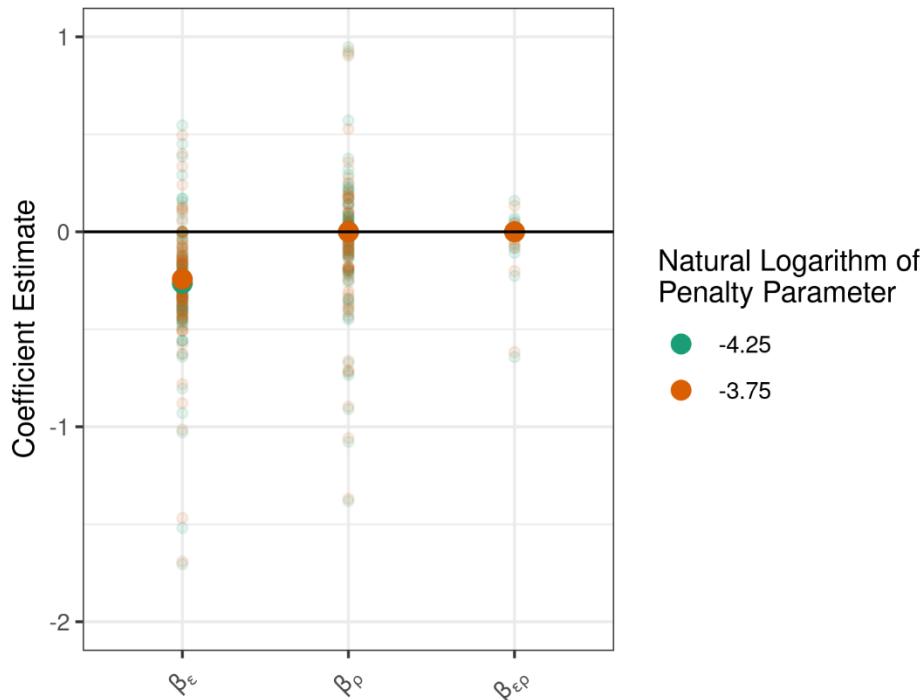


Figure 6.14: Estimated regression coefficients for two LASSO penalties (large dark-colored points) and bootstrap replicates of them (small light-colored points) for M_y/M_n .

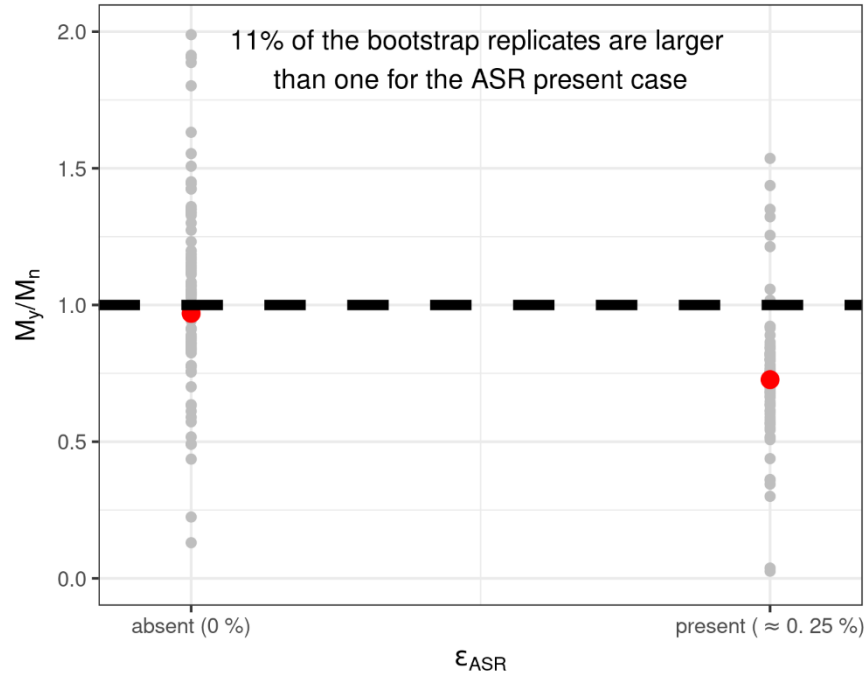


Figure 6.15: Estimated mean normalized yield moment at the ASR present and absent conditions and $\rho_t = 0.5\%$ (large red circles), and 100 bootstrap replicates of the estimated M_y/M_n (small grey circles).

6.2.8 Cumulative Hysteretic Energy

The estimated regression coefficients (shown by large dark-colored points) for cumulative hysteretic energy are shown in Figure 6.16, along with 100 bootstrap replicates (shown by small light-colored points). Similar to cumulative drift capacity, Figure 6.16, shows that both the presence of ASR and decreasing ρ_t negatively affected cumulative hysteretic energy (the presence of ASR decreased cumulative hysteretic energy, and as ρ_t decreased, cumulative hysteresis decreased). It was estimated that for the level of ε_{ASR} in this study the mean cumulative hysteretic energy decreased by about 480 kip·in (54.2 kN m). When $\rho_t = 2.0\%$, this was a decrease of 14%, and when $\rho_t = 0.5\%$ it was a decrease of 17%. Changing ρ_t from 2.0% to 0.5% was estimated to decrease cumulative hysteretic energy by about 580 kip·in (65.5 kN m). When ASR was absent, this was a decrease of 17%, and when ASR was present, it was a decrease of 20%.

The estimated mean cumulative hysteretic energy is shown in Figure 6.17 (shown by large dark-colored points) for four combinations of ε_{ASR} and ρ_t . As expected, based on Figure 6.16, the estimated negative effects of the presence of ASR and decreasing confinement are evident. The highest estimated mean cumulative hysteretic energy was 3332 kip·in (376.5 kN m) for the ASR absent and $\rho_t = 2.0\%$ combination, and the lowest estimated mean cumulative hysteretic energy was 2264 kip·in (255.8 kN m) for the ASR present and $\rho_t = 0.5\%$ combination, which was a decrease of 32%.

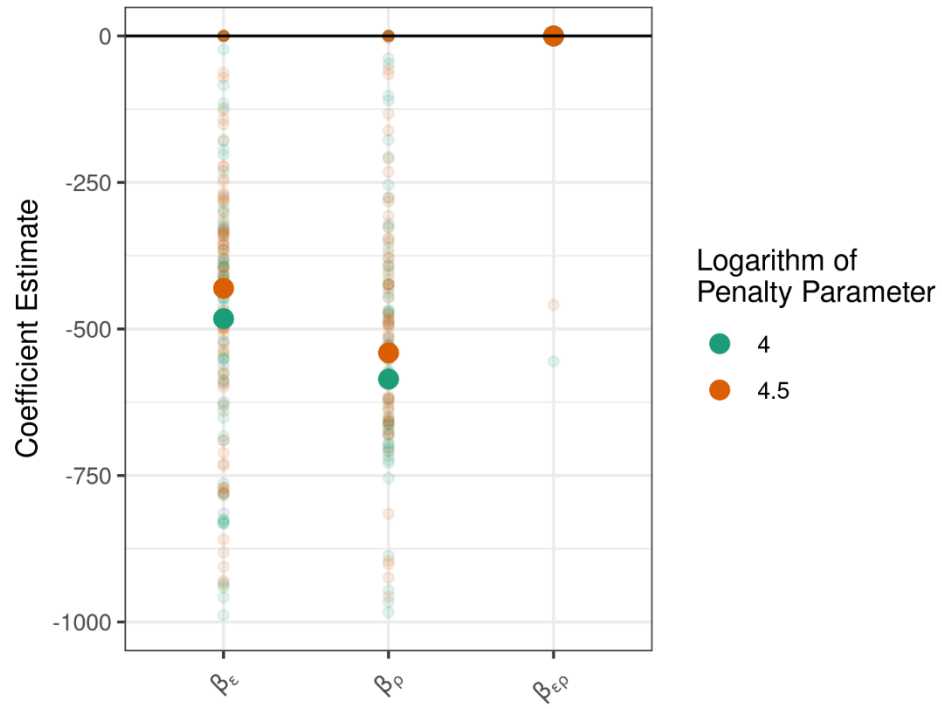


Figure 6.16: Estimated regression coefficients for two LASSO penalties (large dark-colored points) and bootstrap replicates of them (small light-colored points) for cumulative hysteretic energy

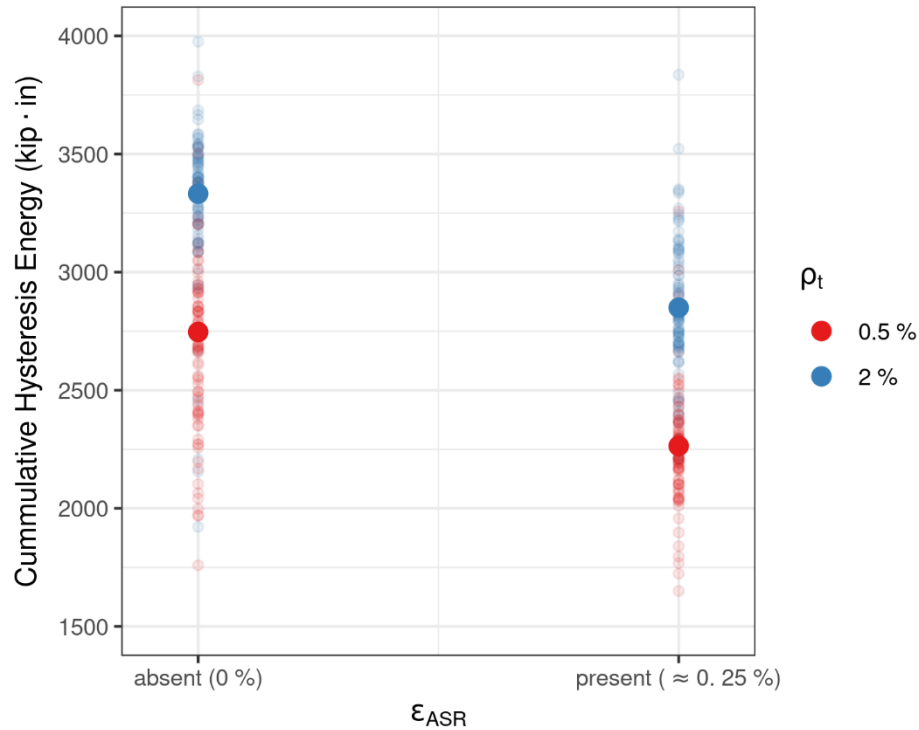


Figure 6.17: Estimated mean cumulative hysteretic energy for four combinations of ϵ_{ASR} and ρ_t (large dark-colored points), and 100 bootstrap replicates of the estimated mean cumulative hysteretic energy (small light-colored points). 1.000 kip in = 0.113 kN m

6.2.9 Cumulative Hysteretic Energy by Stage

An analysis of hysteretic energy at drift ratios corresponding to different stages (performance objectives) in the experiment is considered in this section. The model from Equation (6.1) was modified to allow each effect to vary by the prescribed deformation stages of the experiment, which correspond to the following performance objectives:

1. Elastic
2. Immediate Occupancy
3. Life Safety
4. Collapse Prevention
5. To Failure

The revised regression model is presented in Equation (6.2).

$$\begin{aligned}
y_{hi} = & \alpha + \beta_{\varepsilon} \cdot \varepsilon_{ASR,i} + \beta_{\rho} \cdot \rho_{t,i} + \left\{ \sum_{j=2}^5 \beta_{S,j} \cdot \mathbb{1}(j = h) \right\} + \\
& \beta_{\varepsilon\rho} \cdot \varepsilon_{ASR,i} \cdot \rho_{t,i} + \left\{ \sum_{j=2}^5 \beta_{\varepsilon S,j} \cdot \varepsilon_{ASR,i} \cdot \mathbb{1}(j = h) \right\} + \left\{ \sum_{j=2}^5 \beta_{\rho S,j} \cdot \rho_{t,i} \cdot \mathbb{1}(j = h) \right\} + \\
& \left\{ \sum_{j=2}^5 \beta_{\varepsilon\rho S,j} \cdot \varepsilon_{ASR,i} \cdot \rho_{t,i} \cdot \mathbb{1}(j = h) \right\} + \delta_{hi}
\end{aligned} \tag{6.2}$$

The hysteretic energy for wall i in stage h is denoted by y_{hi} , and $\mathbb{1}(j = h)$ is an indicator equal to one when $j = h$ and zero otherwise. The β symbols in Equation (6.2) represent the regression coefficients, similar to those in Equation (6.1).

The same baseline levels were used for ASR and confinement level, namely absent and high (i.e., Wall 4, with $\varepsilon_{ASR} = 0.0\%$ and $\rho_t = 2.0\%$), respectively. The elastic stage was chosen as the baseline level for the stage (performance objective) effect. The interpretation for the parameter α in Equation (6.2) is then the average value of hysteretic energy for walls that are absent ASR, at high confinement, and in the elastic stage of testing.

One last deviation from the previous analyses is needed. Over the course of the experiment, hysteretic energy varied by more than two orders of magnitude. However, the model in Equation (6.2) assumes that the standard deviation of the random errors, δ_{hi} , are constant, which in this case is not reasonable. Assuming that the standard deviation of δ_{hi} varied proportionally with hysteretic energy is more tenable and implies that y_{hi} should be taken to be the logarithmic transformation of hysteretic energy.

The estimated coefficients (β symbols) and bootstrap replicates representing uncertainty are shown in Figure 6.18. The dominant effects are the main effects for experiment stage, with a positive relationship between hysteretic energy and stage. The other significant effects are the two-way interactions between ASR presence and experiment stage, and confinement level and experiment stage. For example, there is a positive interaction between the presence of ASR and Stage 2 of the experiment (Immediate Occupancy). We interpret this as ASR positively affecting hysteretic energy (the presence of ASR resulted in an increase in hysteretic energy) in Stage 2 of the experiment (Immediate Occupancy). The estimated interaction between the low confinement level and Stage 2 of the experiment (Immediate Occupancy) is also positive. For both ASR presence and the low confinement level, the magnitude of the estimated two-way interactions with experiment stage decreases as the experiment stage increases.

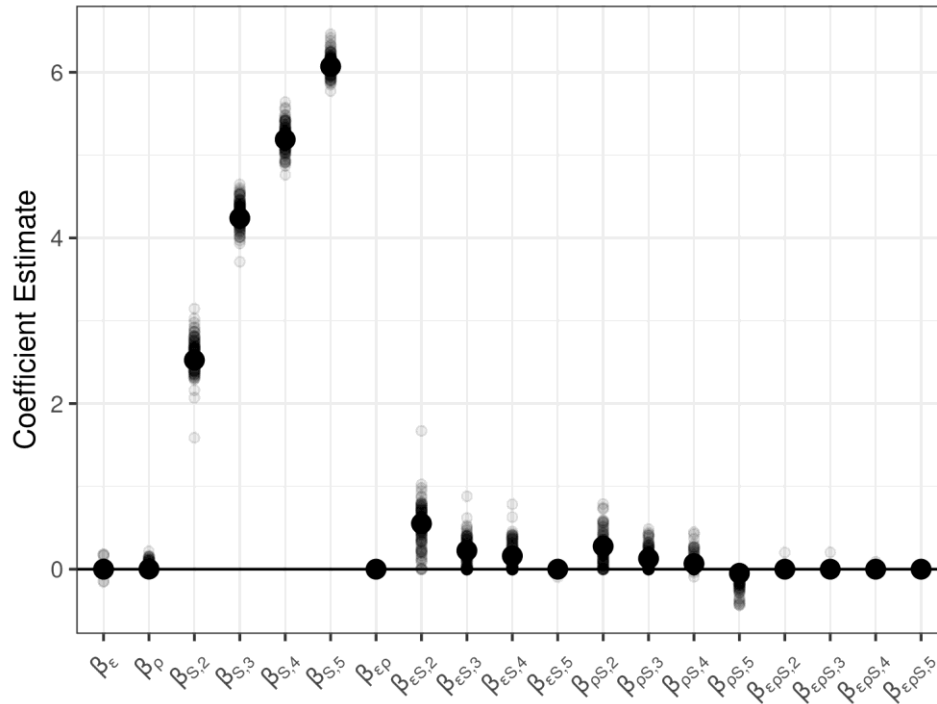


Figure 6.18: Estimated regression coefficients (large dark point) and bootstrap replicates of them (small light-colored points) for the longitudinal hysteretic energy response

The analysis in Section 6.2.8 considered only the total cumulative hysteretic energy. There, increasing ASR and decreasing ρ_t were observed to negatively impact the total cumulative hysteretic energy. As a result, we expect that the sum of the main effect of ASR presence and the two-way interaction between ASR presence and Stage 5 of the experiment (to failure) will be negative. The same is expected for ρ_t . The expectation is met for ρ_t (the sum is -0.048) but not for ASR (the sum is zero). This occurred because the estimated standard deviation of the δ_{hi} in Equation (6.2) was larger than the estimated standard deviation of the δ_i in Equation (6.1), thereby decreasing the signal to noise ratio, and masking the negative effect of ASR presence on hysteretic energy in the “to failure” stage of the test. The increased standard deviation is due to increasing both the size of the data set and the size of the model (number of regression terms).

6.3 AUGMENTED NORMALIZED PEAK FLEXURAL CAPACITY

The normalized peak flexural capacity response, M_{\max}^+/M_n , in the NIST test program may be augmented with three further test results from Oh et al. (2002), all with the ASR absent condition and varying levels of the transverse reinforcement confinement ratio, ρ_v , between 0.0 % and 2.0 %. For the NIST experiment, peak flexural capacity was normalized to the nominal flexural capacity using nominal yield strength of the reinforcing bars used in the specimens (60 ksi [414 MPa]) for consistency with the companion report Thonstad et al. (2021). However, the peak flexural capacities in Oh et al. (2002) were normalized to the

nominal flexural capacity using the measured, rather than the nominal specified, yield strength of the reinforcing bars in the specimens. For comparison with the data in Oh et al. (2002), the peak flexural capacities for the NIST experiment were also normalized to the nominal flexural capacity, computed using the measured yield strength of the longitudinal bars in the boundary elements (65.7 ksi [453 MPa], see Section 4.2). Table 6.2 and Figure 6.19 show the combined data from the NIST and Oh et al. (2002) experiments. The negative effect of the presence of ASR on M_{\max}^+/M_n was evident (the ASR present data were all below the ASR absent data). A weak trend with ρ_t was also visible. The methods of Section 6.1 were applied next to quantify these observations.

The estimated regression coefficients (shown by large dark-colored points) for the combined NIST and Oh et al. (2002) M_{\max}^+/M_n data are shown in Figure 6.20, along with 100 bootstrap replicates (shown by small light-colored points). In contrast to the NIST only M_{\max}^+/M_n data, Figure 6.20, shows that both the presence of ASR and decreasing ρ_t negatively affected M_{\max}^+/M_n (the presence of ASR decreased M_{\max}^+/M_n , and as ρ_t decreased M_{\max}^+/M_n decreased). It was estimated that for the level of ε_{ASR} in this study the mean M_{\max}^+/M_n , decreased by about 0.08. This is a decrease of 7 %. As ρ_t decreased from 2 % to 0 %, the estimated mean M_{\max}^+/M_n decreased by about 0.05. This is a decrease of 4 %. We note that the negative effect of decreasing ρ_t on M_{\max}^+/M_n was driven primarily by the data point from the NIST experiment corresponding to the ASR absent condition with $\rho_t = 2.0$ %

Figure 6.21 depicts the estimated mean M_{\max}^+/M_n for four combinations of ε_{ASR} and ρ_t (shown by large dark-colored points), and 100 bootstrap replicates of the estimated mean M_{\max}^+/M_n (shown by small light-colored points) considering the combined data from NIST and Oh et al. (2002). As with the corresponding NIST data only results in Section 6.2.6, the highest estimated mean normalized flexural capacity was realized for the ASR absent and $\rho_t = 2.0$ % combination and is 1.19. The lowest estimated mean occurred for the ASR present and $\rho_t = 0.0$ % combination and was 1.06. Between the two cases, there was a reduction of 11 %. For the case where ASR was absent, both the estimated mean M_{\max}^+/M_n and most of the bootstrap replicates, were larger than one. For the case where ASR was present and $\rho_t = 0$ %, the estimated mean M_{\max}^+/M_n and 86 % of the bootstrap replicates were greater than one.

Table 6.2. Normalized peak flexural capacity for the NIST wall specimens and the specimens from Oh et al. (2002). In contrast to Table 6.1, the peak flexural capacity is normalized to the measured yield strength of the reinforcing bars instead of the nominal yield strength.

ϵ_{ASR}	ρ_t (%)	Normalized peak flexural capacity (M_{max}^+/M_n)	Experiment
Present (≥ 0.25 %)	0.5	1.089	NIST
Present (≥ 0.23 %)	2.0	1.098	NIST
Present (≥ 0.25 %)	0.5	1.061	NIST
Absent (0.0 %)	2.0	1.261	NIST
Absent (0.0 %)	0.99	1.171	Oh et al. (2002)
Absent (0.0 %)	1.97	1.124	Oh et al. (2002)
Absent (0.0 %)	0.0	1.122	Oh et al. (2002)

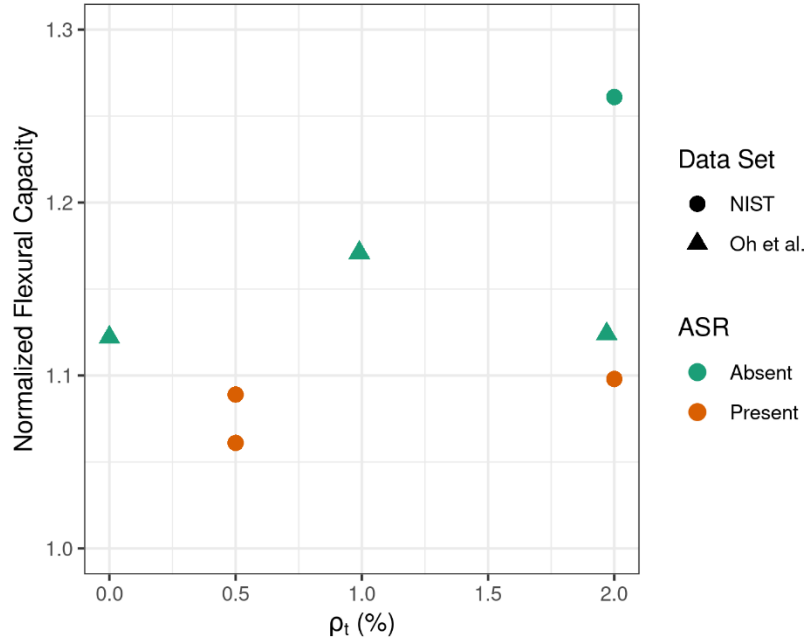


Figure 6.19: Normalized peak flexural capacity response for both the NIST experiments and the experiments from Oh et al. (2002), but with peak flexural capacity from the NIST experiment normalized similarly to the data from the experiments in Oh et al. (2002). Colors delineate ASR condition, and shape delineates experiment.

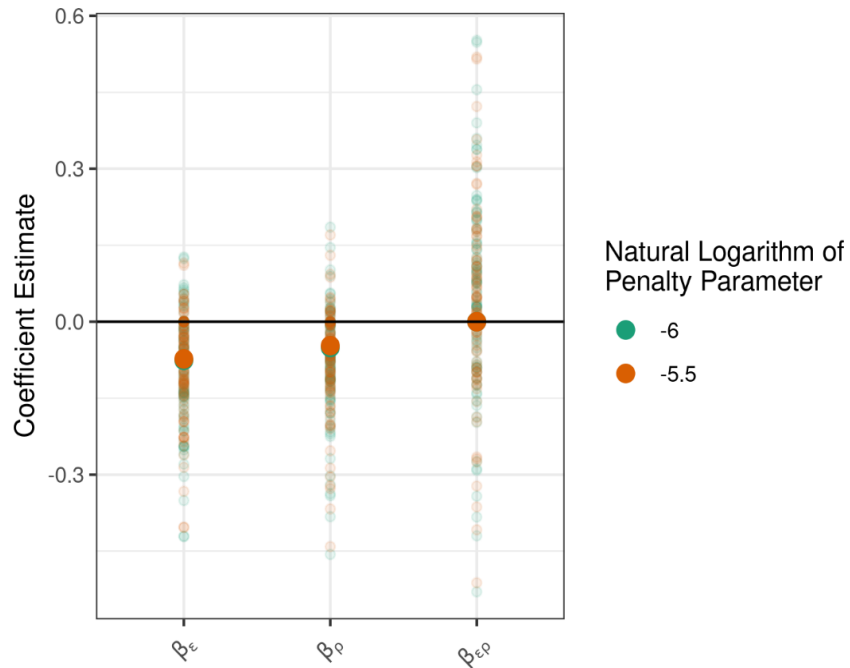


Figure 6.20: Estimated regression coefficients for two LASSO penalties (large dark-colored points) and bootstrap replicates of them (small light-colored points) for the M_{\max}^*/M_n

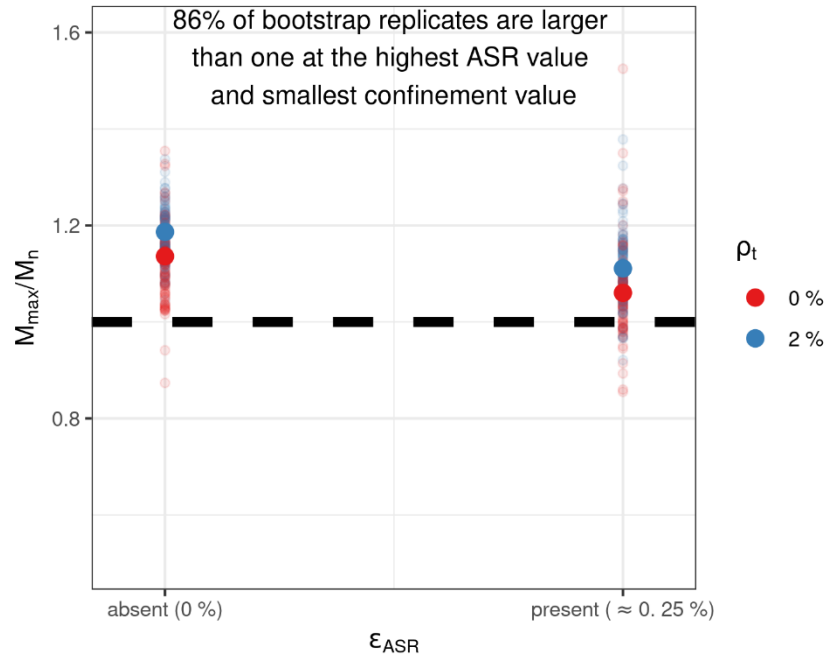


Figure 6.21: Estimated mean normalized peak flexural capacity for four combinations of ϵ_{ASR} and ρ_t (large dark-colored points), and 100 bootstrap replicates of the estimated mean M_{max}^*/M_n (small light-colored-points).

6.4 SUMMARY

A statistical analysis of the measured shear wall test data was conducted to quantify the influence of ASR-induced expansion and ρ_t on the following response variables (indicators of wall performance):

- Deformation capacity variables: including cumulative drift capacity, drift at yield moment, drift at peak flexural capacity, drift at 20 % reduction in peak flexural capacity, and peak drift capacity (or ductility)
- Flexural capacity variables: including normalized yield moment M_y/M_n , and normalized peak flexural capacity, M_{max}^*/M_n
- Energy dissipation capacity variables: including hysteretic energy by stage (at a given drift level corresponding to a certain performance objective) and total cumulative hysteretic energy.

The following provides a summary of the methodology and results. The summary should be interpreted within the scope of the experimental program and the ranges of experimental variables examined including the ASR-induced expansion and the confinement in the boundary elements.

- The least absolute selection and shrinkage operator (LASSO) was used to estimate the effects of the Alkali Silica Reaction (ASR) and confinement on measurements of concrete performance.
- A parametric bootstrap algorithm was used to quantify uncertainty in the quantities being estimated by the LASSO, such as the regression coefficients and the mean values.

Deformation Capacity Variables:

- The presence of ASR and decreasing the ρ_t were both found to reduce the mean cumulative drift capacity, 10 % and 20 %, respectively. When $\rho_t = 2.0$ %, the estimated relative reduction in the mean cumulative drift capacity due to ASR is 8 %, and when $\rho_t = 0.5$ % it is 9 %. When ASR is absent, the estimated relative reduction in mean cumulative drift capacity due to decreasing ρ_t from 2.0 % to 0.5 % is 17 %, and when ASR is present, it is 16 %. There was no evidence that presence of ASR and ρ_t interact for cumulative drift capacity, i.e., the effect of one is not found to depend on the value (magnitude) of the other.
- The presence of ASR was found to reduce the mean drift at yield moment, d_y , by about 54 %, but there was no evidence for d_y that ρ_t had an effect or that ASR and ρ_t interacted.
- The presence of ASR was found to negatively impact (result in a reduction in) mean drift at peak flexural capacity, $d_{M_{\max}}^+$, by about 23 %, but there was no evidence for $d_{M_{\max}}^+$ that ρ_t had an effect or that ASR and ρ_t interacted.
- Decreasing the ρ_t was found to negatively impact (result in a reduction in) drift at 20 % reduction in flexural capacity, d_u , by about 21 % (going from $\rho_t = 2.0$ % to $\rho_t = 0.5$ %), but there was no evidence that the presence of ASR affected d_u , and there was no evidence that the effect of ρ_t changed with the level of ASR, i.e., no evidence of an interaction.
- At the highest $\rho_t = 2.0$ %, both walls, the one affected by ASR and the one that was not, reached a peak drift ratio, d_{fail} , of 4 %. The two walls tested at $\rho_t = 0.5$ % reached a d_{fail} of 3 %.

Flexural Capacity Variables:

- The presence of ASR was found to decrease normalized peak flexural capacity, M_{\max}^+/M_n , by about 0.13 or 0.14 (10 % or 11 %), depending on the chosen LASSO penalty, but no evidence was found that ρ_t affected M_{\max}^+/M_n or that the effect of the presence of ASR changed with ρ_t , i.e., no evidence of an interaction.
- For the combination, ASR present and $\rho_t = 0.5$ %, the estimated mean normalized peak flexural capacity, M_{\max}^+/M_n , is at its lowest, about 1.14, and 94 % of the bootstrap replicates of it are above one.
- The presence of ASR was found to decrease normalized yield moment, M_y/M_n , by about 26 %, but no evidence was found to indicate that ρ_t affects M_y/M_n or that the effect of the presence of ASR changed with ρ_t , i.e., no evidence of an interaction.
- For ASR-affected walls, for both values of ρ_t , the mean value of M_y/M_n was estimated to be less than one. For the combination, ASR present and $\rho_t = 0.5$ %, the estimated mean M_y/M_n is at its lowest, about 0.75, and 89 % of the bootstrap replicates of it are below one.
- When the four NIST measurements of normalized peak flexural capacity, M_{\max}^+/M_n , were combined with three other measurements from Oh et al. (2002), both the presence of ASR and decreasing ρ_t were found to reduce the mean value of M_{\max}^+/M_n , the presence of ASR by about 7 % and ρ_t by about 4 %, but there was no evidence of an interaction between them.
- For the combined NIST and Oh et al. (2002) data, for the combination, ASR present and $\rho_t = 0$ %, the estimated mean M_{\max}^+/M_n was at its lowest, about 1.06, and 86 % of the bootstrap replicates of it were above one.

Energy Dissipation Capacity Variables:

- The presence of ASR and decreasing ρ_t were both found to negatively impact (both result in a reduction in) mean cumulative hysteretic energy: the presence of ASR by about 14 % when $\rho_t = 2.0$ %, and decreasing ρ_t from 2.0 % to 0.5 % by about 20 % when ASR is present. There was no evidence that ASR and ρ_t interact for cumulative drift capacity, i.e., the effect of one is not found to depend on the value (magnitude) of the other.

In all but the final performance objective (to failure), increasing ASR and decreasing ρ_t were found to positively impact (both result in an increase in) hysteretic energy.

Chapter 7

SUMMARY, FINDINGS, AND CONCLUSIONS

7.1 SUMMARY

A series of four reinforced concrete shear wall specimens were tested under vertical (gravity) and lateral cyclic loading. Three specimens had wall panels constructed with reactive aggregates, while one reference specimen had its wall panel constructed using the same reactive aggregates treated with a lithium nitrate solution to mitigate alkali-silica reaction (ASR). The reactive wall specimens were cured in an environmental chamber prior to testing to accelerate ASR-induced expansion. The testing program was developed to examine the influence of ASR-induced expansion/degradation and confinement, provided by stirrups in the boundary elements, on the shear walls' cyclic performance, which was characterized by their strength, ductility, and energy dissipation capacity. In addition, the applicability of existing ACI code equations for the estimation of the flexural capacity of shear walls affected by ASR was assessed.

Specifically, the effects of the following two primary variables were investigated:

- the level of ASR-induced expansion, $0 \% \leq \epsilon_{ASR} \leq 0.25 \%$, measured as averaged maximum recorded strains in the reinforcing bars in the wall panels prior to cyclic testing; and
- the level of confinement in the boundary elements of the wall panels, $0.5 \% \leq \rho_t \leq 2.0 \%$, as measured by the volumetric ratio of transverse reinforcement in the boundary element.

The experiment design specified the following four walls: Walls 1 and 3 with $\rho_t = 0.5 \%$, and Walls 2 and 4 with $\rho_t = 2.0 \%$. Wall 4 used non-reactive concrete ($\epsilon_{ASR} = 0 \%$), while reactive Walls 1, 2, and 3 were tested when the averaged maximum recorded ASR-induced strain was in the range of $0.23 \% \leq \epsilon_{ASR} \leq 0.25 \%$.

The influence of the above two variables on the walls' structural performance was investigated, in terms of their:

- Deformation capacity: including drift at yield moment, d_y ; drift at peak flexural capacity, $d_{M_{max}}^*$; drift at 20 % reduction in flexural capacity, d_u ; peak drift capacity (or ductility), d_{fail} ; and cumulative drift capacity;
- Flexural capacity: including normalized yield moment capacity, M_y/M_n , and normalized peak moment capacity, M_{max}^*/M_n ;
- Energy dissipation capacity: the hysteretic energy by stage (at a given drift level corresponding to a certain performance objective), where the hysteretic energy in a given cycle is calculated as the area bounded by the hysteresis loop; and the total cumulative hysteretic energy.

The geometry and the reinforcement ratios of the NIST wall specimens were selected to match walls previously tested by Oh et al. (2002). Each wall panel had a rectangular cross section of 8.00 in (203 mm) thick \times 60.0 in (1520 mm) long, and a height between the footing and the top cap of 80.0 in (2030 mm).

All four NIST wall specimens had a longitudinal reinforcement ratio ρ_l of 0.61%. The wall panel reinforcement consisted of the following:

- In each boundary element, four No. 4 (0.5 in [12.7 mm] diameter) longitudinal bars were used along with transverse reinforcement consisting of closed No. 3 (0.375 in [9.5 mm] diameter) stirrups, with 135° hooks. The spacing between the stirrups in the boundary elements of Walls 2 and 4 was 4.0 in (102 mm) O.C., resulting in a ρ_t of 2.0%, while for Walls 1 and 3, the stirrups were spaced at 16.0 in (406 mm) O.C., resulting in a ρ_t was 0.5%.
- For the web between the two boundary elements, six No. 3 longitudinal bars, spaced at 8.80 in (224 mm) O.C. along with eight No. 3 transverse bars, spaced at 10.0 in (254 mm) O.C., were used on each face of the wall.

Reactive Walls 1, 2, and 3 were cured in an environmental chamber to accelerate Alkali Silica reaction. For the first four months after casting, the chamber was kept at ambient conditions (temperature of about 75 °F [23.9 °C] to 80 °F [26.7 °C] and RH in the range of 50% to 75%). After this initial period, the curing condition was increased to the range of 95% to 100% RH and 80 °F (26.7 °C) to 90 °F (32.2 °C), which allowed the ASR expansion to accelerate until approximately 10.5 months after casting. At this time, due to the laboratory closure as a result of the COVID-19 pandemic, the environmental controls in the chamber were shut down for almost four months. During the laboratory closure, the three reactive walls were exposed to ambient conditions of about 75 °F [23.9 °C] to 90 °F [32.2 °C] and 50% to 75% RH. Upon reopening of the laboratory 14.5 months after wall panel casting, the environmental conditions were restored to the same RH and temperature levels as those prior to the laboratory closure (95% to 100% RH and 80 °F [26.7 °C] to 90 °F [32.2 °C]) until the walls were removed for structural testing.

To measure their cyclic performance, all four specimens were subjected to a constant axial compression (applied in force control) of 200 kip (890 kN), equivalent to $0.093 A_g f'_c$ (where A_g is the gross sectional area of the wall (480 in² [3096.8 cm²]) and f'_c is the specified compressive strength of concrete (4500 psi [31 MPa])), and reversed cyclic lateral load (applied in displacement control) based on a prescribed protocol with increasing drift ratios to failure. The walls failed primarily in a flexural mode, with yielding, and in some cases rupture, of longitudinal reinforcement in the boundary element on the tensile zone and buckling of longitudinal bars along with spalling/crushing of concrete in the compression zone.

Statistical analyses of the measured data were conducted to quantify the influence of ASR-induced expansion, ϵ_{ASR} , and level of transverse reinforcement in the boundary element, ρ_t , on the deformation, flexural, and energy dissipation capacities of the test specimens. These analyses also assessed the applicability of current ACI code equations for estimating the flexural capacity of reinforced concrete shear walls affected by ASR.

7.2 FINDINGS

The findings of the NIST experimental program are summarized below. These findings are valid only within the ranges of primary experimental parameters examined (ϵ_{ASR} of about 0.25%; $0.5\% \leq \rho_t \leq 2.0\%$ and $h_w/l_w = 2.0$). NIST does not have data to support extrapolation or interpretation of these findings beyond the ranges of the above experimental parameters directly examined by this study.

7.2.1 Effects of ASR on concrete expansion and reinforcing bar strain development, concrete mechanical properties, and concrete cracking

Concrete Expansion and Reinforcing bars Strain Development

- No significant differences were observed between the ASR-induced expansions, ϵ_{ASR} , of the three reactive concrete shear walls, measured as averaged maximum recorded strain on the reinforcements. Taken together, strain data from the three reactive walls showed that the largest recorded strain measurement was about 0.25 % for Walls 1 and 3 and 0.23 % for Wall 2 at the end of the curing period and prior to structural testing. These strain values might have been exceeded in the reinforcing bars that experienced yielding since no meaningful data was available after yielding.
- ASR-induced expansion was less for regions with more restraint. In general, for the longitudinal reinforcing bars in the boundary elements, strain gages near the footings, which were cast from conventional, nonreactive concrete, recorded less strains than those placed at mid-height of the wall panel. Similarly, transverse bars at mid-height of the wall also recorded the largest tensile strains, being farther from the constraint of the wall's footing and top cap. This trend was expected due to the restraint to the wall expansion provided by the non-expansive wall's footing and top cap.
- Unrestrained ASR-induced concrete linear expansion, measured using unreinforced standard prisms made with the same concrete and cured under the same regime as the reactive wall specimens, was up to 0.25 %. This level of unrestrained concrete linear expansion was consistent with the averaged maximum recorded strain measured by strain gages on the reinforcing bars of the reactive wall specimens ($\epsilon_{ASR} = 0.25$ % for Walls 1 and 3, and = 0.23 % for Wall 2, see above and Section 4.5). However, this is likely just a coincidence as the strain recorded at various discreet locations on the reinforcements might actually underrepresent the overall walls' expansion (strain gages not located at places where maximum expansion occurred and gages malfunctioned shortly after yielding of the reinforcements).
- Toward the end of the curing period and prior to structural testing, several reinforcing bars might have yielded or were approaching yielding. These included the longitudinal bars in the boundary elements at approximately mid-height (between 10.0 in [254 mm] and 40.0 in [1016 mm] above the footings) and the transverse reinforcing bars at different heights.
- The average ASR-induced strains in the longitudinal bars in the boundary elements at their interface with the footings was found to be 0.113 % \pm 0.013 %. This value was taken as the pre-existing, ASR-induced, pre-strain at the base of the wall where failure is expected to start and propagate during cyclic testing.

Concrete Mechanical Properties

- Concrete mechanical properties, measured by standard testing at different ages of 4.0 in (102 mm) \times 8.0 in (203 mm) cylinders that were cast at the same time with the wall specimens and cured under the same environmental conditions, decreased with increasing ASR-induced expansion. The maximum reductions, relative to their measured 28-day values, were about 30 %, 70 %, and 40 % for the

compressive strength, compressive modulus of elasticity, and splitting tensile strength, respectively. These decreases in the mechanical properties are consistent with the findings of the Task 1 report (Sadek et al., 2021) and Task 2 report (Thonstad et al., 2021), albeit with different reduction magnitudes. For the non-reactive cylinders from Wall 4, no such reduction in compressive strength, compressive modulus of elasticity, or tensile strength was observed. On the contrary, strengths of the non-reactive concrete were consistently larger than their measured 28-day values.

- The relationship between the concrete modulus of elasticity and the compressive strength for normalweight, nonreactive concrete prescribed by ACI 318-19 (Section 19.2.2.1(b)) overpredicted the compressive modulus of the reactive concrete by up to 50 %. This was particularly evident at higher expansion values and indicates that the modulus of elasticity degraded faster with increased ASR expansion than did the compressive strength. This was consistent with the findings of the Task 1 report (Sadek et al., 2021) and Task 2 report (Thonstad et al., 2021).

Concrete Cracking

- Significant ASR-induced surface cracking was observed on all three reactive wall panels prior to structural testing, along with exudation of a substance, presumed to be ASR gel, from the cracks onto the panel surfaces. The pattern of ASR-induced cracking was randomly oriented and did not appear to be preferentially aligned with the embedded reinforcement. No discoloration was observed that would suggest corrosion of the reinforcement bars prior to structural testing. No discernable differences were found between the cracking pattern on the surfaces of the three reactive wall panels despite their differences in age at the time of observation and the amount of transverse confinement in the boundary elements.

7.2.2 Effects of ϵ_{ASR} and ρ_t on walls' structural capacities

Deformation Capacity

- Both the presence of ASR and decreasing the transverse reinforcement ratio in the boundary elements, ρ_t , were found to have a decrease the walls' cumulative drift capacity, causing a reduction of 10 % and almost 20 %, respectively. Relative to the ASR absent and $\rho_t = 2.0$ % combination, these are decreases of 8 % and 16 %, respectively. The regression model (see Equation 6.1) showed that from a wall without ASR and high ρ_t (ASR absent [$\epsilon_{ASR} = 0$ %] and $\rho_t = 2.0$ %) to a wall with ASR and low ρ_t (ASR present [$\epsilon_{ASR} = 0.25$ %] and $\rho_t = 0.5$ %), the estimated mean cumulative drift capacity decreases by about 10 % + 20 % = 30 % (or 24 % relative). Evidence was not found that the effect of one variable on the walls' cumulative drift capacity depends on the other variable (i.e., no evidence of an interaction).
- The presence of ASR decreased the drift at yield moment d_y (i.e., the presence of ASR decreases d_y). For the level of ϵ_{ASR} examined in this study (≤ 0.25 %), the mean d_y of reactive Walls 1, 2, and 3 decreased by 54 % when compared with that of non-reactive Wall 4. This decrease is attributed to the ASR-induced pre-strain in the longitudinal reinforcing bars of the three reactive specimens prior to structural testing, which led to the onset of inelasticity at lower drift ratios during testing. There was

no evidence that decreasing transverse reinforcement ratio in the boundary element, ρ_t , affects drift at yield moment d_y .

- The presence of ASR also negatively affected drift at peak flexural capacity $d_{M_{max}}^+$. By direct comparison, the average $d_{M_{max}}^+$ in negative and positive flexure of reactive Walls 1 through 3 were 50.7 % and 56.8 %, respectively, relative to those of non-reactive, control Wall 4. The statistical analysis estimated that, for the level of ε_{ASR} considered in this study, there was a reduction of 23 % in the mean $d_{M_{max}}^+$ when ASR is present. There was no evidence that decreasing transverse confinement ratio ρ_t affects drift at peak flexural capacity $d_{M_{max}}^+$.
- There was no evidence that the presence of ASR affected drift at 20 % reduction in flexural capacity, d_u , while decreasing transverse reinforcement ratio decreased d_u . It is estimated that decreasing ρ_t from 2.0 % to 0.5 % caused a 21 % reduction in d_u .
- The walls' ductility, measured by the peak drift capacity d_{fail} , was not adversely affected by the presence of ASR for any of the walls tested; however, ductility was influenced by the transverse reinforcement ratio, ρ_t , in the boundary elements; i.e., decreasing ρ_t resulted in decreasing d_{fail} . Both specimens with $\rho_t = 0.5$ % achieved $d_{fail} = 3.0$ % drift ratio, while both specimens with $\rho_t = 2.0$ % achieved $d_{fail} = 4.0$ % drift ratio. These observations were made only from inspection of the test data. The statistical methods of Chapter 6 were not applied for the reasons discussed within it.
- Reduction of the initial stiffness of the ASR-affected walls' force-drift flexural response, K , (see Chapter 5) was not observed despite the observed ASR-induced cracking and reduction of concrete mechanical properties.

Flexural Capacity

- The presence of ASR led to a statistically significant reduction of the yield moment of the walls of about 26 % in the walls' mean normalized yield moment capacity, M_y/M_n . None of the ASR-affected walls met the ACI 318-19 design criteria, which is based on yielding of the longitudinal bars in the boundary elements ($M_y/M_n < 1.0$), the estimated mean value of M_y/M_n was less than 1.0, and approximately 90 % of the bootstrap replicates of the estimated mean of M_y/M_n were less than 1.0.
- The presence of ASR also led to a statistically significant reduction of the peak flexural capacity of the walls. The measured average peak flexural resistance in negative and positive flexure of reactive Walls 1 through 3 were 85.6 % and 88.1 %, respectively, relative to those of the non-reactive control wall specimen (Wall 4). Averaging the measured flexural capacities in both negative and positive flexure, the presence of ASR was estimated to cause a reduction of about 11 % in the walls' mean normalized peak flexural capacity M_{max}^+/M_n .
- There was no evidence that variation of the transverse reinforcement ratio, ρ_t , in the walls' boundary elements ($0.5 \leq \rho_t \leq 2.0$ %) had an effect on either walls' normalized yield moment (M_y/M_n) or normalized peak flexural capacity (M_{max}^+/M_n).

Energy Dissipation Capacity

- The presence of ASR and decreasing ρ_t reduced cumulative hysteretic energy. Relative to the ASR absent and $\rho_t = 2.0\%$ combination, for the level of ϵ_{ASR} in this study, it is estimated that the mean cumulative hysteretic energy decreases by 14% with the presence of ASR, and changing ρ_t from 2.0% to 0.5% is estimated to cause a decrease in mean cumulative hysteretic energy by about 17%.
- The presence of ASR generally increased the amount of hysteretic energy dissipated in a given cycle, because reactive walls yielded at lower drift ratios, due to the ASR-induced pre-strain in the longitudinal bars of their boundary elements, leading to increased inelasticity and energy dissipation at lower drifts.
- The non-reactive, control Wall 4 specimen dissipated the largest total hysteretic energy, not because it dissipated more energy per cycle, but because it achieved the largest cumulative drift capacity compared with the three reactive Walls 1 through 3.

Behavior and Failure Modes

- Non-reactive Wall 4 and reactive Wall 2, both with $\rho_t = 2.0\%$, exhibited flexural-shear behavior characterized by a combination of horizontal and diagonal cracks. Reactive Wall 1 and 3, both with $\rho_t = 0.5\%$, exhibited predominantly flexural behavior that was characterized primarily by horizontal cracks. In all reactive walls, cracks already present at the beginning of testing due to ASR-induced expansion then grew and propagated with increased drift ratio.
- Under the cyclic load testing of the four walls, the walls failed primarily in a flexural mode, with (1) buckling of longitudinal reinforcement in the boundary element resulting in spalling/crushing of concrete and exposing of the buckled reinforcement at the compression zone, and (2) excessive yielding and in some cases fracture of the longitudinal reinforcing bars of the boundary element on the tensile zone. Reactive Walls 1 and 3 with $\rho_t = 0.5\%$ lost their axial capacity and collapsed in a “squash mode” under the effect of the 200 kip (890 kN) vertical load that was still in effect.

7.3 CONCLUSIONS

This Task 3 study investigated the effects of ASR and transverse reinforcement confinement ratio, ρ_t , on the structural performance of reinforced concrete shear walls by testing a series of four wall specimens: three ASR reactive and one non-reactive (control), under constant axial compression and reversed cyclic lateral displacements. The conclusions presented below, and the specific findings presented above, should be interpreted within the scope of the experimental program conducted and the ranges of experimental variables examined:

- Consistent with observations made in the NIST Task 1 report (Sadek et al., 2021) and Task 2 report (Thonstad et al., 2021), the presence of ASR caused significant cracking and degradation in concrete mechanical properties of the NIST shear wall specimens (30%, 70%, and 40% reduction in compressive strength, modulus of elasticity, and splitting tensile strength, respectively).

- The presence of ASR and its associated effects on concrete material properties and cracking were found to cause statistically significant degradation in the structural capacities of shear walls. Specifically, within the bounds of the experimental parameters examined, the presence of ASR caused a reduction of 11 % in the mean normalized peak moment capacity (M_{max}^*/M_n) and of 26 % in the mean normalized yield moment capacity (M_y/M_n) of the shear walls tested in this program.
- More importantly, the structural capacity degradation resulted from the presence of ASR brought the normalized yield moment capacity ratios M_y/M_n for all ASR-affected walls in this test program to less than 1.0 (0.79, 0.67, and 0.68 for Walls 1, 2, and 3, respectively). As the nominal wall's moment capacity M_n is computed using ACI 318 calculation procedure based on yielding of the longitudinal bars in the wall, the measured yield moment capacity M_y being less than M_n means that ACI 318 capacity calculation procedure is unconservative and not applicable for walls affected by ASR.
- Since the NIST test program effectively examined only two ASR expansion levels ($\epsilon_{ASR} = 0\%$ and $0.23\% \leq \epsilon_{ASR} \leq 0.25\%$), it's not possible to interpolate to determine the effect of intermediate expansion levels within those two limits on the walls' structural capacity with statistical confidence.
- ASR also caused statistically significant degradation in the walls' deformation and energy dissipation capacities, including drift at yield moment d_y , drift at peak flexural capacity d_{Mmax}^* , and cumulative hysteretic energy.
- While increasing the transverse reinforcement ratio in the boundary element ρ_t was not found to influence the walls' peak flexural capacity, the reduction in the deformation and energy dissipation capacity with the presence of ASR was less severe for shear walls with higher ρ_t .
- Finally, the completion of this NIST Task 3 test program has provided the second set of known experimental data examining the effect of ASR on shear wall's structural performance beside that of Habibi et al. (2018) to date. While important knowledge and understanding have been developed as a result, it's important to recognize that there are still limitations, mostly due to the experimental parameters studied, that make comparison and generalization of the findings from both test programs beyond the range of experimental parameters not advisable. Additional test data of shear walls with different cross-sectional geometry (I-shaped and rectangular cross section); wall height-to-length aspect ratios h_w/l_w (between and beyond 1.1 tested by Habibi et al. and 2.0 tested by NIST and Oh et al.), with and without wall boundary elements; and intermediate and additional levels of ASR expansion ($0.0\% \leq \epsilon_{ASR} \leq 0.3\%$) would be needed before interpolation or extrapolation of the experimental results for predicting the performance of walls with different design parameters can be considered appropriate.

REFERENCES

ACI 318-14. Building Code Requirements for Structural Concrete, American Concrete Institute, Farmington Hills, MI, 2014.

ACI 318-19. Building Code Requirements for Structural Concrete, American Concrete Institute, Farmington Hills, MI, 2019.

ACI-ASCE Committee 445-B (2017). *408R-03: Structural Wall Performance Database*. Farmington Hills, MI, American Concrete Institute-American Society of Civil Engineers, 2008, url: https://purr.purdue.edu/dataviewer/view/publication:dsl/prj_db_1217_73f6b9aac89601c528539ffc83c2b7afae6aca35/?v=1.

ASTM C39/C39M-20. Standard Test Method for Compressive Strength of Cylindrical Concrete Specimens, ASTM International, West Conshohocken, PA, 2017.

ASTM C469/C469M-14. Standard Test Method for Static Modulus of Elasticity and Poisson's Ratio of Concrete in Compression, ASTM International, West Conshohocken, PA, 2014.

ASTM C496/C496M-17. Standard Test Method for Splitting Tensile Strength of Cylindrical Concrete Specimens, ASTM International, West Conshohocken, PA, 2017.

ASTM A615/A615M-20, Standard Specification for Deformed and Plain Carbon-Steel Bars for Concrete Reinforcement, ASTM International, West Conshohocken, PA, 2020

ASTM A370-19e1, Standard Test Methods and Definitions for Mechanical Testing of Steel Products, ASTM International, West Conshohocken, PA, 2019

ASTM C1293-20, Standard Test Method for Determination of Length Change of Concrete Due to Alkali-Silica Reaction, ASTM International, West Conshohocken, PA, 2020

ASTM E83-16, Standard Practice for Verification and Classification of Extensometer Systems, ASTM International, West Conshohocken, PA, 2016

ASTM C33 / C33M-18, Standard Specification for Concrete Aggregates, ASTM International, West Conshohocken, PA, 2018

Fournier, B., Bérubé, M.-A., Folliard, K.J., and Thomas, M.D.A. (2010), Report on the Diagnosis, Prognosis, and Mitigation of Alkali-Silica Reaction (ASR) in Transportation Structures, FHWA-HIF-09-004, Federal Highway Administration, McLean, VA.

Habibi, F., Sheikh, S.A., Vecchio, F., and Panesar, D.K. (2018) "Effects of Alkali-Silica Reaction on Concrete Squat Shear Walls" *ACI Structural Journal*, V. 115(5): 1329-1339

- Hansen, W.C., (1944), "Studies relating to the mechanism by which the alkali-aggregate reaction produces expansion in concrete", *Journal of the American Concrete Institute*, Vol. 15, p. 213-227.
- Hastie, Trevor, Robert Tibshirani, and Martin Wainwright. *Statistical learning with sparsity: the lasso and generalizations*. CRC press, 2015.
- Oh, Y.-H, Sang, W. H., and Li-Hyung, L. (2002), Effect of Boundary Element Details on the Seismic Deformation Capacity of Structural Walls, *Earthquake Engineering & Structural Dynamics*, 31 (8): pp. 1583–1602.
- PEER/ATC (2010). Modeling and acceptance criteria for seismic design and analysis of tall buildings, PEER/ATC 71-1 Report, Applied Technology Council, Redwood City, CA, October 2010.
- Phan, L.T., Sadek, F, Thonstad, T.E., Lew, H.S., Marcu, S., Philip, J., (2019), "Effects of Alkali-Silica Reaction on Mechanical Properties and Structural Capacities of Reinforced Concrete Structures" *Structural Mechanics in Reactor Technology (SMiRT) 25*, Charlotte, NC, United States, August 2019.
- Pugh, J., Lowes, L. N., and Lehman, D. E. (2015). "Nonlinear Line-Element Modeling of Flexural Reinforced Concrete Walls", *Engineering Structures*, 104, pp. 174-192.
- Sadek, F., Thonstad, T., Marcu, S., Weigand, J.M., Barrett, T.J., Lew, H.S., Phan, L.T., and Pintar, A.L. (2021) "Structural Performance of Nuclear Power Plant Concrete Structures Affected by Alkali-Silica Reaction (ASR) Task 1: Assessing In-Situ Mechanical Properties of ASR-Affected Concrete" NIST TN 2121, National Institute of Standards and Technology, Gaithersburg, Maryland.
- Stanton, T.E. (1940), "Expansion of Concrete Through Reaction Between Cement and Aggregate," *Proceedings, American Society of Civil Engineers*, Vol. 66, p. 1781-1811.
- Taylor, H.F.W. (1990), *Cement Chemistry*, Academic Press, New York.
- Tibshirani, R. (1996). "Regression Shrinkage and Selection via the Lasso." *Journal of the Royal Statistical Society: Series B (Methodological)* 58 (1): 267–88.
- Thonstad, T., Weigand, J. M., Sadek, F., Marcu, S. Barrett T. J., Lew, H.S., Phan, L. T., and Pintar, A. L. (2021) "Structural Performance of Nuclear Power Plant Concrete Structures Affected by Alkali-Silica Reaction (ASR) - Task 2: Assessing Bond and Anchorage of Reinforcing Bars in ASR-Affected Concrete" NIST TN 2127, National Institute of Standards and Technology, Gaithersburg, Maryland.
- Zou, H., Hastie, T., and Tibshirani, R. (2007). "On the "degrees of freedom" of lasso." *Ann. Statist.* 35 (5), pp. 2173-2192, October 2007.

APPENDIX A

MEASUREMENT UNCERTAINTIES

This appendix presents measurement uncertainties for the instruments/devices used to measure structural responses in this report. The coverage factor k , used in converting the combined standard uncertainty to total expanded uncertainty, was taken as 2.

Table A-1. Measurement Uncertainty

Measurement/Component	Type	Component Standard Uncertainty	Combined Standard Uncertainty	Total Expanded Uncertainty (k=2)
<i>Actuator position</i>				
Uncertainty in secondary standard	B	0.2 mm (0.006 in)	0.2 mm (0.007 in)	0.4 mm (0.015 in)
Uncertainty in calibration procedure (N=32)	A	0.2 mm (0.004 in)		
<i>Actuator load</i>				
Uncertainty in secondary standard	B	1.3 kN (0.3 kip)	1.3 kN (0.3 kip)	2.6 kN (0.6 kip)
Uncertainty in calibration procedure (N=32)	A	0.4 kN (0.1 kip)		
<i>Compressive Stress, 4 in × 8 in Concrete Cylinder</i>				
Uncertainty in secondary standard	B	165 kPa (23.9 psi)	174 kPa (25.2 psi)	347 kPa (50.4 psi)
Uncertainty in calibration procedure (N=32)	A	54.9 kPa (7.96 psi)		
<i>Compressive Stress, 6 in × 12 in Concrete Cylinder</i>				
Uncertainty in secondary standard	B	73.2 kPa (10.6 psi)	77.1 kPa (11.2 psi)	154 kPa (22.4 psi)
Uncertainty in calibration procedure (N=32)	A	24.4 kPa (3.54 psi)		
<i>Compressive Stress, 3 in × 6 in Concrete Core</i>				
Uncertainty in secondary standard	B	341 kPa (49.4 psi)	359 kPa (52.1 psi)	718 kPa (104 psi)
Uncertainty in calibration procedure (N=32)	A	114 kPa (16.5 psi)		

Table A-1 (Continued): Measurement Uncertainty

Measurement/Component	Type	Component Standard Uncertainty	Combined Standard Uncertainty	Total Expanded Uncertainty (k=2)
<i>Axial Extensometer, 4 in gage length</i>				
Uncertainty in secondary standard	A/B	1.52 μm (0.00006 in)	16.9 μm (0.00066 in)	33.7 μm (0.00132 in)
Uncertainty in calibration procedure (N=20)	A	16.8 μm (0.00066 in)		
<i>Axial Extensometer, 2 in gage length</i>				
Uncertainty in secondary standard	A/B	1.52 μm (0.00006 in)	20.2 μm (0.00079 in)	40.3 μm (0.00158 in)
Uncertainty in calibration procedure (N=20)	A	20.1 μm (0.00079 in)		
<i>Axial Compressive Strain, 4 in \times 8 in Concrete Cylinder (calculated using 4 in gage length axial extensometer)</i>				
Uncertainty in secondary standard	A/B	15.0 $\mu\epsilon$	166 $\mu\epsilon$	331 $\mu\epsilon$
Uncertainty in calibration procedure (N=20)	A	165 $\mu\epsilon$		
<i>Axial Compressive Strain, 3 in \times 6 in Concrete Core (calculated using 2 in gage length axial extensometer)</i>				
Uncertainty in secondary standard	A/B	30.0 $\mu\epsilon$	396 $\mu\epsilon$	792 $\mu\epsilon$
Uncertainty in calibration procedure (N=20)	A	395 $\mu\epsilon$		
<i>Displacement Transducer</i>				
Uncertainty in secondary standard (N=8)	A/B	2 μm (0.00006 in)	0.3 mm (0.01 in)	0.6 mm (0.02 in)
Uncertainty in calibration procedure (N=20)	A	0.3 mm (0.01 in)		